Characterizing Early Cancer Biology through Multiplexed and Multiscale Super-Resolution Microscopy Technique Development

By

Matthew James Rames

A DISSERTATION

Presented to the Department of Biomedical Engineering

of the Oregon Health & Science University

School of Medicine

in partial fulfillment of the requirements for the degree of

Doctor of Philosophy

in Biomedical Engineering

June 2022

Department of Biomedical Engineering
School of Medicine
Oregon Health & Science University

CERTIFICATE OF APPROVAL

This is to certify that the Ph.D. Dissertation of

Matthew James Rames

"Characterizing Early Cancer Biology through Multiplexed and Multiscale Super-Resolution

Microscopy Technique Development"

Has been approved

Mentor: Sadik Esener, Ph.D.
Professor of Biomedical Engineering

Member/Chair: David Qian, Ph.D.
Professor of Cancer Biology

Member: Xiaolin Nan, Ph.D.
Professor of Biomedical Engineering

Member: Young Hwan Chang, Ph.D.
Professor of Biomedical Engineering

Member: Terry K. Morgan
Professor of Biomedical Engineering

Dedication

To my Mom, Dad, and Brother

Acknowledgments

First off, I am indebted to the perseverance and higher calling of the Knight Cancer Challenge and related fund-raising efforts, these paved the way for our work in early cancer detection. Back in 2013, Nike co-founder Phil Knight and his wife, Penney, pledged to match a $500 million donation to the Knight Cancer Institute if OHSU could raise the same amount. Thanks to grassroots philanthropy across Oregon, the United States, and even countries around the world, that calling was met, enabling a $1 billion investment to challenging the way we think of early cancer detection, treatment, and ultimately patients' lives. To lead this endeavor, Dr. Sadik Esener, my eventual mentor, came from the University of California at San Diego and joined OHSU as the director of the Cancer Early Detection Advanced Research center aimed at saving lives by developing advanced technologies to detect cancer early. In joining OHSU, I was keen on also learning from my co-advisor, Dr. Xiaolin Nan, an expert in super-resolution microscopy. I give special thanks to Dr. Nan for giving me the chance to embed within his laboratory and drive shared goals for pushing boundaries in imaging cancer biology. It was his daily mentorship that helped push me, while teaching me to be a scientist. Through many collaborations between the Nan Lab and CEDAR, we developed novel imaging systems which expanded beyond traditional limitations in super-resolution microscopy, and helped me achieve my potential to make an impact in this field. Besides my mentor, Dr. Sadik Esener and my co-advisor Dr. Xiaolin Nan, I would like to thank the rest of my dissertation committee, Dr. Young Hwan Chang, Dr. Terry Morgan, and my committee chair Dr. David Qian who supported and guided me to complete my PhD.

I would like to thank researchers from CEDAR, the Nan Lab, and many others across OHSU who helped me on a variety of amazing research. Dr. Fehmi Civitzi, Dr.

John Kenison, and Dr Daniel Heineck in CEDAR provided immense help in microscope design, engineering, optical designs and fluidics, which were invaluable in realizing novel microscopy methods. I am grateful to Dr. Kai Tao, Dr. Ting Zhang, and Julia Shangguan from the Nan Lab for their ongoing collaborations, especially concerning the design and synthesis of DNA-conjugated affinity reagents, which formed the backbone of most imaging techniques utilized throughout my thesis. I am also very grateful to Nan Lab alumni; Dr. Jing Wang, Dr. Tao Huang, Dr. Ying Zhang, and Dr. Yerim Lee, who were there as a fellow lab-mates to teach me all of the essentials of super-resolution microscopy methodologies from the ground up. I am additionally grateful for all of my CEDAR collaborators whose projects I was fortunate to participate in, Dr. Shandee Dixon, Dr. Michael Brasino, Dr. Thuy Ngo, and Dr. Hyun Ji Kim, among many others. I am especially thankful to Hyun Ji Kim who provided a shining example as a fellow CEDAR graduate student, brainstormed the challenging aspects of early cancer together, and showed endless encouragement for me to work hard. Our work was made much easier thanks to the outstanding laboratory management team: Paul Howard, Jakki Martinez, and Samantha Savage Stevens. I also had thoughtful project advisors: Gene Tu, Bruce Braunchaud, and Dr. Yui Jiu Cho. Dr. Beverly Emerson always provided great career advice and encouragement for me as well.

The collection of works within this thesis could not be done without the support I received from all my collaborators. I also thank Dr. Claudia Lopez, director of the Multiscale Microscopy Core for Transmission Electron Microscopy experience. I also thank all the clinical collaborators; Dr. Gordon Mills, Dr. Rosalie Sears, and Dr. Jason Link. I thank biorespository teams; Katie C. Johnson-Camacho, Dorien Hartunian and Meghan Fitzgerald.

Finally, I must thank my family for their never-ending support, boundless love, extended patience, and unflinching admiration through this long journey.

Table of Contents

List of Figures

List of Abbreviations

SRM	Super Resolution Microscopy
SMLM	Single Molecule Localization Microscopy
TIR	Total Internal Reflection
IF	Immunofluorescence
TIRF	Total Internal Reflection Fluorescence
STORM	Stochastic Optical Reconstruction Microscopy
PALM	Photoactivated Localization Microscopy
STED	Stimulated Emission Depletion
PAINT	Point Accumulation In Nanoscale Topology
DNA-PAINT	Deoxyribonucleic Acid PAINT
NA	Numerical Aperture
DS	Docking Strand
IS	Imaging Strand
FOV	Field of View
FWHM	Full Width Half Maximum
FFPE	Formalin-fixed Paraffin-embedded
PEI	Polyethyleneimine
EC	Ethylene Carbonate
PDAC	Pancreatic Ductal Adenocarcinoma
PanIN	Pancreatic Intraepithelial Neoplasm
WD	Working Distance
Dox	Doxycycline
ROI	Region of Interest
DDR	DNA Damage Response
iPALM	Interferometric PALM
OMM	Outer Mitochondrial Membrane
IMM	Inner Mitochondrial Membrane

Abstract

This thesis work highlights technique development and emerging applications for improving super-resolution microscopy (SRM) throughput, analysis and applications in studying early cancer biology. Despite ongoing improvements in SRM strategies and applications, poor scalability has limited more broad utilization and practicality in leveraging the immense detail afforded by SRM methods. More recent SRM methods like DNA-point accumulation in nanoscale topology (DNA-PAINT) are poised to improve reproducibility and throughput versus traditional SRM methods like stochastic optical reconstruction microscopy (STORM) and photoactivatable localization microscopy (PALM). Despite these ongoing improvements, the current literature presents key challenges which limit the broader adoption of these technologies to image early cancer biology: i) DNA-PAINT imaging speed and traditionally small fields of view (FOV) hinder overall throughput for practical implementation at scale. ii) Although advanced methods for SRM image analysis continue to be developed, these remain far out of reach for general utilization by researchers. iii) Despite inherent feasibility, no studies have successfully used SRM imaging to characterize large-scale complex features in tumor tissue samples. iv) Multiple exciting targets for early cancer biology including detailed mitochondrial dynamics have remained out of reach due to insufficient SRM tools to answer complex biological questions.

In the first two chapters, a breakdown of existing technologies and example applications for SRM highlight the need for novel approaches in scaling-up SRM imaging and improving overall throughput. We found that by modifications to how

DNA-PAINT operates, we can dramatically improve imaging speeds versus traditional DNA-PAINT. To further increase throughput, I then helped design, optimize, and demonstrate a novel microscope capable of imaging very large FOVs (LF-PAINT). The methods proven through these first chapters served as the backbone for later chapters.

Chapters 3 and 4 build from the methods proven in chapter 2 to expand utility in accessible large-scale SRM image analysis as well as key optimizations for expanding LF-PAINT applications to patient tissues. Through integrating multiple open-source image analysis tools, we showed how big-data SRM image analysis can readily quantify subcellular and protein level interactions across thousands of cells. Critically, through utilizing microfluidics coupled to our LF-PAINT microscope, we could overcome tissue-specific limitations. These developments open the door to precisely studying patient tumors at nanometer resolutions across millimeters of complex cancer histology.

Finally, chapter 5 explores the role of mitochondrial dysregulation in early cancer biology, and how SRM is poised to help assess the progression of this hallmark of cancer. Guided by growing interest in mitochondrial dynamics under oncogenic or micro-environmental stress, I demonstrate the feasibility in multiplexed SRM imaging and analysis behind the underlying dynamic complexes governing mitochondrial functions.

In conclusion, this thesis demonstrates the evolving power of SRM to accelerate the understanding of complex biological systems like early cancer. Intriguingly, ongoing efforts are set to boost both multiplexity and 3D imaging capabilities, further expanding the toolkits afforded by advanced SRM techniques. Ultimately, these novel methods push the boundaries of traditional SRM, providing a framework to accelerate multiscale and multiplexed characterizations of precise early cancer phenotypes and mechanisms.

Chapter I: Introduction

1. Introduction to microscopy techniques to study early cancer

Understanding the early transformations and mechanisms of oncological disease are urgently needed to screen for earlier, more treatable stages. Although earlier stage cancers can be asymptomatic, identifying the progression and accompanying abnormal signatures could help in both diagnostics and prognostics. One of the cornerstones of understanding cancer biology has been microscopy, where methods like immunofluorescence can provide targeted views of dysregulated proteins and even assess underlying mechanism behind observed disease. While emerging methods have dramatically improved the multiplexity and spatial characterization in patient tumors, these can lack sufficient resolution to visualize molecular level detail which oncogenic processes function on.

Superresolution microscopy (SRM) has emerged to fill this imaging gap, providing both a targeted view of oncogenic proteins and the ability to spatially resolve alterations in their functional states. While initially most often studied using model systems, direct visualization using SRM from patient tissues has opened the feasibility to directly study molecular mechanisms underlying cancers and even their early precancerous diseases. Overall, throughput, multiplexity, and imaging quality have greatly curtailed SRM and its utility to study population-level molecular drivers both within model systems and importantly directly from patient biopsies.

My thesis work serves as a proof of principle that by improving the scalability and utility of SRM imaging methods we are now poised to directly visualize diffraction limited mechanisms in cancer and cancer progression. Joining OHSU after 4 years of studying electron microscopy at LBNL, I changed my focus to the detail that affinity-reagent

targeted SRM can reveal about the spatial relationship of deregulated proteins in cancer. As a part of the technology hub in the growing Cancer Early Detection Advanced Research center, my focus became to develop novel imaging strategies to make studying molecular level details in earlier stage cancers more approachable. In this first chapter I provide a highlight of the current methods and analysis to study mechanisms in cancer and how SRM can be suited to peer into the complex systems behind cancer progression. To serve as a foundation for later chapters, the power of SRM is contrasted with gaps in its utilization, to which this thesis demonstrates that prior technical limitations toward application can largely be overcome.

1.1 The challenges of studying early cancer

Cancer remains one of the biggest causes of morbidity and mortality worldwide, with ample evidence that outcomes can be dramatically improved when detected and treated early [1]. Many studies into cancer have traditionally focused on understanding the molecular/genic drivers behind cancer aggression as well as developing therapies to curtail common hallmarks of cancer. Cell invasion, replication, genetic dysregulation, anti-apoptotic properties, metabolisms, and immune evasion are all critical aspects can which define cancers [2, 3]. Despite the knowledge of these drivers and emerging targeted therapies, tumor heterogeneity [4] and specific mechanisms such as senescence [5] can hamper many therapies [6]. Although the outcomes of advanced cancers are clearer, understanding the detailed mechanisms behind the paths cancer initially progresses through has been more difficult to study.

Broadly, earlier cancers can be identified both from deregulated cellular pathways as well as phenotypic changes which can occur under some forms of oncogenic stress. Although the path to progression varies dramatically for different cell

and tissue types, cells are first thought to acquire a small subset of oncogenic traits which can cause them to undergo local transformations into precancerous lesions/growths (**Figure 1.1**). Examples of cancers with known and diagnosable high-risk precancerous conditions include: breast cancer (ductal carcinoma in situ) [7], liver cancer (liver cirrhosis) [8], and pancreatic cancer (pancreatic intraepithelial neoplasms) [9]. Conditions like these can exhibit clear tissue dysplasia, metabolic changes, and the emergence of driver mutations. Once established as an early cancer, it can still be difficult to discern the lethality that particular tumors may present, and ultimately the tumor burden incurred on the individual over time (**Figure 1.1**). With earlier detection means a more precise disease trajectory and patient risk stratification must also be established, to avoid overtreatments in cases where cancers may not become malignant or lethal [10].

As one of the most lethal cancers, pancreatic ductal adenocarcinoma (PDAC) could present dramatic improvements to patient survival when detected early. Unfortunately, regular screening of pancreatic irregularities and biopsies are not often performed due to either low sensitivity or severe complications such as pancreatitis [11]. As such PDAC is most often detected when more outward symptoms appear with more advanced stage disease [11]. Intriguingly, genetic studies have been performed on common routes to PDAC including PanINs, which have implicated powerful oncogenes such as mutant KRAS and P53 mutations often occur a decade or more before the onset of cancer [12] and are implicated in cancer progression [13] (**Figure 1.2**). Despite clear histological definitions, the prognostic routes for PanIN progression to PDAC remain intensely studied [9, 14]. Of note, Chapter 5 leverages tools established in chapters 2-4 to peer into hypoxic and mitochondrial changes increasingly implicated in PDAC progression [15-18]. Ongoing studies which spatially analyze the microenvironment and

detailed cell behaviors present would prove invaluable to unraveling the mechanisms behind malignant transformations and additional routes for early therapies.

1.2 Imaging cancer via immunofluorescence, the bigger picture

Most cancers are detected and diagnosed in part by their abnormal size, markers, and dysplasia from adjacent healthy tissues. Given the myriad of cancer hallmarks, methods to assess a wide variety of genetic and protein signatures expressed in tumors have become increasingly sought after. Light microcopy and in particular fluorescence microscopy are well suited in addressing this, given their targeted specificity, high contrast and quantifiable image intensities. To characterize the complex interplay between multiple oncogenic and prognostic biomarkers, methods like cyclic IF have been developed [19]. Cyclic IF utilizes multiple cycles of immunolabeling and multi-color fluorescence imaging to spatially and quantitatively assess biomarkers of interest (**Figure 1.3 A**). Paired with image registration, stitching, and analysis, methodologies like this are becoming promising candidates for clinical settings [20].

The scale of the tumor microenvironment and adjacent tissues is typically many millimeters across, while the individual tightly packed cells are typically 5-10 microns wide. Representative of the scale tumors present themselves, a region of PDAC can be seen bordering both healthy pancreatic tissue as well as a portion of the small intestine (**Figure 1.3 B**). While H&E staining is typically used to judge tissue histology and organization, it is often paired with targeted immunolabeling methods like IHC or potentially cyclic IF to help assess biomarker levels (**Figure 1.3 B**). Representative magnified single views reveal regions of normal and cancerous tissue with dramatic differences in some biomarkers such as lower 5HMC and higher Ki67 expression both

as poor prognostic biomarkers (**Figure 1.3 C**) [19]. Through multiple cycles, even more multiplexed marker expressions at a single-cell resolution can be quantified, necessitating methods for dimensionality reduction such as t-SNE plots [21]. Exemplifying this, Lin et. al. demonstrated clear stratification between healthy pancreas, PDAC and small intestine using a panel of 24 biomarkers via cyclic IF [19] (**Figure 1.3 D**). Interestingly, representative of the heterogeneity present in these large regions of tissue, there is a clear gradation of epithelial marker E-Cadherin loss and even EMT marker Vimentin (**Figure 1.3 D**). Studies like this exemplify the ongoing efforts to image and ultimately quantify the heterogeneity and find better prognostic indicators in cancer.

Importantly, tumor samples are typically imaged at 10-20x magnification, which while retaining some information from each cell such as distinct nuclei, smaller cellular features such as organelles are not often imaged/interpreted from clinical samples. Collectively the standard is to retain single-cell specific resolution, as this can most efficiently judge the larger tumor heterogeneity and pair with similar multi-omics studies [22]. To better understand cancer mechanisms, model systems such as cancer cell lines and organoids are commonly imaged instead. Although powerful to identify and broadly characterize markers in a variety of sample types, standard immunofluorescence lacks the spatial detail to see molecular detail and mechanisms at the base of cancer biology.

1.3 Rise of Super-resolution Microscopy

While light microscopy and fluorescence microscopy are ideally suited to study a wide variety of biological systems including cancer, the scale of information provided falls short of the length-scales many proteins/molecules actually function on. Superresolution microscopy techniques which can push spatial resolutions down to the nanometer scale have been developed which leverage temporal separation and

reconstruction for targeted fluorescent events [23]. As shared recipients for the 2014 Nobel prize in chemistry, the methods of Photo-Activatable Localization Microscopy (PALM) [24] and STochastic Optical Reconstruction Microscopy (STORM) [25] were credited with truly advancing the SRM field. These methods proved foundational for studying molecular and subcellular components of biological systems on the protein level.

SRM methods like PALM/STORM use Single Molecule Localization Microscopy (SMLM) based strategies to provide a higher degree of precision for observed structures. While multiple adjacent fluorescing molecules are subject to both the diffraction limit and critically the Raleigh limit [26], separating these into single fluorescent events provides the best performance for approximating their positions [27]. For example, STORM uses photoswitchable dyes and UV to activate a small subset of bound fluorophores at any given moment in time, resulting in a random subset of single fluorescent events on targets of interest (**Figure 1.4**). Typically, tens of thousands of frames are required, although this depends on the density of structures being imaged. Each single fluorescent event is identified through point-spread function (PSF) fitting, which fits a centroid modeling the intensity and apparent width of the fluorescent event to approximate its position below the diffraction limit and render the higher-resolution image [28] (**Figure 1.4**). Filtering and overlaying all observed events into a final rendered image, the complete structure such as microtubules can come into view (**Figure 1.4**). Notably through this process, samples can undergo small amount of drift, while this typically could result in relatively minimal errors for diffraction limited microscopy, they can cause severe distortions in SRM imaging. To counteract this, fiducials such as gold nanoparticles or fluorescent beads are typically used which can provide an anchor to align each frame within an SRM video. Emerging methods for drift corrections can leverage live processing to identify and counteract any drift without the need for fiducials

[29]. While the applications, labeling strategies and fluorescence molecules used can vary widely, these general methods form the backbone of SMLM studies.

Although most commonly performed with 2D imaging, SRM methods can also be expanded to include 3D spatial details as well. The first and most common method for 3D SRM imaging was demonstrated by Huang et al in 2008 with the integration of a cylindrical lens [30]. This method induces a specific astigmatism for observed PSFs wherein vertical positions can be inferred from orthogonal lateral distortions (**Figure 1.5 A**). Calibration files collected using fiducials at differing sample heights can be used to fit vertical positions onto observed fluorescent events (**Figure 1.5 B**). Aside from the cylindrical lens and associated calibration, any samples compatible with 2D STORM can be readily imaged in 3D as well, where distinct SML exhibit distortions according to their relative height (**Figure 1.5 C**). Ultimately, these can be recombined through software packages such as ThunderSTORM [31], which align and pseudo-color observed nanostructures such as mitochondria according to their height (**Figure 1.5 D**). Although additional methods have been developed to enable better 3D precision, they typically rely on PSF alterations to infer sample vertical positions [32]. Although generally not utilized within this thesis, the general amenability of the majority of SRM imaging strategies to 3D applications is addressed within future directions of Chapter 6.

SMLM studies have revealed molecular structures simply not possible with traditional fluorescence microscopy. Example studies have visualized everything from viral infections [33] to transient apoptotic structures on mitochondria [34]. In cancer, as a common oncogenic driver behind multiple cancer, types mutant RAS/ RAF isoforms and their oligomerizations were visualized utilizing both PALM and single molecule tracking to peer into their underlying membrane signaling pathways [35, 36]. Critically, while the majority of SRM studies have focused on imaging model systems such as cancer cell-lines, tissue STORM of various nanostructures from breast [37] and chromatin

organization from multiple cancers [38] have been demonstrated as well. Although prime examples of the feasibility of SRM to study cancer biology, broad applications of these methods have been limited, in part, by overall sample multiplexity and SRM imaging throughput.

1.4 The development and promise of DNA-PAINT

Although powerful, STORM has faced limitations in multiplexity by spectral and photoswitchable fluorophores and throughput in specific buffer chemistries which can be difficult reliably maintain over large sample datasets. In recent years the emergence of Point Accumulation in Nanoscale Topology (PAINT) methods [39, 40] have provided a robust alternative strategy in SMLM imaging. Unlike STORM, which utilizes stochastic imaging of a subset of finite fluorophores pre-immunolabeled on targets of interest, the use of DNA conjugated immunolabels and complimentary fluorophore-DNA conjugates can dynamically bind to generate SMLM events (**Figure 1.6**). An immediate advantage of DNA-PAINT has been the flexibility of multiplexing afforded by unique complimentary DNA sequences used for both the docking strand (DS) and imaging strand (IS) sequences. Another advantage has been the decoupling of photoswitching / photobleaching inherent to STORM, which has long required specific optimizations [41], meaning DNA-PAINT can leverage a wider variety of fluorophores with enhanced quantum efficiency and effective brightness. Methods such as Exchange-PAINT have been developed which utilize several unique DS-IS pairs in cycles of imaging using the same fluorophores to improve multiplexed imaging all using the same optical setup and filters [42]. Finally, DNA-PAINT affords a distinct advantage in imaging throughput, especially when applied to larger fields of view, as photobleaching is prevented via

continual replenishment of imaging strand in solution and common DNA-PAINT buffers do not require unstable oxygen scavengers as used in STORM.

Although developed relatively recently, DNA-PAINT has quickly been optimized to work in a variety of biological settings. The main limitation in DNA-PAINT the requirement to generate DNA conjugated DS and IS reagents in house, as commercial products which can commonly be used in STORM (such as commercially conjugated AF647 antibodies) do not have DNA-PAINT common commercial counterparts. Once generated, DNA-PAINT methods and reagents can reliably image cellular details with ease. Key steps in improving DNA-PAINT imaging quality and throughput are exemplified within Chapter 2, in building from other published methods, and demonstrates these can provide reliable high-quality SRM imaging in a variety of applications. Using our specific DS-IS pairs we can visualize nanostructures such as Mitochondria and Microtubules (**Figure 1.7 A**). Utilizing data analysis pipelines previously developed for STORM [43], we can reconstruct both structures via exchange-PAINT based approaches in Cos7 cells (**Figure 1.7 B-D**). Despite these clear advantages in multiplexity, traditional DNA-PAINT kinetics (as dictated by K_{on} and K_{off} hybridization rates for each DS-IS pair) was very slow, hindering imaging throughput when visualizing more targets from the same sample. Counter-intuitively, given the sudden rise of DNA-PAINT imaging strategies, optimizations, and applications, DNA-PAINT has yet to be demonstrated on tissue samples. Given multiple proven instances of tissue STORM [37, 38], DNA-PAINT on tissues such as FFPE should inherently be feasible.

1.5 Quantifying nanostructures with SRM

The dramatic improvements in spatial resolution provided by SRM methods provides much more than means to a pretty picture, as the nanoscale-level details can be used to more precisely quantify molecular interactions and even mechanisms. SRM images themselves are inherently generated through image-analysis, filtering via PSF quality across thousands to millions of single-molecule events to generate each image. More advanced methods for image analysis have followed the change in imaging data, often being performed on the localization files themselves. Other common SRM image analysis strategies have focused on spatial clustering, where groups of localizations are identified by their proximity, organization, and density to one another. Example strategies include methods like Density Based Spatial Cluster Analysis with Noise (DBSCAN) [44], local density indices [45], and tessellation-based methods [46] (**Figure 1.8**).

Methods like DBSCAN have been around for decades, and have become more commonly used in SRM image analysis [35, 44]. In brief, DBSCAN utilizes a Ripley's K test, which searches for distances between all nearby localizations within a target radius (**Figure 1.8 A**). Depending on the radius and cluster sizes desired, this can be used to find larger regions of adjacent structures within cell membranes and even infer oligomerization of distinct clusters sizes for signaling proteins such as oncogenic mutant KRAS (**Figure 1.8 B**) [35]. Outside of single marker clustering, understanding of multiple marker clusters colocalizing are also of mechanistic importance in unraveling complex protein interactions. Local density indices and overlapping area between clusters for different targets works by finding regions of relatively high density within each input localization-based image (**Figure 1.8 C**) [45]. By calculating the overlapping regions between areas of high density, a colocalization index can infer functional relationship

between proteins such as neuronal synapse complexes (**Figure 1.8 D**). Another recent strategy has utilized geometric tessellation between localizations within each channel to calculate regions of overlapping clusters [46]. A so-called rank density is calculated from the number of adjacent neighbors, and importantly can be normalized to account for differences in localization abundance between image datasets [46] (**Figure 1.8 E**). Regular structures such as distinct proteins within nuclear pore complexes, even when imaging with 3D SRM, have been reliably analyzed by these methods (**Figure 1.8 F**).

Despite the power and emerging multiplexed analysis of methods such as these, accessibility and important scalability/computing power often limit the utilization of these analytical pipelines to labs developing these analytical pipelines. Leveraging methods such as class averaging, dynamic states and complex oligomerization has been demonstrated on structures from rendered SRM images including nuclear pore complexes [47] and even the progression of clatherin endocytosis [48]. By being performed in part on rendered images, these methods boast higher throughput and are well suited for more bulk analysis on SRM structures. Although popular methods such as machine learning based image segmentation have become commonplace for traditional microscopy techniques [49], their utilization with SRM image analysis is rarer.

1.6 Gaps in current understanding & layout of the thesis

Collectively, the current literature presents key challenges which limit the utility of SRM to study early cancer biology: i) There is a lack of SRM imaging throughput to quickly acquire images both quickly and effectively over the larger cell-populations and complex macroscopic tissue structures in cancer. ii) Current SRM analytical methods focus on precise interpretation of small datasets, not large-scale imaging. iii) Despite

efforts using STORM to image patient samples, DNA-PAINT has yet to be successfully utilized. Critically these issues have limited research in areas such as iv) understanding mitochondrial dynamics from a mechanistic level of imaging functional protein interactions in cancer. My central hypothesis is that by accelerating SRM imaging throughput coupled with automated analytics will make scalable SRM imaging of patient samples a reality. The remainder of the thesis is organized as follows. Chapter 2 focuses on foundational work to both dramatically improve DNA-PAINT imaging speeds and fields of view. Chapter 3 aims to demonstrate how automating existing open-source image classification pipelines is poised to quantify orders of magnitude more spatial information at nanometer resolutions. Chapter 4 aims to break down the limitations behind tissue DNA-PAINT, by engineering novel imaging strategies using microfluidics. Chapter 5 aims showcase efforts to study mitochondrial dynamics in cancer, and how improvements to SRM can peer into the mechanisms behind these dysregulations.

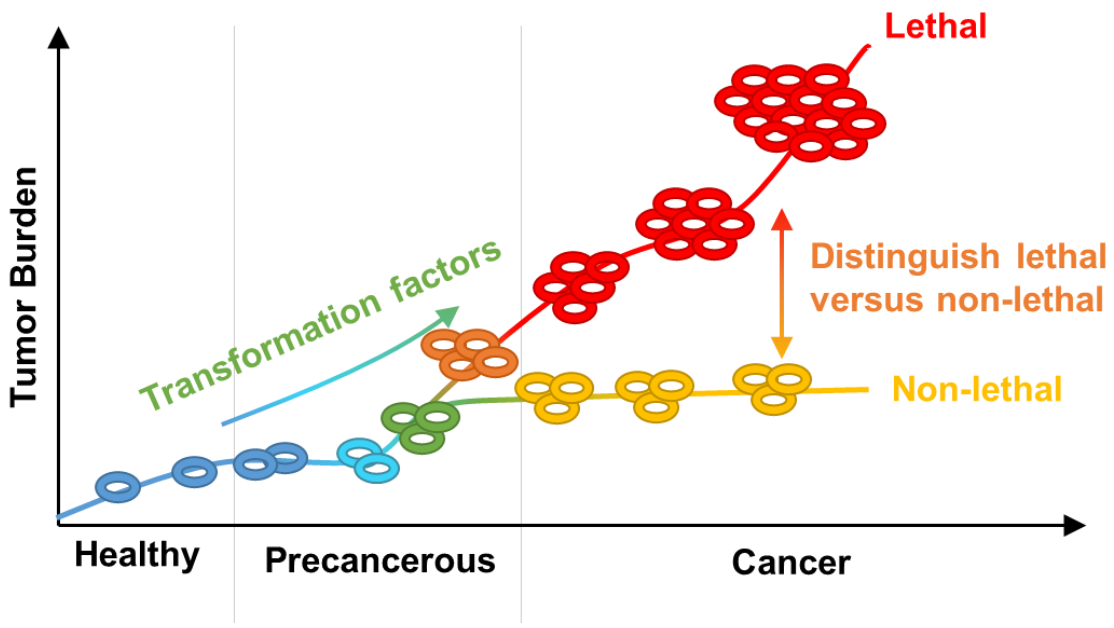

Figure 1.1 | Understanding early cancer progression

Broadly, all cancers arise from originally healthy cells, whereby early transformation factors including oncogenes, environmental, metabolic, infections, and other causes can cause an increase in pre-cancerous behaviors. After cancer is established, some cancers can grow and progress quickly and become lethal, while other cancers may persist in a more benign or non-lethal state. Being able to track and eventually trace in vivo the types of factors which generate not only precancerous conditions but also determinants of indolent vs malignant tumors are critical.

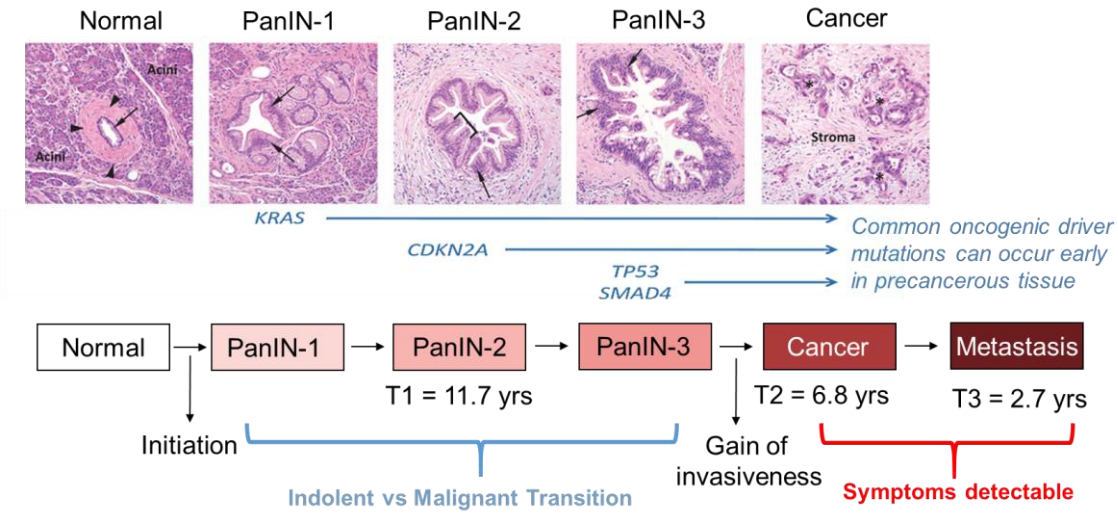

Figure 1.2 | PanINs as precursors to PDAC progression

Precancerous conditions such as Pancreatic Intraepithelial Neoplasms (PanINs) have been identified and in part been subjected to genetic studies. Notably common oncogenic mutations can be linked to these precursors to PDAC and yet other unknown factors trigger the transition to malignancy. By spatially assessing the proteins and other factors which may underly this progression to lethal cancers such as PDAC could be identified and treated at earlier stages. Figure modified from [12].

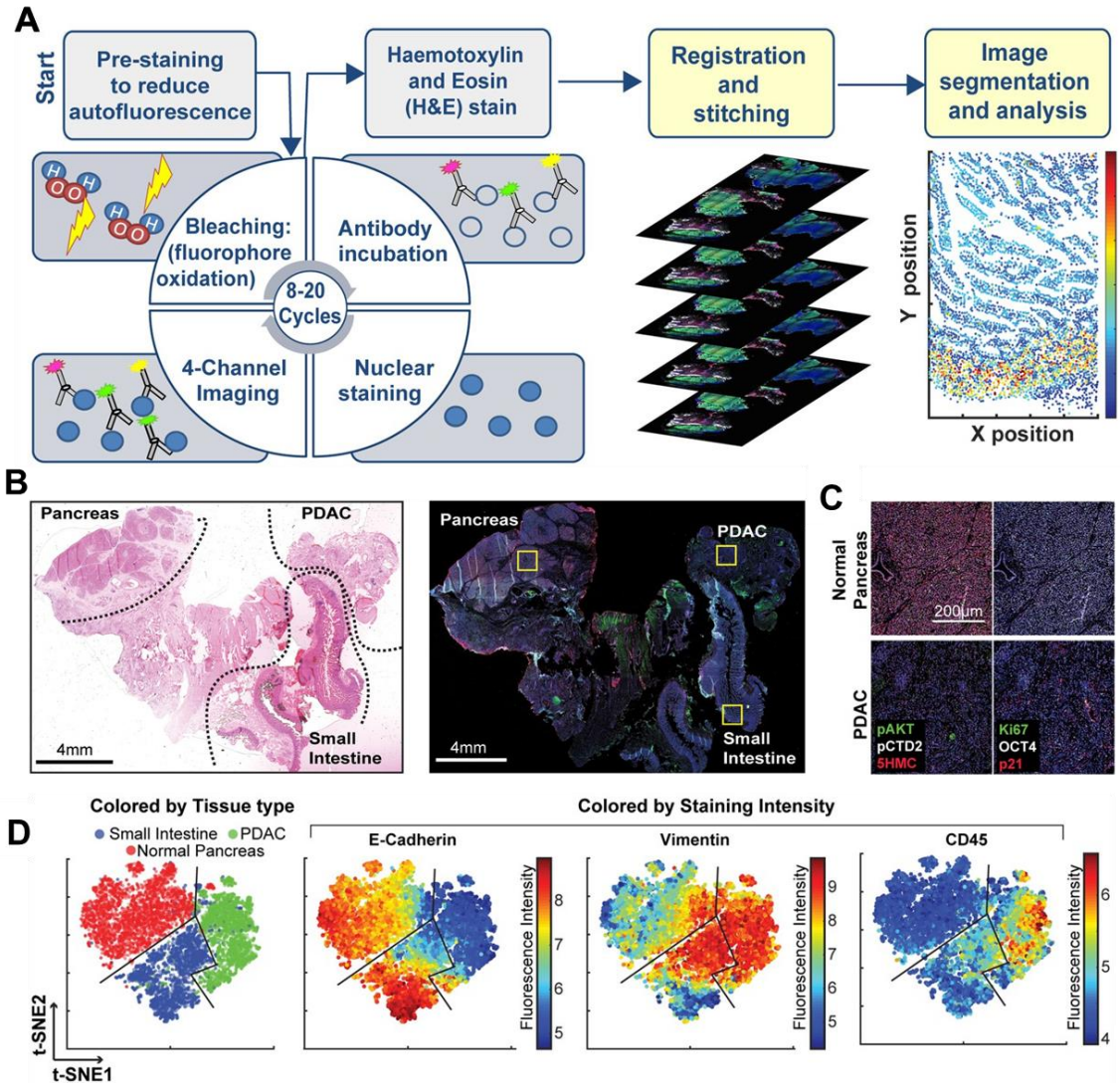

Figure 1.3 | Example cyclic IF imaging for or other multiplexed views of cancer heterogeneity by imaging systems

(A) Cyclic IF workflow diagram, functioning through cycles of antibody incubation, nuclear staining, multi-color imaging, and bleaching. Nuclear staining used in part for registration and stitching, where single-cell marker fluorescence values can be analyzed. (B) Example PDAC biopsy with adjacent healthy pancreas and small intestine, paired with matching cyclic IF image. (C) Representative smaller FOVs taken at 10x magnification showing 2 cycles and select marker expression differences. (D) High dimensional analysis outputs like t-SNE provide distinction of annotated tissue types from cyclic IF single-cell marker expressions. Mapping this single-cell expression back shows heterogeneity in cell expressions within tissue types. Figure modified from [19].

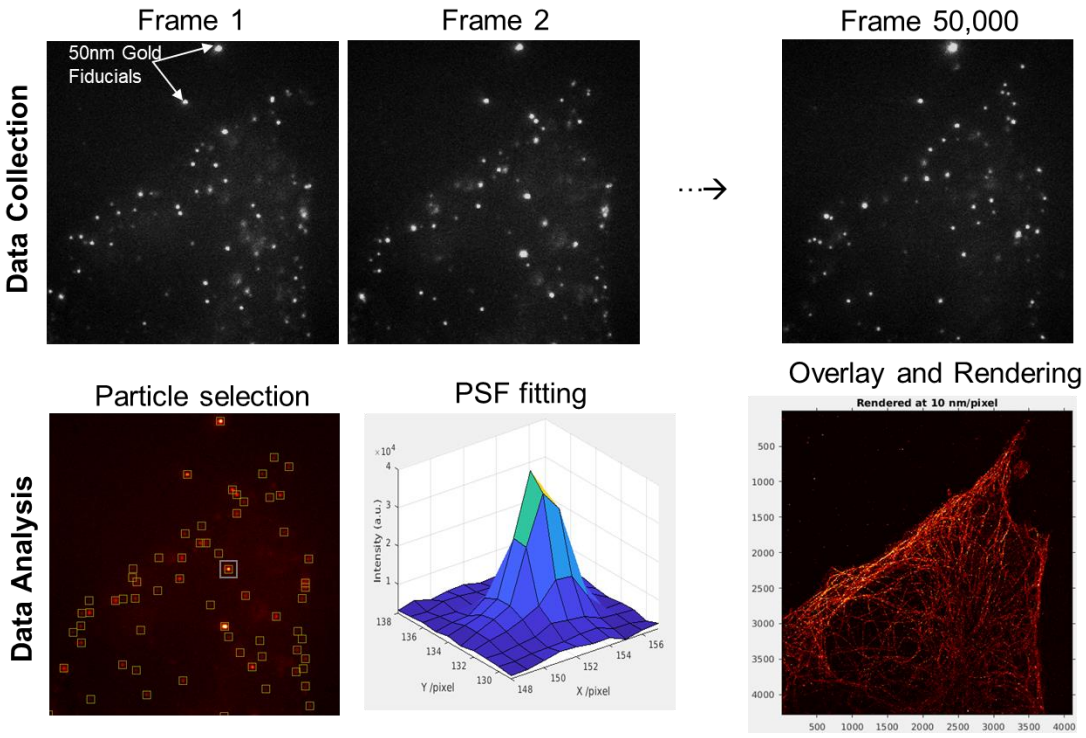

Figure 1.4 | Basics of Single Molecule Localization Microscopy

Superresolution methods such as PALM and STORM are built upon Single Molecule Localization Microscopy (SMLM). SMLM is achieved when individual fluorophores are temporally separated while individual diffraction limited events can be recorded. By collecting tens of thousands of such events (top row), individual frames and observed particles can be more precisely located through modeling of the Point-Spread Function (PSF) for each particle's fluorescent event. Finally, by filtering and overlaying these SMLM events into a single image, a final rendered image typically can have a resolution < 20 nm (bottom row). Data shown is a STORM image of microtubules secondary labeled with AF647 and obtained using 10 ms exposure. Full FOV in each raw image and reconstructed image is 42 μm.

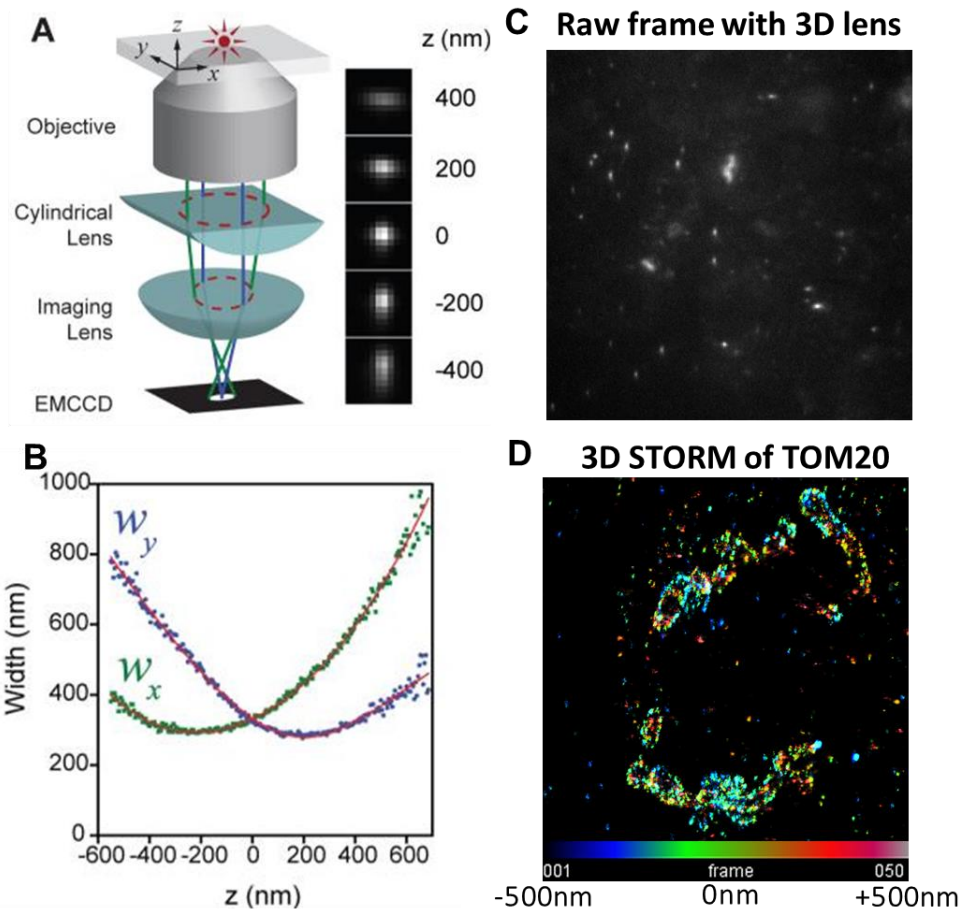

Figure 1.5 | Astigmatism based 3D SRM imaging

(A) Inclusion of a cylindrical lens in the detection path induces a height-dependent distortion to the PSF for each localization during SRM imaging. (B) These intentionally modified PSF events can be fit to a calibration curve to infer relative Z-position from elongation in either x or y for every localization. (C) Example raw frame with localizations at differing heights, tens of thousands of such frames are collected and secondarily fit to 3D calibration curves. (D) Final rendering of all observed localizations can be pseudo-colored to reveal the height-information in imaged structures such as these mitochondria. (A & B) reproduced from [30]. Raw data and associated reconstruction (C & D) collected using 3D cylindrical lens and reconstructed using ThunderSTORM [31]. Example frame collected at 20 ms exposure from 30,000 frames on Tom20 secondarily immunolabeled with AF647. Reconstructed 3D image of Tom20 shown is shown with 20nm axial resolution and 50 nm vertical resolution. STORM image of microtubules secondary labeled with AF647 and obtained using 10 ms exposure. Full FOVs are 42 µm in (C) and 8 µm in (D).

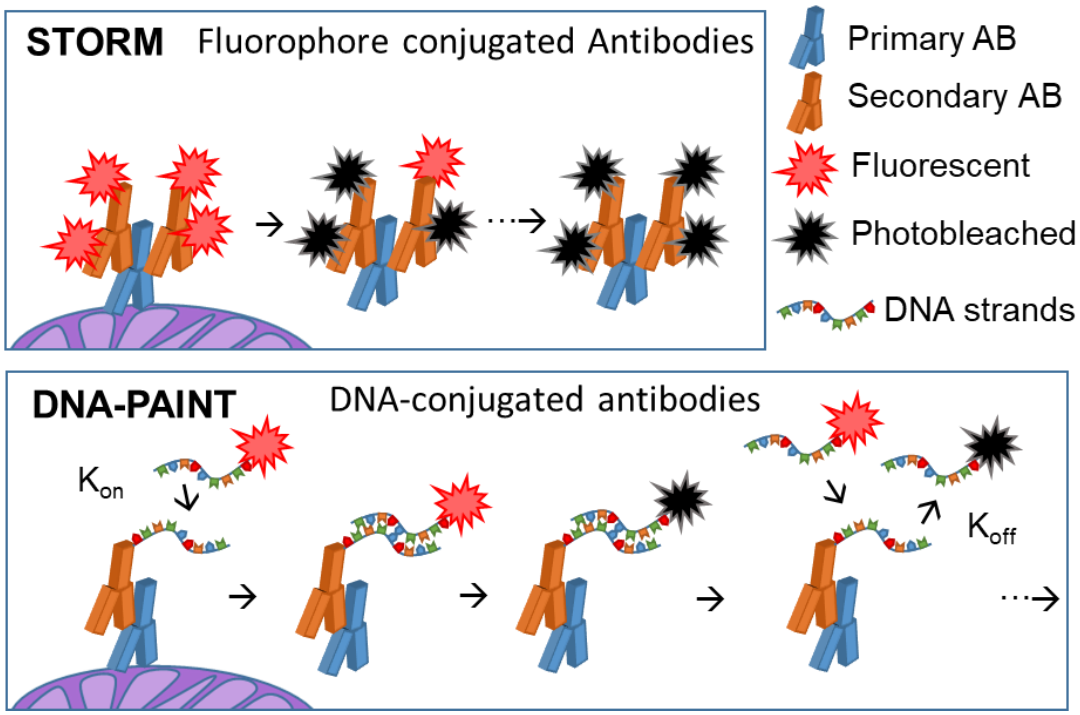

Figure 1.6 | STORM versus DNA-PAINT

Schematic demonstrating essential differences between STORM and DNA-PAINT SMLM methodologies. In STORM, immunolabeling attaches a finite number of fluorophores, which are chemically and optically excited to photoswitch and generate localizations until all fluorophores are bleached. Conversely in DNA-PAINT, DNA-conjugated docking strand (DS) antibodies and complimentary imaging strand (IS) DNA sequences with conjugated fluorophores are used. Photoswitching is achieved through dynamic hybridization of complimentary DS-IS pairs from an available pool of excess IS in solution. Binding kinetics for both DNA hybridization K_{on} and unbinding K_{off} ensures reproducible imaging of immunolabeled structures.

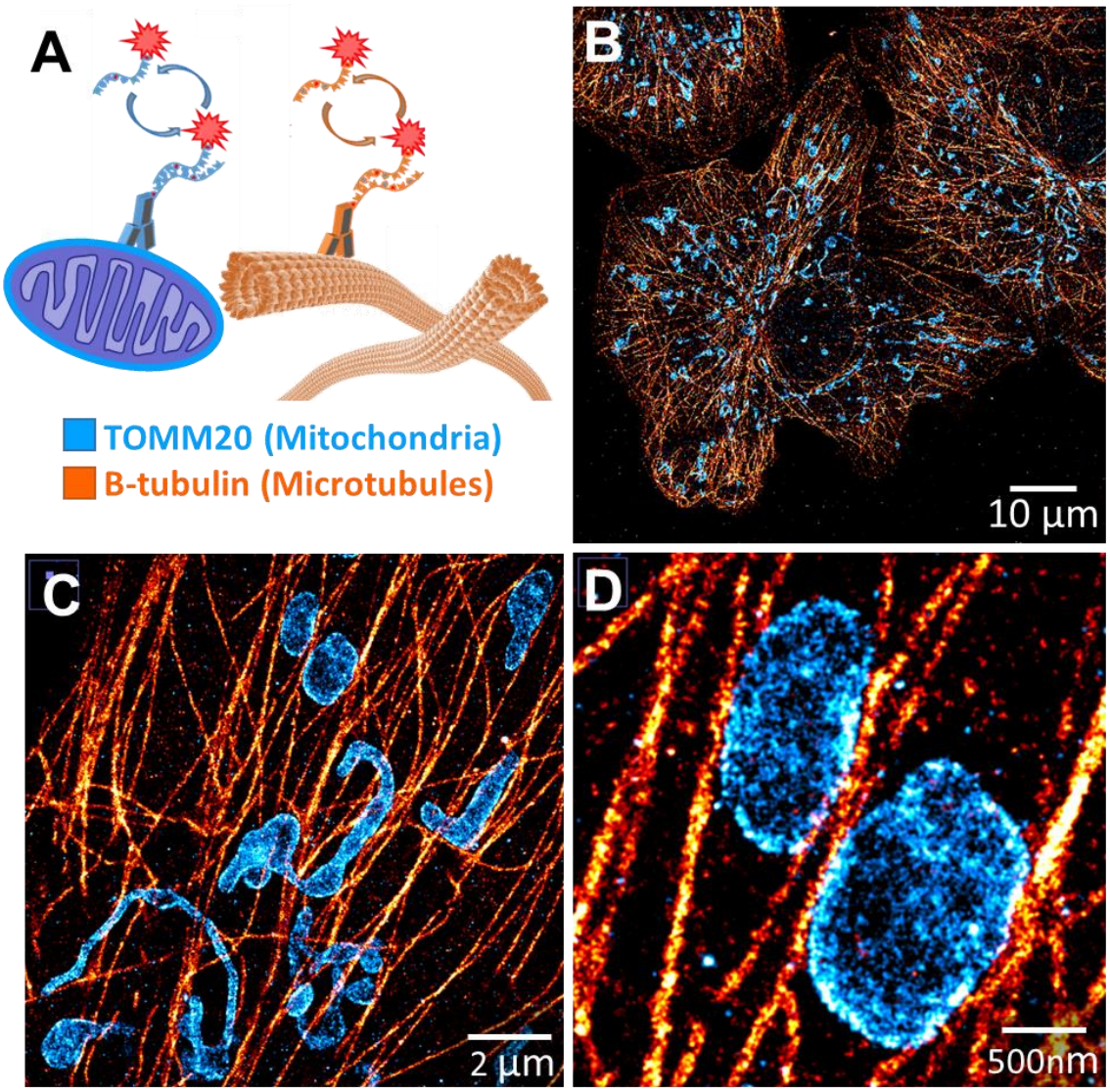

Figure 1.7 | Multiplexing with DNA-PAINT

DNA-PAINT is well suited to multiplexing, as multiple orthogonal sets of DS-IS DNA sequences can be designed to correspond to different immunolabeled targets. (A) Schematic of distinct DS-IS pairs corresponding to different cellular structures such as microtubules (orange) and mitochondria (blue). (B) representative reconstruction of mitochondria (cyan-hot) and microtubules (red-hot) from Cos7 cells using DS1 / IS1 and DS2 / IS2 pairs for mouse and rabbit primary antibodies for each target respectively. (C & D) magnified views from (B) with scale bars indicated. Images were collected using DNA-PAINT reagents and microscopy from [50]. In brief, images were collected using 20,000 frames at 40 ms exposure using 1 nm concentration for both IS1-CF660 and IS2-CF660 for microtubules and mitochondria respectively.

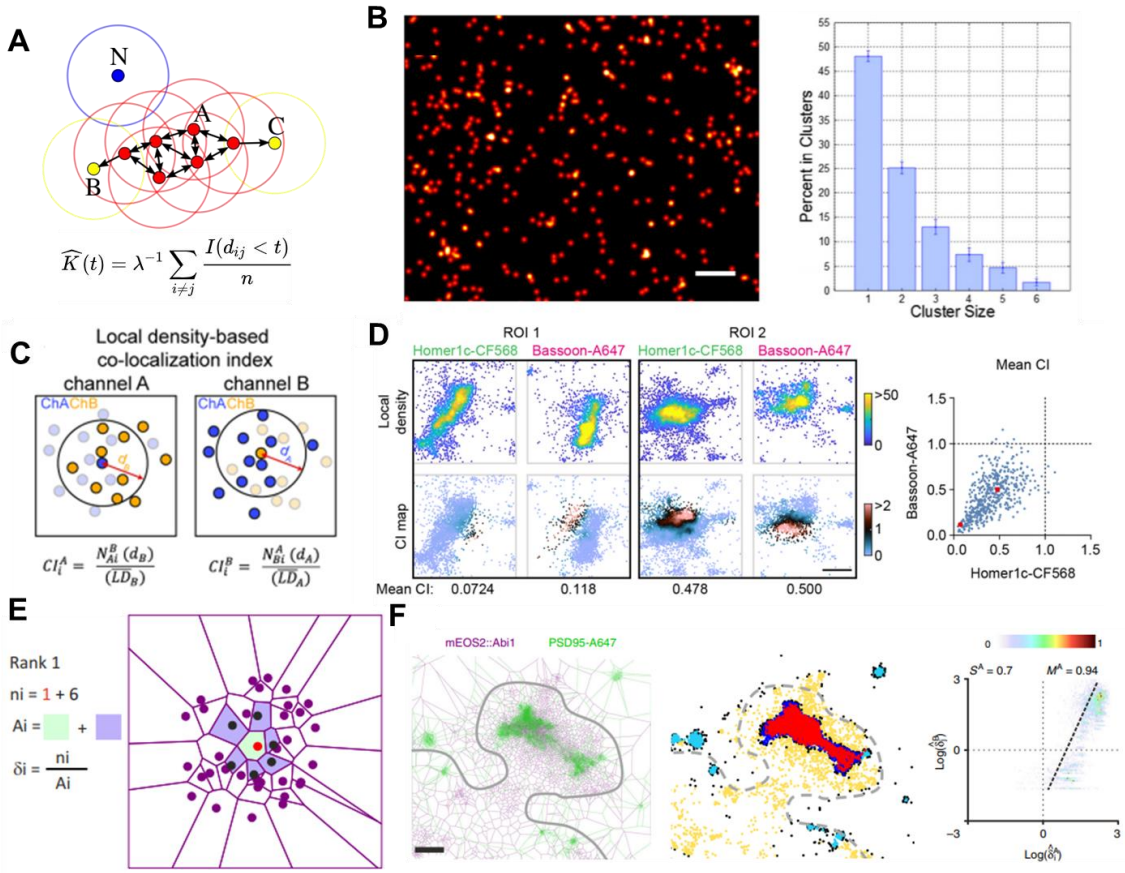

Figure 1.8 | Example SRM clustering and colocalization analysis

Representative techniques and example use cases for SRM clustering and multi-target colocalizations. (A) DBSCAN clustering analysis paired with Ripley's K test, searches paired localizations within search radii across all events. (B) Analysis of KRAS^{G12D} oligomerization through PALM, identifying dense regions of membrane signaling. (C) Density-based co-localization index, compares local density index around each localization to matching regions for each target. (D) Example analysis of neuronal proteins Homer1c and Bassoon via STORM, colocalization index (CI) score maps co-clustering regions. (E) Coloc-Tesseler, employs Voronoi diagrams onto each channel localizations, high numbers of neighbors and overlapping Voronoi overlays infer high rank density values. (F) Example synapse regulator proteins Abi1 and PSD95 via palm and STORM respectively, multi-classification output highlights regions of singular or shared marker clustering.

Chapter II: Enhancing DNA-PAINT scalability through imaging kinetics and Large-field DNA-PAINT

2.1 Abstract

DNA points accumulation for imaging in nanoscale topography (DNA-PAINT) facilitates multiplexing in superresolution microscopy but is practically limited by slow imaging speed and small FOVs. To address the issue of speed, we propose the additions of ethylene carbonate (EC) to the imaging buffer, sequence repeats to the docking strand, and a spacer between the docking strand and the affinity agent. Collectively termed DNA-PAINT-ERS (E = EC, R = Repeating sequence, and S = Spacer), these strategies can be easily integrated into current DNA-PAINT workflows for both accelerated imaging speed and improved image quality. To address the issue of FOV, we demonstrate Large-Field DNA-PAINT (LF-PAINT), a flexible system for multiplexed bioimaging from nanometers (nm) to millimeters (mm). LF-PAINT integrates prism-type illumination and on-stage microfluidics to enable multiplexed DNA-PAINT with single FOVs up to 0.5 mm by 0.5 mm at 20-30 nm lateral resolution. The integrated microfluidics also drastically enhanced superresolution imaging for clinical tissues via flow-assisted DNA-PAINT. We achieved multiplexed SRM imaging of cell populations and tissue sections across millimeter FOVs via robust stitching in 1-4 hours per target. Empowered by automated feature extraction using machine-learning, it is now possible to analyze nanostructures across thousands of cells with LF-PAINT. Primed for automation and further scale-up, LF-PAINT paves the way for building Google-earth-like views of complex and heterogeneous biological systems.

2.2 Introduction

DNA-PAINT imaging kinetics

For single-molecule localization microscopy (SMLM) techniques such as DNA-PAINT [23-25, 40, 51] both the imaging speed and image quality depend on the localization kinetics [28, 41]. A fast onset of localization events allows efficient sampling of the target to develop a super-resolved image quickly. At the same time, the events should also vanish quickly—ideally matching the speed of image acquisition—to mitigate spatially overlapping localizations which would otherwise degrade resolution and image quality. In DNA-PAINT, the localizations arise from reversible hybridizations between a docking strand (DS) oligo immobilized on the target and a complementary, fluorophore-conjugated imager strand (IS) oligo diffusing in solution (**Figure. 2.1**, first panel). This imaging scheme simplifies multiplexed SMLM by eliminating the need for photo-switchable fluorophores and allows multiple targets to be DNA-barcoded and imaged sequentially4. To date, over 15 DS-IS pairs have been validated (out of >50 designed) for multiplexed DNA-PAINT imaging of cellular structures [42].

However, a practical hurdle to using DNA-PAINT for multiplexed SMLM is the slow imaging speed, with each target taking tens of minutes to hours to complete [51]. This is primarily due to relatively slow localization kinetics. On average, the duration of localization events (τ_{on}) in DNA-PAINT is on the order of seconds (s) [52], in sharp contrast to other SMLM (τ_{on} on the scale of 0.01–0.1 s) [41]; the longer lasting events in turn demand a slower onset of events to reduce overlapping localizations. Besides prolonging data acquisition, the slow kinetics can also degrade image quality, necessitating special imaging schemes such as flat-top structured illumination9. DNA-PAINT via Föster resonance energy transfer (FRET-PAINT) affords fast acquisition but suffers a low photon yield [53, 54] and, for unknown reasons, a rapid loss of localization

events as soon as imaging begins ([55] and unpublished data). More recently, a DS-IS pair referred to as PS3 was found to exhibit fast on-off kinetics to speed up DNA-PAINT by about an order of magnitude [56]. At present, it remains unclear how many orthogonal DS-IS pairs like PS3 exist, and other generally applicable methods are necessary for fast and multiplexed DNA-PAINT in biological applications.

To address these issues, we aim to devise strategies for expediting DNA-PAINT that: (a) are compatible with a large panel of DS-IS pairs such as those previously validated for DNA-PAINT; (b) can be easily integrated into current DNA-PAINT workflows; and thus (c) are readily adopted for multiplexed superresolution imaging. Our rationale is that the key step toward fast and high-quality DNA-PAINT imaging is to speed up DS-IS unbinding, ideally without slowing down the binding. This is achieved by including a small molecule, ethylene carbonate (EC), in the same imaging buffer (buffer C) as used in current DNA-PAINT experiments (**Figure 2.1**, second panel). Next, we increase DS-IS binding via two simple strategies: increasing the copy number of the complementary sequence on the DS by using sequence repeats (**Figure 2.1**, third panel), and increasing the accessibility of the DS by inserting a small spacer between the DS and the affinity agent to reduce the steric hindrance (**Figure 2.1**, fourth panel). These strategies, collectively termed DNA-PAINT-ERS (where E = EC, R = Repeating sequence, and S = Spacer), allow us to complete multiplexed DNA-PAINT imaging in merely 2–5 minutes (min) for each target. In addition, we show that DNA-PAINT-ERS significantly improve the quality of the resulting images over current DNA-PAINT, likely also a result of better localization kinetics and accessibility of the DS.

Considerations for SRM FOV, scalability and applications

Life spans a multitude of scales, from whole organisms down to individual cells, organelles and molecules. In complex, multicellular systems such as animal tissues, different cell populations can exhibit distinct gene expression profiles and functional

roles, where the spatial arrangement of and interactions among the different cell types can have profound impact on the underlying biology [4, 6]. Even genotypically uniform cells could diverge functionally due to stochastic or deterministic differences in their molecular compositions and interactions. Thus, a complete understanding of health and disease requires insights across multiple scales. Despite continuous progress in multi-omics approaches [57], however, few techniques can probe biological organization across the molecular to multicellular scales.

Microscopy is instrumental to elucidating the spatial organization of biological entities within their native context, but historically there has been a trade-off between the achievable resolution and field of view (FOV). At the multicellular scale, histology and immunofluorescence are the mainstay for studying tissue organization and probing biomarker expression in single cells [22]. To date, these methods have relied on diffraction-limited imaging systems such as wide-field and confocal microscopy, which can resolve cellular and subcellular structures but provide little information at the scale of individual biomolecules. In the last two decades, superresolution microscopy (SRM) techniques such as PALM [23, 24], STORM [25], PAINT [39, 40], and STED [58] have pushed the resolution of optical microscopy to 10-20 nm, providing unparalleled insights into biological structures and processes at the molecular scale. However, the high spatial resolution of SRM comes at a cost of FOV compared with diffraction-limited microscopy approaches. At present, most SRM systems have an effective FOV around 50 – 100 μm, including in emerging commercial systems developed to enable more widespread use of SRM [59]. This, however, limits the imaging throughput of SRM.

In attempts to bridge the larger length scales in biology, emerging research has pushed the limits of SRM to larger FOVs. High power homogenous illumination was first used to obtain FOV of ~200 μm x 200 μm with STORM [60], through employing three 2 W lasers (~640 nm) to reach the power density needed for efficient STORM imaging

across such FOVs. Utilizing a line-scanning illumination scheme, Mau et al. have also pushed the FOV of SRM to ~200 μm x 200 μm with a moderate laser power input (~250 mW) [61]. Another illumination strategy from Archetti et al. used the coverglass substrate as a waveguide for propagating evanescent waves which illuminate the sample across FOVs of > 1 mm (along the direction of light propagation) x ~200 μm (the perpendicular dimension) [62].

Despite the initial success, previous efforts have faced limitations toward scalability and flexibility to even larger FOVs, primarily due to constraints imposed by the optics and illumination strategies. SRM typically employs high numerical aperture (NA) objectives coupled with through-objective, total internal reflection (TIR) for sample illumination and signal detection. These objectives are typically 60x or 100x in magnification with practical FOVs at ~200 μm x 200 μm, beyond which optical aberrations become limiting. Through-objective wide-field illumination also requires that the illumination laser be focused on the back aperture, which risks damaging the objective when high power lasers are used to achieve large FOVs. In this regard, methods that can decouple illumination and detection can be more flexible. For example, illumination based on a coverglass waveguide affords TIR illumination across millimeters along the length of the microscope slide, but this is limited to strict TIR for the need to maintain evanescent waves across the sample. Additionally, in their current implementation, the FOV for a single imaging session was still ~200 μm x 200 μm due to the use of high NA objective for detection. In practice, local differences in sample refractive index can lead to beam propagation inhomogeneity, further limiting the reproducibility and scalability of this method to larger FOVs. Works such as these highlight the need for new optical configurations to further overcome the current limits on the achievable FOV in SRM.

Another important consideration in developing SRM across large FOVs is the applicability to imaging complex biological samples. Multiplexed (or multicolor) imaging is desired in most biological applications, and current SRM methods – namely PALM, STORM, (DNA-)PAINT, and STED – differ significantly in their ability to multiplex. Among these, DNA-PAINT is the most convenient in terms of multiplexing (through exchange-PAINT [63]), but the need to exchange imaging buffer between acquisitions requires additional engineering efforts, particularly in a large FOV setting.

In this work, we have developed a large-field DNA-PAINT (LF-PAINT) microscope and the associated workflow for multiscale and multiplexed imaging of both cells and patient tissue samples. We overcame limitations of the through-objective and waveguide illuminations by utilizing a prism-based illumination scheme, which achieves SRM imaging over large FOV from ~300 µm x 300 µm up to >500 µm x 500 µm at 20-30 nm spatial resolution and is compatible with both TIR and epi-fluorescence imaging. Coupled with a microfluidic chamber to facilitate imaging buffer exchange, this setup enables multiplexed LF-PAINT imaging that can be further extended to 1 mm x 1 mm or larger FOVs. The integrated microfluidics also enabled “Flow-Assisted DNA-PAINT”, significantly enhancing the quality and speed of multiplexed SRM on patient FFPE tissue sections, which has been difficult with current DNA-PAINT (discussed in chapter 4). Finally, we demonstrate open-source, machine learning-based image segmentation and quantitation of the resulting, multiscale SRM images, offering insights into important nanostructures and molecular interactions across large cell populations not yet addressable with SRM (discussed in chapter 3). Collectively, we present LF-PAINT as a novel approach to enable high-resolution, high-throughput spatial mapping of cells and clinical samples across the scales from molecules to multicellular systems.

2.3 Materials and Methods

Materials

A step-by-step guide for generating the labeling reagents, preparing immunostained samples, and performing image acquisition and initial analysis can be found at Protocol Exchange [64]. All DNA oligonucleotides were synthesized from Integrated DNA Technologies. Docking strand sequences contained a 5′ amino modifier C6 and a 3′ 6-FAM fluorophore or Cy3™ fluorophore. Imaging strand sequences contained a 3′ amino modifier that were later conjugated to CF®660R (Biotium, 92134) via succinimidyl ester chemistry. DBCO-PEG12-NHS ester was purchased from BroadPharm (BP-24149). DBCO-PEG4-NHS ester, DBCO-Sulfo-NHS ester, and Azido-PEG4-NHS ester were purchased from Click Chemistry Tools (A134, A124, and AZ103 respectively). Invitrogen™ UltraPure™ DNase/RNase-Free Distilled water (Fisher Scientific, 10977023), sodium bicarbonate (Fisher Scientific, M-14636), sodium acetate (Sigma, 55636), and ethanol 200 proof (Fisher Scientific, 04355223) were used in oligo conjugation and purification.

AffiniPure Donkey anti-Rabbit IgG (H+L) (cat.no. 711–005–152) and AffiniPure Donkey anti-Mouse IgG (H+L) (cat.no. 715–005–150) antibodies were purchased from Jackson Immuno Research. Gibco™ Dulbecco's Phosphate-Buffered Saline (PBS) (Fisher Scientific, 14190–144), 50 kDa and 100 kDa Millipore Sigma™ Amicon™Ultra Centrifugal Filter Units (Fisher Scientific, UFC505096 and UFC510024, respectively) were used in protein conjugation and purification. Primary antibodies used in this work include beta tubulin monoclonal antibody (ThermoFisher Scientific, 32–2600), anti-clathrin heavy chain antibody (Abcam, ab21679), and anti-caveolin-1 antibody (Abcam, ab2910).

The following reagents were used for immunostaining: paraformaldehyde (Sigma, P6148), Triton X-100 (Sigma, X100), 25% glutaraldehyde (Millipore Sigma, G6257), bovine serum albumin (Fisher Scientific, BP1600), sodium hydroxide (Fisher Scientific, S318-100), sodium borohydride (Sigma, 452882), Invitrogen™ Salmon Sperm DNA (Fisher Scientific, AM9680), sodium azide (Fisher Scientific, AC190381000), Gibco™ Dulbeccos PBS with calcium and magnesium (PBS+) (Fisher Scientific, 14–040–182), and 50 nm gold particles (BBI Solutions, EM.GC50/4). The fixation buffer was made from 2x PHEM buffer, which consists of 0.06 M PIPES (Sigma, P6757), 0.025 M HEPES (Fisher Scientific, BP310-500), 0.01 M EGTA (Fisher Scientific, O2783-100), and 0.008 M MgSO4 (Acros, 4138–5000) in distilled water, with pH adjusted to 7 with 10 M potassium hydroxide (Sigma, 221473). The imaging buffer used in all PAINT experiments in this work is based on buffer C (500 mM sodium chloride in PBS) and contains different concentrations of EC (Fisher Scientific, AC118412500) as indicated.

Antibody conjugation with DNA oligos

Secondary antibodies were conjugated to docking strand (DS; see Supplementary Table 1 for the sequences) oligos via DBCO-azide click chemistry. First, DS oligos were conjugated to either DBCO-PEG12-NHS ester, DBCO-PEG4-NHS ester, or DBCO-Sulfo-NHS ester (no PEG). DBCO-ester was added in 20x molar excess to the DNA in a total reaction volume of 50 uL. The reaction ran for 3 h at room temperature and was carried out in ultra-pure water, pH adjusted to 8.5 with 1 M sodium bicarbonate. After the reaction, ethanol precipitation with 0.3 M sodium acetate at −80 °C was repeated twice on the mixture to purify the DS-DBCO product. Final DS-DBCO products were suspended in ultra-pure water. To prepare antibody-PEG4-azide conjugates, azido-PEG4-NHS was added in 100x molar excess to secondary antibodies; the reaction was carried at pH~8.5 adjusted by 1 M sodium bicarbonate and ran for 3 h at room

temperature. Antibody-PEG4-azide conjugates were flowed through a 50 kDa size exclusion column and washed with PBS 15 times on the column via centrifugation 4 °C (6000 g, 2.5 min each).

Next, DS-DBCO was reacted in 5x molar excess to the antibody-PEG4-azide via copper-free click chemistry; the reaction took place overnight on a shaker at room temperature. The resulting antibody-PEGx-DS (x = 4, 8, or 16 depending on the PEG linker of DS-DBCO) product was purified by flowing through a 100 kDa size exclusion column and washing in PBS 5 times by centrifugation (at 6000 g, 2.5 min each, 4 °C). The final product (antibody-PEGx-DS) was suspended in PBS. Product concentrations were measured with a NanoDrop UV-Vis spectrophotometer (ThermoFisher Scientific, 2000c). Peak signals at 280 nm, 495 nm (for 6-FAM), or 550 nm (for Cy3™) were used to calculate the protein concentrations and the degrees of labeling. The antibody-PEGx-DS used in this work typically had a degree of labeling of 4–5 (i.e., 4–5 DS oligos per antibody).

Imaging strand oligo conjugation

Imaging strand oligos (see Supplementary Table 1 for the sequences) were reacted with 5x molar excess of CF®660R-succinimidyl ester. The reaction was carried out in ultra-pure water with pH 8.5 adjusted by 1 M sodium bicarbonate and ran on a shaker for 3 h at room temperature. The conjugated imaging strand oligos were purified by one round of ethanol precipitation using a procedure similar to that on DBCO-DS. Peak signals at 260 nm and 660 nm (CF®660 R) were used to calculate DNA concentration and degree of labeling.

Cell culture and immunostaining

U2OS cells (ATCC, HTB-96) were maintained in Gibco DMEM (ThermoFisher, 11995073) or phenol red-free DMEM (Fisher Scientific, 21–063–045) supplemented with 10% fetal bovine serum (Fisher Scientific, 26–140–079). U2OS cells were passaged

every 3–4 days and used under passage number 15. Trypsin-EDTA (0.25%) was purchased from ThermoFisher (25200056). Corning tissue culture dishes were purchased from Fisher Scientific (08–772–22). Lab-Tek® II eight-well chambered coverglasses were purchased from ThermoFisher Scientific (155360). For superresolution imaging experiments, cells were grown on 8-well chambered coverglass in phenol red-free DMEM until 50–60% confluency on the day of fixation.

For immunostaining of clathrin or caveolin, cells were fixed for 20 min with 3.7% paraformaldehyde (PFA) in 1x PHEM buffer following a quick PBS wash. After two PBS washes, cells were quenched with fresh 0.1% sodium borohydride in PBS for 7 min, washed with PBS (3x), and then permeabilized with 0.5% saponin in PBS for 20 min. For immunostaining of microtubules, cells were fixed for 20 min with 3.7% PFA and 0.1% glutaraldehyde (GA) in 1x PHEM before quenching with sodium borohydride and permeabilization in 0.2% Triton X-100 in PBS. Blocking in 5% BSA in PBS for 30 min was done on a rocker, followed by incubation with the primary antibody for clathrin, caveolin, or tubulin antibody (0.5 mg mL−1 or 1:200 dilution from stock) in PBS buffer containing 3% BSA and 5% salmon sperm DNA. The incubation took place on a rocker at room temperature for 1 h. Next, cells were washed three times (5 min each) with PBS before incubation with DS-conjugated secondary antibody at a final concentration of ~8 µg mL−1 in PBS buffer containing 3% BSA and 5% salmon sperm DNA; the incubation also took place on a rocker at room temperature for 1 h. For DS secondary antibody addition and subsequent steps, the sample was kept in the dark to avoid bleaching conjugated fluorophores. Cells were washed three times with PBS (5 min each).

For immunostaining in extracted samples (microtubules alone, or microtubules co-labeled with clathrin), cells were pre-permeabilized with cold 0.1% Triton X-100 in 1x PHEM buffer for 45 s preceding 3.7% PFA fixation in 1x PHEM for 20 min. The cells

were rinsed two times with PBS and subsequently quenched with fresh 0.1% sodium borohydride in PBS for 7 min. Microtubule single staining was performed similarly to the unextracted samples described above. For co-stained samples, the cells were further permeabilized and blocked with 3% BSA and 0.2% Triton X-100 for 60 min. The cells were first labeled for beta-tubulin as described above, post-fixed with 3.7% PFA for 10 min, and then stained for clathrin as described above.

All cell samples were post-fixed for 10 min with 3.7% PFA and 0.1% GA in 1x PHEM. Before imaging, cells were incubated with 2.5% 50 nm gold particles in PBS+ for 10 min, followed by a PBS wash.

Microscopy

All superresolution and regular fluorescence data in this work were taken on a custom single-molecule imaging system. Briefly, three lasers emitting at 488 nm (Coherent Sapphire 488, 200 mW), 561 nm (Opto Engine LLC, 150 mW), and 647 nm (Coherent OBIS 647, 140 mW) were combined and introduced into the back of a Nikon Ti-U microscope equipped with a 60× TIRF objective (Nikon, Oil immersion, NA 1.49). An f = 400 mm lens was placed at the back port of the microscope to focus the collimated laser light to the back aperture of the objective to achieve through-objective total internal reflection (TIR) illumination. The excitation light can be continuously tuned between epi-fluorescence and strict TIR modes by shifting the incident laser horizontally with a translational stage before entering the back port of the microscope. Most images in this work were acquired with moderately relaxed TIR, so structures such as the microtubules could be probed adequately. A custom focus stabilizing system based on detection of the reflected excitation laser was used to stabilize the focus during data acquisition.

A multi-edge polychroic mirror (Semrock, Di01-R405/488/561/635) was used to reflect the lasers into the objective and clean up fluorescence signals from the sample. Emission filters used for the 488 nm (for imaging FAM on the DS), 561 nm (for imaging

Cy3 on the DS), and 647 nm (for imaging CF660R conjugated ISs) were FF01-525/45, FF01-605/64, FF01-708/75, respectively (all from Semrock). Fluorescence signals were collected through the objective by an electron-multiplied charge-coupled device (EM-CCD, Andor, iXon Ultra 897) using a typical EM gain setting at 200–300 in frame transfer mode. Unless otherwise indicated, the power density of the 647 nm laser (for DNA-PAINT imaging using CF600R conjugated IS) was typically around ~500 W cm−2.

Data acquisition and analysis

Superresolution images were acquired using the open source micromanager software suite (https://micro-manager.org/) [65] and saved as OMERO TIF files. Image analyses for extracting single-molecule localization and subsequent localization filtering, sorting, and rendering was performed using in-house Matlab scripts [43]. Briefly, raw localizations were first filtered based on localization fitting parameters such as signal to noise ratio, widths of point spread functions in the x and y dimensions, aspect ratio, etc. Next, the localizations were sorted, during which events that appeared within a defined number of frames (typically 2–3) and distance (typically 80 nm) were then combined into a single event with averaged coordinates. The sorted localizations were then used for final image rendering, and the rendered images were saved as TIF files for further analysis and annotations in Fiji.

LF-PAINT Specific Materials and Methods Materials

Methods utilized for generating labeling reagents followed established protocols for DNA-PAINT-ERS [50]. In brief, all starting DNA oligonucleotides were obtained from Integrated DNA Technologies. Docking strands included a 5′ amino modifier C6, for further conjugation with DBCO-PEG4-NHS (Click Chemistry Tools, A134-2) via succinimidyl ester chemistry, and a 3′ Cy3™ fluorophore for confirming antibody labeling. Imaging strands carried a 3’amino modifier for conjugation with NHS-ATTO 643 (ATTO-TEC, AD 643-31) via succinimidyl ester chemistry. All reactions were performed

at pH~8.5 adjusted by 1 M sodium bicarbonate (Fisher Scientific, M-14636) for 3 h at room temperature. Conjugated DNA oligos were purified via ethanol precipitation, and resuspended in Invitrogen™ UltraPure™ DNase/RNase-Free Distilled water (Thermo Fisher Scientific, 10977023).

Secondary antibodies used were: AffiniPure Donkey anti-Rabbit IgG (H+L) (Jackson Immuno Research 711–005–152), AffiniPure Donkey anti-Mouse IgG (H+L) (Jackson Immuno Research 715–005–150) and AffiniPure Donkey anti-Chicken IgG (H+L) (Jackson Immuno Research 703-005-155); these were conjugated with azido-PEG4-NHS via succinimidyl ester chemistry. Antibody-PEG4-azide conjugates were purified through a 50 kDa Millipore SigmaTM AmiconTM Ultra Centrifugal Filter Unit (Fisher Scientific, UFC505096). Next, purified antibody-PEG4-azide were reacted with excess DBCO-DS (molar ratio 1: 5) via copper-free click chemistry. The reaction was performed overnight on a rocker at room temperature. The resulting antibody-DS products were purified through a 100 kDa Millipore SigmaTM AmiconTM Ultra Centrifugal Filter Unit (Fisher Scientific, UFC510096). Peak signals at 260, 280 nm, 550 nm (for Cy3™) in a Nanodrop UV-Vis spectrophotometer (ThermoFisher Scientific, 2000c) were used to calculate the protein concentrations and the degrees of labeling. The antibody-PEG4-DS used in this work typically had a degree of labeling of 4–5 (i.e., 4–5 DS oligos per antibody).

The SNAP-tag substrate BG-PEG4-Azide was synthesized by the Medicinal Chemistry Core at Oregon Health and Science University. Briefly, it was synthesized in two steps via an amine-reactive key intermediate prepared from commercially available BG-NH2 as the starting material, followed by an NHS-ester crosslinking reaction. The final crude product was purified by preparative HPLC. The structure and purity of BG-PEG4-Azide were further confirmed by analytical HPLC analysis and high-resolution mass spectrometry prior to the click oligonucleotide labeling. BG-PEG4-Azide was

reacted with excess DBCO-DS (molar ratio 1:10) via copper free click chemistry, on a rocker at room temperature overnight. The resulting BG-DS was purified via ethanol precipitation, and suspended in UltraPure™ DNase/RNase-Free Distilled water. The concentration was determined by the Nanodrop UV-Vis spectrophotometer, similarly as mentioned above.

Primary antibodies used were: Mouse-beta tubulin monoclonal antibody (Thermo Fisher Scientific, 32–2600), Rabbit-anti-Tom20 polyclonal antibody (Abcam, ab78547), Rabbit-anti-caveolin-1 antibody (Abcam, ab2910), Chicken-anti-vimentin antibody (Sigma Aldrich, AB5733), and Mouse panCytokeratin (Abcam, ab7753).

Fixation, permeabilization, and immunostaining reagents were: paraformaldehyde (Sigma-Aldrich, P6148), Triton X-100 (Sigma-Aldrich, X100), 25% glutaraldehyde (Sigma-Aldrich, G6257), bovine serum albumin (Fisher Scientific, BP1600), sodium hydroxide (Fisher Scientific, S318-100), sodium borohydride (Sigma-Aldrich, 452882), Invitrogen™ Salmon Sperm DNA (Thermo Fisher Scientific, AM9680), sodium azide (Fisher Scientific, AC190381000), Gibco™ Dulbeccos PBS with calcium and magnesium (PBS+) (Thermo Fisher Scientific, 14–040–182), and 50 nm gold particles (BBI Solutions, EM.GC50/4). The fixation buffer was made from 2x PHEM buffer, which consists of 0.06 M PIPES (Sigma-Aldrich, P6757), 0.025 M HEPES (Fisher Scientific, BP310-500), 0.01 M EGTA (Thermo Fisher Scientific, O2783-100), and 0.008 M $MgSO_4$ (Acros, 4138–5000) in distilled water, with pH adjusted to 7 with 10 M potassium hydroxide (Sigma-Aldrich, 221473). The imaging buffer used in all PAINT experiments in this work is based on buffer C (500 mM sodium chloride in PBS) and contains different concentrations of EC (Sigma-Aldrich, 676802) as indicated.

Flow-chamber preparation and cell culture

Flow chamber substrates were made using: 25x75mm fire-polished microscope slides(Schott, Nexterion® Slide Glass B 1025087). Fire-polished microscope slides were

each drilled twice using a 1/16th inch bit diamond coated drill bit (Lasco Diamond #F6) for later use as microfluidic inlet and outlet ports, at the coordinates of (4 mm, 16 mm)- and (21 mm, 59 mm) on the 25x75mm coverslide. After drilling, slides were rinsed with DI water (3x), and sonicated in 100 % EtOH for 10 minutes. Following 3x DI water rinses, slides were etched in 1M NaOH for 20 minutes. After three rinses with DI water, cleaned slides were left in 100% EtOH prior to cell culture/tissue slide preparation.

Cell samples for LF-PAINT

U2OS cells (ATCC®, HTB-96) and COS7 cells (ATCC® CRL-1651™) were maintained in Gibco DMEM (Thermo Fisher Scientific, 11995073) or phenol red-free DMEM (Thermo Fisher Scientific, 21–063–045) supplemented with 10% fetal bovine serum (Thermo Fisher Scientific, 26–140–079). U2OS and Cos7 cells were passaged every 3–4 and 2–3 days respectively, and used under passage number 15. Trypsin-EDTA (0.25%) (Thermo Fisher Scientific 25200056) was used for passaging. For SRM imaging experiments, cells were grown on custom drilled coverslides within a sterile oval silicon cutout until 50-60% confluency prior to fixation.

Immunostaining

For immunostaining of caveolin and SNAP, cells were fixed for 20 min with 3.7% paraformaldehyde (PFA) in 1x PHEM buffer, after a quick PBS wash. Following two PBS washes, cells were quenched with fresh 0.1% sodium borohydride in PBS for 7 min, and followed 3 washes with PBS (5min each). Cells were permeabilized with 0.3% saponin in PBS for 20 min. For immunostaining of microtubules, Tom20 and vimentin, cells were fixed for 20 min with 3.7% PFA and 0.1% glutaraldehyde (GA) in 1x PHEM, followed by 3x PBS washes, quenching with sodium borohydride and permeabilization in 0.2% Triton X-100 in PBS. Blocking in PBS with 3% bovine serum albumin, 5% salmon sperm DNA (Thermo Fisher Scientific, AM9680) for 45 min was done on a rocker, followed by incubation with the primary antibody for Tom20 (1:250), caveolin (1:200), tubulin (1:100)

or vimentin (1:250) antibodies in PBS buffer containing 3% BSA. The incubation took place overnight on a rocker at 4°C in a humidity chamber. Next, cells were washed three times (5 min each) with PBS before incubation with respective secondary antibody-DS described above at a final concentration of ~8 μg mL−1 in PBS buffer containing 1% BSA and 5% salmon sperm DNA; the secondary antibody incubation also took place on a rocker at room temperature for 90 min. For DS secondary antibody incubation and subsequent steps, the sample was kept in the dark to avoid bleaching of conjugated fluorophores. Cells were washed three times with PBS (5 min each). All cell samples were post-fixed for 10 min with 3.7% PFA and 0.1% GA in 1x PHEM. Before imaging, cells were incubated with 15% 50 nm gold particles in PBS+ for 1 min, followed by a quick PBS wash.

After PBS washes, tissues were blocked with 3% BSA and 0.3% saponin in PBS for 1 hour. Next, tissues were incubated with primary antibodies: Tom20 (1:200 dilution), and panCytokeratin (1:150 dilution) in PBS containing 3% BSA and 5% salmon sperm DNA. The incubation took place on a rocker overnight at 4°C in a humidity chamber. Following three PBS washes (5 min each), tissues were incubated with respective DS-conjugated secondary antibodies at a final concentration of ~8 μg mL−1 in PBS buffer containing 1% BSA and 5% salmon sperm DNA. The incubation also took place on a rocker at room temperature for 2 hours, followed by three PBS washes (5 min each). After which, all tissue samples were post-fixed by 3.7% PFA and 0.1% GA in 1x PHEM at room temperature for 30 min. Before flow chamber assembly, tissues were incubated with 15% 50 nm gold particles in PBS+ for 1 min, followed by a quick PBS wash.

Flow Chamber assembly

Flow chamber exterior was made using a CNC-cut aluminum holder which fits gently outside the sample sandwich, providing compression to meet matching 1/16 fractional width O-rings (McMaster-Carr, 2418T11) and Tygon tubing (Cole-Parmer, EW-

06419-01) at the pre-drilled points on the coverslide. This external holder and microfluidic tubing can be easily reused for each sample (see .CAD file, data S3). Since the sample coverslide still provides the backbone of the fully assembled sample and fluidics for imaging, both the microscope objective and prism can be used at nearly identical positions between samples.

To complete flow chamber interior assembly around immunolabeled cells/tissues mounted to pre-drilled coverslides, 24 mm x 40 mm high-precision #1.5 coverslips (Thorlabs, CG15KH), and 2-inch wide Behmis® Parafilm (Thermo Fisher, 12-374-16) were first combined. After sonicating coverslips in 100 % EtOH for 10 minutes, coverslips were quickly air dried using a gentle stream of compressed air. Parafilm was cut into 1 inch wide sections and stretched length-wise until just prior to tearing. Stretched Parafilm was placed onto coverslips such that no folds or air-pockets were present. Excess Parafilm was removed from the coverslip border using a razorblade, and fluid profile stencil was used to cut the flow chamber interior into the parafilm. After peeling the inner part of the Parafilm, the coverslip and fluidic profile were ready for final assembly. After removing excess PBS from cells/tissues, coverslips with fluidic profiles were slowly placed on top of the coverslide with sample such that no excess solution contacted the Parafilm border. A 110 W glue gun tip (with glue removed) was used to gently press the coverslip along the Parafilm border to melt the Parafilm and seal the fluidic chamber.

Fluidic components used were MX Series II™ 10 Position/11 Port Selector Valve (IDEX Health & Science, MXX778-605) and RP-TX Peristaltic Pump (Takasago Electric, RP-TXP5S-P04A-DC3VS). Pump control was achieved through Arduino Uno (Amazon, X7375-10G) and Adafruit Motor/Stepper/Servo Shield for Arduino v2 Kit (Adafruit, 8541582581). Both the port selector and peristaltic pump were controlled via custom C code (see data S1,2,4).

Microscopy

Through-objective TIRF superresolution data in this work were taken on a custom single-molecule imaging system described previously [50]. Briefly, two lasers emitting at 561 nm (Opto Engine LLC, 150 mW), and 647 nm (Coherent OBIS 647, 140 mW) were combined and introduced into the back of a Nikon Ti-U microscope equipped with a 60× TIRF objective (Nikon, Oil immersion, NA 1.49). An f = 400 mm lens was placed at the back port of the microscope to focus the collimated laser light to the back aperture of the objective to achieve objective TIR illumination. The excitation light can be continuously tuned between epi-fluorescence and strict TIR angle modes by shifting the incident laser horizontally with a translational stage before entering the back port of the microscope. A custom focus stabilizing system based on detection of the reflected excitation laser was used to stabilize the focus during data acquisition. A multi-edge polychroic mirror (Semrock, Di01-R405/488/561/635) was used to reflect the lasers into the objective and clean up fluorescence signals from the sample. Emission filters used for the 561 nm (for imaging Cy3 on the DS), and 647 nm (for imaging ATTO643 conjugated ISs) were FF01-605/64 and FF01-708/75, respectively (all from Semrock). Fluorescence signals were collected through the objective by an electron-multiplied charge-coupled device (EM-CCD, Andor, iXon Ultra 897) using a typical EM gain setting at 200–300 in frame transfer mode. Unless otherwise indicated, the power density of the 647 nm laser (for DNA-PAINT imaging using ATTO643 conjugated IS) was typically around ~500 W/cm^2.

Prism-type TIRF LF-PAINT data was collected using a custom single-molecule imaging system as outlined in **Figure 2.3 A**. Key system components used from the laser to the camera were: 1W 639 nm laser (Opto Engine, MRL-FN-639-1W), 2x beam expander (ThorLabs BE02M-A), cylindrical lens f=1000 mm, 5x beam expander (ThorLabs GBE05-A), 2-5x continuous beam expander (ThorLabs BE02-05-A), 4π lens

cage (using an f = 100 mm and an f = 80 mm lens), 10 mm Square Aperture UV Fused Silica Prism (Pellin Broca, ADBU-10), 40x silicon oil objective (Nikon, Plan APO 40x/1.25 Sil λS WD 0.3, MRD73400), 647nm long pass filter (Semrock, LP02-647RU-50), 633 nm Stopline® notch filter (Semrock NFD01-633-25x36), and finally either a side-mounted Prime-95B sCMOS (Teledyne Photometrics, Prime 95B 25MM) or Kinetix sCMOS (Teledyne Photometrics). All detection path components housed within a Nikon Eclipse Ti2-E microscope body. Perfect Focus Unit (Nikon PFS, TI2-N-NDA-P) was integrated into the microscope body and provided stable autofocusing even during mild “Flow-Assisted LF-PAINT”.

Data acquisition and image processing

Superresolution images were acquired using the open source micromanager software suite (https://micro-manager.org/) [65] and saved as OMERO TIF files. Image analyses for extracting single-molecule localization and subsequent localization filtering, sorting, and rendering was performed using in-house Matlab scripts [43]. Briefly, raw localizations were first filtered based on localization fitting parameters such as signal to noise ratio, widths of point spread functions in the x and y dimensions, aspect ratio, etc. Next, the localizations were sorted, during which events that appeared within a defined number of frames (typically 2–3) and distance (typically 80 nm) were then combined into a single event with averaged coordinates. The sorted localizations were then used for final image rendering, and the rendered images were saved as TIF files for further analysis and annotations in Fiji. Multi-color images were co-registered using an average of observed gold fiducial positions within each FOV, while multi-FOV stitched images were aligned using average position of observed overlapping gold fiducials along shared image boundaries.

2.4 Results

Results within this chapter fall within 2 categories, each providing a fundamental improvement for DNA-PAINT imaging throughput. Within the first half, the development of accelerated and higher quality DNA-PAINT through DNA-PAINT-ERS will be broken down. As a foundational method for DNA-PAINT in all subsequent chapters and findings, this research proved invaluable in a variety of applications and further technique development. The figures and findings related to DNA-PAINT-ERS are re-emphasized from the initial publication [50]. In the second half, efforts to develop a novel microscope technique coined LF-PAINT showcases critical improvements to expand DNA-PAINT imaging regions ~50x larger than traditional SRM microscopes. Together with the second half of chapter 3 and all of chapter 4, these works were incorporated into the LF-PAINT publication.

Accelerated DS-IS unbinding by ethylene carbonate

EC is a water-soluble, aprotic solvent previously identified as a low-toxicity substitute for formamide in fluorescence in situ hybridization [66]. A 1:1 mixture of EC and water (v/v) as the solvent was shown to dramatically speed up hybridization between target DNA and oligonucleotide probes, possibly by improving the solubility of the hydrophobic core of the bases. Surprisingly, we found that EC actually accelerated the dehybridization of DS-IS with little impact on the reverse process when added to a DNA-PAINT imaging buffer (buffer C [51]; see Methods) at concentrations as low as 5% (v/v). We first noticed a significant decrease in the instantaneous number of IS probes bound to the sample upon addition of EC (**Figure A 2.1A**, left panel, top row). Of note, all images shown in the left panel of **Figure A 2.1A** were acquired from the same field of view (FOV) on the same sample via careful buffer exchange between imaging cycles without shifting the FOV. To understand how EC affects the kinetics of DS-IS

hybridization, we measured the τon for individual localization events using a pair of oligos referred to DS1-IS1. The DS1-IS1 pair has a 10-base complementary sequence derived from a previously published DNA-PAINT construct ‘P1’ (9 bp; see Supplementary Table 1), with an A appended at the 3′-end of the DS. On average, the τon for DS1-IS1 showed a steady decrease at increasing EC concentrations, from >2 s in the absence of EC to ~0.4 s and ~0.2 s at 10% and 15% EC, respectively (**Figure A 2.1A**, middle panel). By contrast, the binding rate between DS1 and IS1, measured as the sorted number of localization events per unit time (frame), remained largely the same (**Figure A 2.1A**, right panel). Here sorting refers to the process of combining events that likely arise from the same molecules (see Methods). Thus, by using imaging buffers containing 10–15% EC, the rate of DS-IS unbinding could be accelerated by 5–10-fold without reducing the rate of binding.

The accelerated unbinding and unaffected binding rates between the DS and the IS can also be seen by examining the difference images between successive image frames. In particular, binding events could be detected by subtracting the previous image frame from the current (**Figure A 2.1A**, left panel, middle row) and unbinding by doing the opposite (**Figure A 2.1A**, left panel, bottom row). At each EC concentration, the net number of binding events per frame was similar to that of the unbinding, which reflects the fact that the binding and unbinding processes are at equilibrium during DNA-PAINT imaging. By comparing the difference images for binding (**Figure A 2.1A**, left panel, middle row) at different EC concentrations, we observed that the numbers of binding events per frame were similar in the full range of EC concentrations tested (0–15%). This confirms that the binding rate between DS1 and IS1 stayed largely unaffected by EC; here, the binding rate is the net number of localizations per unit time normalized to the concentrations of free IS1 in the buffer (kept constant at all EC concentrations) and free DS1 (essentially the same as total DS1 thus also approximately constant). Based

on similar analyses, the unbinding rate is inversely proportional to the concentration of DS1-IS1 duplexes or the density of IS1 bound to the sample. Thus, the 5–10-fold reduction in the density of IS on the sample at 10–15% EC (**Figure A 2.1A**) corresponds to a 5–10-fold increase in the unbinding rate, or equivalently, a 5–10-fold decrease in the τ_{on}.

Accelerated DS-IS binding by tandem sequence repeats and spacer

The accelerated unbinding of DS-IS by EC made it now practical to use strategies to accelerate DS-IS hybridization without concerns of spatially overlapping localizations. One approach to achieving this is to increase the IS concentration, but this is typically limited to below 3–4 nM due to increased background signal from the diffusing IS. In addition, the binding rate could be significantly increased if there are multiple copies of the complementary (docking) sequences on the DS (**Figure 2.1**, third panel). We therefore constructed new DS1 oligos with 2 or 3 tandem repeats of the docking sequence (referred to as DS1-2x and DS1-3x, respectively) and tested their performance for DNA-PAINT. Indeed, both the 2x and 3x constructs showed dramatically increased binding of IS, resulting in much more continuous structures of the target (microtubules in this case) than using the original 1x construct under the same imaging conditions **Figure A 2.1B**, left). All the DS constructs had a fluorophore (Cy3 or FAM) attached at a 1:1 stoichiometric ratio, allowing us to normalize the DNA-PAINT signal (measured as the total number of sorted localization events) to the total DS signal (measured as the total signal from the fluorophore conjugated to the DS) from the same FOV. Using this normalization approach, we estimated that the use of 2x and 3x DS1 yielded ~3.5x and ~5x faster binding rates, respectively, compared with DS-1x (**Figure A 2.1B**, right), demonstrating the effectiveness of using repeating sequences to accelerate the binding between the DS and the IS.

The fact that using 2x and 3x DS constructs increased the binding rates by more than 2 and 3 times, respectively, led us to hypothesize that docking sites on the DS farther away from the affinity agent (a secondary antibody in this case) may be more efficiently probed by the IS, potentially due to reduced steric hindrance (**Figure 2.1**, third and fourth panels). We therefore asked whether inserting a spacer between the DS and the antibody would serve the same purpose. For the antibody-DS conjugates tested thus far, we had used a short spacer comprising a 4-unit polyethyleneglycol (PEG4) between the antibody and the DS. The spacer is part of a reagent used to prepare the conjugates and can be conveniently replaced with a different moiety (see Methods). When we extended the spacer on DS1-1x to PEG8 or PEG16, we observed a clear acceleration similar to that observed using DS1-2x or -3x, albeit to a lesser extent. The microtubule structure in the reconstructed DNA-PAINT images appeared much more continuous from a 10 min acquisition when using DS1-1x with the longer spacers (**Figure A 2.1C**, left). After normalizing to the total DS1 signal, we found the use of PEG8 and PEG16 spacers to increase the binding rate by ~40% and ~60%, respectively (**Figure A 2.1C**, right). This result confirms that the effect of using DS1-2x or -3x was indeed in part due to the alleviated steric hindrance on the 2nd and 3rd repeats of the docking sequence. We note that the spacer strategy was previously used to expedite hybridization to surface-anchored DNA [67], a situation similar to that in DNA-PAINT where the DS is typically immobilized on the target.

Accelerated DS-IS binding by tandem sequence repeats and spacer

The accelerated unbinding of DS-IS by EC made it now practical to use strategies to accelerate DS-IS hybridization without concerns of spatially overlapping localizations. One approach to achieving this is to increase the IS concentration, but this is typically limited to below 3–4 nM due to increased background signal from the diffusing IS. In addition, the binding rate could be significantly increased if there are

multiple copies of the complementary (docking) sequences on the DS (**Figure 2.1A** third panel). We therefore constructed new DS1 oligos with 2 or 3 tandem repeats of the docking sequence (referred to as DS1-2x and DS1-3x, respectively) and tested their performance for DNA-PAINT. Indeed, both the 2x and 3x constructs showed dramatically increased binding of IS, resulting in much more continuous structures of the target (microtubules in this case) than using the original 1x construct under the same imaging conditions (**Figure A 2.1B**, left). All the DS constructs had a fluorophore (Cy3 or FAM) attached at a 1:1 stoichiometric ratio, allowing us to normalize the DNA-PAINT signal (measured as the total number of sorted localization events) to the total DS signal (measured as the total signal from the fluorophore conjugated to the DS) from the same FOV. Using this normalization approach, we estimated that the use of 2x and 3x DS1 yielded ~3.5x and ~5x faster binding rates, respectively, compared with DS-1x (**Figure A 2.1B**, right), demonstrating the effectiveness of using repeating sequences to accelerate the binding between the DS and the IS.

The fact that using 2x and 3x DS constructs increased the binding rates by more than 2 and 3 times, respectively, led us to hypothesize that docking sites on the DS farther away from the affinity agent (a secondary antibody in this case) may be more efficiently probed by the IS, potentially due to reduced steric hindrance (**Figure 2.1**, third and fourth panels). We therefore asked whether inserting a spacer between the DS and the antibody would serve the same purpose. For the antibody-DS conjugates tested thus far, we had used a short spacer comprising a 4-unit polyethyleneglycol (PEG4) between the antibody and the DS. The spacer is part of a reagent used to prepare the conjugates and can be conveniently replaced with a different moiety (see Methods). When we extended the spacer on DS1-1x to PEG8 or PEG16, we observed a clear acceleration similar to that observed using DS1-2x or -3x, albeit to a lesser extent. The microtubule structure in the reconstructed DNA-PAINT images appeared much more continuous

from a 10 min acquisition when using DS1-1x with the longer spacers (**Figure A 2.1C**, left). After normalizing to the total DS1 signal, we found the use of PEG8 and PEG16 spacers to increase the binding rate by ~40% and ~60%, respectively (**Figure A 2.1C**, right). This result confirms that the effect of using DS1-2x or -3x was indeed in part due to the alleviated steric hindrance on the 2nd and 3rd repeats of the docking sequence. We note that the spacer strategy was previously used to expedite hybridization to surface-anchored DNA [67], a situation similar to that in DNA-PAINT where the DS is typically immobilized on the target.

Combining E, R, and S for fast and multiplexed DNA-PAINT

By combining the three components (EC, Repeating sequence, and Spacer), DNA-PAINT-ERS obtains fully developed images of cellular structures in a matter of minutes. For example, by using the DS1-2x construct attached to an anti-mouse secondary antibody via a PEG16 linker (DS1-2x-PEG16), we were able to image microtubules in detergent-extracted U2OS cells in merely 150 s (**Figure 2.2A**). DNA-PAINT-ERS imaging of non-extracted cells typically warrants a longer acquisition due to slower probe diffusion, which could both decrease binding rate and cause higher background, but the imaging was still routinely completed within 200–300 s. In either case, the significantly accelerated DS-IS localization kinetics yielded clean and bright single-molecule images to afford a lateral localization precision better than 10 nm, corresponding to a spatial resolution of ~23 nm or better, consistent with the apparent width of microtubules measured in the resulting images (**Figure 2.2A**, right panels).

DNA-PAINT-ERS is also readily applicable to the DS2-IS2A pair (IS2-A is referred to as IS2 hereafter). Here, we conjugated DS2-2x to an anti-rabbit antibody using a PEG16 spacer and tested its use for DNA-PAINT-ERS imaging of clathrin. This allowed us to complete DNA-PAINT imaging and obtain well-resolved clathrin structures within 200–300 s (**Figure 2.2B**). Owing to the high-quality single-molecule images, the

resulting images clearly resolved the circular clathrin-coated pits commonly seen in prior superresolution [68] and electron microscopy [69] studies. In addition, we also observed many irregularly shaped structures that may be attributed to flat clathrin plaques [69, 70]. A close-up inspection of individual clathrin structures even began to reveal details reminiscent of the underlying triskelion lattice (**Figure 2.2B**, right panels and insets). These results demonstrate the applicability of DNA-PAINT-ERS to broad DS-IS pairs, including those validated in previous DNA-PAINT experiments with slight modifications.

We next combined DS1-2x-PEG16 and DS2-2x-PEG16 in the same experiment on U2OS cells dual-labeled for microtubules (DS1) and clathrin (DS2), which was carried out in two cycles via probe exchange (exchange-PAINT [51]) in either order. Similar to the single-color experiments, we were able to obtain complete structures of the microtubules within ~200 s and those of clathrin-coated pits within ~300 s, thus completing a two-color imaging session in a little more than 8 min (**Figure 2.2C**). There were no signs of crosstalk between the DS1-IS1 and DS2-IS2 imaging cycles, demonstrating the conserved specificity of these probes despite the use of 2x DS constructs, addition of a PEG spacer, and the presence of EC. These results suggest that multiplexed imaging with DNA-PAINT-ERS can be implemented in a manner essentially identical to those previously done with DNA-PAINT, except that now each cycle is about an order of magnitude faster.

DNA-PAINT-ERS improves superresolution image quality

Besides the increased imaging speed, we also routinely obtained higher quality images using DNA-PAINT-ERS than using current DNA-PAINT. Specifically, by bringing τ_{on} from >2 s to ~0.2 s, EC allows clean, single-molecule images to be obtained even in areas of high target density, where a slow IS turnover can be problematic in causing degradations in image quality. This is demonstrated in **Figure A 2.1A**, where densely packed structures such as caveolae appeared blurred in the reconstructed images at the

periphery (areas 1 and 4), although the situation improved somewhat near the center (areas 2 and 3) of the FOV. This problem is not specific to the DS2-IS2 construct as the same has been recently reported by Steher et al. on at least the ‘P1’ construct (from which DS1-IS1 was derived) [52]. In all these cases, the problem is likely attributed to the gradient in the rate of photobleaching from the center to the periphery of the FOV. In DNA-PAINT, photobleaching helps remove IS already bound to the sample, thus increasing the apparent unbinding rate of the IS and reducing the cluttering of the fluorescent probes to result in better resolved images. When using a Gaussian beam, the excitation power density is lower at the periphery compared with the center of the FOV, causing non-optimal localization kinetics at the periphery when the power density is optimized for best kinetics around the middle of the FOV. Steher et al. addressed this issue by creating a flat-top illumination pattern to homogenize the power density across the FOV9. By contrast, inclusion of 10–15% EC in the imaging buffer drastically increases the unbinding rate of the IS to result in consistent, well-resolved structures of caveolae across the entire FOV without the negative impact of the laser intensity gradient (**Figure A 2.2B**).

Extending the DS-antibody spacer further helped improve the image quality. When using a short spacer (PEG4), we found that some caveolae structures detected in epi-fluorescence (visualized via Cy3 attached to the DS) failed to be reconstructed in DNA-PAINT (**Figure A 2.2C**, left column, top three rows) even with extended imaging time (**Figure A 2.2C**, left column, bottom two rows), suggesting that the absence of those structures in DNA-PAINT images was likely caused by the relative inaccessibility of the DS (DS2-1x) in those regions. The reason for this inaccessibility is currently unclear, but steric hindrance or local interactions between the DS and the antibody may be the culprit; crowding in a cellular environment may also contribute to the steric hindrance. This artifact was resolved by using PEG8, particularly with long acquisitions

(20–30 min; **Figure A 2.2C**, middle column). With PEG16, all caveolae were detected and well reconstructed at 10 min, and it was no longer necessary to perform long acquisitions (**Figure A 2.2C**, right column). Aside from helping to better resolve structures, the spacers should also benefit quantitative PAINT [71] where consistent accessibility of the DS is critical. Of note, these tests were all carried out using the DS2-1x construct, and a PEG8 spacer might suffice if a DS-2x or -3x construct were used. In addition, although we have only tested the PEG spacers, other types of moieties may prove effective or as superior spacers.

Implications for larger FOVs in SRM imaging

Over the past few years, growing interest has attempted to expand effective FOVs for super-resolution imaging, since throughput and imaging area restrictions limit usage for unparalleled image quality. As a scalable method to overcome these limitations, we present Large-Field DNA-PAINT, a flexible method to accelerate DNA-PAINT throughput and downstream applications.

Integrating prism-type illumination and microfluidics for LF-PAINT

Our LF-PAINT system was designed to combine a prism-type illumination scheme with an on-stage microfluidic system for programmable fluid exchange. This combination was essential to enabling multiplexed SRM via exchange-PAINT over much larger FOVs compared with the microscope configurations used in prior work.

We chose DNA-PAINT as the imaging strategy for large-field SRM for several reasons. First, DNA-PAINT allows convenient multiplexing. DNA-PAINT is based on subdiffractive localization of single-molecule events that arise from reversible binding between short, dye-labeled imaging strand (IS) oligos and their complimentary docking strands (DS) [39]. This simplifies multiplexed imaging into cycles of single-color imaging via buffer exchange, an approach properly termed exchange-PAINT [63]. Second, DNA-PAINT can use fluorophores with higher single-molecule brightness [56] than those that

photoswitch (as required in PALM [72] and STORM [41]). This relaxes the need for using high NA objectives for detection, an important factor to extending the detection FOV. Third, DNA-PAINT is amenable to FOV stitching. This is because the imaging process only probes the dye-labeled IS, which is 'indefinitely' replenished from the excess present in solution, therefore imaging of the current FOV does not degrade the adjacent FOVs. Fourth, DNA-PAINT has a mild requirement on laser power, especially with recent improvements in imaging kinetics through DNA-PAINT-ERS and alternative approaches [50, 73]. Instead of 2-10 kW/cm2 used in STORM and conventional DNA-PAINT, in DNA-PAINT-ERS we typically use 0.2-0.5 kW/cm2 without compromising the imaging kinetics (hence image quality) or resolution [50]. This has permitted illumination across FOVs >300 μm x 300 μm with sufficient power density using a moderate 0.5 – 1 W input laser power.

We achieved large field illumination with tunable FOVs using a prism-based optical configuration. Prism-type TIR, which preceded the now more popular objective-type TIR, allows for more flexible beam shaping and can accommodate higher laser power than the latter [74]. We developed our prism-type illumination system to allow flexible adjustments in both beam expansion and the incident angle (at the sample interface) to tune in and out of TIR (**Figure 2.3A**). A cage-mounted, 4π lens pair maintains the beam position on the sample while adjusting the TIR angle using a mirror placed upstream. Additionally, we utilized a weak cylindrical lens to compensate for longitudinal beam widening during prism-type illumination to maintain power density over a round FOV for efficient single-molecule excitation and DNA-PAINT imaging. The sample is placed on a glass coverslide and sandwiched between the slide and a coverglass, with the space in between filled with imaging buffer. Signals generated at the top glass - solution interface travel through the solution and the coverglass before being detected by an objective placed at the bottom (**Figure 2.3B**).

With illumination decoupled from detection, we could choose objective lenses best suited for single-molecule detection across large FOVs instead of being constrained to those (e.g. high NA TIR lenses) for both illumination and detection. While most prism-type TIR setups used a 60x oil immersion objective (NA ~1.4) for single-molecule detection, we found that a 40x, silicone oil immersion (Sil, Nikon) objective (NA 1.25) provided better overall performance than a 60x oil objective with higher NA. With a large working distance (0.3 mm), the 40x Sil lens was designed for imaging through aqueous media at extended depths (as in our case) [75]. Despite the lower NA, it yielded better or comparable single-molecule brightness than the 60x lens. The 40x Sil lens also exhibits superior field flatness than the higher NA, oil immersion lenses to afford high quality single-molecule imaging across whole FOVs as large as ~0.5mm x 0.5mm (**Figure 2.3C and 2.7**). Lastly, at 40x magnification, the Sil lens works well with both scientific CMOS (sCMOS) cameras used in this work, namely the Prime 95B and Kinetix, to yield FOVs of 291 µm x 291 µm (using the built-in 1.5x tube lens) and 521 µm x 521 µm (using the 1x tube lens), respectively. The resulting, effective imaging pixel sizes in the two cases are 188 nm and 161 nm, respectively, both well suited for single-molecule localization.

Another enabling feature of our LF-PAINT setup is the on-stage microfluidics. To adapt multi-target DNA-PAINT multiplexity using specific, complementary DS and IS oligonucleotides through exchange-PAINT, we designed a microfluidic flow cell based on the sandwiched sample format and developed a workflow to prepare and image cells and tissue sections using LF-PAINT. The sample chamber of the microfluidic cell takes a tear-drop shape for efficient and complete buffer exchange, modeled similarly to other expansion/contraction designs [76]. We found that fire-polished glass coverslides yielded minimal background autofluorescence. Drilled and cleaned coverslides are directly used with conventional tissue cell-culture, or coated with polyethyleneimine (PEI) for use with FFPE tissue sections (see methods). When imaging cultured cells, we first grew cells on

the coverslide using a temporary silicone ring to hold the culture media, which also was used during sample labeling and then removed prior to sample sandwich assembly. In the final assembly, we used stretched, cut, and melted parafilm as an easy-to-use microfluidic seal between the sample-mounted coverslide and the bottom coverslip (**Figure 2.3B**). We found stretching reduces parafilm thickness versus previous similar chamber applications [77], typically achieving an interior chamber thickness of ~35 ± 5 µm (as measured by a micrometer before and after assembly).

This resulting assembled microfluidic chamber was then mounted within our custom microfluidic exterior holder (**Figure 2.3B**). This computer-designed (see CAD file, data S3) and precision-machined aluminum exterior provides stable mounting and microfluidic seals for Tygon tubing (**Figure 2.3B**). Inlet and outlet fluid ports were connected to both a computer controlled rotary valve and peristaltic pump, allowing stable hands-free fluid exchange while mounted and during imaging. The exterior mounting system can be easily removed and attached to new samples.

Multiplexed LF-PAINT for membrane and cytosolic targets in cells

Utilizing our LF-PAINT setup, and the ease of imaging with stable kinetics over extended durations, we obtained arrays of LF-PAINT images of both membrane-adjacent caveolae and cytosolic mitochondria (**Figure 2.4 & 2.5**). Through focus stabilization both within DNA-PAINT video collections and between each FOV, images taken from adjacent FOVs can be stitched together to generate an even larger view of cell populations. Examples are shown in **Figure 2.4 & 2.5**, where individual FOVs are ~300µm x300µm with a ~40µm overlap in each dimension. Gold nanoparticles were added to the sample during preparation and used for both drift correction and as alignment fiducials between FOVs to aid in image stitching. The stitched images reveal an area of up to 1 mm2, exemplifying the substantial range of spatial and target specific information obtainable by LF-PAINT.

With optimized imaging kinetics via DNA-PAINT-ERS [50], a single FOV was imaged in 10-15 minutes depending on the target, with full 3x3 and 4x4 FOV arrays acquired within 1.5-2 and 3-4.5 hours, respectively. Stitching based on 520µm x520µm FOVs using the Kinetix camera should further reduce the imaging time need for covering a 1mm x 1mm sample area to <1 hour per target, since only a 2x2 array is needed. A practical challenge to using the larger FOV for stitched imaging is the need to perfectly level the sample such that the whole FOV is in the same focal plane, which is nontrivial at present for the 520µm x 520µm FOV. For this reason, the majority of the data presented in this work is based on the smaller, ~300µm x 300µm FOV configuration.

By adjusting the laser incident angle and hence TIR imaging depth, both membrane and cytosolic targets can be imaged with LF-PAINT. Using strict TIR, membrane-adjacent caveolae (**Figure 2.4A-D**) were imaged to reveal distinct membrane invaginations ~50-150 nm in diameter as well as smaller potential precursor structures by labeling Caveolin-1 (Cav-1). By relaxing the TIR angle (~0.5° adjustment of the mirror from strict TIR), targets such as mitochondria that are more cytosolic and located deeper in the cells can be reliably imaged (**Figure 2.5A-D**). Of note, even with relaxed TIR, some mitochondria – for example those next to the nucleus – were beyond the imaging depth and not imaged well. To address this, 3D LF-PAINT imaging at multiple focal planes (covering whole cells) is necessary [30, 78]; this is currently under development. These results demonstrate the utility of our LF-PAINT setup for imaging various cellular targets without the need to keep strict TIR as in the case of coverslide-based waveguide illumination [62].

Building from demonstrated LF-PAINT for single targets, we next tested the capability for reproducible fluidic exchange and multi-target LF-PAINT based on exchange-PAINT. The integrated microfluidics (**Figure 2.3C**) system comprising the custom sample holder and the fluid pump allowed programmable exchange of DNA-

PAINT imaging buffer. For exchange-PAINT, we incorporated a washing buffer with 15% ethylene carbonate (EC) in DPBS- for 2 minutes and reintroduced the new imaging solution for 2 minutes after each imaging cycle and prior to subsequent acquisitions (**Figure A 2.3**). We found that flowing the washing buffer through the chamber for 2 minutes effectively removed all observed localizations, and a full buffer exchange could be completed in well under 5 minutes. By iteratively imaging microtubules, we confirmed that the fluid exchange process did not induce any noticeable alterations to the structures after five cycles of imaging and washing (**Figure A 2.3**). As such, the same buffer exchange scheme was used for all subsequent, multi-target acquisitions.

For multiplexed LF-PAINT imaging, we prepared three DS-conjugated secondary antibodies (anti-mouse DS1, anti-rabbit DS2 & anti-chicken DS3) and used them for labeling microtubules, mitochondria and vimentin in cultured COS7 cells. Each target was then imaged using complimentary fluorescent IS conjugated to ATTO643 (**Figure 2.6A**), and imaging of the three targets was completed in three cycles (IS1, IS2, IS3 & intermediate washes) as described above (**Figure 2.6B**). In the co-registered multitarget images all three targets were well resolved, revealing their spatial relationships such as occasional associations between mitochondria and the two cytoskeletal filaments (**Figure 2.6C, D**). We similarly obtained a two-target LF-PAINT image of microtubules and vimentin over the larger, 520µm x 520µm FOV by switching to the Kinetix camera (**Figure 2.7A-C**). These results further demonstrate the flexibility and extensibility of our LF-PAINT setup for a variety of length-scales and targets of interest.

Quantitation of the resulting images showed comparable image quality and resolution between LF-PAINT and the traditional, objective-type based DNA-PAINT(-ERS) (**Figure A 2.4**). Line profiles of microtubules had Full Width Half Maximum (FWHM) of 47 ± 3 nm (objective-type) and 51 ± 4 nm (prism-type) (**Figure A 2.4**). Assuming an inherent width of microtubules (with the bound antibodies and the DS)

around 40 nm, these measurements suggest an effective resolution at ~25nm for our objective-type DNA-PAINT, which is typical and consistent with our previous results [50], and ~30 nm for the prism-type LF-PAINT.

2.5 Discussion

In summary, we have shown that by optimizing both imaging kinetics and effective FOV, DNA-PAINT can become a scalable imaging strategy for large FOV imaging all at SRM quality. For kinetics we have shown that by enabling rapid DNA on-off kinetics and improved DS accessibility, DNA-PAINT-ERS allows fast superresolution imaging with high resolution and improved image quality. Compared with the recent attempt by Schueder et al [56], DNA-PAINT-ERS not only affords similar imaging speed and resolution, but also offers important additional advantages. Most notably, DNA-PAINT-ERS does not require specific, sequence-optimized DS-IS pairs and should be applicable to most, if not all, existing DS-IS pairs (e.g., DS1 and DS2) with minor and straightforward modifications. Furthermore, DNA-PAINT-ERS uses DS-IS pairs with longer (9–11 bps) complementary sequences than current standards (8–9 bps) [51] or PS3 (6–7 bps) [56]. Thus, we anticipate DNA-PAINT-ERS to be compatible with a large, existing panel of DS-IS pairs to allow fast and high-quality superresolution imaging in potentially tens of colors. A systematic effort to both adopt existing8 and identify new DS-IS pairs for DNA-PAINT-ERS is currently underway.

The excellent performance of DNA-PAINT-ERS is achieved through steps easily incorporated into current workflows without the need for special optics or an oxygen scavenger (OS). In the case of Schueder et al., an OS was used to increase photon yield from individual localization events [56]; this adds cost and complexity to the experiments, since the OS can lose activity in a matter of hours. In contrast, DNA-

PAINT-ERS utilizes sequence repeats (R) and a spacer (S) that are incorporated through slight modifications to the antibody and DS preparation steps, and EC (E) is conveniently added to the standard DNA-PAINT imaging buffer (buffer C). By decoupling the localization kinetics from laser illumination, EC ensures uniform, high-quality imaging across the entire FOV on a standard wide-field imaging setup (**Figure A 2.2**), a goal previously achieved by using structured illumination [52]. By eliminating complicating factors, DNA-PAINT-ERS should facilitate automated superresolution microscopy over extended durations, such as multiplexed imaging across large FOVs [56, 62] and multiple focal planes.

We have also demonstrated a new, large-field DNA-PAINT (LF-PAINT) imaging platform for multiplexed and multiscale imaging of cells and tissues across roughly five orders of length scales (~10 nm to 1 mm). Our approach capitalizes on improvements in the optical design (prism-type illumination in the up-right position, and efficient signal detection in the inverted position), DNA-PAINT imaging kinetics (based on DNA-PAINT-ERS), sample preparation, as well as the integration of a programmable microfluidic system. By decoupling the illumination and detection paths, LF-PAINT achieved single FOVs up to ~520 µm x 520 µm instead of being optically capped at 150-200 µm in at least one image dimension as in previous attempts [60-62]. The integration of a microfluidic imaging chamber and buffer exchange system enabled flow-assisted DNA-PAINT to yield high-quality LF-PAINT images on clinical, FFPE sections. Leveraging the benefits of DNA-PAINT(-ERS), LF-PAINT inherently supports multiplexed imaging (through exchange-PAINT [63]) and robust FOV stitching for imaging even larger sample areas (>1 mm^2). As such, LF-PAINT can readily address large cell populations in model and clinical samples, laying the foundation for broad biomedical applications.

A key attribute of the LF-PAINT setup was the flexibility to accept various sample formats. Despite the slight complexity in working with the sandwiched sample chamber,

the same design is fully compatible with tissue culture and standard tissue section workflows. The sample chamber also allowed integration of programmable microfluidic capability to not only facilitate multiplexed LF-PAINT but also high-quality tissue (and to a lesser extent, cell) imaging via flow-assisted LF-PAINT. The mechanical stability of this chamber holder also permitted long-term imaging, especially when stitching multiple FOVs. Moving forward, these characteristics will make the LF-PAINT ideally suited for full automation to image even larger areas on various biological specimens.

LF-PAINT is permissive to further improvements in both imaging throughput and spatial resolution. The imaging time for a single FOV is typically 5-20 minutes for DNA-PAINT-ERS and LF-PAINT depending on the target, with targets of higher abundance requires more time to complete imaging. Thus, imaging time needed to complete a full 1 mm x 1 mm sample area is 1.5-6 hours and 0.5-1.5 hours when using the Prime 95B (291 µm x 291 µm single FOV) and the Kinetix (521 µm x 521 µm single FOV), respectively. With optimized sample and camera alignment procedures, we expect imaging with the Kinetix to become routine LF-PAINT should be compatible with 3D SRM with modifications to the optical configuration and data analysis routines. We also expect the spatial resolution for LF-PAINT to increase to ~20 nm or better (currently ~30 nm) by using a more powerful laser (currently ~1 W at 640 nm). Finally, the LF-PAINT system is amenable to automation. In fact, automated FOV stitching and buffer exchange [79] as well as on-line data processing [29, 80] should all be possible with existing hardware and software.

2.6 Conclusion

In conclusion, our study demonstrated improved DNA-PAINT imaging speed and multiplexity are poised to greatly accelerate SRM imaging. Notably this makes imaging

larger and complicated model systems more feasible, where thousands of cells can be visualized with multiplexed SRM quality in under a day of imaging. DNA-PAINT-ERS has proven utility not just within this chapter, or subsequent chapters of this thesis, but also as a foundation for all ongoing SRM imaging projects as well. The amenability of the DS-conjugation strategy developed in part with DNA-PAINT-ERS is being developed for use with a variety of other affinity reagents, including affibodies, nanobodies, and even small-molecule probes.

Importantly for imaging model systems at scale, LF-PAINT in particular pushes the boundary of FOV to not just larger populations of cells, but also large regions of cancer. Paired with unique optimizations in chapter 4, the next frontier of scalable imaging cancer patient samples is demonstrated using LF-PAINT. Combining these improvements and recent advances in sample labeling and multiplexing strategies [19, 42, 81], 3D LF-PAINT imaging of ~10 or more targets over >1 mm2 sample areas should become readily feasible. We anticipate more sophisticated automated imaging tools to become available to facilitate more common utilization of LF-PAINT.

Acknowledgements

The authors thank Drs. Joe W Gray, Gordon Mills, Terry K Morgan, Young Hwan Chang, Jason Link, Sean Speese, Yu-Jui (Roger) Chiu, David Qian, and many other colleagues at OHSU for their helpful discussions. M.J.R, F.C., J.K., D.H., T.Z., S.E., and X.N. are members of and supported by the Cancer Early Detection Advanced Research (CEDAR) Center of the OHSU Knight Cancer Institute.

Funding:

Research in the Nan lab was supported by the OHSU Knight Cancer Institute, the Damon Runyon Cancer Research Foundation, the M. J. Murdock Charitable Trust, the Prospect Creek Foundation, the Cancer Systems Biology Consortium from the

National Cancer Institute (CSBC, grant number U54 CA209988, PI: Joe W. Gray), and the National Institute of General Medical Sciences (grant number R01 GM132322, PI: X.N.).

Author Contributions

XN and FC conceived the project and SE helped supervise. MR, FC, JK, DH and XN developed the initial workflows and established the microscope design and fluidic design. KT and JS performed all reagent synthesis and purifications for DNA-conjugates. MR and XN developed the image processing pipelines used. MR, and JK acquired and performed data analysis. MR and XN wrote the manuscript. XM, MR, KT, MS, TZ and SE reviewed and edited the manuscript. All authors have reviewed and approved the LF-PAINT manuscript.

Declaration of Interest

The authors report no conflicts of interest.

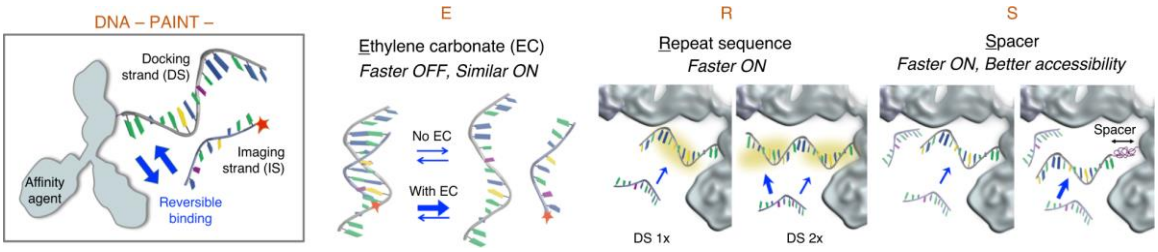

Figure 2.1 | Schematics of DNA-PAINT-ERS

First panel illustrates the standard DNA-PAINT process; where affinity-reagents conjugated with docking strand (DS) oligomers reversibly hybridize with fluorophore-conjugated imaging strand (IS) oligomers. Second to fourth panels depict the effect of ethylene carbonate (E), repeating sequence (R), and spacer (S), respectively. In the latter two cases, the DNA oligos and the antibody are drawn roughly to scale.

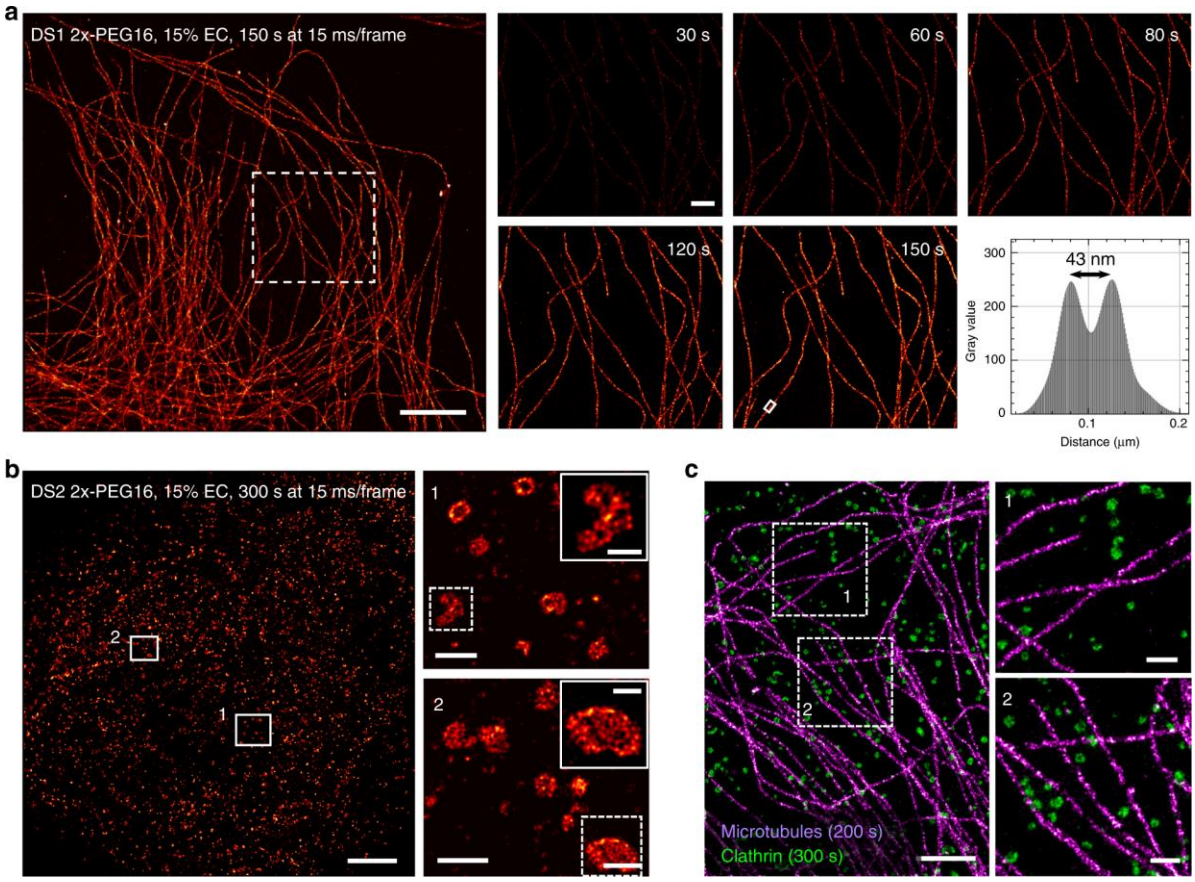

Figure 2.2 | Fast superresolution imaging with DNA-PAINT-ERS using multiple DS-IS pairs.

a DNA-PAINT-ERS imaging of microtubules in U2OS cells using the DS1-2x-PEG16 construct paired with IS1-CF660R. Left panel shows the reconstructed superresolution image of the whole FOV, with zoom-in-views at different acquisition times shown on the right. Bottom right plot shows the intensity profile of the structure in the boxed area in the reconstructed image at 150 s. b DNA-PAINT-ERS imaging of clathrin in U2OS cells using the DS2-2x-PEG16 construct paired with IS2-CF660R. Left panel shows the reconstructed image of the whole FOV, and the right panels are the zoom-in views of the boxed areas in the image on the left. Insets in the two images on the right are the zoom-in views of the regions in the dashed boxes. c Two-color imaging of microtubules (purple) and clathrin (green) in U2OS cells with DNA-PAINT-ERS, using the same DS1-IS1 (tubulin) and DS2-IS2 (clathrin) constructs as used in (a) and (b). The left panel shows a ~10 × 15 μm2 FOV, and the right panels are the zoom-in views of the two regions in the dashed boxes. Scale bars: 5 μm (a, left), 500 nm (a, right), 5 μm (b, left), 500 nm (b, right), 200 nm (b, right insets), 2 μm (c, left), and 500 nm (c, right).

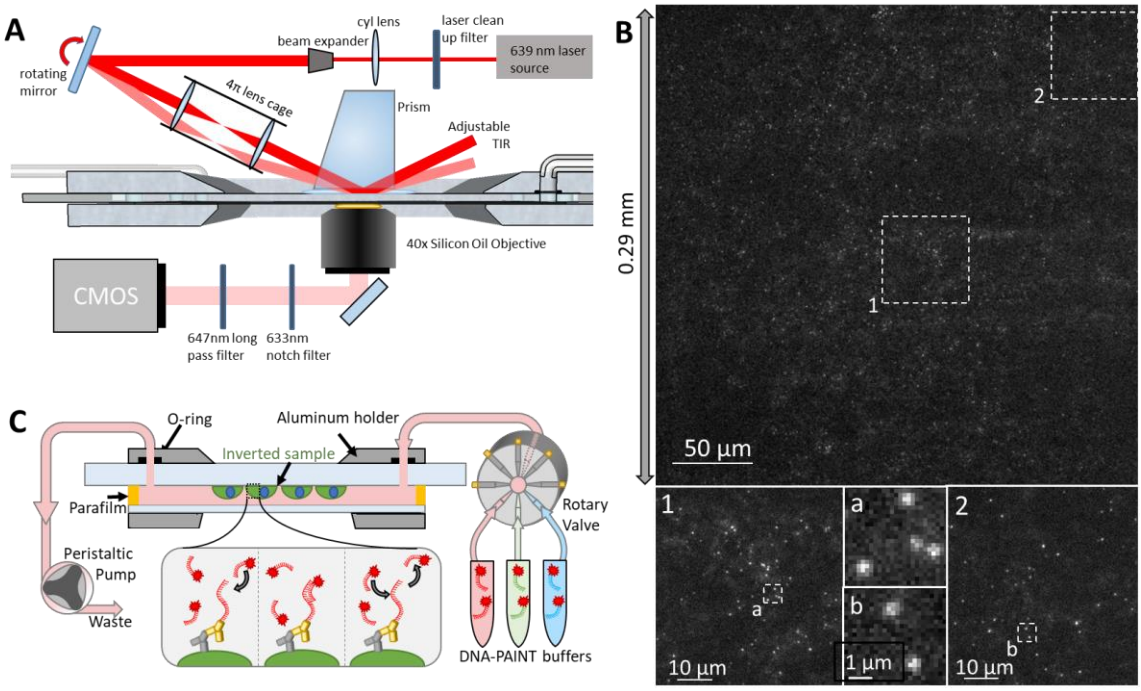

Figure 2.3 | Schematic of the LF-PAINT optical setup, fluidics integration, and example SMLM.

(A) Schematic of the LF-PAINT microscope design and general imaging strategy, with the widened laser beam and controllable TIR angle. (B) Representative LF-PAINT raw image at 30 ms exposure highlights single-molecule localization quality. Single-molecule events are clearly resolved both in the center on the FOV, and near the corners, exemplifying the 300 µm x 300µm FOV. (C) Schematic cross-section of the flow chamber assembly and sample position. Notably, cultured cells/mounted tissue are attached on an inverted sample coverslide, enabling both encapsulation of imaging solutions and buffer exchange for multi-target DNA-PAINT imaging. DNA-PAINT imaging utilizes oligonucleotide-conjugated antibodies (DNA in red, antibody in yellow) and complimentary imaging strand (IS, also shown in red with a fluorophore represented by a red star) to provide transient single-molecule localizations while freely diffusing strands contribute only slightly to background fluorescence.

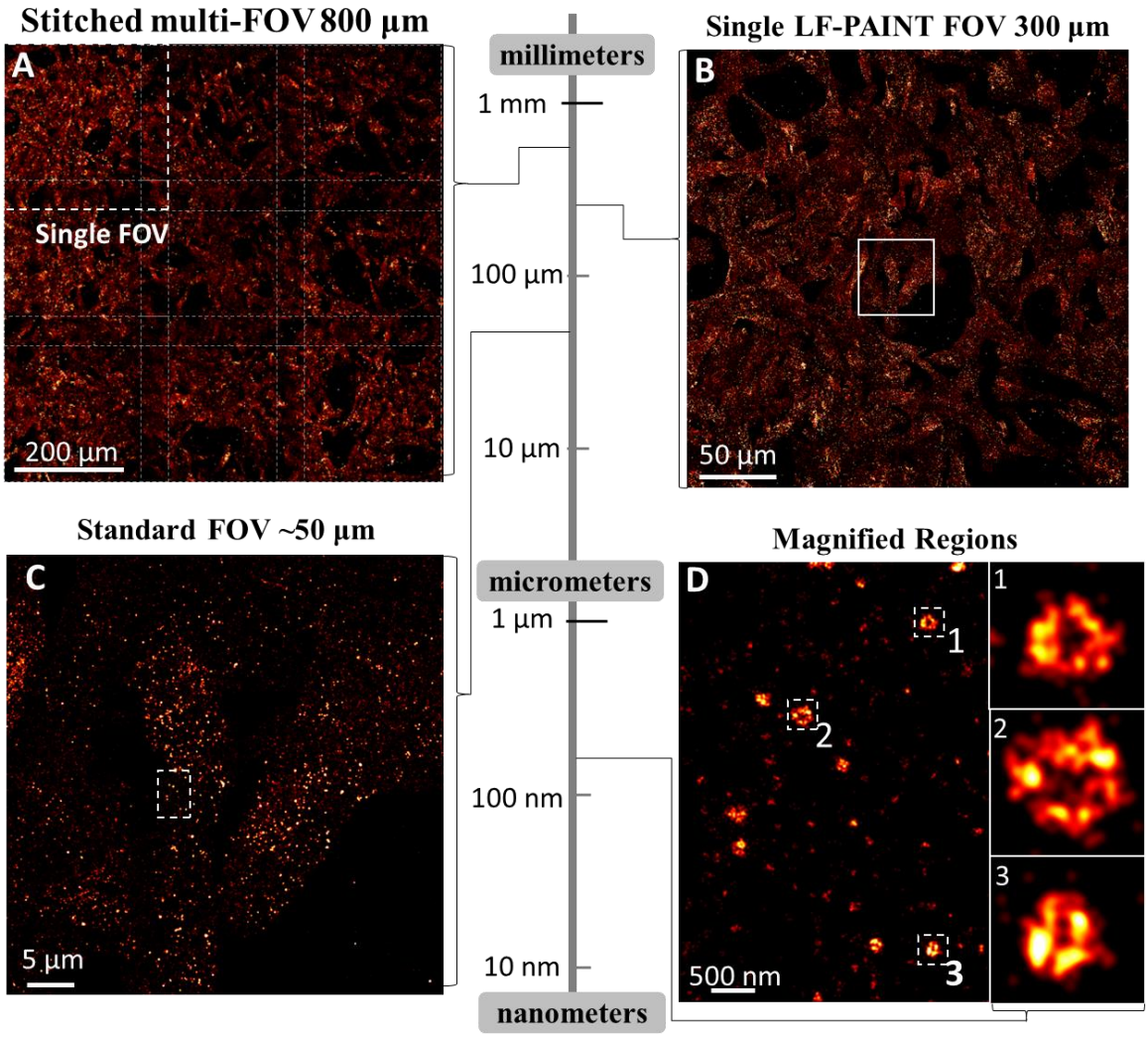

Figure 2.4 | LF-PAINT of membrane adjacent Caveolae

(A) Stitched 3x3 array of membrane-adjacent caveolae at 800 µm x 800 µm FOV with 40 µm overlaps. (B) Single LF-PAINT FOV at nearly 300 µm x 300 µm of Caveolin-1 imaged with strict TIR angle. (C) Magnified region from B highlighting the detail within a more standard smaller FOV of ~50 µm. (D) Magnified cell region from C and 3 insets showing high-quality super-resolution detail of caveolae vesicles. Each single LF-PAINT image (B) was acquired in 15 minutes (30,000 frames at 30 ms exposure) using 1 nM IS2-ATTO643 and 12.5% EC for Caveolin-1. Stitched 3x3 FOV was acquired in 135 minutes. Scale bars are 200 µm in (A), 50 µm in (B), 5 µm in (C), and 500 nm in (D). Insets in (D) are 300 nm wide.

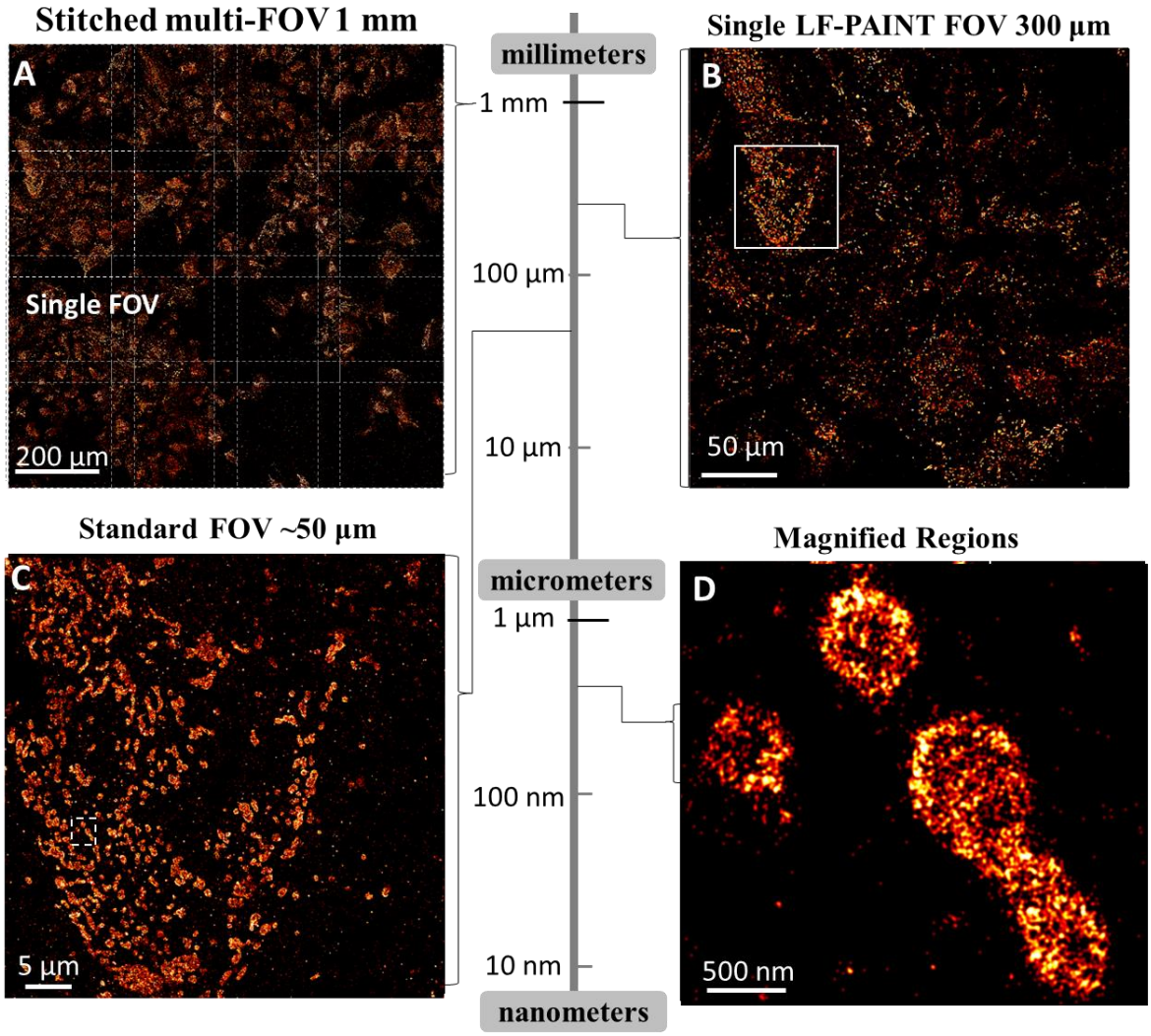

Figure 2.5 | LF-PAINT of cytosolic Mitochondria

(A) Stitched 4x4 array of cytosolic Tomm20 over 1 square millimeter. (B) Single LF-PAINT FOV at nearly 300 µm x 300 µm. (C) Magnified region from F highlighting mitochondria within a more standard smaller FOV of ~50 µm. (D) Magnified cell region from G with distinct mitochondria. Each single LF-PAINT image (B) was acquired in 15 minutes (30,000 frames at 30 ms exposure) using 1 nM IS2-ATTO643 and 12.5% EC for Tom20. Stitched 4x4 FOV was acquired in 240 minutes. Scale bars are 200 µm in (A), 50 µm in (B), 5 µm in (C), and 500 nm in (D).

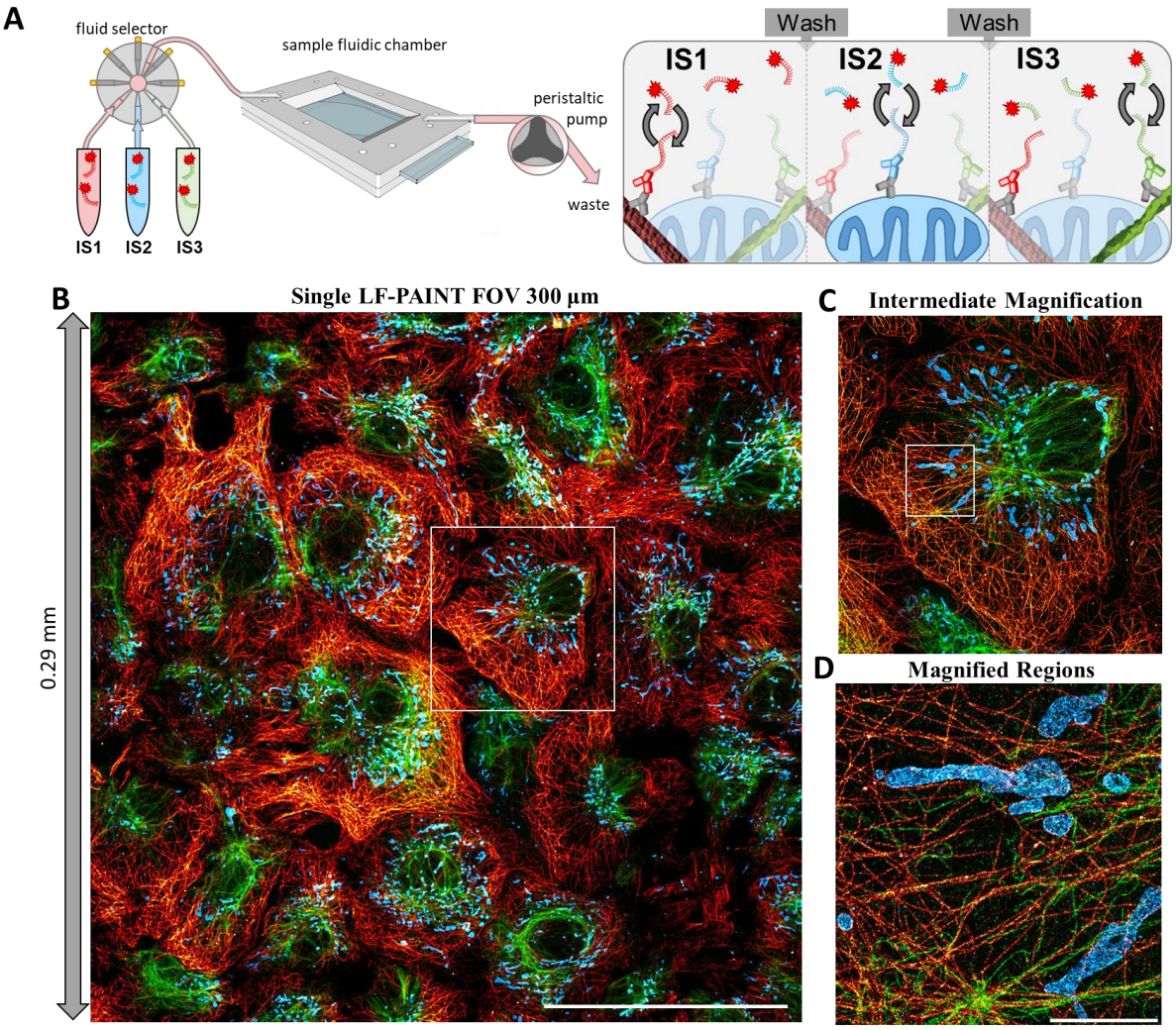

Figure 2.6 | Microfluidic Exchange Enables Multiplexed LF-PAINT

(A) Schematic of multiplexed imaging with complimentary imaging strand (IS) targeting docking strand (DS) to microtubules (red), mitochondria (blue), and vimentin (green). (B) Single LF-PAINT 3-target image of Cos7 cells at 300 µm x 300 µm. (C) Magnified region from (B) highlighting image quality over a more standard ~50 µm FOV. (D) Magnified region from C showing distinct cytoskeletal structures and mitochondria. The 3-target image (B-D) was acquired in 45 minutes total (30,000 frames at 30 ms exposure for each target) using 1 nM IS1-ATTO643 and 12.5 % EC, 1 nM IS2-ATTO643 and 12.5 % EC, and 500 pM IS3-ATTO643 and 13.75 % EC for microtubules, mitochondria, and vimentin respectively. Scale Bars are 100 µm in (B), 20 µm in (C), and 5 µm in (D).

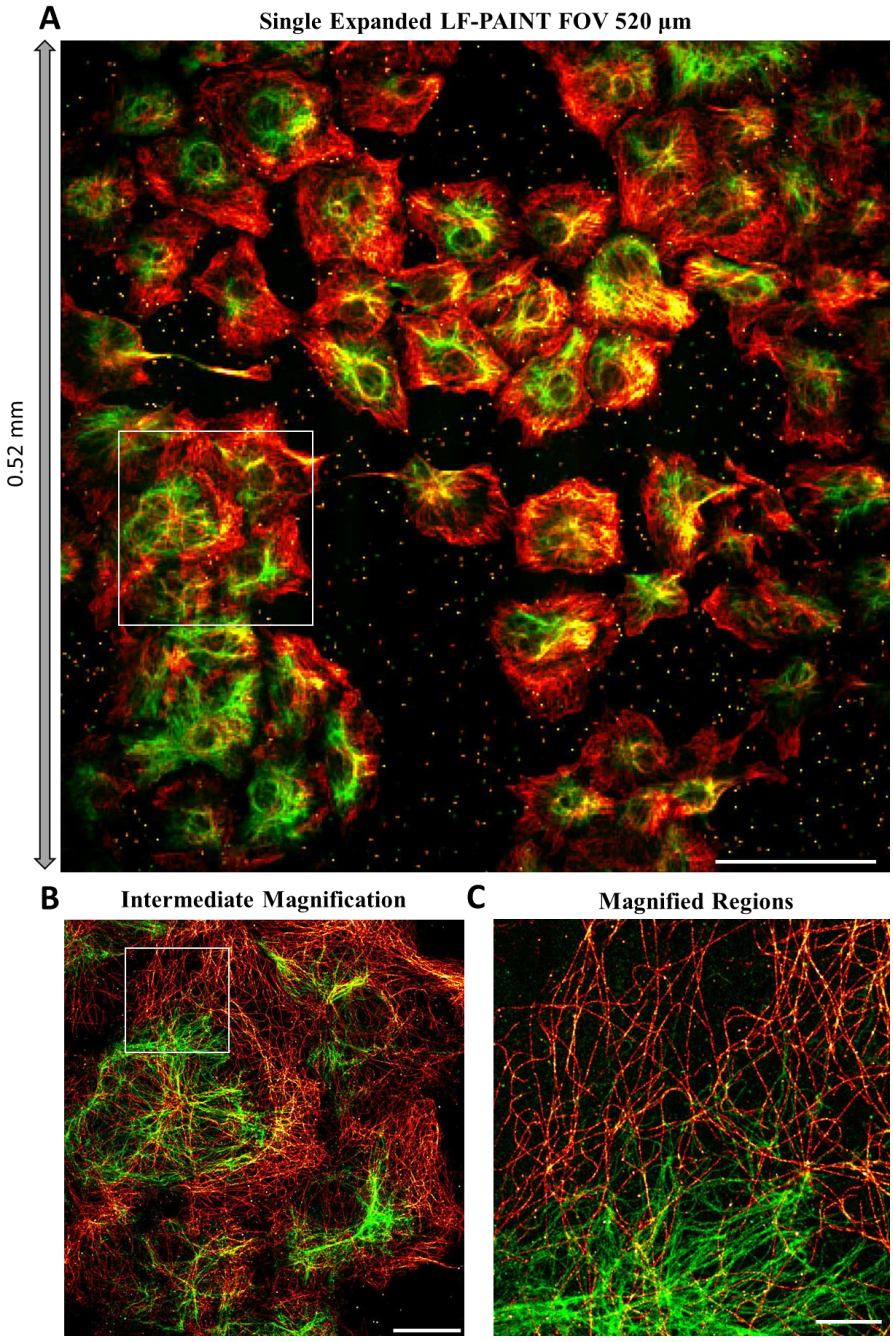

Figure 2.7 | Expanding LF-PAINT FOV

(E) Expanded LF-PAINT 2-target FOV at 521 µm x 521 µm. (F) Intermediate magnification from (E) at 100 µm FOV. (G) Magnified region from (F) highlighting dense perinuclear vimentin and extended microtubule networks. Expanded LF-PAINT FOV 2-target image (E-G) was acquired in 30 minutes total (30,000 frames at 30 ms exposure for each target) using 1 nM IS1-ATTO643 and 12.5 % EC, and 500 pM IS3-ATTO643 and 13.75 % EC for microtubules and vimentin respectively. Scale Bars are 100 µm in (B,E), 20 µm in (C,F), and 5 µm in (D,G).

Chapter III: Developing Analytical Pipelines for quantifying population level molecular details

3.1 Abstract

A growing trend in microscopy is the ability to utilize machine learning to help identify and ultimately quantify observed features of complex biological systems like cancer. A key requirement for expanding the use of these methods lies in encouraging both ease-of-use as well as throughput to more quickly put these tools into the hands of clinical research. This work presents a set of proof of concept image analysis workflows which leverage established open-source methods through a semi-automated process to increase reproducibility from both traditional IF and SRM based applications. Exemplifying the utility for traditional microscopy techniques, we assessed the changes to DNA damage response proteins and their functional foci within a clinical pilot PDAC cohort. Anticipating the large degree of spatial information afforded by SRM methods like LF-PAINT, we codeveloped pipelines to quantify vast numbers of subcellular features to rebuild population analyses under oncogenic stress. Future improvements to multiplexity, paired with analyses demonstrated here, are poised to accelerate mechanistic studies in both clinical biology and mechanistic studies at SRM level details.

3.2 Introduction

A key aspect of microscopy is increasingly how to quantify the complex information and biological significance of observed structures. Methods like machine learning and artificial intelligence are increasingly utilized to help quantify visual structures in complex biological systems [82]. The majority of these methods have been tailored to traditional diffraction limited microscopy, but methods utilizing the unique improvements to resolution from SRM are being developed as SRM throughput and multiplexity have improved in recent years [83].

DNA damage response (DDR) proteins and their role in cancer biology are a growing area of clinically relevant research [84]. DDR proteins have been shown to have observable alterations in expression through trajectories of BRCA mutated PDAC progression [85]. DDR-related proteins like yH2AX, pRPA32, Geminin, and Rad51 collectively reveal stages of unregulated cell-division, DNA-damage, and foci attempting to correct these mistakes in DNA function [86]. For example, in PDAC patient samples Rad51 can form distinct foci visible by immunofluorescence (**Figure 3.1**), which have been implicated in prognostic outcomes for certain types of chemotherapies [86].

While traditionally imaged and judged by cancer specialists to judge patient biopsies [86], markers such as these are prime targets for automated machine-learning facilitated image analysis which can objectively help to stratify patients and assist in determinations for precision therapies in cancer. Leveraging semi-automated proof of concept workflows, we developed a proof of concept image analysis pipeline through integrating flexible open source methods to help quantify changes within individual PDAC nuclei from pilot cohort biopsies (**Figure 3.1**). While methods such as these can demonstrate potentially direct clinical utility, additional development in SRM-based

image analysis using similar pipelines could more directly quantify diffraction limited protein structure differences in cancer.

SRM imaging itself has always necessitated corresponding image analysis, as inherently images are stochastically reconstructed as a central function in PALM [24]. Aside from the ability to resolve structures below the diffraction limit of light [26, 27], ongoing efforts to better quantify observed molecular interactions have followed suit [43]. Efforts to quantify SRM images can broadly fall into 2 categories with distinct tradeoffs, localization-based methods and analysis directly on rendered images.

Localization-based methods have inherently more flexibility to analyze observed interactions between the localizations which comprise the final SRM image, with common examples in molecular cluster analysis from cell-signaling pathways [35, 63]. More recent methods are being developed to facilitate spatial clustering of biological complexes from SRM images, using methods like [45] and tessellation analysis [46]. By leveraging the advantages of the quality and positional attributes of each localization, these methods boast the most promising direction for ongoing SRM image analysis workflows. As an unfortunate side effect of their strengths, localization-based methods: are computationally intensive, require targeted areas for image analysis, and finally still provide a relatively inflexible way to judge complex associations between adjacent protein complexes. Collectively, despite their strengths, localization-based methods remain out of reach for the average microscopist and indeed ease of use in addressing biological questions of interest.

A much more straightforward method for image analysis is to capitalize on the wide-variety of traditional image analysis pipelines developed for diffraction-limited images [82], through utilizing the rendered SRM images as a starting point. Notably this comes at a dramatic tradeoff of losing much of the localization specific details, which become essentially compressed into the rendered image. However, what is initially lost

in highly detailed quality can be compensated by dramatically improved flexibility in image analysis options, associated throughput, and importantly ease of use. The advent of machine-learning based image analysis pipelines puts even more flexibility into understanding the complexities of observed biological structures/complexes, although this has rarely been utilized within the SRM community.

As a proof of principle leveraging open-source image analysis pipelines we demonstrate the utility of semi-automated workflows for either immunofluorescent or SRM based image datasets. To exemplify the ease of these methods toward clinical samples we quantified the expression/Foci levels for DDR proteins across PDAC patient samples. While traditionally judged directly by clinical researchers, this type of analysis opens the possibility into automated and quantifiable patient stratifications from clinical workflows. Utilizing open-source WEKA machine learning classification [49] and custom automated macros written for Fiji [87], we demonstrate the potential for clinical analysis. Additionally, in the context of SRM, we demonstrate how the immense datasets afforded by LF-PAINT can be quantified using similar pipelines through modifications tailored to the advantages in SRM image quality to measure oncogenic effects on cellular caveolae.

3.3 Materials and Methods

For initial proof of concept machine learning applications on clinical FFPE tissue samples, samples, preparations, imaging and analysis (for **Figures 3.1 - 3.3 and Figures A 3.1 & A 3.2**) were performed as follows:

DDR Tissue samples and slide preparations

Formalin-fixed paraffin-embedded (FFPE) pancreatic ductal adenocarcinoma (PDAC) tissues were obtained from the Brandan Colson Center at Oregon Health and

Science University (OHSU) following institutional review board (IRB) approved protocols and including written consent from patients for research applications. Biopsies were collected before and after receiving chemotherapy and/or combined chemotherapy and a PARP inhibitor. FFPE tissue blocks were cooled down by a cold pack, followed by serial section cuts using a microtome (RM2125 RTS, Leica Biosystems, Germany) at 2 µm thickness. Sections were mounted onto 25 mm-diameter round coverslips that were previously coated with polyethylenimine (Sigmaaldrich, 408727).

FFPE sections were baked at 65oC for 1 hr. FFPE sections were then deparaffinized in two washes of xylenes (10 min / each wash), followed by rehydration in a series of graded ethanol to water: from 100% (2 washes, 10 min / each wash), 95% (5 min / wash), 70% (5 min / wash), to 50% (5 min / wash), respectively. After a brief wash in deionized water, tissue sections were immersed in DPBS for 10 min. For heat-induced antigen retrieval, deparaffinized and rehydrated tissues section were placed into pre-heated 1x Target Retrieval Solution (pH9) (Agilent, S236784-2), and incubated at 97oC for 40 min. After heating, the tissue sections in the solution were allowed to cool down to room temperature. Tissue sections were then mounted on Attofluor™ Cell Chamber (ThermoFisher Scientific, A7816). After twice washes with DPBS, tissue sections were permeabilized with 0.4% Triton X-100 in DPBS on a rocker for 45 min. Following three washes with DPBS, tissue sections were blocked with Image-iT® FX signal enhancer at room temperature for 45 min.

After PBS washes, tissues were blocked with 3% BSA and 0.3% saponin in PBS for 1 hour. Next, tissues were incubated with primary antibodies: Rad51, Geminin, yH2AX, and pRPA32 in PBS containing 3% BSA and 5% salmon sperm DNA. The incubation took place on a rocker overnight at 4°C in a humidity chamber. Following three PBS washes (5 min each), tissues were incubated with respective secondary commercial antibodies at a final concentration of ~8 µg mL−1 in PBS buffer containing

1% BSA. The incubation also took place on a rocker at room temperature for 2 hours, followed by three PBS washes (5 min each). After which, all tissue samples were post-fixed by 3.7% PFA and 0.1% GA in 1x PHEM at room temperature for 30 min. Before imaging, samples were cover slipped and sealed with nail-polish.

Fluorescence Microscopy

Wild field fluorescence imaging was performed on a Zeiss Apotome3 system using a 20x Plan-Apochromat objective (NA 0.8, WD=0.55) and a color MRm camera driven by ZEN (Carl Zeiss, Version 3.4). The confocal imaging was performed on a ZEISS LSM 880 system equipped with a 40x Plan-Apochromat objective (water immersion NA 1.2) and a 63x Plan-Apochromat objective (DIC oil immersion, NA 1.4). The acquisition was performed using a 405 nm diode laser for Hoechst 33342, a 561 nm diode laser for Cy3TM, and a 633 nm HeNe laser for AF647. For 2D maximal intensity projection images, slice thickness in the z-axis direction of scanning was optimized at ~0.6 µm with a total thickness ranging from ~4 to 6 µm. For tile scanning, it was performed using the 40x Plan-Apochromat objective (NA 1.2) with the Zeiss tile-scan model combined with the Zeiss in-depth model. The histological imaging was performed on a Zeiss Axioscan Z1 slide scanner (Carl Zeiss) with a Colibri 7 (Carl Zeiss) light source and a HV-F202 bright field camera (Hitachi). A 20x Plan-Apochromat objective (NA 0.8 WD=0.55) was used for imaging. Images were processed using the ZEN2 (Blue edition) program.

Custom Machine-learning integrated Fiji Macro for DDR

Our DNA-damage protein and Foci analysis Macro was built using the Fiji macro language in .ijm format, whose general workflow can be seen in **Figure A 3.1**. Machine learning segmentation/classification was performed using Trainable WEKA Segmentation plugin within Fiji [87]. Two models were trained to identify cell nuclei (through DAPI channel images) and Rad51 foci (through Rad51 immunolabeling).

Training was performed using input images with manually annotated Nuclei and Rad51 foci versus off-target background/no obvious structures.

This pilot macro workflow (visually shown in **Figure A 3.1**) begins by opening 3-color .czi images saved in numbered sub-folders from each patient and converting RGB channels into separate .tif images for segmentation/quantification. First, nuclear classification on Dapi channel images is run to identify, number, and save nuclei positions within each input ROI. Second, these nuclear positions are then used on corresponding Geminin and Rad51 channels at matching ROIs to extract marker-specific intensity values per nuclei. Finally, aggregate nuclear positions and channel specific intensities are measured and saved in into .czi files for each patient, and used for downstream analysis. Identical workflows were used to extract nuclear positions and protein expression levels within RPA32 and gH2AX pilot analysis as well.

Rad51 foci segmentation and quantification was ran after initial nuclei segmentation to define nuclear boundaries this quantification. First, after opening previously trained Rad51 foci classification model into WEKA, classification was performed within each previously identified nuclear .roi from DAPI classification. Identified Rad51 foci positions were saved, masked back onto input images, and image information per foci per nuclei were obtained using Fiji measure function and saved into .csv files per numbered patient FOV and nuclei for downstream analyses using programs such as R.

DNA-damage nuclear analysis and other plots

All plots were generated in R using the ggplot package. Rad51+ foci determination per nuclei was picked in consultation with clinical researchers who provided these patient samples. Rad51+ cell nuclei must have passed the following 3 criteria: 1) foci sizes within each nucleus must be larger than 400 nm, 2) foci intensity was above a minimum average value of 11 (intensity from raw RGB averaged within the

foci area), and 3) three or more total foci within a single nucleus must be present which pass criteria 1 and 2. Statistical significance values shown in **Figure A 3.2** were made using pairwise wilcox text in *stat_compare_means()* function in ggplot across 10 FOVs measured from each patient both before and on treatment.

LF-PAINT sample preparation and imaging

Superresolution microscopy methods for generating DNA-PAINT labeling reagents followed established protocols from DNA-PAINT-ERS [50] and LF-PAINT respectively for microscope design and data processing as outlined in Chapter 2. Additional steps specifically designed for data analysis pipelines and population analyses/visualizations (for **Figures 3.4 - 3.8 and Figure A 3.3**) are outlined below:

Custom Machine-learning integrated Fiji Macro for LF-PAINT

Our analysis Macro was built using the Fiji macro language in .ijm format, and can be found here (data S5). Machine learning segmentation/classification was performed using Trainable WEKA Segmentation [49] plugin within Fiji [87]. Training was performed using input images with manually drawn caveolae particle boundaries trained against background diffuse cytoplasmic caveolin-1. Subsequent testing of trained model performance against manually annotated caveolae on three additional datasets resulted in a DICE coefficient of 84 % ± 8 %.

Macro workflow is visually shown in (**Figure 3.6**). This begins by opening a multi-target LF-PAINT rendered image, typically 29,100 x 29,100 pixels, and using Fiji ROI manager to manually draw boundaries for each cell of interest to quantify. After initiation, the full LF-PAINT image is loaded into the WEKA plugin and the trained .model file for caveolae is loaded, with all subsequent steps happening automatically. For each picked cell ROI, the macro will cut the cell out of the full LF-PAINT image, masking signal outside the ROI, and automatically generate sub-images with an adjustable overlap to tile across each cell ROI analyzed. Each sub-image is temporarily saved, and WEKA

classification is performed on each cell's sub-image. After classifying each sub-image of a particular cell, dynamic offsets initially added during sub-image generation are removed and the full classified cell is combined using original coordinates. Distinct ROI for all detected vesicles are saved and used to measure original cell image attributes at the positions indicated from WEKA classification outputs. In practice, our custom Fiji macro would automatically segment caveolae from input cells at a rate of ~30 minutes per cell, although this performance will vary depending on the computer specifications used. These per-cell caveolae measurements are saved as .csv outputs and can be post-processed using programs such as R.

Population analysis and other plots

Outside of rendered images, all plots were generated in R using the ggplot package. Caveolae particles smaller than 20 nm were excluded from downstream analysis as their border could not be reliably determined and were not considered as a part of initial manual annotation for observed caveolae particles. Population analysis was performed using the nls() function in R, which was used to model a two gaussian population within the total observed populations of caveolae particle sizes according to diameter.

Statistical analysis

Image analysis was performed using custom semi-automated machine learning macro installed in ImageJ (**Figure A 3.6**). DNA-PAINT images with manually annotated cell boundary .roi were input to extract caveolae particle positions as .roi lists. Mapping these per-caveolae particle .roi positions onto the original image, the ImageJ "Measure" function was used to extract and save .csv files per cell, with image attributes including Area, Diameter, Mean intensity, etc. All downstream analysis and visualization was performed in R. P-value calculations in **Figure 3.7B** were performed using the Wilcoxon test in the stat_compare_means() function within the ggplot package in R. For **Figure**

3.7C, the Y axis of size population prevalence calculated using the geom_density function in ggplot from log10-transformed X axis of all caveolae particle diameters.

3.4 Results

Results within this chapter fall within 2 categories, each leveraging proof of principle semi-automated image analysis pipelines integrated with machine learning segmentation and classifications. Within the first half, initial analysis and related findings for centers of DNA-damage response with PDAC patient nuclei infer not only patient prognostics, but can also be related to treatment efficacy while treating for these mechanisms underlying cancer genomic instability. Initial patient analysis presented here will be expanded into later works. In the second half, efforts to quantify immense spatial information now afforded by LF-PAINT developed in chapter 2 will showcase the potential in quantifying nanoscopic features across thousands of cells. LF-PAINT analytical pipelines and representative analysis are included in the LF-PAINT publication.

Understanding DNA damage response in early pancreatic cancer

DNA-damage response proteins typically aggregate into foci, visible by IF, which indicate not only their expression, but sites within the nucleus which are being targeted due to damaged DNA. Clinical significance of these protein expressions in the context and treatment of cancer have spurred substantial interest in developing better imaging and analysis to aid in patient diagnostics/prognostics [86]. We targeted yH2AX/ pRPA32 and Geminin/ Rad51 marker pairs to serve as indicators of both cell-state and mechanisms of DDR which are known to be targeted by PARP treatment (**Figure 3.1**). Through a pilot cohort of 6 PDAC patient samples both before or on PARP inhibitor

treatment we demonstrate proof of principle analysis of DDR protein expression levels and pilot foci analysis.

Machine learning based quantification of DNA-damage response proteins

To help quantify prognostic DDR proteins within the pilot PDAC cohort under PARP treatment we developed an open-source semi-automated machine learning classification pipeline. Leveraging the flexible macro language within Fiji, we used WEKA trainable segmentation to both identify nuclei ROI within patient FFPE tissue samples as well as perform pilot foci analysis on markers such as Rad51 (**Figure A 3.1**). In brief, nuclear ROI were first identified using Dapi-channel staining and associated classification model for finding nuclear positions, followed by extraction of average DDR protein expression levels per each unique nucleus identified as well as pilot Foci analysis on Rad51 (see methods).

Subsequent testing of trained model performance against manually annotated nuclei resulted in a DICE coefficient of >80% for DAPI guided nuclei classification (data not shown). DICE coefficients were calculated by comparing the classified pixel area overlap between model outputs versus 5 separately annotated ground truth images of nuclear positions. Notably a DICE coefficient for Rad51 foci was not performed as a reliable ground truth could not be determined manually. Due to the large inherent variability in Rad51 intensities and apparent aggregations, we instead chose to train a more intentionally vague classification model and perform secondary filtering/cutoffs from known positive/negative clinical sample types. As seen in **Figure A 3.1**, the Rad51 classification identified both bright and dim apparent “Foci” within patient nuclei. Confirmation from common visual clinical expectations helped determine cutoffs used in downstream analysis to determine Rad51+ foci nuclei from these patient biopsies (see methods). Aggregate outputs from this proof of principle segmentation pipeline were saved as .csv files for each patient quantified per nuclei, to aid in downstream analysis.

In comparing DDR from the pilot patient cohort, we assessed the relationship between Geminin/ Rad51 foci+ nuclei and yH2AX and pRPA32. As indicators in changes to DDR, the ratio of Rad51+ foci nuclei which are also geminin positive has been implicated in prognostic studies [86]. Similar to prior studies we identified patients whose levels of Rad51+ foci nuclei were unaffected by PARP treatment, while some patients exhibited a relatively strong response (**Figure 3.2**). Importantly this type of pilot analysis can be used in developing patient specific precision therapy outcomes and identify significance response on a per-patient basis (**Figure A 3.2**). Indicative of the role of a wider group of DDR proteins we also analyzed the expression levels of yH2AX and pRPA32 within a subset of these patients. We found a consistent reduction in the expression of both markers as well as the ratio of pRPA32+ / yH2AX+ nuclei after PARP treatment (**Figure 3.3**). Analyses such as these are being expanded into ongoing clinical studies.

Machine learning based quantification from LF-PAINT images

Developed leveraging similar open-source image analysis pipelines, we also assessed the potential for open-source SRM image analysis from LF-PAINT images. The substantial increase in imaging area coupled with the speed and resolution afforded by LF-PAINT results in immense image datasets, offering a unique opportunity to link biological alterations at the nanoscale to phenotypic changes at the cell population scale. Among the challenges is the need to quantitate nanoscopic structures and molecular interactions across such large areas. The growing implementation of machine-learning based image analysis is a promising strategy for addressing this challenge. In this work, we took advantage of WEKA [49], an open-source platform for machine-learning with a built-in plugin for Fiji [87], for automated segmentation of LF-PAINT images. To this end, user defined regions of interest (ROIs) in training images are first manually assigned to different feature classes, with which WEKA trains a model for

identifying features that best match the user-defined ROIs. The model is then applied to new LF-PAINT images to identify the nanostructures. For the LF-PAINT images, we needed to develop a Fiji macro for dividing the full image into smaller subregions for analysis and combining the segmentation results after each subregion has been analyzed (see Methods).

In developing this custom machine learning classification pipeline for SRM images, especially across larger FOVs like LF-PAINT, we encountered some notable considerations when using machine learning from SRM images. A first practical limitation came in the form of the image sizes themselves, wherein the 10 nm rendered pixel size in input images would severely limit both training and classification computational performance. This necessitated sub-dividing input images for both training and classification into substantially smaller ROI, a feature which is also commonly used in analyzing large image datasets such as from cyclic IF of patient tissues [19, 88]. Second, recombining smaller segmented ROI after classification proved initially challenging using traditional stitching plugins within Fiji. Unlike images from traditional microscopy methods which have a variety of intensities to aid in commonly used stitching plugins [87], SRM images often have relatively large regions of zero intensity where no structures/proteins of interest were present. Critically, when using traditional plugins like Grid-collection Stitching [87] on LF-PAINT images regions with minimal structures present were unable to correctly recombine (**Figure A 3.3**), despite giving the image order and exact overlap distances from each sub-image. We developed a simple workaround, leveraging the known initial sub-image coordinates and overlap distances to crop overlap boundaries and re-insert classified sub-images back to their exact initial coordinates (**Figure A 3.3**). Third, multiple rounds of model training were required to ensure features from complex structures in cells were correctly identified, such as the relatively dim interior structure of mitochondria. In practice, the higher degree of detail in

SRM images necessitated more careful training annotations versus relatively lower resolution images, such as nuclear positions identified using Dapi earlier in this chapter. Finally, to facilitate quantification of classified structure, running the Fiji function *analyze particles* on binarized classification outputs enabled the saving of each structure positions as well as masking for secondary analysis per structure using the *measure* function. A snapshot of these 4 considerations in practice can be seen in **Figure 3.4**, highlighting the utility to extract image information from complex images such as OMM Tom20 from U2OS cells imaged using LF-PAINT.

As further proof of principle, and to aim toward a later biological questions, we tested WEKA segmentation on LF-PAINT images of Caveolin-1. In this case, the small size of caveolae necessitates imaging with SRM (**Figure 3.5A**). Using WEKA, we trained our model using ~100 manually segmented structures and obtained a model with a DICE coefficient (% overlap between ground truth and model outputs from a separate test sample set of 3 groups of 100 particles each) of 84 % ± 8 %. Applying this model to the full LF-PAINT dataset revealed two populations of caveolae with average diameters ~50 nm and ~150 nm (**Figure 3.5B**). A small, additional population of caveolae at ~20 nm diameter was observed but was not annotated as this size was below our resolution limit. These classified image outputs were then traced back onto the original image to confirm the segmentation and extract details of each caveolae structure for subsequent analysis (**Figure 3.5C**). Analysis of other cellular nanostructures can be carried out similarly using this semi-automated pipeline.

Imaging population level molecular detail with LF-PAINT

With the image segmentation pipeline established, we next sought to demonstrate the utility of LF-PAINT toward observing cell-specific molecular interactions across cell populations. In studying how the small GTPase KRas functions on the cell membrane, we initially observed that U2OS cells that express higher levels of mutant

KRas (KRasG12D) apparently showed a lower abundance of caveolae (**Figure 3.7A**). These cells were engineered to express SNAP-KRasG12D upon doxycycline (dox)-induction (see methods), allowing us to switch KRas expression on or off [89]. Of note, as is common from lentiviral infection, heterogeneity in KRas expression after dox-induction could be used to assess relative effects in KRasG12D expression. The SNAP tag was used to label KRasG12D using DNA oligo-conjugated SNAP substrate (see Methods). We then imaged dox-induced mutant KRas (SNAP-DS1) and endogenous caveolae (Caveolin-1, anti-rabbit-DS2) with LF-PAINT. To systematically investigate the relationship between KRasG12D expression and caveolae assembly, we obtained dual-color LF-PAINT images of both targets across 12 FOVs (291 μm x 291 μm), of which 10 were from cells induced with Dox (KRasG12D positive) and 2 uninduced (KRasG12D negative). Each FOV contained ~50-100 cells. We manually annotated 925 cell boundaries and analyzed caveolae in each with WEKA using our custom Fiji macro. Each cell was also analyzed for KRas expression (in terms of DNA-PAINT localizations in the KRas channel).

In total over 630,000 individual caveolae were extracted for downstream analysis. Individual caveolae image attributes (area, intensity, diameter) were further analyzed using custom R scripts (see methods). Notably, the total number of caveolae per cell was significantly lower in cells with induced KRasG12D expression, while the average expression level of Caveolin-1 per cell (as measured by the number of DNA-PAINT localizations in the Caveolin-1 channel) only decreased minimally over the same ranges of KRasG12D expression levels (**Figure 3.7B**). This indicated an overall perturbation in the caveolae assembly as a result of KRasG12D overexpression.

To further explore the structural changes in caveolae-assembly upon increased KRasG12D expression, we plotted caveolae diameter versus KRasG12D level. The plot revealed that the percentage (prevalence) of larger caveolae decreased as KRasG12D

expression level increased (**Figure 3.7C**). In uninduced cells, caveolae exhibited two clearly separated populations with peak diameters at ~54 nm and ~154 nm. The two populations may be attributed to fully formed caveolae (~60 nm) and larger precursor caveolae plaques (~150 nm) [90]. Caveolae size distributions in KRasG12D positive cells could be similarly modeled as a mixture of two populations (**Figure 3.8**). The peak positions for each population remained highly similar across all KRasG12D expression levels, suggesting that these indeed represent distinct structures made with caveolin-1. We found that the ratio of large to small caveolae structures is the largest at 0.44 in KRasG12D negative cells and shifted to 0.42, 0.20, and 0.22 when the KRasG12D expression increased gradually from 1-15, 15-60, and >60 (measured as DNA-PAINT localization densities in the KRasG12D channel). Together, these analyses indicate that increased mutant KRasG12D expression may promote the maturation of caveolae (thus higher fractions of caveolae structures with ~60 nm diameter). Indeed, ongoing research has found interplay between caveolae function with mutant KRas [5, 91], which may be cell-line specific.

3.5 Discussion

In summary, we have shown how utilizing open-source semi-automated image analysis pipelines can reveal trends in both clinical patient samples as well as models assessing oncogenic effects in cancer. In the context of PDAC and DDR proteins, the pilot phase of this project could soon be adopted into clinically guided studies to expand the patient cohorts for this type of analysis. Compared with similar findings, these preliminary workflows have reliably resolved Rad51+ foci within a PDAC samples reflecting the prognostic value in the ratio of Rad51+ foci nuclei out of Geminin positive cells [85, 86]. Notably with advancements in multiplexity on patient tissues for traditional

IF, a wider panel of DDR proteins can be analyzed in tandem. Finally, since many of these DDR proteins are known to function in diffraction limited foci complexes [86], methods like LF-PAINT are poised to better resolve differences in diffuse structures vs active centers of DDR. Not only can this then provide even more detail in understanding the basic biology of DDR dysregulations in the context of earlier cancers, but tied to targeted therapeutics opens a key method to study early PDAC therapies we well.

Imaging at the throughput afforded by the LF-PAINT system raises new challenges in data storage and processing. Raw LF-PAINT datasets are commonly >1 terabytes (TB) per target, and there is an urgent need for more efficient data storage and organization solutions to handle the massive amounts of data to come. Processing these images also is nontrivial, although recent efforts on developing GPU-enabled single-molecule localizations will likely ease the pressure on this front [29, 92-94]. Lastly, building from works inferring dynamic superresolution complexes [48], interpretation of the superresolution images (i.e., images into knowledge) increasingly requires new tools such as those based on artificial intelligence. In this work, we utilized the open-source WEKA platform [49] to extract nanostructures in the LF-PAINT images followed with statistical analysis to infer changes in these structures across cell populations. Leveraging this analytical workflow, we were able to analyze over 630,000 caveolae from ~1000 cells.

3.6 Conclusions

The ease of use of leveraging emerging and flexible image classification software are poised to accelerate meaningful quantification of complex biology in cancer from both traditional IF microscopy as well as SRM data such as LF-PAINT. Our pilot PDAC patient cohort and associated changes to DDR proteins after PARP treatment is a

foundation of ongoing clinical interest from the OHSU Knight Cancer, as an avenue for assessing precision therapy in chemotherapies to aid in PDAC clinical outcomes. Expanding this type of analysis to known model systems, clinical baselines and importantly expanded patient cohorts have the potential to be adopted into clinical sample workflows.

Importantly in the context of SRM, our pilot analysis demonstrates the flexibility of higher-throughput analysis directly on rendered SRM images such as the relationship between caveolae and $KRAS^{G12D}$. While a full validation of this result and its mechanistic interpretation warrant a more extended study, this example further demonstrates the feasibility in utilizing LF-PAINT in combination with machine-learning based image segmentation in probing alterations in nanoscopic structures across large cell populations, which would have been difficult if not for both the SRM resolution and the large FOVs. Needless to say, what we demonstrated is only a primitive version of what is possible with the large image datasets. We anticipate more sophisticated analytic tools to become available to tackle this exciting challenge.

Acknowledgements

The authors thank Drs. Joe W Gray, Gordon Mills, Terry K Morgan, Young Hwan Chang, Jason Link, Sean Speese, Yu-Jui (Roger) Chiu, David Qian, and many other colleagues at OHSU for their helpful discussions. M.J.R, F.C., J.K., D.H., T.Z., S.E., and X.N. are members of and supported by the Cancer Early Detection Advanced Research (CEDAR) Center of the OHSU Knight Cancer Institute.

Funding:

Research in the Nan lab was supported by the OHSU Knight Cancer Institute, the Damon Runyon Cancer Research Foundation, the M. J. Murdock Charitable Trust, the Prospect Creek Foundation, the Cancer Systems Biology Consortium from the

National Cancer Institute (CSBC, grant number U54 CA209988, PI: Joe W. Gray), and the National Institute of General Medical Sciences (grant number R01 GM132322, PI: X.N.).

Author Contributions

XN and FC conceived the project and SE helped supervise. MR, FC, JK, DH and XN developed the initial workflows and established the microscope design and fluidic design. KT and JS performed all reagent synthesis and purifications for DNA-conjugates. MR and XN developed the image processing pipelines used. MR developed the segmentation and population analysis strategy. MR, and JK acquired and performed data analysis. MR and XN wrote the manuscript. XM, MR, KT, MS, TZ and SE reviewed and edited the manuscript. All authors have reviewed and approved related analysis for the LF-PAINT manuscript.

Declaration of Interest

The authors report no conflicts of interest.

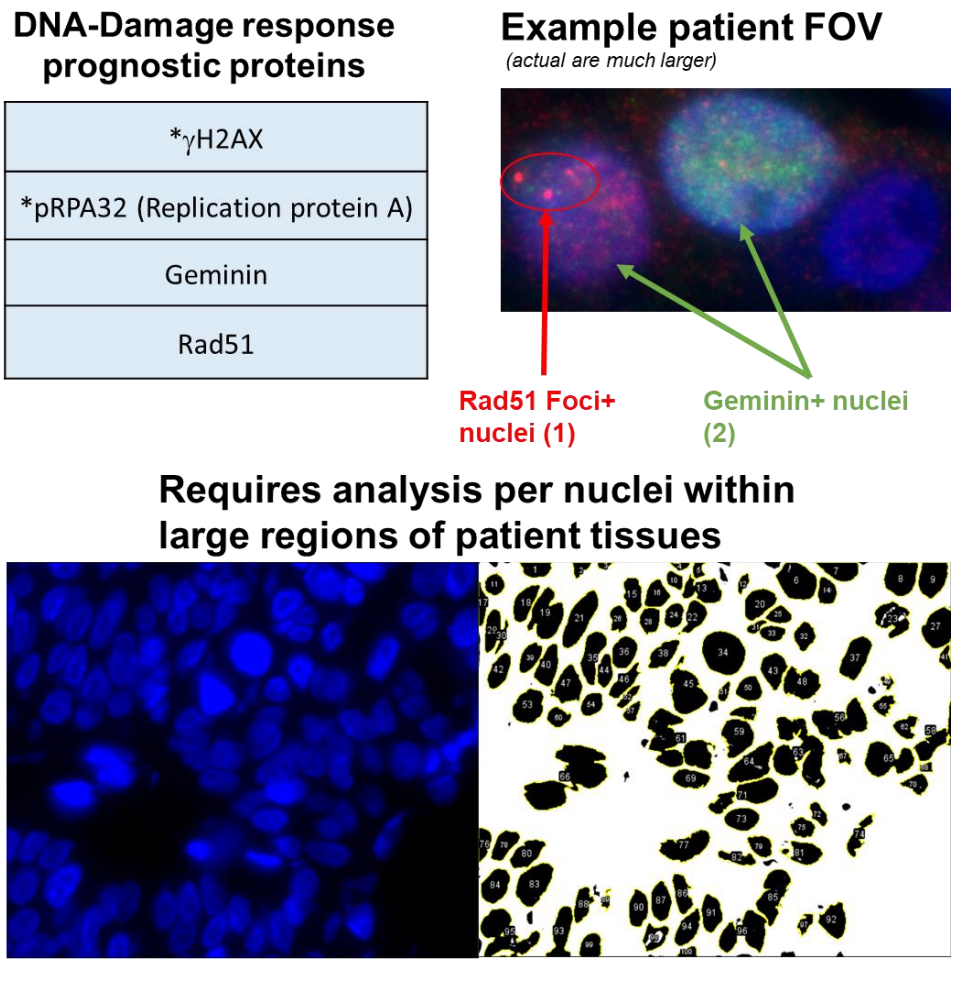

Figure 3.1 | Example mechanism necessitating expanded image analysis
DNA-damage response proteins in cancer can form distinct Foci within affected nuclei, measuring these can assist in prognostics. Automated analysis over hundreds of nuclei could help stratify patient, needs a pipeline to accomplish this.

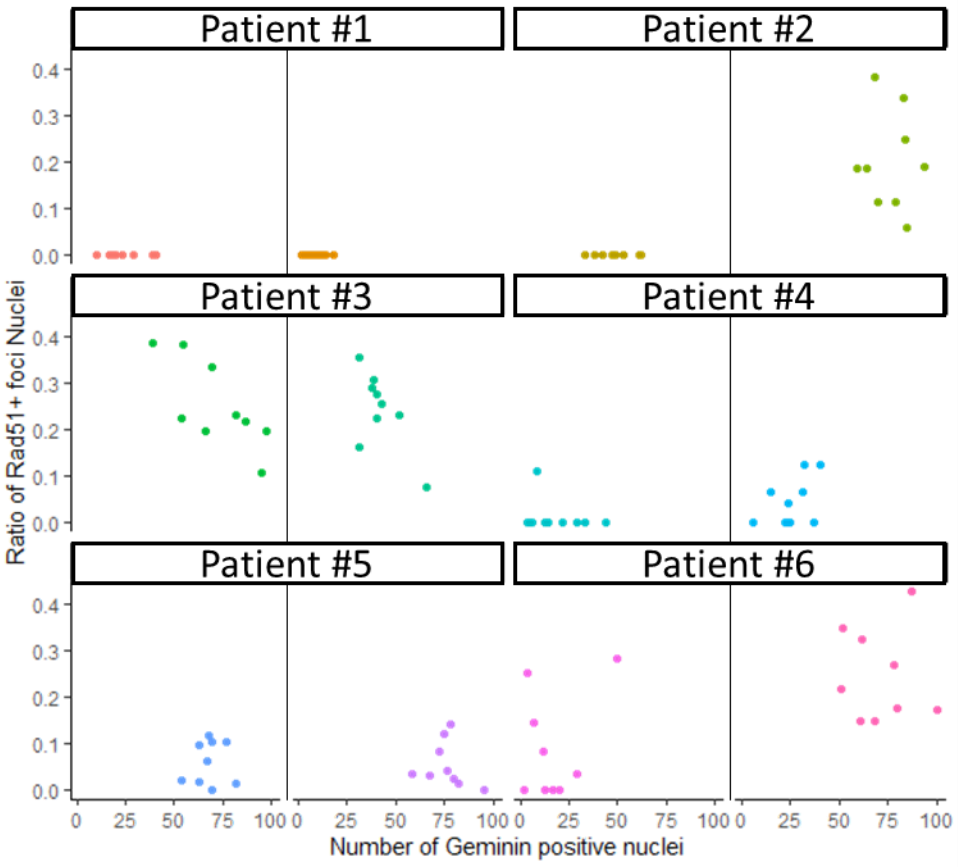

Figure 3.2 | Per-patient analysis assessing DNA-damage response via Rad51+ foci nuclei from automated analysis.

Proof of concept nuclear classification and Rad51+ foci extraction from 6 PDAC patients before and after PARPi treatment (left and right plots respectively). Geminin positive nuclei cells (x axis) indicates G1-S transition cell cycle. Rad51+ cells identified with classified foci which are: sufficiently bright above background (average pixel intensity > 8), >400nm in size, and sufficiently abundant within individual nuclei (≥ 3 foci).

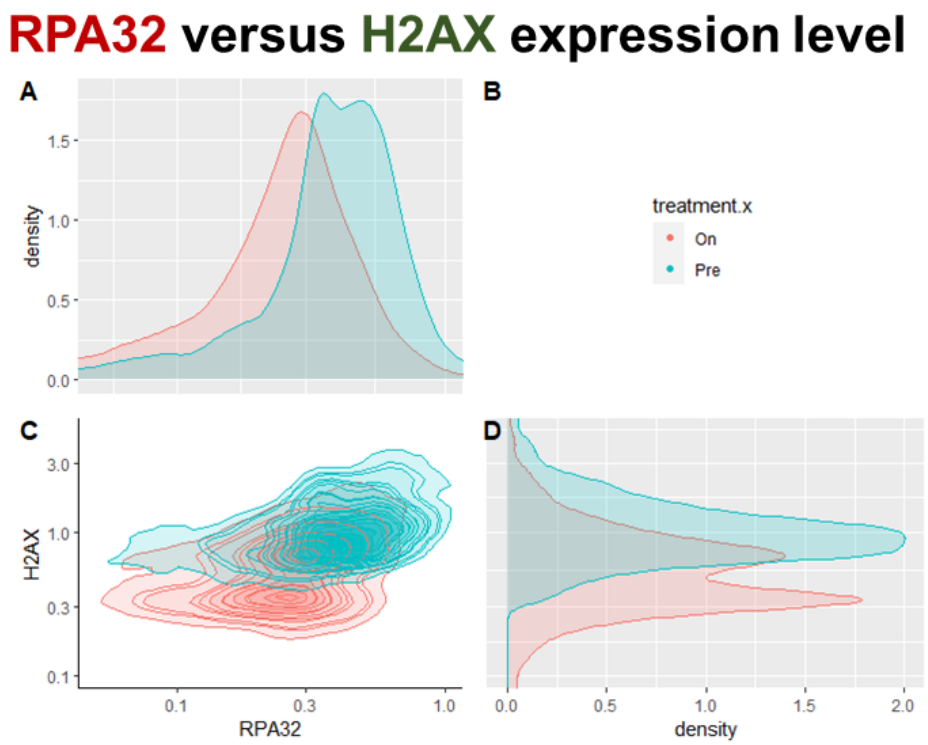
RPA32 versus H2AX expression level
A
B
C
D
density
treatment.x
On
Pre
H2AX
RPA32
density

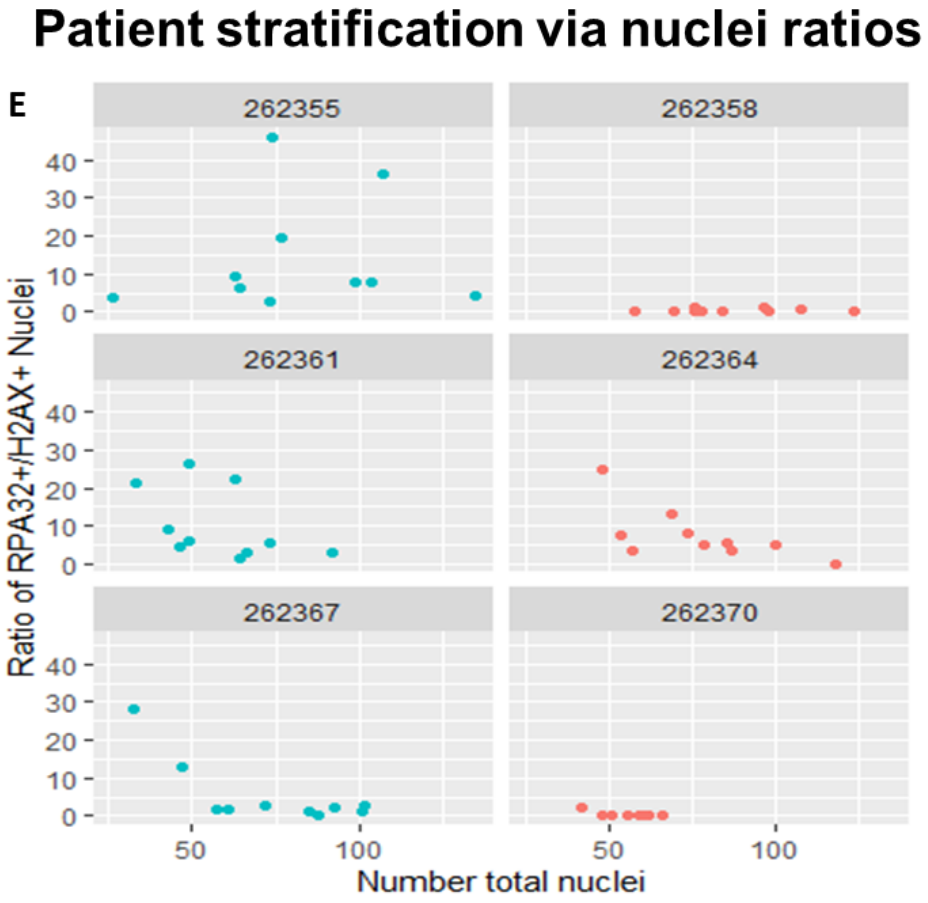
Patient stratification via nuclei ratios
E
262355
262358
262361
262364
262367
262370
Ratio of RPA32+/H2AX+ Nuclei
Number total nuclei

Figure 3.3 | Pilot Expression level analysis of DNA-damage response by semi-automated ML classification per nuclei.

Proof-of-concept characterization of patient treatment effects on RPA32 & gH2AX expression in PDAC cell nuclei. (A) Relative expression level abundancies for RPA32 expression. (B) Key for pre-treatment (blue) and on-treatment (red). (C) Population contours of both RPA32 and gH2AX expression levels. (D) Relative expression level abundancies for gH2AX expression. (E) per patient ratio of RPA32 positive nuclei divided by gH2AX positive nuclei.

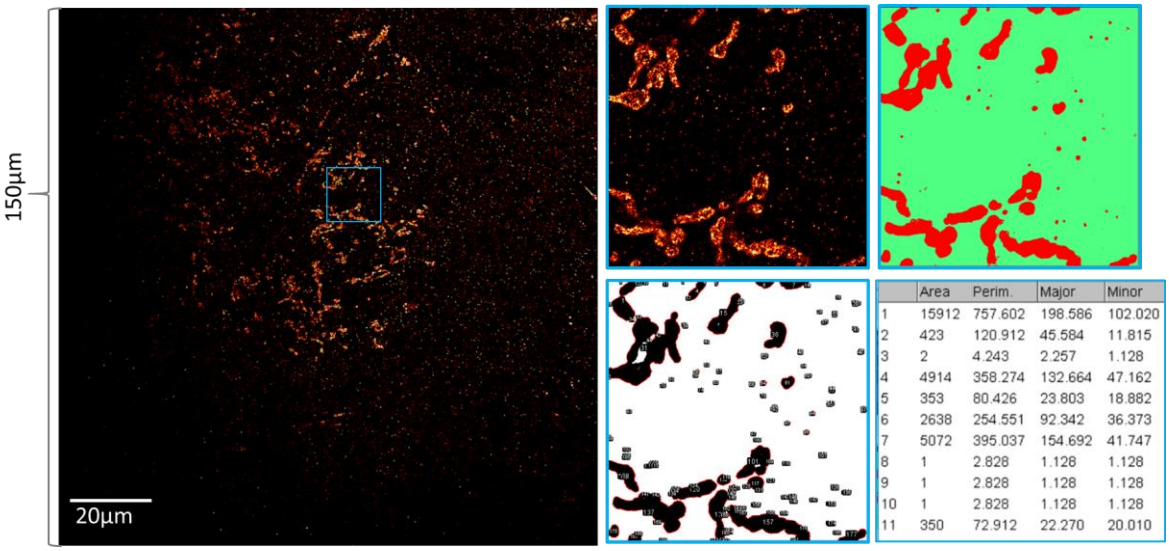

Figure 3.4 | Example WEKA segmentation from LF-PAINT ROIs.
Proof-of-concept WEKA classification of mitochondria from an LF-PAINT image. A grouping of 2 classes can be trained to distinguish mitochondria (in red) from cytoplasmic and extracellular background (in green). Classified regions can be mapped back onto the original image, allowing for downstream image measurements using ‘measure’ function per mitochondrial ROI.

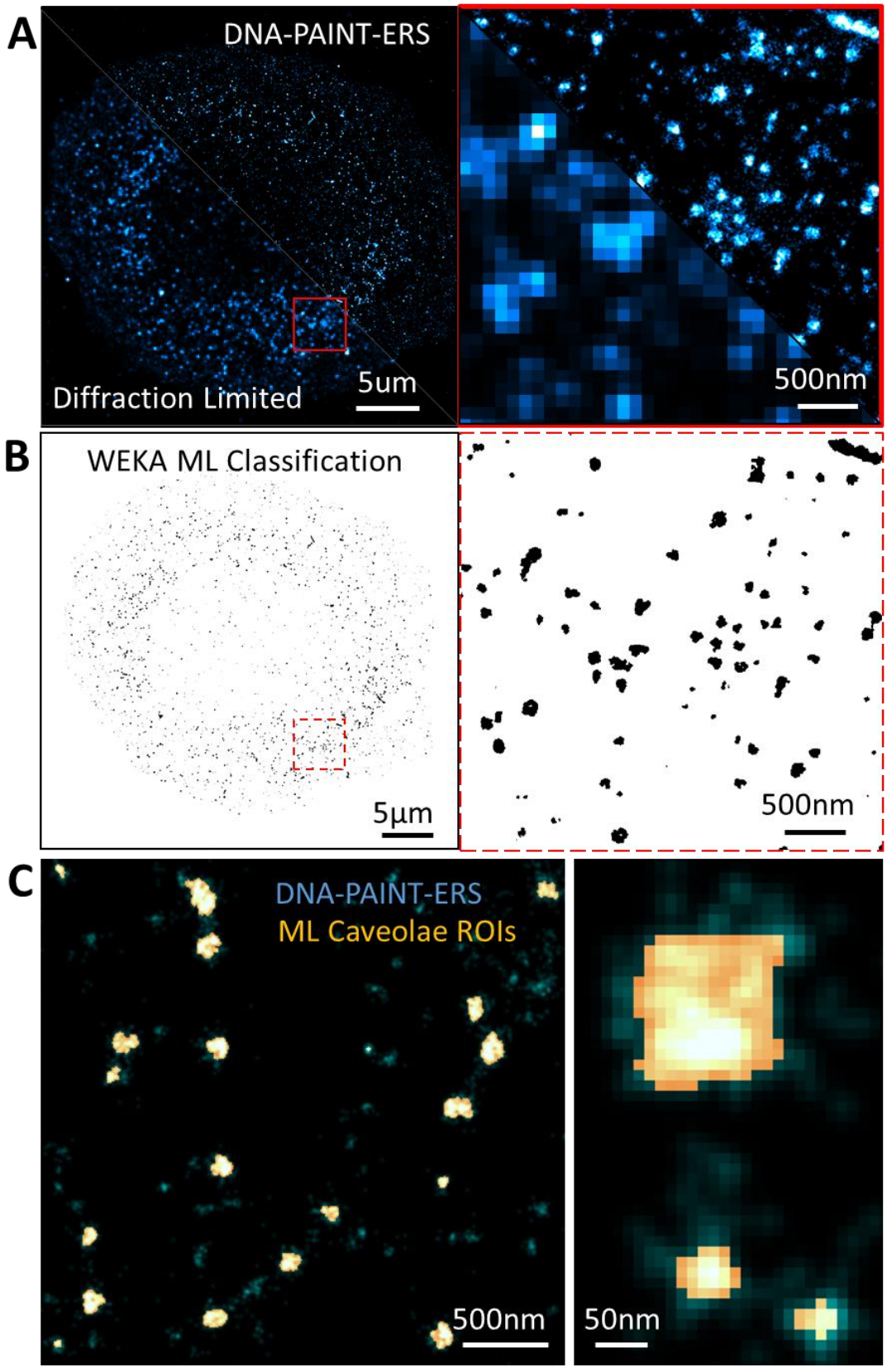
A
DNA-PAINT-ERS
Diffraction Limited
5um
500nm
B
WEKA ML Classification
5µm
500nm
C
DNA-PAINT-ERS
ML Caveolae ROIs
500nm
50nm

Figure 3.5 | Machine Learning Segmentation from DNA-PAINT images
(A) Representative DNA-PAINT image of Caveolin-1 within a single U2OS cell from an LF-PAINT image, diffraction limited view shown via diagonal split (left). Magnified region from solid red square where notably a diffraction limited resolution (200 nm resolution and 100 nm pixel size) is insufficient to see distinct caveolae vesicles (right). (B) Machine learning based image segmentation for caveolae vesicles using the input cell from (A), as analyzed by custom Fiji-macro utilizing open-source WEKA classification (left). Magnified region from dotted red square showing caveolae outlines identified in (A) (right). (C) Representative overlays showing both caveolae vesicles as imaged via LF-PAINT in blue with corresponding caveolae outlines identified via machine learning segmentation in yellow (top). Inset showing both larger caveolae plaques and punctate caveolae vesicles, at ~150 nm and ~60 nm wide, respectively (bottom).

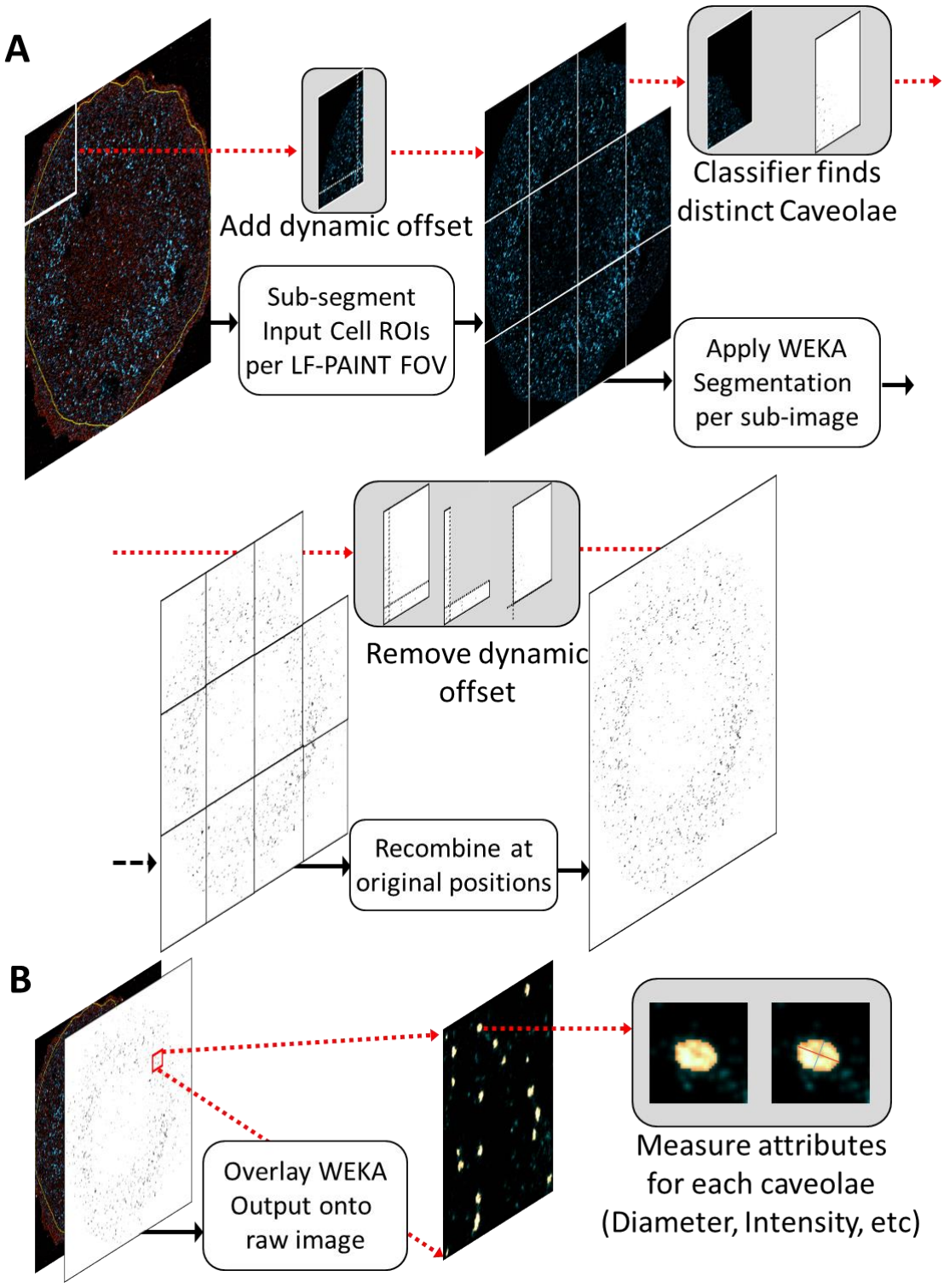
A
Add dynamic offset
Classifier finds distinct Caveolae
Sub-segment Input Cell ROIs per LF-PAINT FOV
Apply WEKA Segmentation per sub-image
Remove dynamic offset
Recombine at original positions
B
Overlay WEKA Output onto raw image
Measure attributes for each caveolae (Diameter, Intensity, etc)

Figure 3.6 | Schematic workflow of custom Fiji macro integrating WEKA segmentation:

(A) Representative steps for a single input cell ROI. 1) sub-divide total input cell ROI into smaller squares dynamically and add an offset (dynamic means: this will auto-adjust the number of squares and corresponding offsets within predefined upper bounds for square sizes in order to fill different size cell ROIs) , 2) WEKA segmentation is applied serially to each sub-image using optimized classifier .model file for caveolae classification, 3) dynamic offsets are removed (to avoid edge effects) and full cell input with classified caveolae is recombined at original sub-image positions. (B) Caveolae feature extraction workflow. 1) recombined WEKA output per cell (from A) is overlaid back onto input cell LF-PAINT reconstructions, 2) using this mask, individual caveolae ROI are saved and used to measure image attributes such as diameter, mean intensity, etc., using Fiji measure function, 3) aggregate measurements per cell and per LF-PAINT FOV are saved into .csv files for downstream processing and visualization using R. Representative input cell shown was from the dox-induced KRASG12D datasets as quantified in **Figure 3.7**.

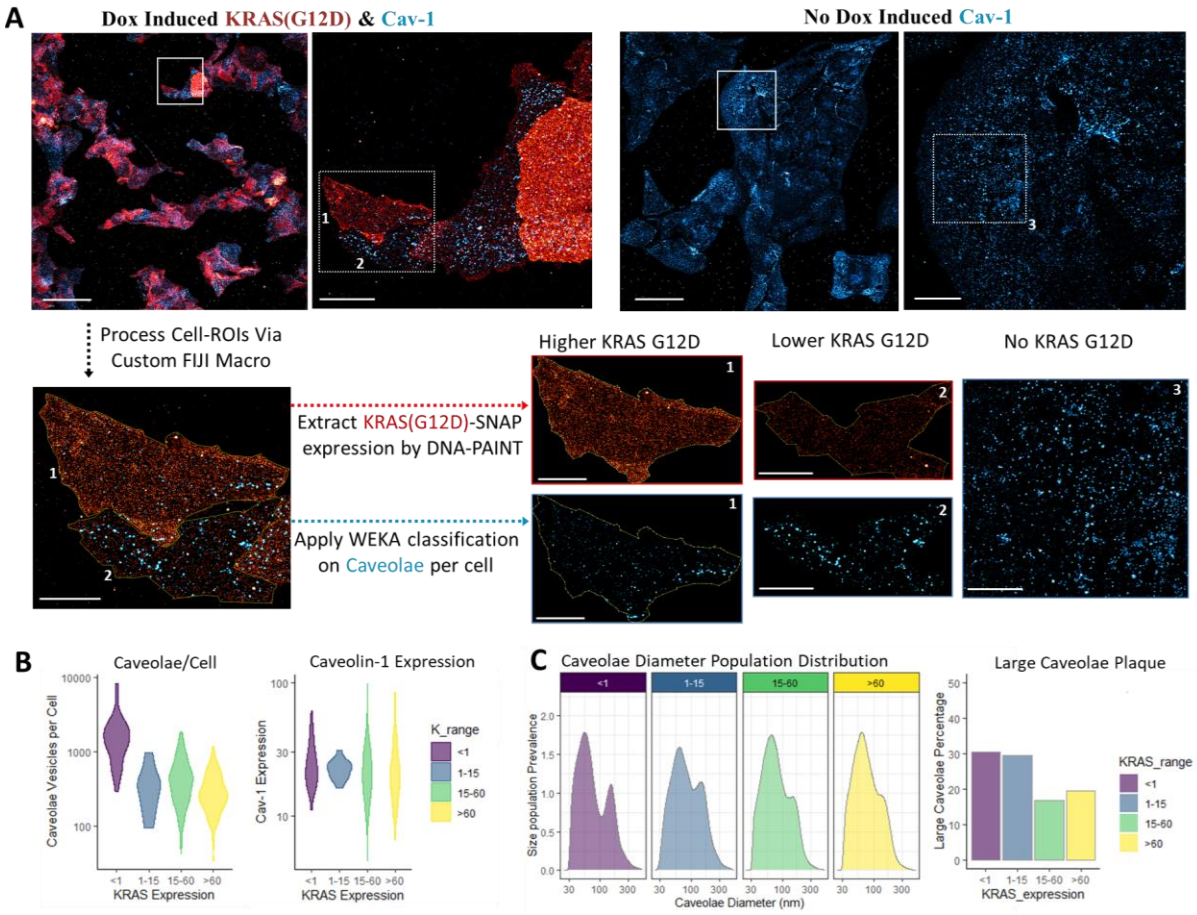

Figure 3.7 | LF-PAINT image analysis of the effect of KRASG12D overexpression on caveolae formation:

(A) Representative LF-PAINT images of both dox-induced and non-dox induced KRASG12D and Caveolin-1. KRASG12D labeled via SNAP-tag DS-1 conjugate shown in red, with Caveolin-1 DS2 shown in blue. Magnified regions show representative cells numbered 1,2, and 3 with higher, lower, and no KRASG12D expressions respectively. Manually annotated cell boundaries were subsequently input into custom Fiji macro for both KRASG12D expression and WEKA classification of caveolae vesicles per cell. (B) Violin plot of the abundance of quantified caveolae vesicles versus ranges of KRAS expression for non-dox (<1), 1-15, 15-60, and >60 KRAS/um2. Violin plot of total Caveolin-1 expression per cell versus ranges of KRAS expression, with both expression values shown in protein / µm2. (C) Population analysis of caveolae diameters for indicated KRAS expression ranges, notably showing two main peaks at ~60 nm and ~150 nm from non-dox induction. Higher KRASG12D expression anti-correlates with the larger caveolae size population. Plots in (B,C) were generated using ggplot package in R. Analysis was performed on 10 images of dox-induced and two images of non-dox induced cells acquired with 30,000 frames at 30 ms exposure for each target, using 1 nM IS1-ATTO643 and 12.5 % EC, and 500 pM IS2-ATTO643 and 13.75 % EC for KRASG12D-SNAP-DS1 and Caveolin-1-DS2 respectively. Scale bars in (A) are 50 µm for full FOV images (left for each cell condition), 10 µm for matching magnified views (right), and 5 µm for all example cells (bottom panels).

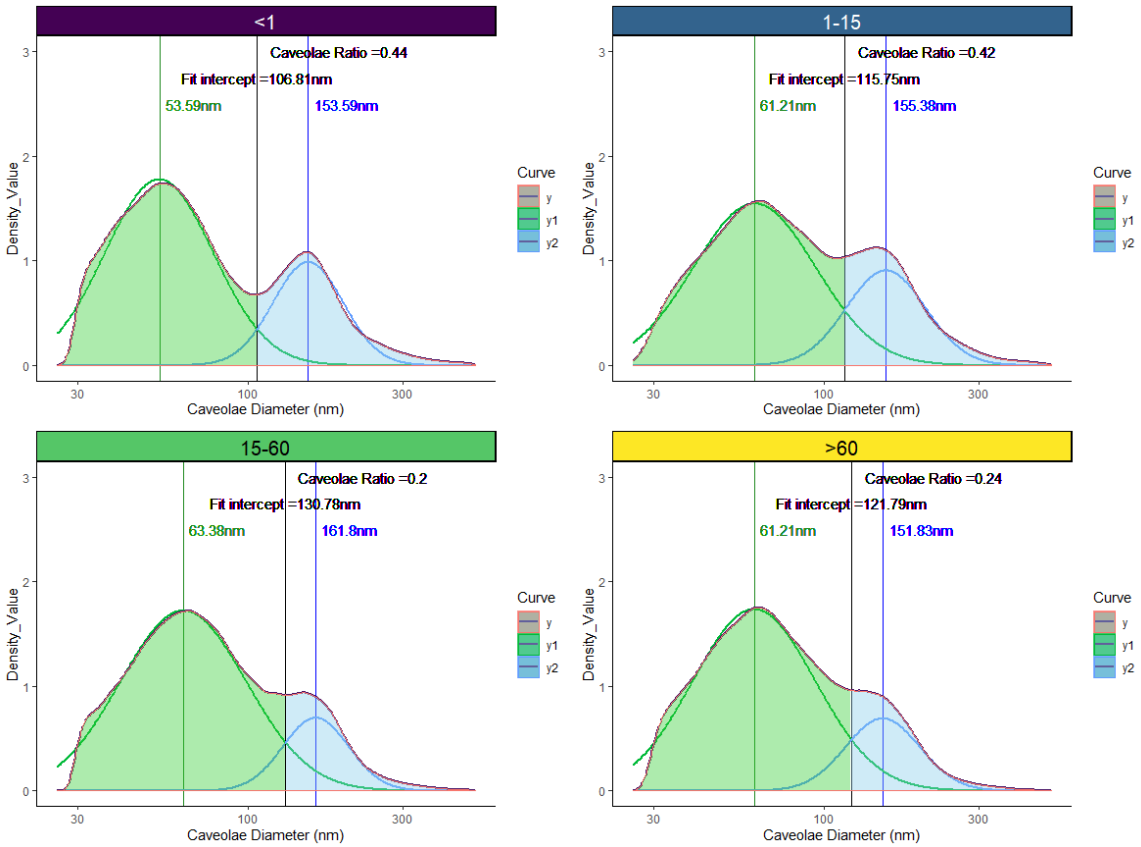

Figure 3.8 | Population analysis for the effect of KRASG12D on Caveolae diameter distributions:

Proof-of-concept population analysis of caveolae vesicles from dox-induced KRASG12D experiment (**Figure 3.7**). Density plot of caveolae diameter (in nm) shown per indicated KRAS expression ranges: (<1, i.e. non-dox induction), (1-15), (15-60), and (>60) KRAS / µm2. The R function nls() was used to fit two gaussian curves within the larger total population distribution resulting in a prominent smaller population size with peak ~60 nm (green), and larger population peak at ~155 nm (blue). The intercept of these two population curves was used to approximate the relative contribution of both size ranges within the total caveolae population observed for each expression range of KRASG12D. The indicated caveolae ratio shows the relative abundance of the larger caveolae population area (blue) divided by the smaller population area (green).

Chapter IV: Enabling Clinical FFPE Tissue SRM through Flow Assisted DNA-PAINT

4.1 Abstract

A key next step in the development in DNA-PAINT would be its implementation on tissue samples. Unfortunately, current literature has been unable to address this, likely due in part to poor imaging quality when directly incorporating FFPE workflows previously optimized for tissue STORM. This work presents dramatic improvements in tissue DNA-PAINT which enables clinical samples to be imaged with the full benefits of multiplexity and throughput afforded by DNA-PAINT. In combination with LF-PAINT, we developed flow-assisted DNA-PAINT, which was critical in improving binding on-rates for tissue DNA-PAINT. Additional improvements in sample blocking/labeling enabled proof of concept imaging across nearly a millimeter of clinical PDAC FFPE tissue samples.

4.2 Introduction

Most SRM studies are performed on cultured cells for their amenability to high-resolution imaging, but clinical tissue sections are also of immense value in medical research and should be similarly addressed with higher-resolution methods than traditional microscopy. Indeed, the desire to image patient tissues at high resolution has been most notably pioneered through electron microscopy [95]. Studies capitalizing on the resolution afforded by electron microscopy have analyzed structures including: mitochondrial abnormalities [96], cell morphology changes during cancer treatment [97]

and even correlating specific cellular detail within larger tumor imaging strategies [98]. While studies like these demonstrate the advantages to visualizing tissue samples with very high resolutions, they have a variety of aspects which limit their broader utility to study and assess patient samples.

Clinical implementation of EM to image patient tissues is limited by four major aspects. First, typical workflows for tissue electron microscopy are limited to freshly prepared tissue samples [99], as freezing/ paraffin fixation is incompatible with the high degree of charging caused during electron microscopy imaging [37]. This means that the large degree of archived and more commonly utilized FFPE sample preservation from the majority of clinical settings limits available sample pools. This requirement for fresh samples also restricts usage to institutions equipped with both medical services to get fresh samples and advanced microscopy services to perform EM preparation/ imaging either on-site or nearby. Notably, there is the practical limitation inherent to all EM studies, and that is the common lack of specificity outside of immunogold labeling [100]. Finally, this lack of specificity means that often intense data processing and annotation must occur in order to correctly qualify what EM images are portraying. Collectively, these factors make the broader implementation of these methods outside research highly impractical.

Through the development of SRM like STORM [25], work quickly followed that was able to perform similar immunolabeling and imaging by tissue STORM [37]. Studies utilizing tissue STORM, even with smaller (50-100 μm) FOVs, have already shown promise in revealing structural and molecular details in FFPE sections [37] such as chromatin organization [38], and mitochondria organization [37]. As evidenced by Creech et al. and Xu et al., SRM imaging of FFPE sections could provide insight into the biology of disease progression and therapeutic responses [37, 38]. For these applications, extending the FOV in SRM imaging of FFPE samples to a millimeter scale

is necessary for covering important tissue structures and cell populations. To date, none of the existing strategies for large FOV SRM have been demonstrated on FFPE tissue sections.

In this work, through capitalizing on inherent flexibility from the LF-PAINT system, and developing improved DNA-conjugated immunolabeling conditions, we performed proof of concept imaging from clinical FFPE tissue samples of PDAC. We found that treatment with RNase and Image-iT® FX signal enhancer improved both labeling density and quality. Critically, through incorporating fluid flow during image acquisition, a novel method coined flow-assisted DNA-PAINT, imaging of FFPE tissue samples was dramatically improved. Proof of concept tissue DNA-PAINT imaging strategies demonstrated here are poised to accelerate targeted imaging of clinical patient samples to better understand diseases like cancer.

4.3 Materials and Methods

Methods for generating DNA-PAINT labeling reagents followed established protocols from DNA-PAINT-ERS [50, 64] and LF-PAINT respectively for microscope design and data processing as outlined in Chapter 2. Additional steps specifically optimized for tissue DNA-PAINT are outlined below:

Tissue samples and slide preparations

All patient FFPE tissue samples (including HER2+ breast cancer and PDAC samples) were collected through either the OHSU Biorepository or the Brenden Colson Center following IRB approved protocols including patient consent for research applications. Standard human pancreas samples obtained by BCC were FFPE sections from otherwise healthy cadavers and were used for most tissue imaging optimizations.

FFPE tissue samples were cut using a ultramicrotome in 2 µm thick sections (RM2125 RTS, Leica Biosystems, Germany).

Pre-drilled and cleaned fire-polished coverslides were prepared for tissue mounting using Poly-Ethylene-Imine (PEI) (Sigma--Aldrich, 904759-100G) coating. In brief, cleaned coverslides were treated for 20 minutes with 0.1% PEI solution in ultrapure H2O. After coating, excess PEI was rinsed 3x with ultrapure H2O for 5 minutes each. After aspirating excess H2O, coated slides were left to dry flat at 42°C for 2+ hours, or until completely dried. Fluidic chamber profile outlines were drawn onto the non-PEI-coated backside using an ultrafine sharpie to assist in tissue mounting positioning. All tissue samples were sectioned at 2um ±0.5um thickness, floated on a 42°C waterbath immediately prior to mounting onto PEI-coated coverslides. Mounted tissues sections were dried vertically for 1 hour at 60°C before storage. Mounted tissue sections were stored vertically in this manner for up to 1 month prior to antigen-retrieval, labeling and imaging.

FFPE tissue sample preparation

For immunostaining of FFPE tissue samples, FFPE sections were first deparaffinized using xylene (2x, 10 min), 100% EtOH (2x, 10 min) 95% EtOH in DI water (5 min), 70% EtOH in DI water (5 min), 50% EtOH in DI water (5 min) and left in PBS. Tissues underwent antigen retrieval in a decloaking chamber (Bio SB, BSB-7087) first in Tris buffer (300mM Tris, 0.05% Tween 20, PH 8). Tissues were transferred into a pre-heated citrate buffer (300mM NaCitrate Monohydrate, 0.05% Tween 20, PH 6), also heated during decloaking, and allowed to cool to room temperature. After two PBS washes, tissues were further permeabilized with 0.4% Triton X-100 in PBS for 45 minutes. After removing excess permeabilization solution and three PBS washes, a hydrophobic barrier (company product) was applied around the mounted tissue following the fluidic outline of the chamber design. Tissues were either further treated with RNAse

A/ Image-iT® FX signal enhancer (ThermoFisher Scientific, I36933) or directly blocked prior to antibody labelling. In brief, RNAse A and signal enhancer treatment both occurred prior to antibody labeling as optional optimizations. After permeabilization, tissue samples could be treated with RNAse A (ThermoFisher Scientific, EN0531) at 50x dilution in PBS on a rocker for overnight at room temperature. After a rinse with PBS, sections were quenched with fresh 0.1% sodium borohydride in PBS for 7 min, and followed by three washes with PBS (5min / each). Tissue was further incubated with signal enhancer at room temperature for 30 minutes, followed by three washes with PBS wash (5 min/each).

After PBS washes, tissues were blocked with 3% BSA and 0.3% saponin in PBS for 1 hour. Next, tissues were incubated with primary antibodies: Tom20 (1:200 dilution), and panCytokeratin (1:150 dilution) in PBS containing 3% BSA and 5% salmon sperm DNA. The incubation took place on a rocker overnight at 4°C in a humidity chamber. Following three PBS washes (5 min each), tissues were incubated with respective DS-conjugated secondary antibodies at a final concentration of ~8 μg mL−1 in PBS buffer containing 1% BSA and 5% salmon sperm DNA. The incubation also took place on a rocker at room temperature for 2 hours, followed by three PBS washes (5 min each). After which, all tissue samples were post-fixed by 3.7% PFA and 0.1% GA in 1x PHEM at room temperature for 30 min. Before flow chamber assembly, tissues were incubated with 15% 50 nm gold particles in PBS+ for 1 min, followed by a quick PBS wash.

4.4 Results

As a final portion of the LF-PAINT manuscript, this chapter focuses on pioneering a novel imaging strategy invaluable for scalable SRM from FFPE tissues, coined Flow-Assisted DNA-PAINT. Along with improvements in labeling protocols for tissue,

integrated microfluidics during imaging dramatically improved DNA-PAINT within patient tissues. Together with the second halves of both chapters 2 and 3, results in this chapter comprise the last portion of the LF-PAINT manuscript.

Despite constant improvements in cell-based DNA-PAINT, applications toward tissue samples have been challenging. Given the adoption of tissue super-resolution imaging, as tissue STORM has been previously demonstrated [37], we sought to overcome limitations otherwise preventing tissue DNA-PAINT. We obtained LF-PAINT images of tissue sections by modifying existing workflows by integrating additional blocking steps, RNase treatment, and critically the addition of gentle flow during image acquisition. These improvements are compatible with standard tissue preparations and could be incorporated into clinical FFPE workflows.

Basics of Tissue STORM vs DNA-PAINT

With cell-based LF-PAINT demonstrated, we next sought to apply the imaging platform to clinical FFPE sections. Despite previous work on tissue imaging with STORM and STED, multiplexed SRM imaging of tissue sections across large FOVs has not been achieved. Furthermore, for SRM imaging of tissue structures, the ability to reliably stitch together images from adjacent FOVs is especially critical, because views at the millimeter scale is often needed to capture the organization of multicellular structures. Despite its growing usage, tissue STORM is limited in FOV stitching, as fluorophores in adjacent regions are often significantly lost when imaging the current FOV (**Figure A 4.1**). By contrast, in DNA-PAINT adjacent FOVs can be reliably imaged and reconstructed (**Figure 4.2B**). This further assures our choice of using DNA-PAINT as the basis for our large FOV SRM development on tissues.

While LF-PAINT inherently excels at multiplexing, the FOV, and multi-FOV stitching, we encountered significant challenges in attempting DNA-PAINT(-ERS) on FFPE tissue sections. Specifically, we found that tissue DNA-PAINT image quality was

noticeably lower compared to that of cells (**Figure 4.1 & 4.2).** Compared with the latter, we routinely observed much fewer DNA-PAINT localizations when using similar imaging buffers and IS concentrations as optimized for cells. Of note, for LF-PAINT, we used 2 µm sections which yielded low background as previously optimized from tissue STORM [37] and STED [58]. We also confirmed that tissue staining was done properly by examining signals from Cy3 attached to the DS (conjugated to secondary antibodies; data not shown). This suggests sufficient labeling with DS and points instead to inefficient DS-IS interactions.

Critical role of Flow-Assisted DNA-PAINT for FFPE tissue DNA-PAINT

In testing different strategies for improving DNA-PAINT on tissue sections, we found that a mild flow of imaging buffer during imaging drastically improves the localization kinetics and hence the image quality (**Figure 4.3A**). We termed this approach “Flow-assisted DNA-PAINT”. While DNA-PAINT(-ERS) works well on passive diffusion of IS when imaging cells, tissue DNA-PAINT under passive diffusion alone yielded a low abundance DS-IS binding events, which translated into poor image quality over comparable time to cells (**Figure 4.3B**). When exchanging buffers on FFPE samples, we incidentally discovered that the localization kinetics could be drastically improved when the pump was left on during image acquisition. In fact, a weak flow at 1 µL / min already increased the observed localizations by ~10-fold and resulted in significantly better resolved structures (**Figure 4.3B & C**). No obvious additional benefits were observed when the flow rate was increased to 5 µL / min. At a 1 µL / min flow rate, we only slightly increased overall consumption of the imaging buffer during a typical 10-20 min acquisition.

The effect of Flow-assisted DNA-PAINT on cells

Considering the dramatic improvement in imaging quality by “Flow-Assisted DNA-PAINT” on FFPE tissue samples, we also compared the effect it may have on cell-

based imaging. Unlike with tissue samples, the inclusion of flow with cell samples exhibited situational improvements in image quality, in a buffer dependent manner. Flow using previously optimized buffers with higher EC concentration yielded no change, while conditions with lower EC concentrations exhibited a relative improvement, which appeared better at 1 µL / min flow. Compared with tissue samples, the addition of imaging buffer flow provided situational improvements for high-quality cell imaging (**Figure 4.4**).

Optimizing tissue Imaging buffers and labeling treatments

Another adjustment we made for tissue LF-PAINT was the imaging buffer composition, specifically the concentration of EC. In DNA-PAINT-ERS, EC was a key ingredient in the imaging buffer for tuning the localization kinetics. While most LF-PAINT images of cells were acquired at 10-15% (v/v) EC, tissue samples had substantial diffusive background and non-uniform illumination with this level of EC, even at different flow rates (**Figure A 4.2A**). Instead, lower EC concentrations at 5-8% dramatically reduced the background, enabling clear visualization of on-target single molecule localization painting events (**Figure A 4.2B**). The reason for this increased background is unclear, but may be related to refractive index differences at higher EC concentrations [101]. As such, an EC concentration a ~7% with a 1 µL / min flow rate was used for subsequent tissue LF-PAINT images.

Additional improvements on SRM imaging of FFPE tissue sections came from optimized sample preparations. We found that treatment of tissue sections with RNase A and Signal Enhancer (SE) after the antigen retrieval steps helped to enhance antibody labeling which is already visible under a wide-field fluorescence microscope (See Methods). Under a 1µl / min flow, we found that both RNase A and RNase A + SE treated samples exhibited improved mitochondrial labeling versus the PBS control, while SE alone appeared to lower cytosolic background (**Figure 4.5A-F**). Notably, RNase A +

SE treatment revealed optimal Tomm20 labeling and reconstruction with reduced spurious cytoplasmic background (**Figure 4.5G, H**). In all cases, the inclusion of a 1 µl / min flow remained critical to obtain higher quality images for tissue.

Multiplexed clinical FFPE tissue imaging with LF-PAINT

With the above improvements in sample preparation and imaging kinetics, we next used LF-PAINT for multiplexed SRM imaging of FFPE sections. In initial work, we chose to use FFPE sections of Pancreatic Ductal Adenocarcinoma (PDAC). PDAC development is theorized to involve changes in mitochondrial structure and function, which are difficult to visualize clearly with conventional microscopy [15, 17, 18, 102]. We dual-labeled both Tom20 and prognostic pan-cytokeratin targeting ductal adenocarcinomas in the tissue sections. Typically surrounded by thick stroma, these tumor regions can be ~300-500 µm wide or larger, significantly larger than the FOV afforded by traditional SRM. With flow-assisted LF-PAINT and sample optimizations described earlier, we were able to obtain high-quality, SRM images of both targets across an entire cancerous duct (**Figure 4.6**).

A histological overview photographed with a 20x objective revealed a moderately differentiated PDAC within desmoplastic stroma (**Figure 4.6A & B**). Using Cy3-labeled DS-conjugated antibodies as a reference, immunofluorescence imaging confirmed strong pan-cytokeratin signal along the duct and faint mitochondria both in and around the duct itself (**Figure 4.6C**). By acquiring six FOVs via flow-assisted LF-PAINT with 40µm overlaps, we imaged the entire duct and adjacent stroma covering an area over 800 µm by 500 µm (**Figure 4.6D**). At 30 minutes per FOV per target, the entire imaging took ~6 hours to obtain this dual-target image. A single FOV demonstrates the uniform image quality over the 300 µm x 300 µm area and highlights regions of the tumor with subtle differences in pan-cytokeratin expression (**Figure 4.6E**). In smaller ROIs, subcellular details and morphology can be seen at unparalleled detail versus an

otherwise diffraction limited resolution (**Figure 4.6F-H**). We noted that, not only can distinct mitochondria of varying size and shape be seen, but dense pan-cytokeratin also tapers to fine filamentous networks often enclosing the cell periphery and contained mitochondria. Interestingly, cells in regions such as in panel G are somewhat similarly organized and differentiated, while regions in panels F and H are significantly more unorganized.

To further exemplify the full range of spatial information obtainable by LF-PAINT on FFPE tissue sections, we serially magnified a second ductal adenocarcinoma from the millimeter-scale of the histological overview down to distinct mitochondrial membrane structures (**Figure A 4.3**). We targeted another ductal boundary view at 0.5mm x 0.5 mm, rebuilt from 4 overlapping LF-PAINT images (**Figure A 4.3A-D**). Serial ~4x magnification from a single LF-PAINT image highlights a cluster of cells, a cytokeratin boundary with some adjacent mitochondria, a branched mitochondrion with cytokeratin filaments nearby, and finally distinct clusters of Tom20 present along the border of the outer-mitochondrial membrane, respectively (**Figure A 4.3E-I**).

4.5 Discussion

With the growing interest in imaging tissue microenvironments to study disease, the ability to image prognostic markers has relied on methods such as cyclic IF [19] and other -omics studies to analyze single-cell resolution data [22, 57]. Despite the broad power and utility of these methods, they often lack highly detailed and more mechanistic level information, especially when considering large-FOV areas of patient samples. While studies utilizing electron microscopy can directly visualize general structures [95, 99], they are FFPE incompatible, lack specificity and are very low throughput versus more targeted imaging methods like tissue STORM [37]. Notably, among the types of

sample formats, FFPE tissue sections are particularly important for their dominant presence in archived patient samples.

Imaging patient tissue sections with nanoscopic details has already shown great promises in helping understand disease progression and therapeutic responses, but previous attempts with SRM were severely limited in FOVs [37, 38]. LF-PAINT was inherently capable of multiplexed SRM imaging over large FOVs, but imaging FFPE tissue sections with LF-PAINT was still faced with several challenges, most notably poor image quality. We addressed these challenges with a combination of flow-assisted LF-PAINT and modifications to sample preparation, which ultimately resulted in high-quality tissue images. By offering the unique ability to visualize nanoscopic details of multiple targets across large areas of patient samples, LF-PAINT will join the growing list of tools for high-throughput, spatial omics analysis of biology in vivo and in other complex settings

4.6 Conclusion

Combining improvements to sample labeling and multiplexing strategies [19, 42, 81], LF-PAINT imaging of ~10 or more targets over >1 mm2 sample areas should become readily feasible, even with 3D detail. Collectively, LF-PAINT enables comprehensive visualization of millimeters of cells and tissues with details at the nanometer and molecular scales, leading us closer to building a ‘Google-earth’ like view of complex biological systems. Empowered with such imaging throughput and span of length scales, LF-PAINT will find broad applications in biomedicine.

Acknowledgements

The authors thank Drs. Joe W Gray, Gordon Mills, Terry K Morgan, Young Hwan Chang, Jason Link, Sean Speese, Yu-Jui (Roger) Chiu, David Qian, and many other colleagues at OHSU for their helpful discussions. M.J.R, F.C., J.K., D.H., T.Z., S.E., and X.N. are members of and supported by the Cancer Early Detection Advanced Research (CEDAR) Center of the OHSU Knight Cancer Institute.

Funding:

Research in the Nan lab was supported by the OHSU Knight Cancer Institute, the Damon Runyon Cancer Research Foundation, the M. J. Murdock Charitable Trust, the Prospect Creek Foundation, the Cancer Systems Biology Consortium from the National Cancer Institute (CSBC, grant number U54 CA209988, PI: Joe W. Gray), and the National Institute of General Medical Sciences (grant number R01 GM132322, PI: X.N.).

Author Contributions

XN and FC conceived the project and SE helped supervise. MR, FC, JK, DH and XN developed the initial workflows and established the microscope design and fluidic design. KT and JS performed all reagent synthesis and purifications for DNA-conjugates. MR and XN developed the image processing pipelines used. MR and KT developed the workflow for tissue specific optimizations. MR, and JK acquired and performed data analysis. MR and XN wrote the manuscript. XM, MR, KT, MS, TZ and SE reviewed and edited the manuscript. All authors have reviewed and approved the manuscript.

Declaration of Interest

The authors report no conflicts of interest.

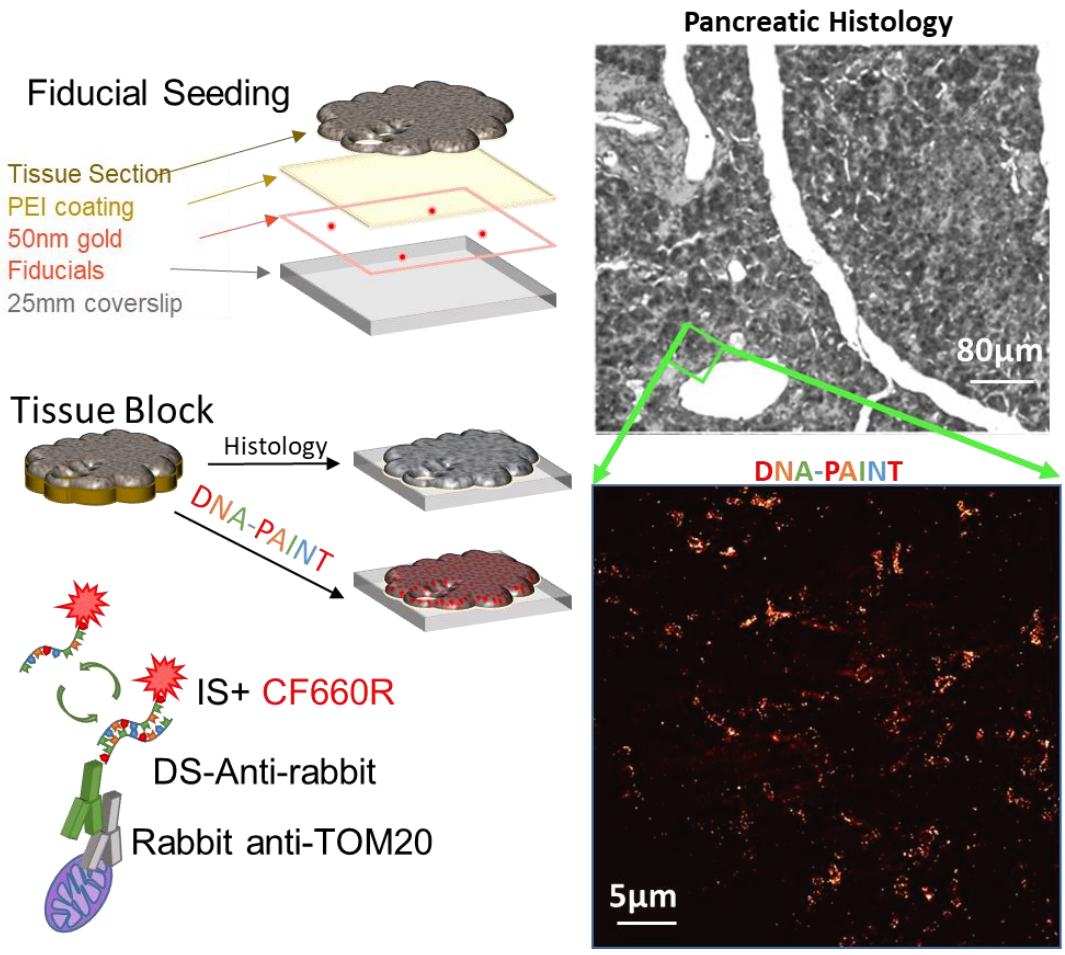

Figure 4.1 | Correlative histology coupled with DNA-PAINT

Schematic of considerations to facilitate co-registered imaging of patient tissues. Fiducial seeding of gold below the sample provides stable uniform gold through all tissue preparation steps. Adjacent sections can be prepared for histological staining (i.e. Hematoxylin and Eosin), or immunolabeled with DS-conjugated antibodies for DNA-PAINT. Representative H&E stained region of healthy pancreatic FFPE tissue with matching magnified proof of concept DNA-PAINT image of Tom20 from acinar cells adjacent a duct. Tissue DNA PAINT images were acquired for 20,000 frames at 100 ms exposure using 500 pm IS2-CF660R and 10 % EC. Scale bar for H&E is 80 µm, (B) is 10 µm, (C) is 2 µm, and (D) is 250 nm.

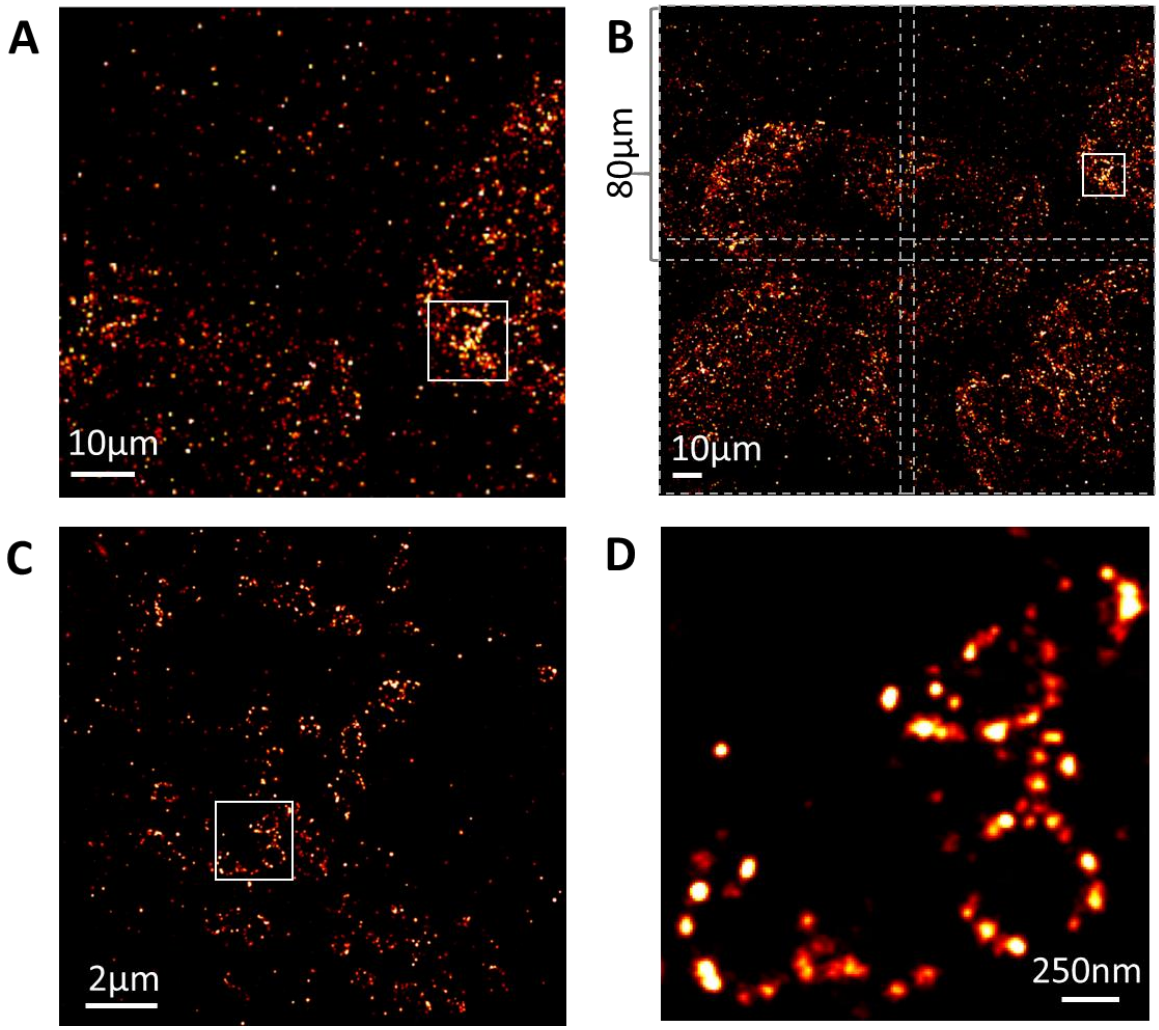

Figure 4.2 | Tissue DNA-PAINT via objective-type TIRF

(A) Tissue DNA-PAINT of Tom20 within HER2+ breast cancer FFPE using largest FOV from our objective-type TIRF microscope of 80 µm x 80 µm. (B) Stitched 2x2 view of tumor boundary shows imaging of adjacent regions with tissue DNA-PAINT. (C) Magnified view from (A) of two cells within the tumor boundary. (D) Highest zoom-in showing rough mitochondria with poorly resolved boundaries. Tissue DNA PAINT images in were acquired for 50,000 frames at 100 ms exposure using 1 nm IS2-ATTO643 and 12.5 % EC. Scale bar for (A) is 10 µm, (B) is 10 µm, (C) is 2 µm, and (D) is 250 nm.

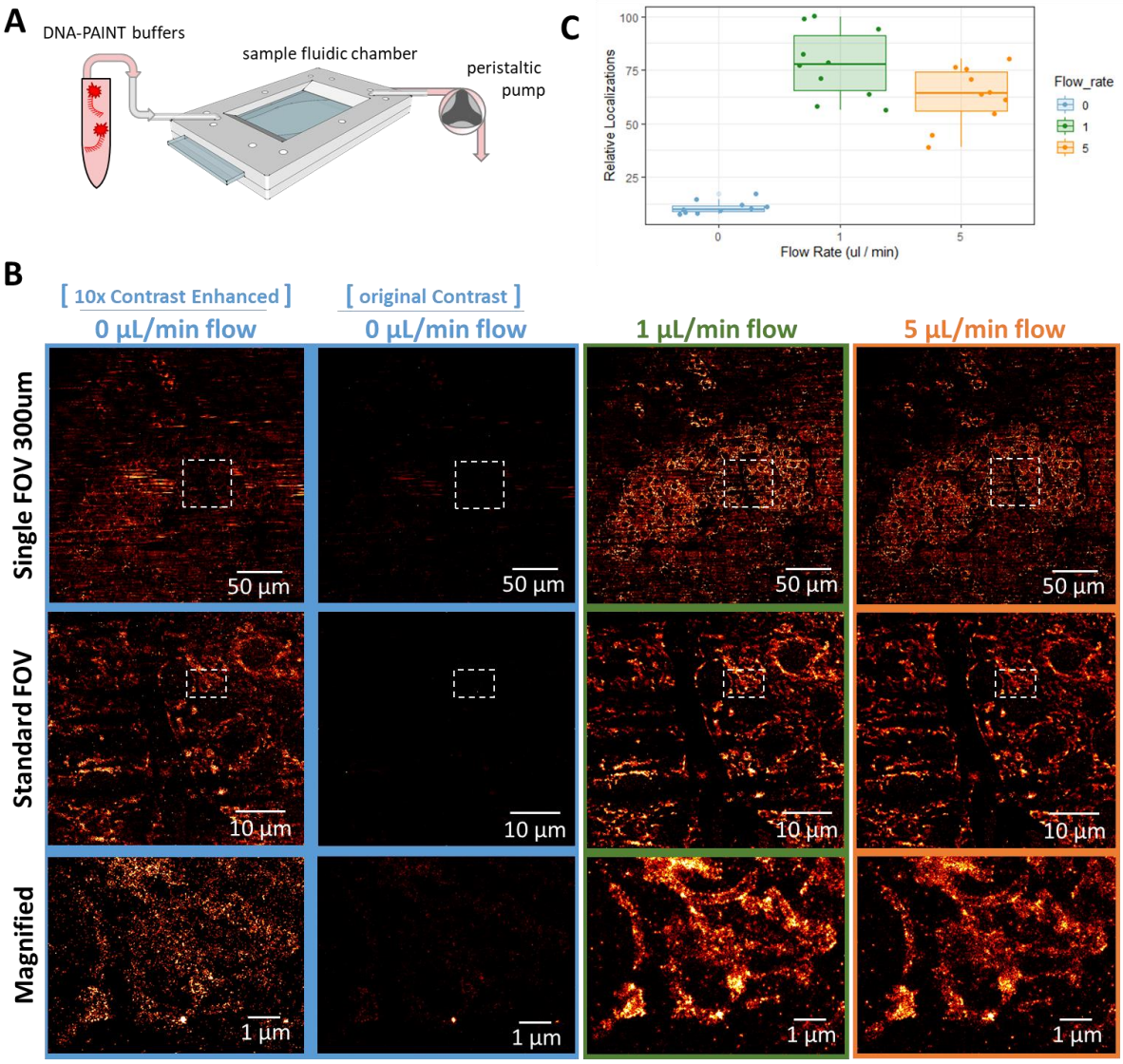
A
DNA-PAINT buffers
sample fluidic chamber
peristaltic pump
C
Relative Localizations
Flow Rate (ul / min)
Flow_rate
0
1
5
B
[10x Contrast Enhanced]
[original Contrast]
0 µL/min flow
0 µL/min flow
1 µL/min flow
5 µL/min flow
Single FOV 300um
Standard FOV
Magnified
50 µm
10 µm
1 µm

Figure 4.3 | Flow-Assisted DNA-PAINT on FFPE tissue samples
(A) Schematic overview of “Flow-Assisted DNA-PAINT” where a peristaltic pump is used to provide gentle flow within the thin (~35 µm) sample chamber. (B) Representative single FOVs of tissue DNA-PAINT imaged with or without “Flow-Assisted DNA-PAINT” (top row). Zoom-in view from the single 300 µm FOV at a more standard FOV of 50 µm (middle row). Highest magnified view showing tissue mitochondria within a single cell (bottom row). Given the incredibly low relative signal without flow, we additionally showed a 10x contrast-adjusted views of the condition for each magnification (left column). Except for varying imaging buffer flow-rates, all images were acquired for 30,000 frames at 60 ms exposure using 500 pM IS2-ATTO643 and 7 % EC. Scale bars in (B) are 50 µm (top row), 10 µm (middle row), and 1 µm (bottom row). (C) Relative localization density for Tom20 from 10 FOVs imaged within a pancreatic FFPE tissue sample using the indicated flow rates 0, 1, and 5 µL / min.

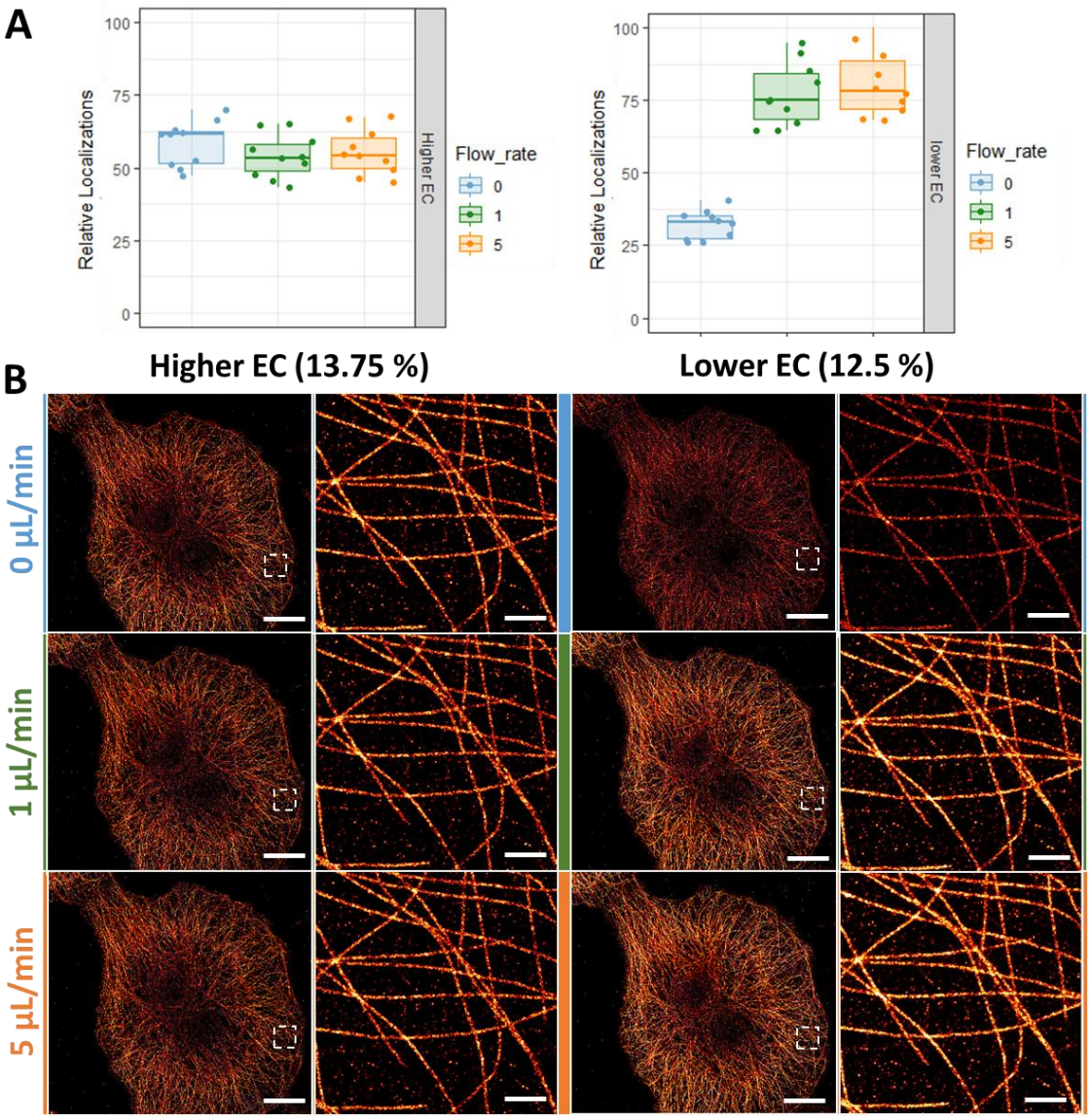

Figure 4.4 | Effect of Flow-Assisted DNA-PAINT on cell samples

(A) Relative localization density for microtubules from 10 FOVs imaged within a single Cos7 cell sample using the indicated flow rates of 0, 1, and 5 µL / min and either higher (13.75 %) or lower (12.5 %) EC. (B) Reconstructed views of cells imaged with or without "Flow-Assisted DNA-PAINT", with all images rendered with the same relative intensity. Except for varying imaging buffer % EC and flow-rates, all images were acquired for 20,000 frames at 30 ms exposure using 1nM IS1-ATTO643. Scale Bars in (B) are 5 µm and 500 nm.

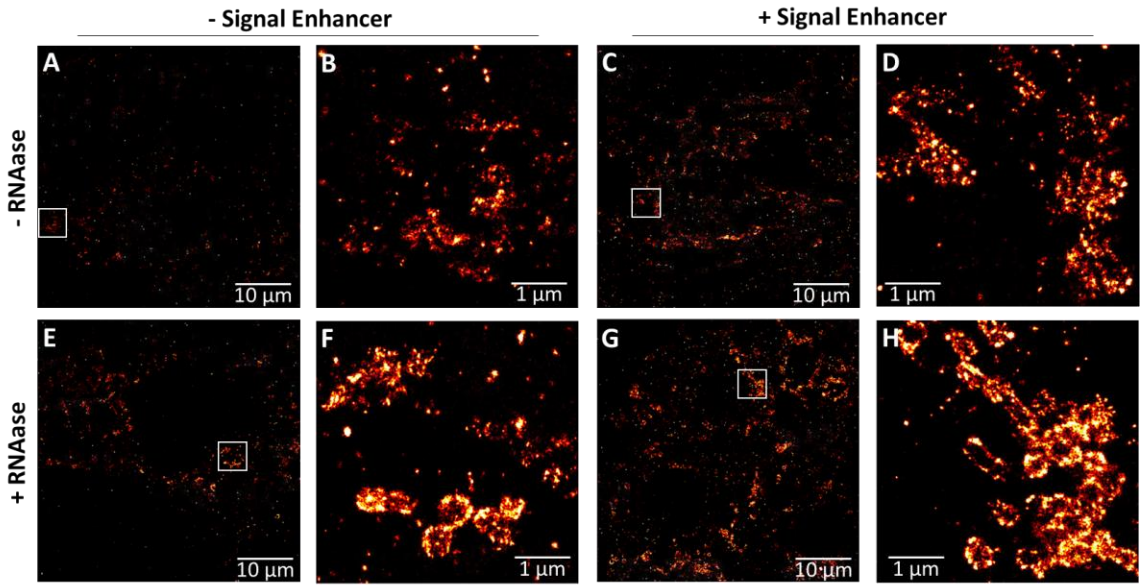

Figure 4.5 | Enhancing Tissue DNA-PAINT labeling via RNase pre-treatment The effect of both RNase A and Signal Enhancer (SE) treatments on tissue-DNA-PAINT targeting Tom20 from pancreatic FFPE tissues. (A,C,E,G) Representative FOVs and (B,D,F,H) magnified regions from: control sample prepared identically to tissue STORM (A,B), sample with SE treatment prior to antibody labeling (C,D), sample with overnight RNase A treatment at RT prior to antibody labeling (E,F) and sample with sequential SE and RNase A treatment prior to antibody labeling (G,H). Outside of indicated treatment variations, all samples were prepared the same way and images were acquired using 30,000 frames at 60 ms exposure using 500 pM IS2-ATTO643 and 7 % EC. Scale bars are 10 µm in (A,C,E,G) and 1 µm in (B,D,F,H).

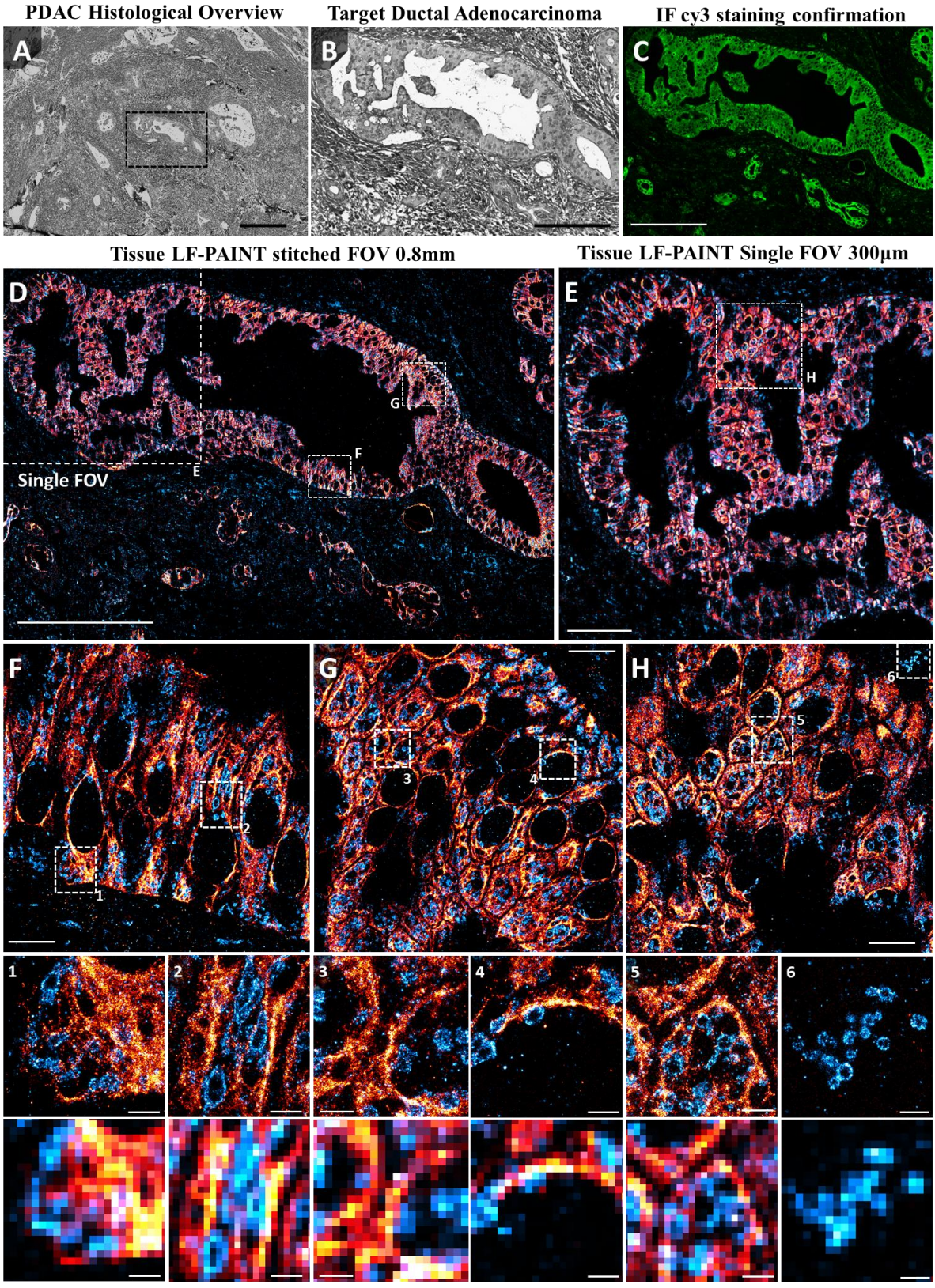
PDAC Histological Overview
Target Ductal Adenocarcinoma
IF cy3 staining confirmation
A
B
C
Tissue LF-PAINT stitched FOV 0.8mm
Tissue LF-PAINT Single FOV 300µm
D
E
Single FOV
E
F
G
H
F
G
H
1
2
3
4
5
6
1
2
3
4
5
6

Figure 4.6 | Multiplexed FFPE tissue DNA-PAINT via LF-PAINT
Representative tissue DNA-PAINT from clinical pancreatic cancer FFPE tissue. (A) Histological overview of moderately differentiated PDAC within desmoplastic stroma acquired at 20x magnification. (B) Targeted ductal adenocarcinoma for imaging with LF-PAINT. (C) Immunofluorescent confirmation of Cy3 signal from secondary antibodies with DNA-PAINT oligomers showing strong pan-cytokeratin staining along the tumor and diffuse mitochondrial labeling within the tumor and adjacent stroma. (D) Stitched tissue DNA-PAINT image of entire 800 µm long ductal adenocarcinoma with both prognostic pan-cytokeratin in red and mitochondrial Tom20 in blue. (E) Single tissue LF-PAINT image using “Flow-Assisted DNA-PAINT”. (F-H) Select magnified regions from (D,E) highlighting the high quality of cellular features seen within different regions of the tumor. Numbered insets shown with matching diffraction limited views (300 nm pixel size). Tissue DNA-PAINT 2-target images (E-G) were acquired in 6 hours total (30,000 frames at 60 ms exposure for each target) using “Flow-Assisted DNA-PAINT” at 1 µL / min flow and 500 pM IS1-ATTO643 and 7 % EC, and 500 pM IS2-ATTO643 and 7% EC for pan-cytokeratin and Tom20 respectively. Scale bars are 500 µm in (A), 200 µm in (B-D), 50 µm in (E), 10 µm in (F-H), and 2 µm for both DNA-PAINT and diffraction-limited bottom insets.

Chapter V: Mitochondrial dynamics dysregulation in cancer, an alluring target for large-scale SRM imaging and analytics

5.1 Abstract

Pancreatic cancer begins with precancerous PanINs characterized by increased cell proliferation through early oncogene activations, accompanied by gradually thickening tissue stroma and worsening hypoxia. Pre-malignant cells adapt to changing metabolism through alterations in their mitochondrial networks, whereby hypoxia triggers increased reactive oxygen species generating a cancer-promoting environment. This chapter aims to characterize the effect of mitochondrial network transformations in precancerous and early PDAC stages, to better understand what drives malignant transformation through directly imaging mitochondrial network morphology and molecular compositions from model cell lines and later patient tissue sections. Leveraging recent progress in image feature extraction and classifications we can understand novel drivers of mitochondrial dynamics such combined hypoxia and oncogenic signals. Expanding from pilot DNA-PAINT validations, we demonstrate the strengths of multiplexed DNA-PAINT super resolution imaging to reconstruct snapshots into these dynamic processes. The imaging and image analysis pipelines established here will pave the way for investigations in the next stage, where tissue ultrastructures and molecular functions can be used to understand mechanisms of PDAC progression and to potentially differentiate lethal vs nonlethal PanIN lesions.

5.2 Introduction

Pancreatic ductal adenocarcinoma (PDAC) has one of the deadliest prognoses of any cancer type [1], due to both a lack of early detection schemes and a limited understanding of the biology through early PDAC progression. Prior to PDAC, digestive enzyme-secreting pancreatic cells (acini) change their morphology through pancreatic intraepithelial neoplasia (PanIN) stages 1-3, becoming increasingly abnormal or dysplastic as the surrounding stroma thickens and local hypoxia increases versus healthy normoxic tissue [12]. In healthy cells, nutrient deprivation and hypoxia trigger programmed cell death or apoptosis from increased reactive oxygen species production and organelle damage, yet prolonged low-level hypoxia can inhibit apoptosis and promote cancer progression [103]. Mitochondria are key consumers of oxygen, which dynamically undergo fusion to form tubular networks that can undergo fission or separation in response to hypoxia as they alter their metabolism [104]. In particular, aberrant mitochondrial dynamics can allow cancer progression by reducing apoptotic signaling, enhancing aerobic glycolysis, and increasing reactive oxygen species [105]. Thus far, studies have implicated abnormal mitochondrial fission and fusion in cancer progression [106], yet limited imaging tools exist to characterize this phenomenon with sufficient detail and especially in patient samples.

Although prolonged metabolic stress including hypoxia typically causes a loss of outer mitochondrial membrane potential, triggering apoptotic pathways to kill unhealthy cells including cancer, oxygen levels between 1-3% [107] are paradoxically theorized to be cancer promoting [103]. Despite well-categorized histological [9] and genetic [12] initiations of PDAC progression through pancreatic intraepithelial neoplasia (PanIN) stages (**Figure 1.2**), limited understanding of the biology in early PDAC restricts early detection and treatment options. PDAC begins by slowly progressing through increasing

precancerous tissue dysplasia, typically PanINs or sometimes intraductal papillary mucinous neoplasms [9]. Recent genetic studies have found the earliest stages of precancer to begin with the oncogenic driver KRAS, which causes continual signals for cell proliferation and growth [11]. Around the earliest stages of PanIN staging progression, overstimulated fibroblast cells in the adjacent stroma deposit excess extra-cellular matrix to thicken the stroma and increase tissue hypoxia [108, 109]. The combined fibroblast-increased stromal density and metabolic demand from KRAS+ precancerous cells further lowers available oxygen and generates hypoxic regions in PDAC [13]. Importantly, hypoxia triggers hypoxia inducible factors (HIF) shifting the normal balance of mitochondrial fission and fusion to favor fission, causing normoxic tubular networks to fragment and form distinct organelles (**Figure 5.1**) [104]. Although efforts have been made to characterize the extent of hypoxia directly in late-stage PDAC tumors [110], the low intensity initial metabolic and mitochondrial changes difficult to quantify by bulk tissue analysis can be quantified directly using SRM on mitochondrial networks.

Mechanistic studies have identified mitochondrial dynamics proteins that govern network morphology through fission or fusion in response to multiple metabolic demands [111], with several implicated for different cancer types [106]. Activated dynamin related protein 1 (Drp1) is recruited to the mitochondrial membrane by mitochondrial fission protein 1 (Fis1), whereby Drp1 forms a ring which contracts and causes fission. Under normoxia Drp1 is phosphorylated and inactivated, yet during hypoxia HIF inhibits Drp1 phosphorylation to increase mitochondrial fission (**Figure 5.2**). KRAS involvement coupled with Drp1 activation have been shown to promote mitochondrial fission and drive early cellular reprogramming and tumor growth in PDAC models [112, 113]. Mitochondrial fusion is mediated by both inner membrane optic atrophy 1 (Opa1) oligomers that interact with outer membrane mitofusin 1&2 (Mfn1/2), where during

hypoxia HIF disrupts Opa1 oligomers to limit fusion (**Figure 5.2**). Intriguingly, inhibition of Drp1 coupled with activation of Mfn2 suppresses pancreatic cancer growth through increased mitochondrial fusion [16], providing rationale for future treatment options based on mitochondrial dynamics proteins. Despite well-characterized molecular pathways, structural or functional roles in patient cancers are poorly understood. Identifying how mitochondrial dynamics proteins change during precancerous PDAC progression can provide both an early indicator of malignant disease and treatment.

Typically, tissue histology employs Hematoxylin and Eosin (H&E) staining that highlights different cell types to enhance contrast, while immunofluorescence and immunohistochemistry on adjacent sections characterize specific biomarkers in patient tissue sections. Unfortunately these general methods lack sufficient spatial resolution to identify distinct mitochondria or specific biomarkers affecting their dynamics [114]. Electron microscopy (EM) has long provided very high structural detail of mitochondria within cancer tissue sections [115, 116], yet limited biomarker labeling strategies hinder its applicability. Correlating light and electron microscopy brings fluorescent protein specificity to EM, yet this usage is limited by access to fresh frozen patient samples [117]. Recently, tissue based SRM utilizing STORM has been validated within tissue sections [37], providing high resolution (< 20 nm) reconstructions of mitochondria within breast cancer [118], but difficulties remain with spectrally distinct fluorophores, photobleaching, buffer oxidation, and buffer pH that limit imaging multiplexity and throughput.

Capitalizing on our improvements to DNA-PAINT and LF-PAINT imaging system, we are uniquely poised to characterize these mitochondrial biomarkers following disease progression and comparisons to annotated histology. We hypothesize that through precancerous PanIN stages during PDAC progression, mitochondrial networks will undergo fission in response to increasing tissue hypoxia. To initially test this hypothesis,

we demonstrate proof of concept findings for: 1) combined effect of oncogenic $KRAS^{G12D}$ and hypoxia to drive stress-induced hyperfusion, 2) analytical pipelines to characterize mitochondrial networks from patient FFPE, 3) multiplexed DNA-PAINT and its advantages to visualize functional protein complexes behind bulk mitochondrial network phenotypes. Ultimately, paired with optimizations in Chapter 4, this work is poised to characterize the early mitochondrial network changes through PanIN stages of PDAC patient samples, and identify potential markers for early cancer detection and therapy.

5.3 Materials and Methods

Methods for generating DNA-PAINT labeling reagents followed established protocols from DNA-PAINT-ERS [50, 64] and LF-PAINT respectively for microscope design and data processing as outlined in Chapter 2. Tissue labeling was performed identically to tissue STORM within Chapter 4. Additional methods specifically utilized within this chapter are outlined below:

Cell / tissue samples and hypoxic incubators

U2OS cells (ATCC®, HTB-96), Panc1 cells (ATCC® CRL-1469 ™), and Capan1 cells (ATCC® HTB-79 ™) were maintained in Gibco DMEM (Thermo Fisher Scientific, 11995073) or phenol red-free DMEM (Thermo Fisher Scientific, 21–063–045) supplemented with 10% fetal bovine serum (Thermo Fisher Scientific, 26–140–079). U2OS, Panc1 and Capan1 cells were passaged every 3–4, 2–3, and 4-5 days respectively, and used under passage number 15. Trypsin-EDTA (0.25%) (Thermo Fisher Scientific 25200056) was used for passaging. For hypoxia plus KRAS experiments, U2OS $KRAS^{G12D}$ dox-inducible cells were initially seeded at ~15 confluency for ~12 hrs in DMEM +10% FBS. After adherence, media was switched to DMEM without FBS and cell were transferred to either 20% or 3% hypoxic cell incubators

(Thermo Forma 3110 CO2 Water Jacketed Incubator, Thermo Fisher) and grown for an additional 24 hrs.

Pancreatic FFPE tissue samples were collected through the Brenden Colson Center following IRB approved protocols including patient consent for research applications. Standard human pancreas samples obtained by BCC were FFPE sections from otherwise healthy cadavers. FFPE tissue samples were cut using a ultramicrotome in 2 πm thick sections (RM2125 RTS, Leica Biosystems, Germany).

Immunostaining

For immunostaining of mitochondrial dynamics proteins, cells were fixed for 20 min with 3.7% paraformaldehyde (PFA) in 1x PHEM buffer plus 0.1% Glutaraldehyde (GA), except if Mfn1 was to be labeled is it required no GA fixation for proper targeting. Immunostaining concentrations for primary antibodies were: Tom20 (Rabbit 1:200), Fis1 (Rabbit 1:200), CHCHD3 (Rabbit 1:100) and Mfn1 (Mouse 1:100). IF style images from both hypoxia and pancreatic mitochondrial network analysis was obtained after labeling with 1:500 Anti rabbit AF647 (ab15075, Abcam) according to manufacturer's protocol. Respective secondary antibody-DS described in Chapter 2 were used identically at a final concentration of ~8 μg mL−1. Pilot CHCHD3 and Mfn1 co-labeling was performed using anti-mouse AF488 (ab150113, Abcam) and anti-rabbit AF647 ab15075, Abcam) co-labeled following manufacturers protocol. Overnight labeling was performed for all primary antibodies used as it appeared to yield more consistent labeling quality for all targets.

Semi-automated mitochondrial analysis utilizing MitoGraph

Our analysis Macro was built in part using the Fiji macro language in .ijm format, functioning somewhat similarly in its ability to sub-divide input images for higher-throughput downstream quantifications as demonstrated in Chapter 3. Unlike prior methods utilizing WEKA, after initial input image sub-divisions, looped MitoGraph

analysis was performed on input images following its respective guidelines [119]. An example view of the semi-automated mitochondrial network analysis can be seen in **Figure A 5.1**). After running MitoGraph analysis on each sub-divided input image, MitoGraph results were compiled using modified .R files developed by MitoGraph which aggregated key mitochondrial network quantified outputs [119]. Custom .R analysis and visualization using the ggplot package were used for **Figure 5.3** and **Figure 5.4** for hypoxic and pancreatic network analysis respectively.

5.4 Results

Unlike the strictly technology focused development within chapters 2-4, this chapter leverages analytical pipelines and SRM strategies to peer into the biology of mitochondrial organization in the context of cancer. Results within this chapter reflect a central biological theme in which the earlier chapters were developed to overcome technical limitations in answering the complex biology behind mitochondrial dynamics.

While $KRAS^{G12D}$ signaling and hypoxia have independently been demonstrated to affect mitochondrial networks, few studies have sought to characterize the combined response of these factors and how they may relate to early cancer biology. To assess this relationship, we cultured U2OS cell lines with dox-inducible $KRAS^{G12D}$ under both Normoxic and hypoxic conditions. By growing cells for 24 hours in oxygen controllable incubators, we cultured cells for 24 hours under 20% (Normoxic) and 3% (hypoxic) Oxygen. Direct visualization of Tom20 labeling for mitochondria reveals a variety of mitochondrial network organizations reflecting snapshots into mitochondrial dynamics under these conditions (**Figure 5.3A**). Unlike many initial studies into mitochondrial dynamics, we opted to leverage advancements in image analysis to characterize observed network changes, rather than visual approximation by eye.

Utilizing open-source mitochondria network analysis package MitoGraph [119] we found we could measure the relative connectivity of the observed mitochondria. In brief, MitoGraph uses iterative masking to fit geometric skeletonizations to reflect the mitochondria from input IF images. By coupling MitoGraph into semi-automated image analysis workflows using custom Fiji macros, similar to methods in Chapter 3, we could automatically extract mitochondrial network details across larger input images of cells (**Figure A 5.1**). Notably, automated image analysis using dynamic modeling and machine learning type plugins can lead to erroneous classifications if performed on the wrong images. If MitoGraph analysis we performed on an image without mitochondria present, auto-scaling built into MitoGraph analysis would incorrectly find mitochondria networks within the background noise from the microscope. To alleviate this concern, we incorporated check-points which would remove sub-images which did not contain any cells and their mitochondria (**Figure A 5.1**). This workflow demonstrates another example of how automation can accelerate the utility of existing open-source image analysis plugins and programs.

Utilizing our semi-automated mitochondrial network analysis pipeline, we next characterized the changes in mitochondrial networks observed under oncogenic $KRAS^{G12D}$ signaling and hypoxia. We found an inverse response to growth under 3% hypoxia, which caused an increased and decreased mitochondrial connectivity for the KRAS WT and $KRAS^{G12D}$ cells (**Figure 5.3B**). We theorized this may relate broad categories of mitochondrial organization response from literature [18, 105, 111], namely stress-induced hyperfusion and severe-stress induced fission (**Figure 5.3C**). Overall, these may manifest as the observable changes in average mitochondrial connectivity, schematically shown with circle size reflecting the degree of connectivity (**Figure 5.3C**).

We next sought to determine if we could leverage these types of image analysis pipelines to characterize mitochondrial networks from patient FFPE tissues. As a proof

of concept, we labeled healthy cadaver pancreatic tissue sections for IF imaging of Tom20. Utilizing a pilot region of 1.5 x 2 mm, we could identify large areas of the tissue for expected cell types including acinar cells, ductal cells, and islets of Langerhans (**Figure 5.4A**). Since acinar cells were the predominant cell-type observed, we grouped them into 7 larger clusters which were clearly connected, smaller separated acinar cells on the tissue border were excluded. As expected, our semi-automated mitochondrial network analysis pipeline could classify mitochondria from FFPE IF images as well (**Figure 5.4A, right panel**). Sub-segmenting these regions into ~16 μm wide sub-images (**Figure 5.4B, right panel**), we characterized mitochondrial connectivity over > 3,000 ROIs from the input image spread across the 9 cell clusters identified (7 acinar, 1 islet, and 1 ductal). By plotting different aspects of mitochondrial network geometry, as output from MitoGraph, we could visualize the potential differences in % free-ends, % three-way junctions, longest connected network proportion (PHI ratio), and the total number of observed mitochondria (**Figure 5.4B**). Our analysis revealed that ductal cells contained a significantly larger fused mitochondria versus other cell types, and that islets of Langerhans contained significantly more mitochondria than other cell types. These findings are consistent with known higher metabolic activity in islets of Langerhans [120], and a potential difference in oxygen availability for ductal cells versus acinar cells. Notably, these bulk network trends did not significantly impact the number of either free-end or three-way fractions, however a clear drop in free-end fractions were compensated by an increase in three-way junctions for ductal cells. Although preliminary, these findings demonstrate the potential to perform similar quantifications in the context of early PDAC and precursor lesions.

Building from initial studies leveraging the ease of use of IF to study mitochondrial networks, we next sought to demonstrate the power of DNA-PAINT to visualize substantially more detail in both mitochondrial morphology and mitochondrial

dynamics proteins which regulate their connectivity and functionality. As a first example into the potential relationship in mitochondrial structure and PDAC aggressiveness, we performed DNA-PAINT imaging on two PDAC cell lines. Representative images from both a highly aggressive Panc1 cell line (**Figure A 5.2A & C**) and a slower growing Capan1 cell line (**Figure A 5.2B & D**) reveal dramatic differences in mitochondrial organization. Critically, unlike with diffraction-limited imaging, the precise hollow structure from the outer mitochondrial membrane protein Tom20 can be readily visualized, providing unparalleled detail into the highly fragmented mitochondria in Panc1 cells and the long/fused mitochondria from Capan1 cells **(Figure A5.2**). This additionally agrees with the Broad Institute cancer cell encyclopedia which identified Drp1 expression is 3 times higher for Panc1 cells than Capan1 cells. Although ripe for image analysis into this new level of detail in mitochondrial morphology, images such as this to not reveal how the mitochondria have adopted these organizations.

An important next step into understand mitochondrial dynamics would be the ability to co-localize the competing functional protein complexes which govern their rates of fission and fusion. Notably, although methods such as multi-color STORM can be used to visualize multiple sets of protein targets, difficulty in reliable detection for complex structures using spectrally distinct fluorophores can be challenging, and give a warped perspective on the complexes involved. Representative 2-color STORM on mitochondrial fission protein Drp1 and mitochondrial fusion protein Mfn1, imaged with AF647 and AF488 respectively, reveals clear punctate aggregates of Drp1 (red hot) along the mitochondrial exterior (**Figure 5.5A, C, E, G**). However potential functional aggregates of Mfn1 (cyan hot) are difficult to discern with as much accuracy, potentially hindered by relatively poor photo switching of AF488 (**Figure 5.5 E, G**). Critically, when imaging these same two primary antibodies with DNA-PAINT-ERS secondary antibodies as shown in Chapter 2, distinct punctate structures for both mitochondrial targets can be

more readily observed (**Figure 5.5B, D, F, H**). These small aggregations along apparently mitochondrial outlines provide a glimpse into the competing signaling that they perform from the surface of the mitochondria.

Another intriguing target for mitochondrial morphology and structure is CHCD3, which has a reported role in anchoring the inner and outer mitochondrial membranes together in conjunction with a variety of other proteins. Although the precise structure of this complex has yet to be directly visualized, pilot imaging has revealed its potential role in mitochondrial stability. Again, utilizing DNA-PAINT, we can image aggregations of CHCHD3 within a U2OS cell, which at first glance appear to be organized into even spaced out small puncta (**Figure A 5.3A & B**). Although not a lightly expressed protein, these puncta appear to be ~100 nm apart on average. To our surprise, this matches current models [121] of the CHCHD3 role in anchoring both the OMM and IMM membranes (**Figure A 5.3 D**), while also largely agreeing with the spacing of cristae within mitochondria (**Figure A 5.3 D**) as commonly seen via electron microscopy [95]. Armed with this thinking, we can hypothesize the cristae anchors directly along the mitochondrial exterior (**Figure A 5.3E**). In addition, by building panels of such proteins into a larger panel of mitochondrial dynamics proteins, we are equipped to study different interactions. As a final example labeling both CHCHD3 and Mfn1 in U2OS cells, IF imaging appears to indicate an inverse relationship with mitochondrial size and CHCHD3 expression, whereby long and thin fused mitochondria express predominantly Mfn1, and shorter wider mitochondria exhibit substantially stronger CHCHD3 staining (**Figure A 5.4A**). Subsequent imaging by 2-target DNA-PAINT reveals a complicated pattern of Mfn1 and CHCD3 aggregations, likely as only 2 members of the variety of mitochondrial proteins which govern their form and function (**Figure A 5.4B & C**).

5.5 Discussion

This work reflects ongoing efforts to leverage the advantages of improvements to DNA-PAINT imaging to address critical questions about cancer biology which have remained elusive. Despite being a target of growing research, direct visualization of mitochondrial dynamics proteins, coupled with model systems to infer their effects, has largely been performed using IF based approaches [102, 112]. While these mitochondrial dynamics proteins are expressed at relatively lower levels compared to abundant mitochondrial proteins such as Tom20, their functional roles have been implicated in dynamic aggregates, such as transient formations of Drp1 prior to mitochondrial fission [122]. These types of studies have been foundational, providing novel insights into the highly dynamic nature of the protein complexes involved. Indeed, structural biologists have also begun to piece together the larger protein complexes built-up from these proteins, including numerous studies leveraging electron microscopy and modeling to find mechanistic intermediates necessary for oligomerization in proteins like Drp1 and its binding partners [123]. SRM studies such as our initial proof of concept images, are poised to visualize the in-vivo nature of these complexes at much higher resolution, giving insights into the dynamic states each protein and complex may undergo while performing their roles in either fission or fusion.

In tandem with developments in multiplexed high-quality SRM images of these proteins, further work is required to analyze their co-localizations, aggregations, and spatial orientations along the mitochondrial surface correlated to larger-order mitochondrial organization. Initial clustering analysis can be performed using existing custom PALM software [124] and cluster analysis [35] will quantify changes in biomarker grouping within mitochondrial networks, these can be compared with the overall mitochondrial network morphology as obtained from MitoGraph. Next generation cluster

analysis can leverage interpretations across many different protein targets, similar to as developed through exchange-PAINT based studies [63]. Through imaging with multi-target LF-PAINT, the opportunity to analyze the complex interplay between mitochondrial dynamics proteins can expand from a per-mitochondrion, to per-cell, and even cell-population levels. Paired with model systems such as PDAC cell-lines and hypoxic differences, we are now equipped to study both normal and abnormal mitochondrial functions at unpresented scales and resolution.

Ultimately, these findings may prove more valuable in studying patient tissue sections, giving the capability to gauge the functional status and dysregulations directly from patient tissues. After characterizing the basic biology of in vitro hypoxic response, we will assess these phenomena through a translational pilot cohort of healthy and PDAC patient tissue sections. Our preliminary data shows that tissue DNA-PAINT can provide super-resolution detail to map mitochondrial networks within the human pancreas, which can be visualized with high precision over large areas with LF-PAINT. Through geometric characterizations of mitochondria to characterize mitochondrial connectivity can now compare PanIN annotated histology with aberrant mitochondrial dynamics with the potential impact to both diagnose early tumor progression and possibly treatment of hypoxia-induced PDAC [107]. Studies from cell-culture have already implicated several mechanistic directions to target mitochondrial dynamics and signaling pathways, to revert otherwise aggressive phenotypes seen in PDAC cell-lines [102, 112, 125]. Small-molecule inhibitors are even being developed to target key proteins including Drp1 [102], further exemplifying the potential therapeutic effects to both understand and target dysregulated mitochondrial functions in the context of cancer.

5.6 Conclusion

In summary, we report proof-of-principle model systems and SRM imaging applications into studying dysregulated mitochondrial dynamics under oncogenic and hypoxic signaling, and potentially directly from patient tissues. Co-development of advanced image registration and analysis pipelines will enable powerful quantitative analysis of biomarkers in the tissue environment and within cells and organelles. Through this combined approach, we will validate a powerful new tool to characterize molecular functions in early and malignant cancers without relying on surrogate systems of study. Future forms of this project will: i) provide direct insight into mechanisms of early onset and malignant transformation, and ii) be combined with patient outcome data potentially leading to novel approaches in determining lethal vs. non-lethal PanINs based on understanding tissue ultrastructure.

Acknowledgements

The authors thank Drs. Rosalie Sears, Jason Link, Terry K Morgan, Young Hwan Chang, Yu-Jui (Roger) Chiu, David Qian, and many other colleagues at OHSU for their helpful discussions. This work was performed by members of and supported by the Cancer Early Detection Advanced Research (CEDAR) Center of the OHSU Knight Cancer Institute.

Funding:

Research in the Nan lab was supported by the OHSU Knight Cancer Institute, the Damon Runyon Cancer Research Foundation, the M. J. Murdock Charitable Trust, the Prospect Creek Foundation, the Cancer Systems Biology Consortium from the National Cancer Institute (CSBC, grant number U54 CA209988, PI: Joe W. Gray), and

the National Institute of General Medical Sciences (grant number R01 GM132322, PI: X.N.).

Author Contributions

This work has yet to be finalized into a manuscript at this time, but work presented thus far was contributed by members highlighted in previous chapters: MR conceived the project, which XN and SE helped supervise. MR, FC and KT designed experiments performed. KT JS, and TZ designed and performed all reagent synthesis and purifications for DNA-conjugates. MR and XN developed the image processing pipelines used. MR acquired and performed data analysis.

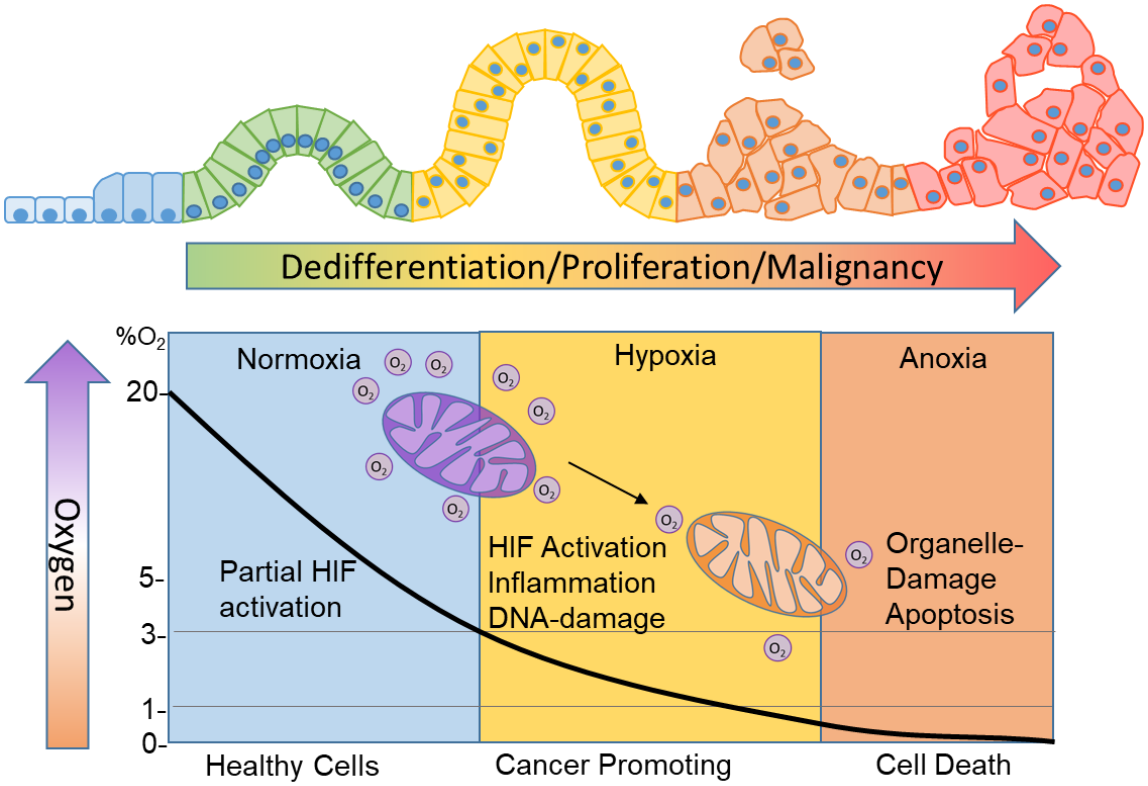

Figure 5.1 | Theory of mitochondrial dysregulation within PDAC development co-occurring with worsening tissue hypoxia.

Qualitative summary of processes which can occur under worsening tissue hypoxia traced to increasing dedifferentiation, proliferation, and malignancy.

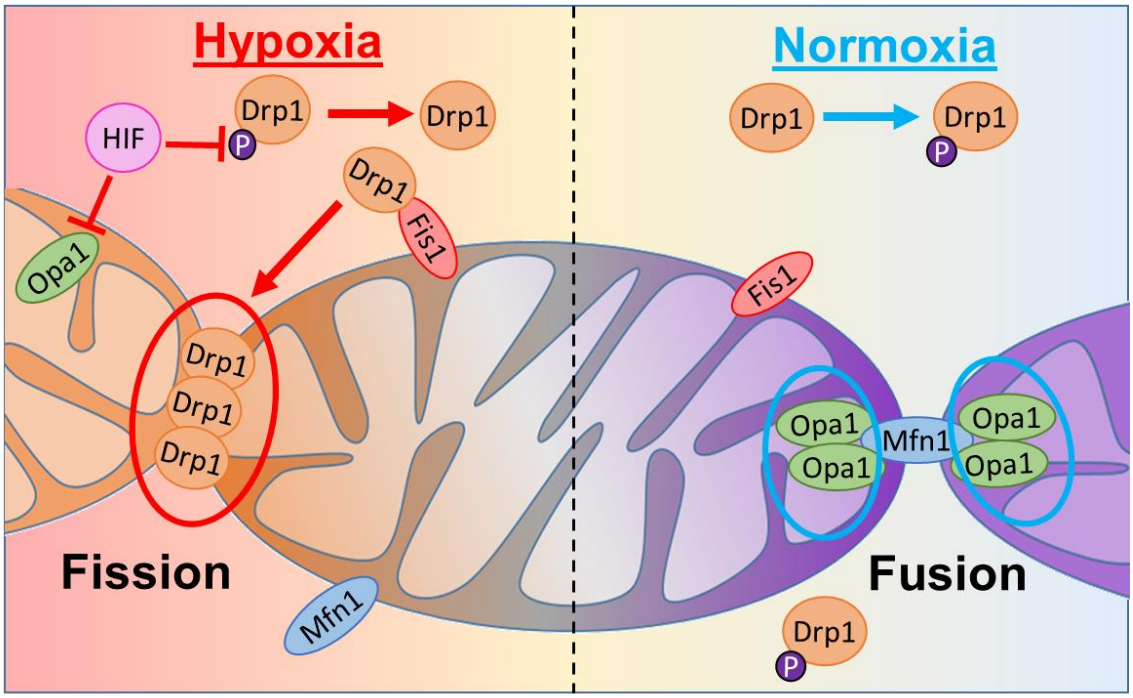

Figure 5.2 | Simplification of mitochondrial dynamics proteins and altered functions in Fission and Fusion under hypoxic stress

Hypoxia generally favors function of Fis1 and Drp1 to promote mitochondria fission, while normoxia generally favors function of Opa1 and Mfn1 to promote mitochondria fusion.

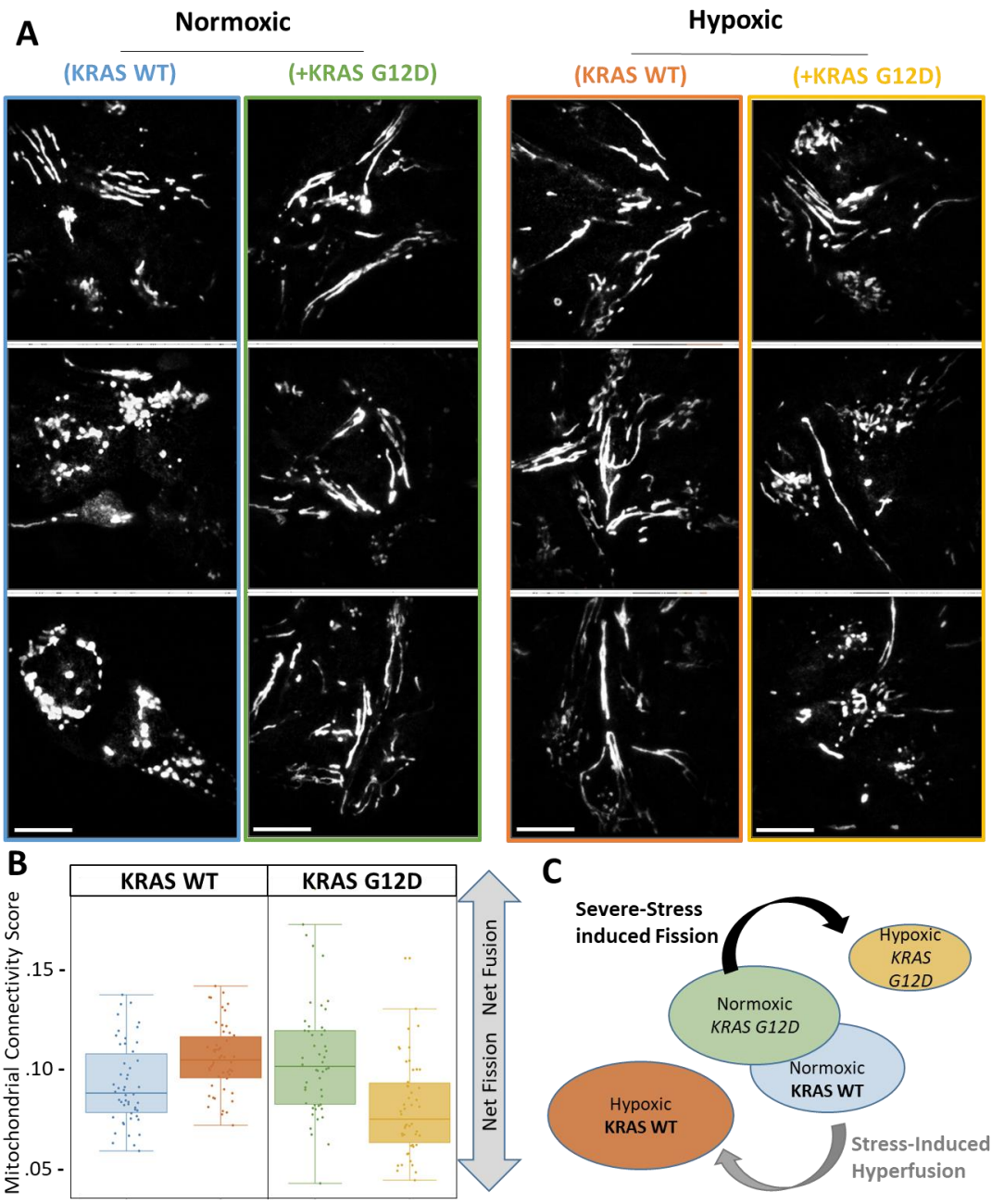

Figure 5.3 | Combined effect of KRAS^{G12D} and Hypoxia response through mitochondrial reorganization

(A) Representative IF images of AF647 labeled Tom20 in U2OS cells expressing WT or additional KRAS^{G12D} cultured for 24 hours under normoxic or moderately hypoxic conditions (20 % vs 3 % Oxygen). (B) Mitochondrial network connectivity analysis utilizing open-source MitoGraph network analysis across 50 FOVs per condition. (C) Schematic model of mitochondrial reorganization via hypoxic/ oncogenic stress, bubble size indicates more fused mitochondrial networks.

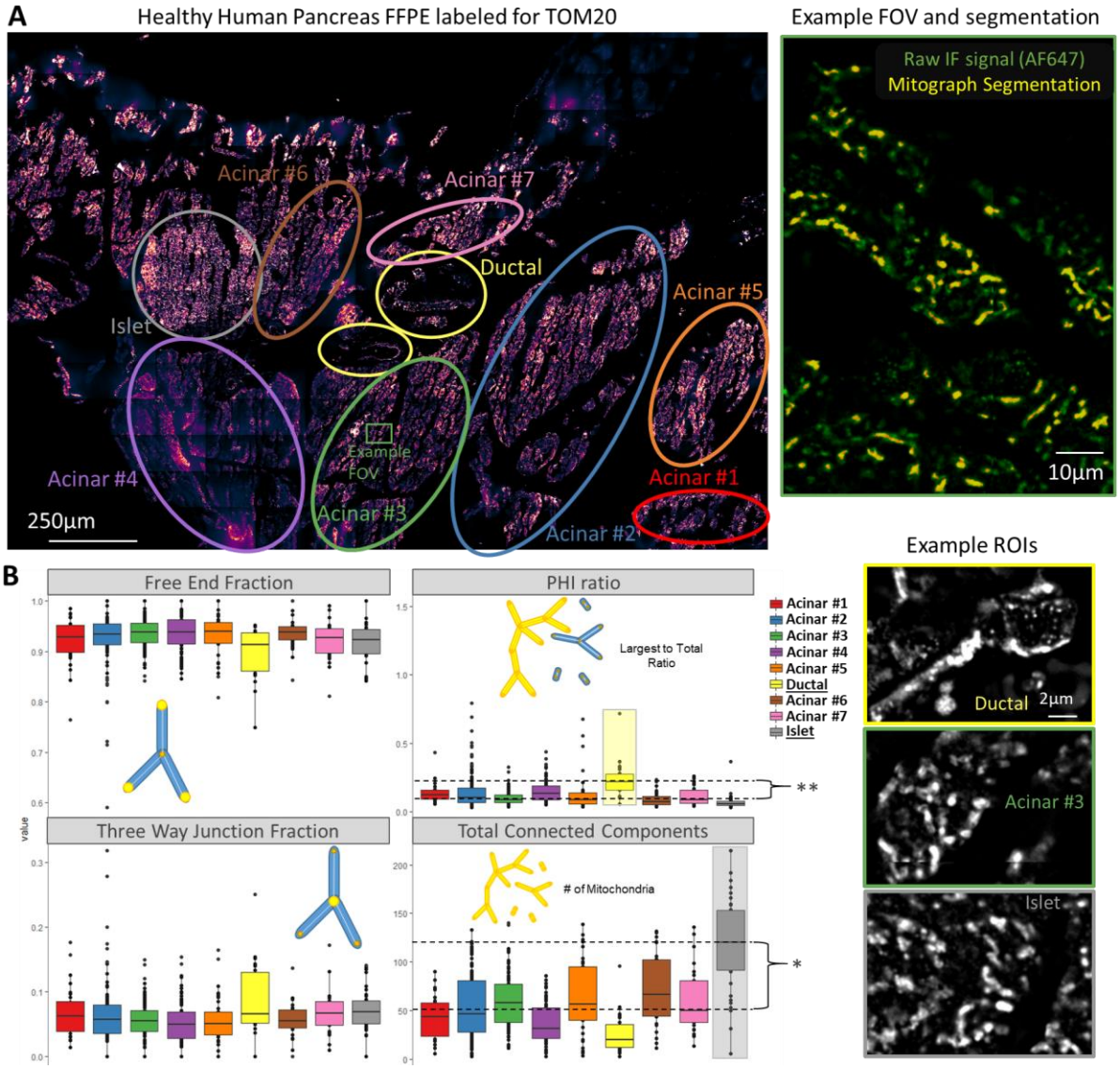

Figure 5.4 | Large-scale proof of concept analysis of mitochondrial networks from healthy pancreatic FFPE tissue.

(A) Immunofluorescent labeling of Tom20 via AF647 across 1.5 mm x 2 mm region taken via 40x magnification images and stitched with 10 um overlaps. Example boxed region from Acinar group #3 (green) shown with raw mitochondria signal (green) and Mitograph segmented mitochondrial networks (yellow). (B) Graphical visualization of mitochondrial network attributes as measured via Mitograph analysis. Plots generated via R with statistical significance calculated using Wilcox test. Scale bars are 250 µm and 10 µm (A, left and right respectively) and 2 µm for example ROIs in (B).

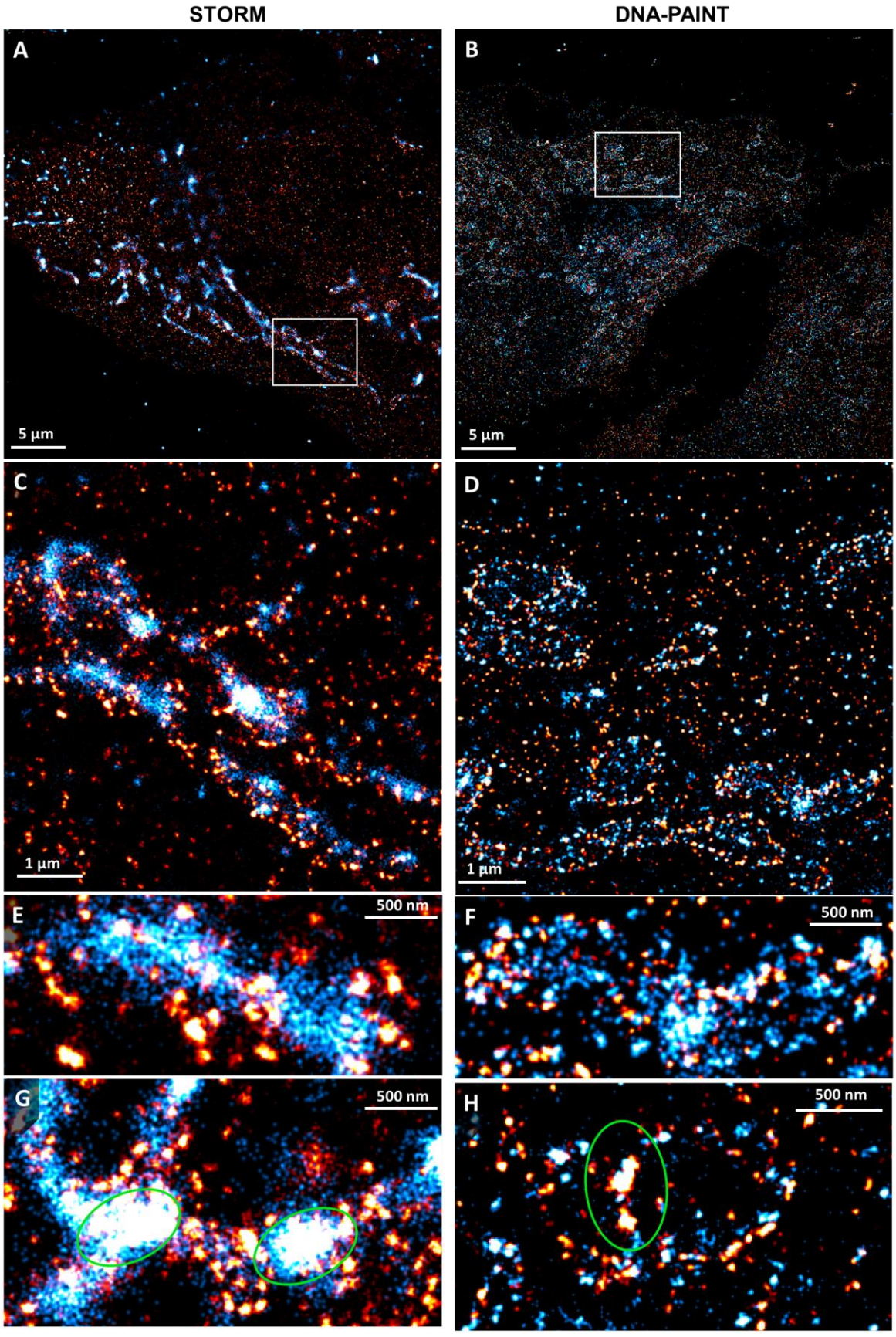
STORM
DNA-PAINT
A
5 µm
B
5 µm
C
1 µm
D
1 µm
E
500 nm
F
500 nm
G
500 nm
H
500 nm

Figure 5.5 | Comparison of Multi-color STORM vs Multi-target DNA-PAINT for mitochondrial dynamics protein complexes.

Qualitative assessment of 2 color STORM vs 2 target DNA-PAINT on mitochondria fission protein Drp1 (red) and mitochondria fusion protein Mfn1 (blue) in U2OS cells. (A) 40 um FOV of 2 adjacent cells imaged with AF647 and AF488 for Drp1 and Mfn1 respectively. (B) 40 um FOV of two adjacent cells images with DS2 and DS1 for Drp1 and Mfn1 respectively. (C) Magnified region from A highlighting dense labeling. (D) Magnified region from B with more uniformly resolved mitochondrial borders. (E & G) example magnified regions showing aggregations of Drp1 and Mfn1 along mitochondria. (F & H) example magnified regions showing similarly resolved Drp1 and Mfn1 complexes. Example punctate structures circled in green better resolved through DNA-PAINT. Both samples were prepared the same way except for utilizing STORM or DNA-PAINT secondary antibodies and respective STORM /DNA-PAINT imaging buffers. STORM images were acquired using 60,000 frames at 20 ms exposure first for AF647 then for AF488. DNA-PAINT images were acquired for 30,000 frames at 40 ms exposure using sequential 1 nM IS1-CF660R and 1 nM IS2-CF660R at 12.5 % EC. Scale bars are 5 µm in (A & B), 1 µm in (C & D), and 500 nm in (E-H).

Chapter VI: Conclusions and further directions toward new PAINT imaging modalities and multiplicity.

6.1 Conclusions

Advances in SRM and related applications have continued to grow over recent years. Coming-of age methods like DNA-PAINT are capitalizing on all of the foundations laid by complex photo physics from traditional STORM/PALM, ushering in improvements to multiplexing, throughput, and most importantly ease of use and reliability. These foundations coupled with ever-growing utilization and the expansion of commercial systems and analytics are poised to put SRM squarely in the hands of many more researchers. From humble beginnings in custom laboratory settings, methods such as LF-PAINT are poised to revolutionize the accessibility once thought limiting for SRM based studies.

The aim of this thesis was to demonstrate the roadmap to unlocking the immense potential of SRM to study complex biological systems. The overview of my central thesis includes: 1) improved DNA-PAINT imaging speed and FOVs, 2) automating next generation image analysis pipelines for SRM, 3) innovating integrated fluidics for tissue SRM imaging, and 4) proof of principle applications of SRM innovations to study mitochondrial dynamics in cancer. In chapters 2, the foundational capabilities in both accelerated imaging speed and FOVs were established. By redesigning DNA-PAINT sequences, conjugation, and buffers we demonstrated the utility of DNA-PAINT-ERS to improve DNA-PAINT imaging kinetics and even structural quality. By coupling the latest

FOV EMCCD cameras with a Prism TIRF microscope design, we could dramatically improve the area throughput in DNA-PAINT imaging, while integrated microfluidics enabled DNA-PAINT buffer exchange for multiple targets through the narrow imaging chamber. Automating these fluidics with multi-FOV acquisition schemes is poised to further accelerate large-scale imaging and later analytics for studying cellular biology across thousands of cells at nanometer resolutions. Collectively, this work demonstrated progress toward making SRM imaging scalable, as a model for others to adopt and collectively accelerate SRM research.

One of the major gaps in expanding SRM imaging capabilities, is how to handle and analyze the immense data it can generate. Unlike traditional SRM studies which may perform careful clustering analysis and spatial analytics over tens of cells and biological models, steps toward higher-order spatial characterization while at SRM level detail remain limited. In chapter 3, and in tandem with LF-PAINT microscope design, we developed semi-automated image analysis workflows which can be used to extract detailed measurements of subcellular nanosomic features across thousands of cells. Notably these pipelines can leverage existing open-source image analysis packages in a scalable and reproducible manner. We demonstrated that using WEKA machine learning classification plugins, we could train models which reliably distinguished SRM-level detail nanoscopic structures. Then by iterating these classification models across hundreds to thousands of cells, we could extract population level detail both within and between cells. Our pilot studied characterized over half a million distinct caveolae vesicles, and demonstrated proof of concept analysis of oncogenic effects on these 60-150 nm cellular features.

Despite the advancements in SRM imaging, tissue SRM has remained limited, with studies relying on low-throughput tissue STORM methods. In chapter 4, we innovated an entirely new imaging modality, which was crucial for tissue DNA-PAINT,

coined “Flow-Assisted DNA-PAINT”. Capitalizing on integrated microfluidics already useful for multiplexed DNA-PAINT buffer exchange via LF-PAINT, we demonstrated how mild-fluid flow can dramatically improve tissue DNA-PAINT imaging quality via enhanced on rates. We reasoned this dramatic improvement had to do with accessibility of the IS strand during imaging into the tissue section. Equipped with this new imaging strategy, we demonstrated the power of LF-PAINT to image PDAC ductal regions nearly a millimeter long, at 10 nm resolutions. This novel imaging strategy now poised to revolutionize clinical FFPE imaging by providing an unparalleled view directly into the molecular features and mechanisms in cancer biology.

Finally, and admittedly a foundational interest of mine in cancer biology, Chapter 5 takes a look into progress in understanding mitochondrial dynamics dysregulation in cancer. Long recognized in part by dramatic abnormalities in cellular metabolism, mitochondrial reprogramming, re-organization, and dysregulation are growing hallmarks underpinning not just cancer biology, but potentially early cancer biology as well. Motivated by increased interest in mitochondrial dynamics in pancreatic cancer aggressiveness and invasiveness we demonstrate the power of SRM to characterize the molecular mechanisms behind some known changes from literature. We demonstrated how high-throughput imaging and mitochondrial network analysis can infer mitochondrial differences within patient tissues, and how oncogenic and hypoxic signaling perturb mitochondrial organizations. Critically, coupled with advancements for DNA-PAINT-ERS and later LF-PAINT, we can now rebuild the mechanistic underpinnings of deregulated mitochondrial biology in early cancers. Overall, our work demonstrated the technique development, analytical pipelines, and even proof of concept biological systems which are ripe for expanded analysis via the power of SRM.

6.2 New frontiers in DNA-PAINT

On top of the variety of efforts to improve DNA-PAINT imaging, applications, and analytical pipelines, ongoing frontiers have unique potentials to further enhance the capabilities of SRM for early cancer biology. This section serves to highlight proof of concept research in a variety of exciting new frontiers: i) 3D DNA-PAINT imaging, ii) functionalizing small-molecules for DNA-PAINT iii) leveraging secondary nanobodies for enhanced multiplexity, and finally iv) PAINT-ing without DNA. Each sub-section demonstrates proof of principle research as the foundation for continued research in each of these directions.

6.2.1 Moving to the 3rd dimension, applications of DNA-PAINT in 3D SRM modalities.

Although this thesis has focused on 2D SRM, efforts for 3D SRM imaging were pioneered in tandem with 2D SRM imaging capabilities. As briefly introduced in chapter 1.2, 3D SRM imaging typically utilizes vertical perturbations in PSFs to encode height information into each SML event [30]. However, despite a variety of improved methods, these cannot match the lateral resolution which is often sub 20nm. A completely alternative strategy was developed for 3D SRM imaging which can push the vertical resolution below 20nm, relying on interfering with the single photon sources themselves. Interferometric PALM (iPALM), is a unique optical and microscope design which forces single point sources of photons from fluorescent events to interfere with themselves [126] (**Figure 6.1A**, left). The basic design features two matching objective both above and below the thinly sandwiched sample, while TIRF illumination is achieved through the bottom objective. Fundamentally, differing path lengths traveled due to small differences in SML event vertical position will either constructively or destructively interfere based on

their difference in phase. Critically, by using a custom 3-way beamsplitter, these two inputs will interfere on 1/3 phase periodicity spread across 3 cameras. Fitting the intensity of this single event across each camera by varying sample height can precisely reveal the vertical position down to 10nm or even lower (**Figure 6.1A, right**).

The flexibility of DNA-PAINT imaging means we could leverage existing DNA-PAINT-ERS antibodies or even small-molecule conjugations to image with the iPALM system. As initial proof of concept we demonstrate imaging of dense actin cyctoskeleton with a DS-phalloidin conjugate (**Figure 6.1B**), achieving lateral localizations around 12 nm and axial resolution at 8 nm. Example raw 3-camera image reveals how localizations exhibit differing intensity across the 3 cameras (**Figure 6.1C**), notably the red camera was slightly misaligned from the others meaning those matching red camera localizations appear above the blue and green. Given sufficient initial alignment and interference, small misalignments in individual camera positions can be corrected for using PeakSelector software [126], which was used to align and render these iPALM images. As further evidence of iPALM DNA-PAINT capabilities we imaged caveolae vesicles using labeling optimized within chapter 2. Here you can see a variety of vesicle sizes and vertical positions near the membrane surface of a U2OS cell (**Figure 6.2A**). Unlike with imaging in earlier chapters, here can see individual caveolae vesicles and how their oval shapes extend vertically (**Figure 6.2B**). Intriguingly, the vesicle on the right may exhibit both a narrow shape ~75nm position and a wider circular shape ~150-300nm, implicating it might be the “flask” shaped internalization as often seen from TEM studies [127]. These iPALM DNA-PAINT images reveal an exciting new direction for 3D SRM, and with ongoing design efforts for mutli-color or exchange-PAINT based approaches iPALM DNA-PAINT could leverage all the multiplexed advances DNA-PAINT offers as well.

6.2.2 Leveraging Small-molecules for DNA-PAINT, developing stable SRM imaging of Actin

Actin plays a vital role in a huge variety of cellular processes including mitochondrial dynamics [122], making studies into its form and function enticing targets for many microscopists and importantly SRM imaging. Despite the myriad of engineered affinity reagents, the small and tight packed nature of the actin filament has proved challenging to label, which is why we still can't beat mother nature's specificity and affinity from the small molecule mushroom toxin Phalloidin. Phalloidin and fluorophore conjugates have been commonly imaged with STORM [30], often used to exemplify both 2D and even 3D imaging quality. Unfortunately despite the initial high quality of these images, phalloidin suffers a known problem of dissociation overt time even with newer commercial products [128], making multiplexed and reproducible imaging with actin an ongoing challenge. Indeed, even when using a DS-phalloidin conjugate for DNA-PAINT based imaging of actin, we see that although dense structures of actin are clearly visible the cortical actin is sparsely labeled (**Figure 6.3A**). To alleviate this and stabilize actin DNA-PAINT imaging we developed an amine modified phalloidin-DS conjugate which could be postfixed. This modification enables DNA-PAINT imaging of actin to not dissociate over time, and also preserves fine cortical actin structures (**Figure 6.3B**). Schematic of this strategy can be seen in **Figure 6.3C**.

An important output of this modification is not only the stability and reproducibility of actin imaging by DNA-PAINT, but importantly the ability to perform high-quality multiplexed imaging of actin and other cellular targets. As proof of concept for this, we paired our actin-DS conjugate with existing DS1 and DS2 antibodies targeting both caveolae and microtubules (**Figure 6.4**). These resulting multiplexed images demonstrate preserved high-quality actin imaging along with other targets through

exchange-PAINT on Cos7 cells, with magnified and representative FOVs. Importantly, when paired with ongoing efforts toward scalable imaging and analysis outlined in chapters 2 and 3, mechanistic studies of fine molecular interactions of various proteins with actin are now feasible. Pairing with ongoing efforts for 3D iPALM imaging, our custom DS-amine-phalloidin conjugate could unravel complex structures involving actin in 3D, such as mitochondrial fission and ER complexes [122].

6.2.3 Unlocking Species limitations, Secondary Nanobodies for DNA-PAINT

Throughout this thesis antibody labeling of targets for DNA-PAINT was performed via primary antibodies and matching secondary DS-conjugated antibodies. As is common when using multiplexed antibody labels, care had to be taken to ensure species cross-reactivity or redundancies were prevented. For example, predominately Donkey secondary antibodies against respective primary antibodies species ensured minimal cross-reactivity, but this comes at the cost of antibody species availability and important upward bounds on multiplexity cause by antibodies. Unlike other SRM imaging modalities like STORM which are limited by spectral differences in fluorophores, the versatility of exchange-PAINT means species limitations are a more pressing boundary for feasible multiplexity. Commercial secondary nanobodies (NBs^{2nd}) are an emerging area of development [129], to facilitate stable multiplexed immunolabeling strategies, however the addition of long DS-oligomers can limit these approaches. When using multi-round or even co-incubation of premixed primary and NBs^{2nd}, a portion of these NBs^{2nd} could either fall off or inadvertently “hop” from one primary target antibody to a different one (**Figure 6.5A,B**). As an alternative strategy for stable NBs^{2nd} we developed a bivalent NBs^{2nd} utilizing the DS-oligomer as the tether between the identical NBs^{2nd}

(**Figure 6.5C**). We hypothesized that the bivalent nature of this new engineered NBs^{2nd} may provide a stable method to improve multiplexed DNA-based imaging.

As evidenced from initial IF-style imaging, we confirmed that off-target labeling as a byproduct of hopping can occur using monovalent-DS nanobodies (mono-NBs^{2nd}), while bivalent-DS nanobodies (Bi-NBs^{2nd}) retained their specific pre-mixed primary antibody target labeling (**Figure 6.5D**). To help visualize and ultimately quantify the degree of off-target hopping we performed DNA-PAINT imaging of both nanobody types labeled at either room temperature or overnight at 4°C (**Figure 6.5E**). As expected from hopping observed in IF imaging, DNA-PAINT images do show off-target labeling and subsequent imaging and reconstruction of diffuse microtubules when imaging with IS1 and dim clatherin structures when imaging with IS2. Through selecting 30 target-specific ROIs from each condition and measuring the normalized relative intensity, we demonstrated that the degree of hopping is ~10-20% depending on the labeling temperature for mono-NBs^{2nd}, while Bi-NBs^{2nd} are highly specific and shared off-target background signal of <1% normalized intensity. This helps demonstrate not only distinct multiplexed imaging, but the potential to quantitatively confirm labeling in-vivo.

As further proof of principle we demonstrate the flexibility of the Bi-NBs^{2nd} for both IF and DNA-PAINT style imaging of 4 rabbit primary antibodies (**Figure 6.6A,D**). Notably, longer complimentary IS sequences (~14 bp) can stably bind and provide clear IF style imaging, and yet can be washed away with EC (data not shown), opening the possibility of these same constructs for cycIF-style imaging. Representative of this, we imaged Clatherin, Microtubules, Lamin B1, and Tom20 all via rabbit primary antibodies pre-mixed with respective DS Bi-NBs^{2nd} (**Figure 6.6B**). The incubation and washing time between targets could be as short as ~5 minutes, meaning after careful pre-incubation and labeling of a larger panel of antibody/ Bi-NBs^{2nd} pairs cycIF imaging through this method could be performed in hours as opposed to many days for traditional cycIF

cycles. To demonstrate clinical utility, the same Bi-NBs^{2nd} against 3 prognostic markers for a PDAC cancer patient were used similarly to obtain cycIF composite images from clinical FFPE tissue sections (**Figure 6.6C**). Composite and zoom-in views reveal activated fibroblasts via α-SMA, as well as tumor cells themselves with high LaminB1 and pan-cytokeratin staining. Finally, to demonstrate similar multiplexity via DNA-PAINT, we obtained SRM images of the same 4 targets using shorter IS matching each respective target via exchange-PAINT based cycles (**Figure 6.6E**). These improvements to multiplexity are fully compatible with imaging optimizations in chapters 2-4, as well as helping to unravel cancer biology questions which were previously challenging via antibody species limitations such as mitochondrial dynamics proteins in chapter 5.

6.2.4 PAINT-ing without DNA: The potential for engineering affinity reagents for “Scarless PAINT”

PAINT in theory could generate SRM images from a variety of transient binding events, not just DNA, making innovations in other strategies for PAINT an exciting prospect. Indeed, PAINT has been demonstrated on transient binding of peptides pairs [130] and fluorogenic dyes [131] for example. These strategies still rely on either targeted genetic conjugation (peptide PAINT) or the unique but still non-specific properties of broad structures like membranes to generate high-quality images. Ultimately though, any PAINT strategy can work, as long as the affinity reagent used is highly specific, but exhibits transient affinity. A pilot strategy also being developed can modify existing high-affinity reagents into low-affinity binders, enabling potentially transient but highly specific binding. Such a strategy would not require any initial sample modification, just a highly engineered affinity reagent, but would result in a so-called “scarless PAINT” image.

To test this hypothesis, we began using engineered nanobodies which target GFP, and could demonstrate high-quality STORM imaging with commercially available high-affinity versions (**Figure 6.7A**). Notably these work as GFP genetically encoded onto microtubules are labeled with nanobodies and post-fixed prior to imaging. The alternative strategy would be to design a nanobody which specifically, but transiently, binds to GFP on the time-scales necessary for PAINT (**Figure 6.7B**), as is abundantly demonstrated using DNA-conjugates throughout this thesis. While commercial GFP-nanobodies have near nanomolar affinities, this means they are quite stable for methods such as STORM, relying on full binding prior to imaging. As proof of concept for scarless PAINT, we utilized lower affinity GFP nanobodies Lag42 and Lag29, which have affinities ~600 nM and 110 nM respectively. When added into solution identically to imaging strand DNA-conjugates, we demonstrate reconstructed images of target GFP microtubules at differing probe nanobody concentrations (**Figure 6.8**). Intriguingly both constructs demonstrate feasible PAINT imaging, exemplifying that engineered affinity reagents around 100-600 nM affinity might be imaged against other targets. In theory, this strategy could be developed against any protein/molecular target, given that it is sufficiently specific and exhibits transient affinity necessary to separate distinct localizations.

6.3 Future Directions

The new frontiers just outlined in 6.2 demonstrate the novel directions which can further improve SRM imaging dimensionality, labeling, multiplexity, and even fundamental dynamic imaging strategies. Importantly, these are poised to augment ongoing projects, and open the possibilities for new ones as well. In the context of early RAS signaling biology, the improvements in both 3D imaging, actin imaging, and

multiplexity via Bi-NBs^{2nd} could enable more complete imaging and ultimately quantification of the signaling complex used when under early oncogenic stress in cancer progression. Mitochondrial dynamics are also quickly able to capitalize on these same improvements, as imaging of the complex interplay between actin, ER folds, and mitochondrial fission proteins like Drp1, Fis1, and mid49 could better understand both normal and hypoxic-perturbed functions of these inherently large and dynamic 3D complexes. Extending to patients, clinical interpretation of both early and treatment outcomes in PDAC could capitalize on the multiplexity and improved FOVs from LF-PAINT. Ongoing efforts to obtain larger cohorts of PanINs and early PDAC would be able to truly address the underlying biology posed in chapter 5. Similarly, expansion of the patients and DDR proteins initially quantified in chapter 3 are poised to provide a more powerful glimpse into the deregulation and patient specific targeted therapy response of PARP inhibitors on DDR, highlighting a concerted effort to understand molecular-level differences directly from patient tumors. Armed with these strategies and more currently under development, we are now abundantly equipped to answer broad questions behind molecular level differences in early cancer model systems and importantly directly from patient biopsies as well.

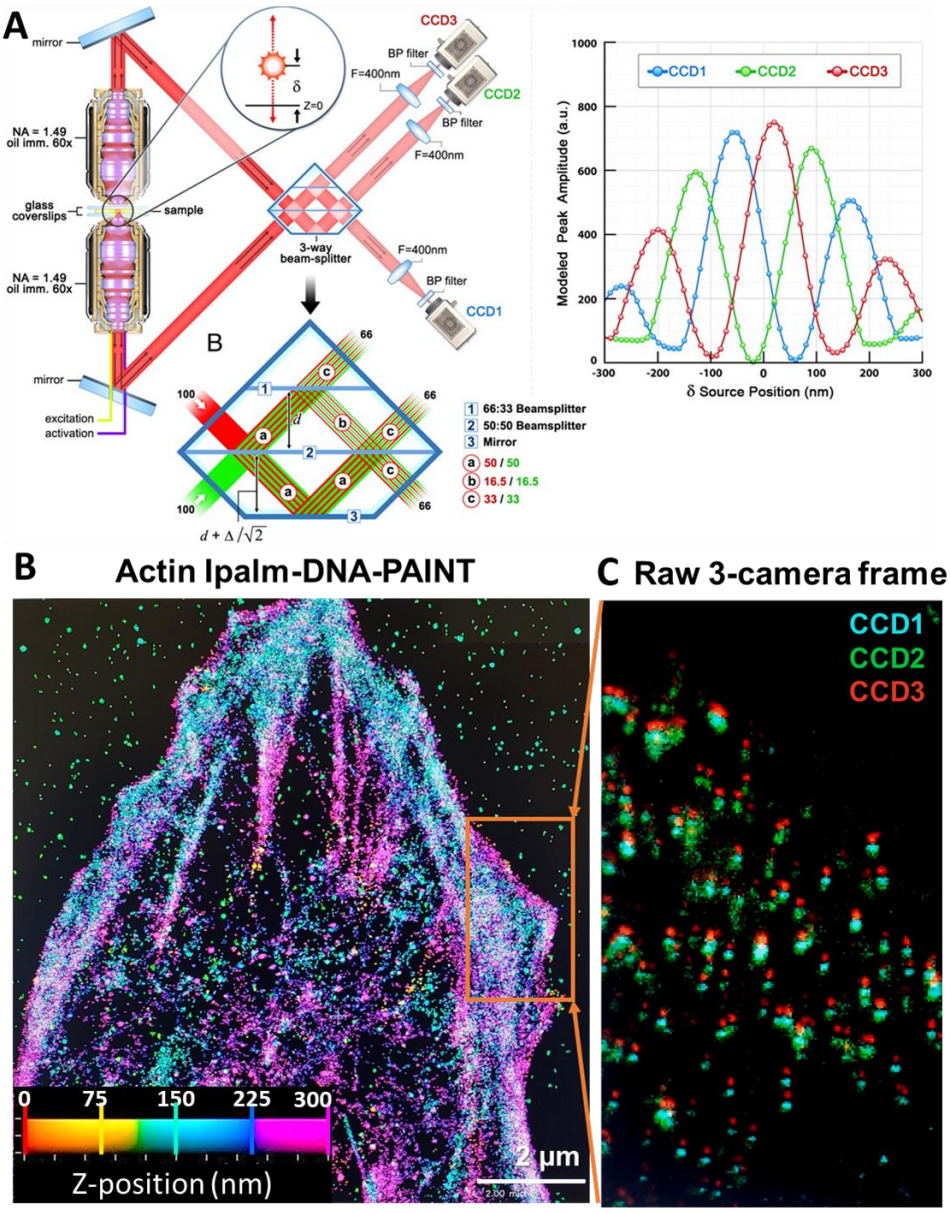

Figure 6.1 | iPALM DNA-PAINT principles and example images

(A) Schematic of iPALM microscope design, leveraging dual-objective interference across 3 cameras for extremely high axial resolution. (B) Proof of concept iPALM DNA-PAINT image of Actin, shown with localizations with 12 nm lateral resolution and 8 nm axial resolution. (C) Example raw unaligned frame from each camera, demonstrating the variable intensity per DNA_PAINT localization according to Z-height. (A) Reproduced from [126].

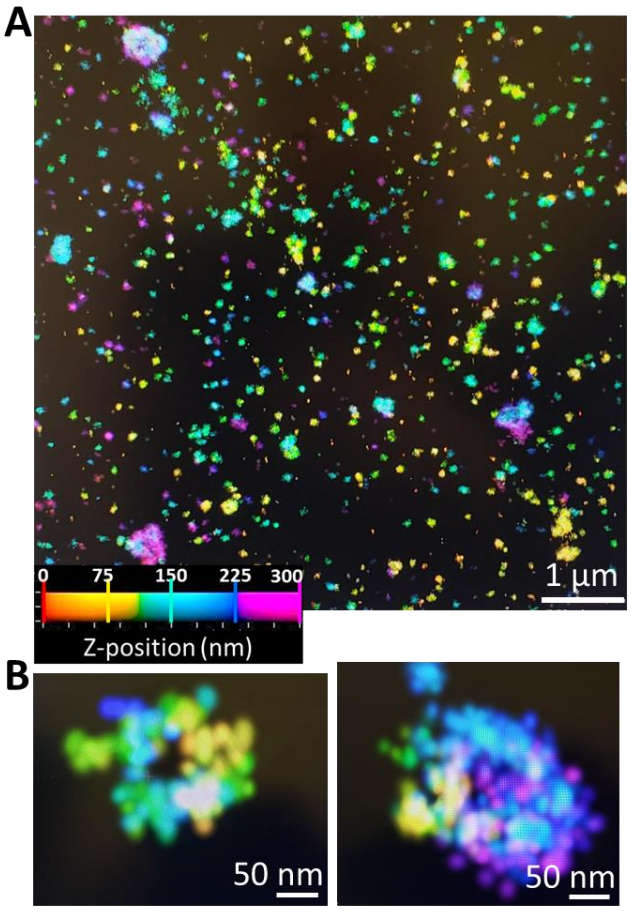

Figure 6.2 | iPALM DNA-PAINT of Caveolae Vesicles

(A) Flat bottom membrane of a U2OS cell with various caveolae vesicles at differing heights via internalization. (B) Example individual caveolae vesicles with varied potentially rounded or flask shaped structures. DNA-PAINT iPALM images shown acquired for 50,000 frames at 30 ms exposure using 2nm IS2-Atto643 at 12.5 % EC.

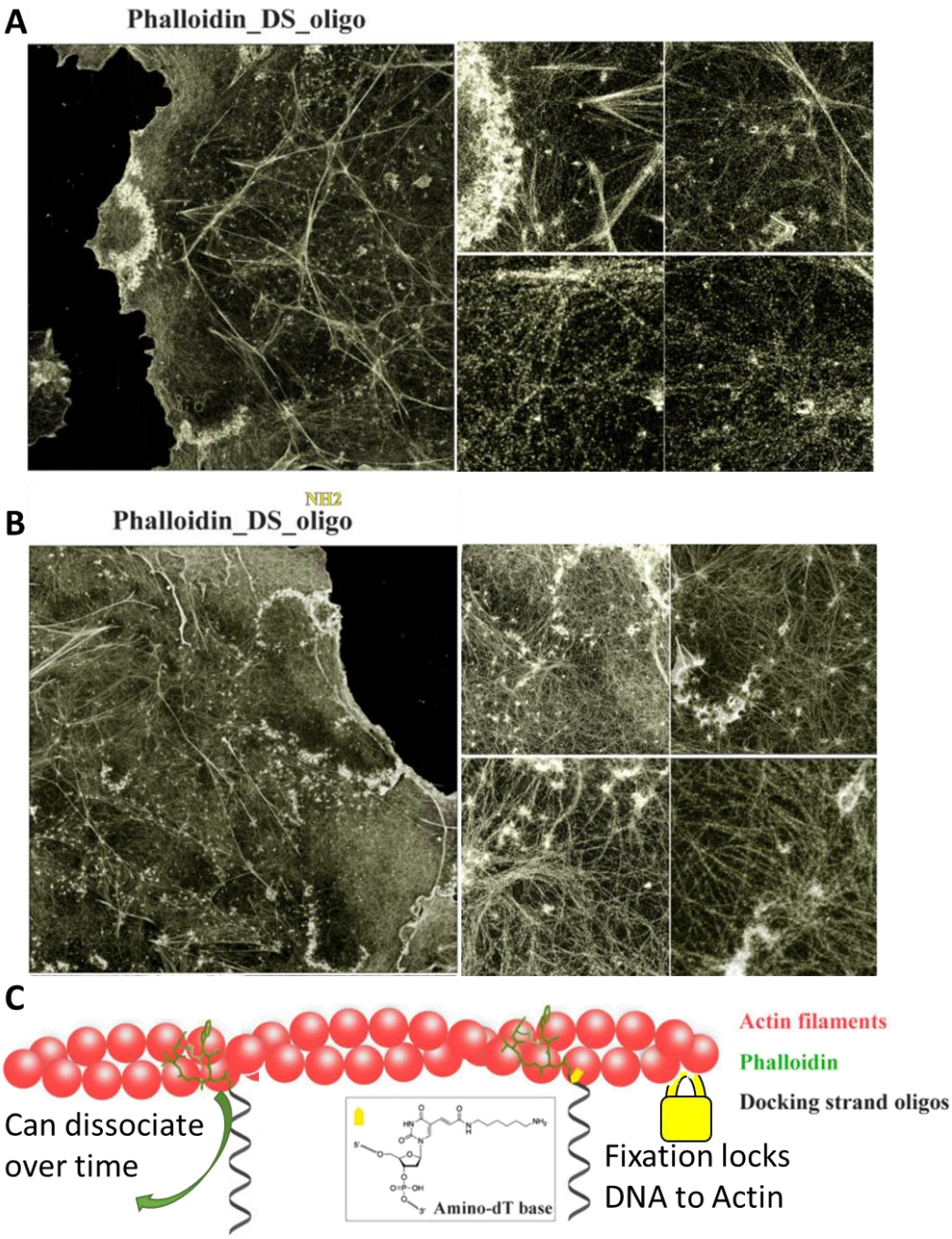

Figure 6.3 | Stabilizing Phalloidin for robust DNA-PAINT imaging of actin. (A) Representative DNA_PAINT images obtained with a traditional Phalloidin-DS conjugated small molecule, notably magnified views highlight sparse labeling. (B) Representative DNA_PAINT images of integrated amino Phalloidin-DS small molecule, notably magnified views preserve fine details in actin cytoskeleton. (C) Schematic of the labeling strategy where actin filaments (red) have reversible binding via Phalloidin (green). Conversely, DS-amino-Phalloidin can be cross-linked via post-fixation to preserve highly specific Phalloidin labeling.

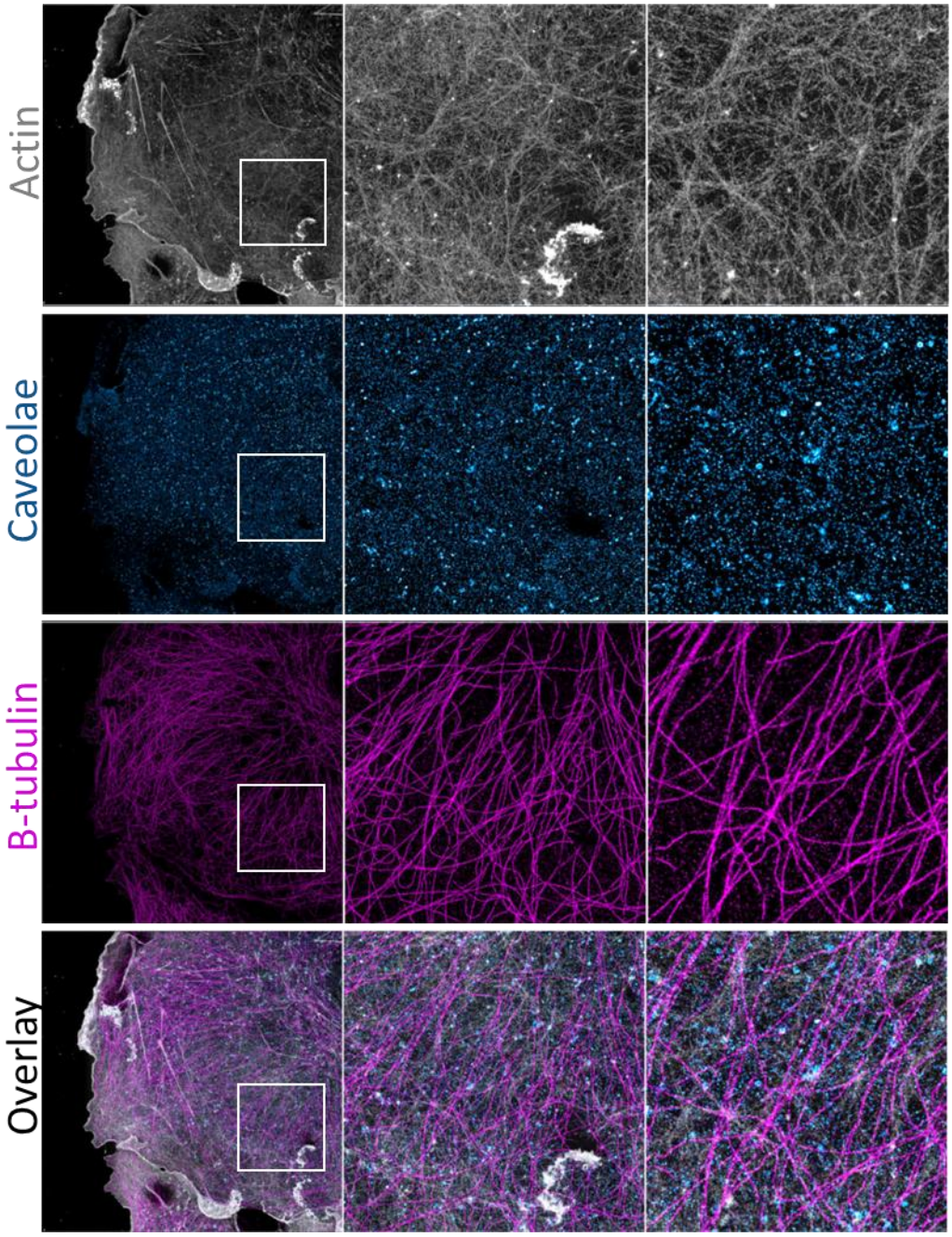

Figure 6.4 | Multiplexed Actin DNA-PAINT imaging.
Representative DNA-PAINT exchange-paint images in a Cos7 cell of actin (grey) Caveolae (blue) and B-tubulin (magenta). Resulting overlay image highlights fine detail in cortical actin cytoskeleton with both larger microtubule cytoskeletons and membrane trafficking via Caveolae endocytosis. DNA-PAINT images were acquired for 200,000, x0,000 and x0,000 frames at 30 ms exposure using cycles of IS6, IS2, and IS1 for Actin, Caveolae, and B-tubulin respectively. Scale bars are xx µm for the full FOV and xx µm for magnified regions.

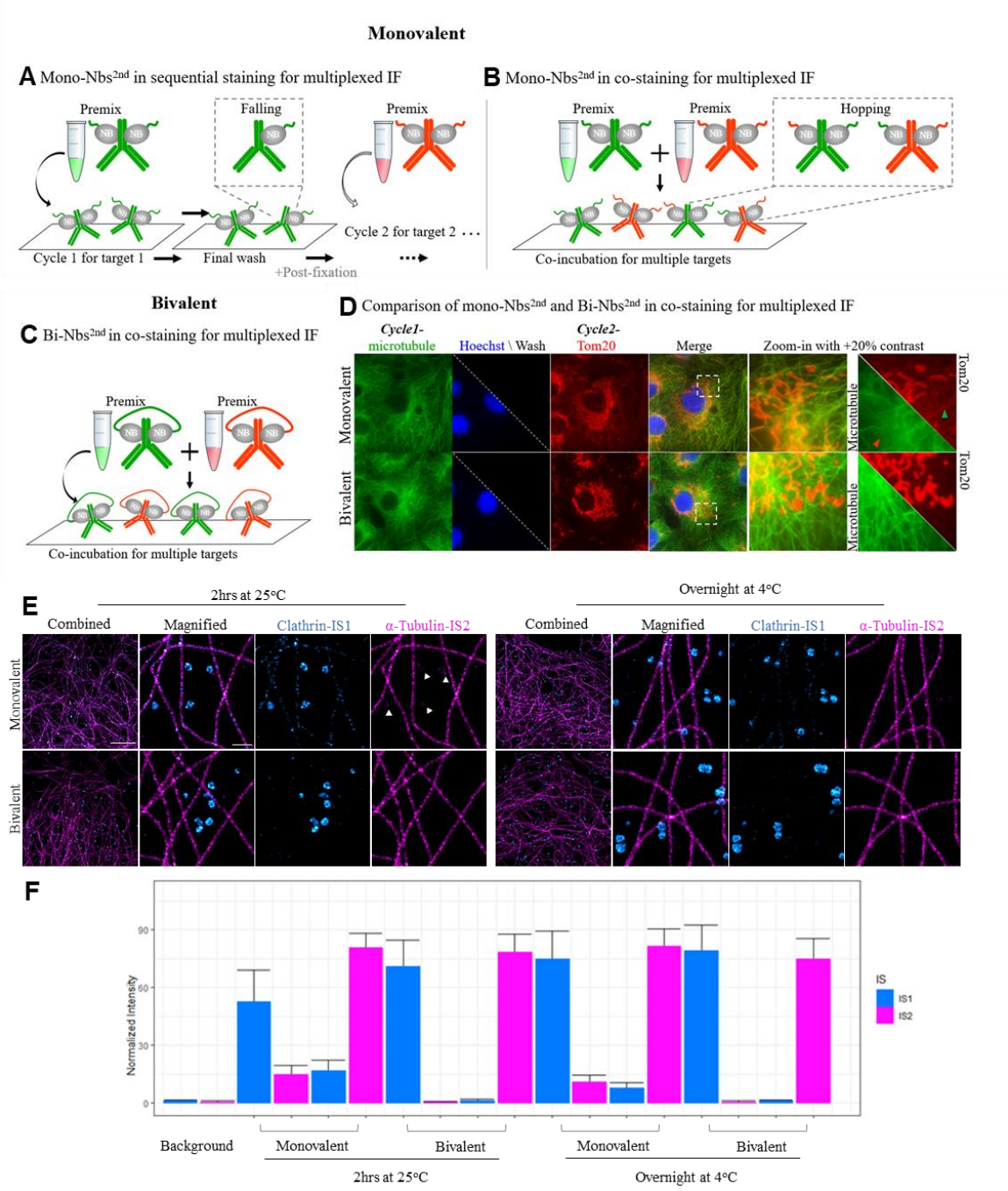
Monovalent
A Mono-Nbs2nd in sequential staining for multiplexed IF
Premix
Falling
Premix
Cycle 2 for target 2 ...
Cycle 1 for target 1
Final wash
+Post-fixation
B Mono-Nbs2nd in co-staining for multiplexed IF
Premix
Premix
Hopping
Co-incubation for multiple targets
Bivalent
C Bi-Nbs2nd in co-staining for multiplexed IF
Premix
Premix
Co-incubation for multiple targets
D Comparison of mono-Nbs2nd and Bi-Nbs2nd in co-staining for multiplexed IF
Cycle1- microtubule
Hoechst \ Wash
Cycle2- Tom20
Merge
Zoom-in with +20% contrast
Monovalent
Bivalent
Microtubule
Tom20
E
2hrs at 25°C
Overnight at 4°C
Combined
Magnified
Clathrin-IS1
α-Tubulin-IS2
Monovalent
Bivalent
F
Normalized Intensity
90
60
30
0
IS
IS1
IS2
Background
Monovalent
Bivalent
Monovalent
Bivalent
2hrs at 25°C
Overnight at 4°C

Figure 6.5 | Monovalent vs bivalent DS secondary nanobodies on rabbit primary antibodies

Schematic of monovalent mono-NBs^{2nd} by: (A) multi-round and (B) co-incubation, which may exhibit unbinding/hopping, during either labeling/washing with different mono-NBs^{2nd}. (C) Bi-NBs^{2nd} which when pre-mixed would stay on their respective primary antibodies. (D) IF style comparison of both mono-NBs^{2nd} and Bi -NBs^{2nd}, monovalent forms exhibiting cross-labeling indicating mono-NBs^{2nd} undergo hopping during sample incubation. (E) DNA-PAINT imaging of both mono-NBs^{2nd} and Bi-NBs^{2nd} from both room temperature (25°C) and overnight 4°C labeling. Clatherin primary rabbit antibody premixed with (Mono or Bi)-NBs^{2nd} (DS1) and alpha-tubulin rabbit primary antibody premixed with (Mono or Bi)-NBs^{2nd} (DS2), for DNA-PAINT imaging using IS1 and IS2 on complimentary DS oligos. (F) DNA-PAINT quantification of normalized on-target vs off-target signal by both IS1 and IS2. Each bar-plot generated from 30 representative ROI selected for each structure and measured from both IS1 and IS2 PAINT reconstructions. Scale bars for (E) combined views scale bar is 5 µm, magnified views are 500 nm.

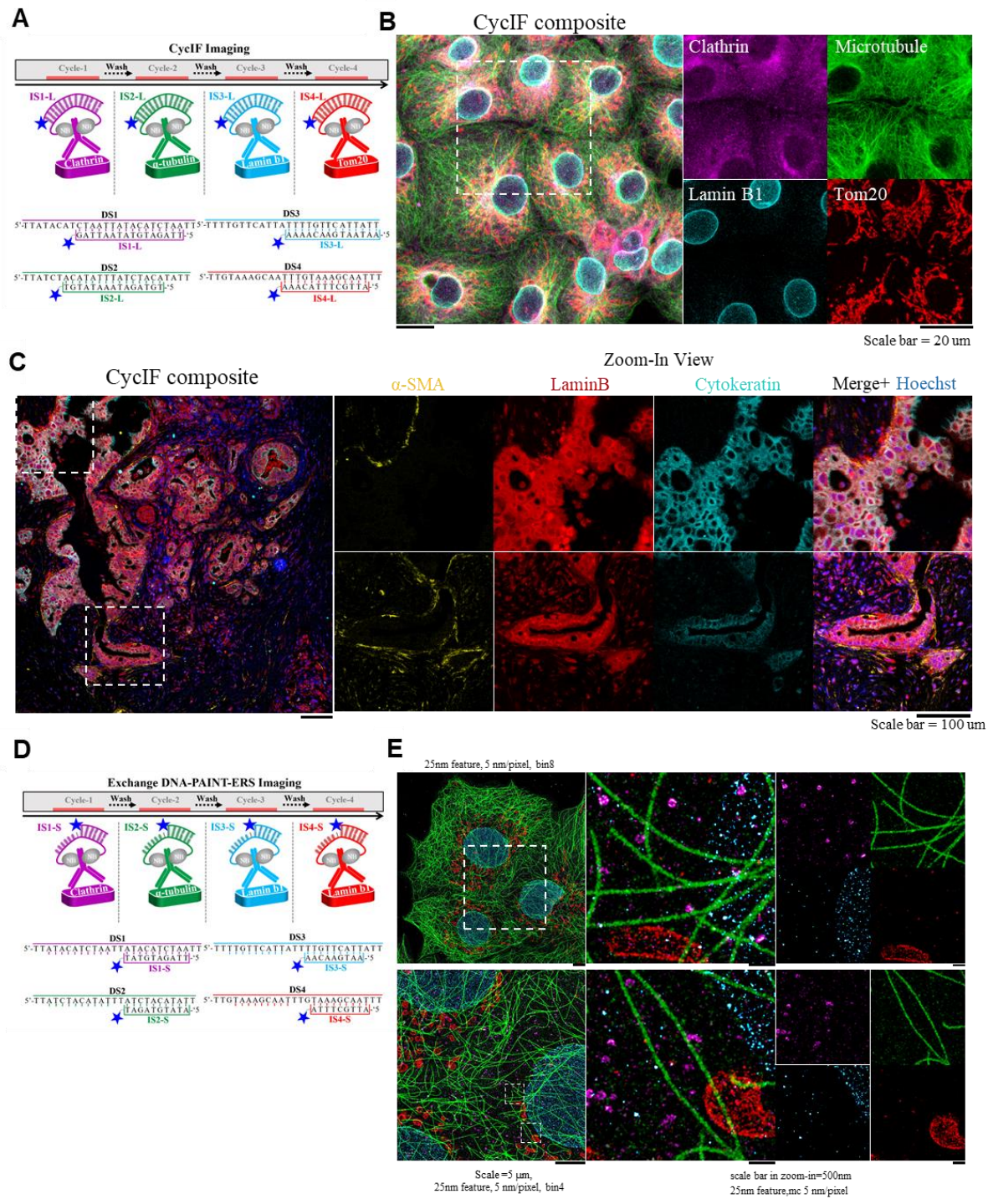
A
CycIF Imaging
Cycle-1
Wash
Cycle-2
Wash
Cycle-3
Wash
Cycle-4
IS1-L
IS2-L
IS3-L
IS4-L
Clathrin
α-tubulin
Lamin B1
Tom20
DS1
DS2
DS3
DS4
B
CycIF composite
Clathrin
Microtubule
Lamin B1
Tom20
Scale bar = 20 um
C
CycIF composite
Zoom-In View
α-SMA
LaminB
Cytokeratin
Merge+ Hoechst
Scale bar = 100 um
D
Exchange DNA-PAINT-ERS Imaging
IS1-S
IS2-S
IS3-S
IS4-S
E
25nm feature, 5 nm/pixel, bin8
Scale =5 μm,
25nm feature, 5 nm/pixel, bin4
scale bar in zoom-in=500nm
25nm feature,mc 5 nm/pixel

Figure 6.6 | Multiplexed cycIF and exchange PAINT imaging via bivalent DS secondary nanobodies

(A) Schematic of longer DS-IS oligomer pairs for stable, yet washable, multi-round cycIF-style imaging. (B) Composite cycIF-style image of cos7 cells co-labeled with Bi-NBs^{2nd} preincubated with: Clatherin (purple), Microtubule (green), LaminB1 (cyan) and Tom20 (red) rabbit primary antibodies. Split view shows retained specific labeling despite 4 rabbit primary antibodies used. (C) CycIF style imaging performed on a PDAC FFPE tissue section. Cycles for α-SMA, LaminB1 and pan-cytokeratin show prognostic labeling within the larger ductal adenocarcinoma and adjacent tumor microenvironment. (D) (A) Schematic of shorter DS-IS oligomer pairs for transient DNA-PAINT style cycles via exchange-PAINT. (E) Representative 4-target DNA-PAINT imaging of Clatherin (purple), Microtubule (green), LaminB1 (cyan) and Tom20 (red) rabbit primary antibodies exemplify preserved high-quality on target labeling despite the same primary species. Scale bars shown as indicated.

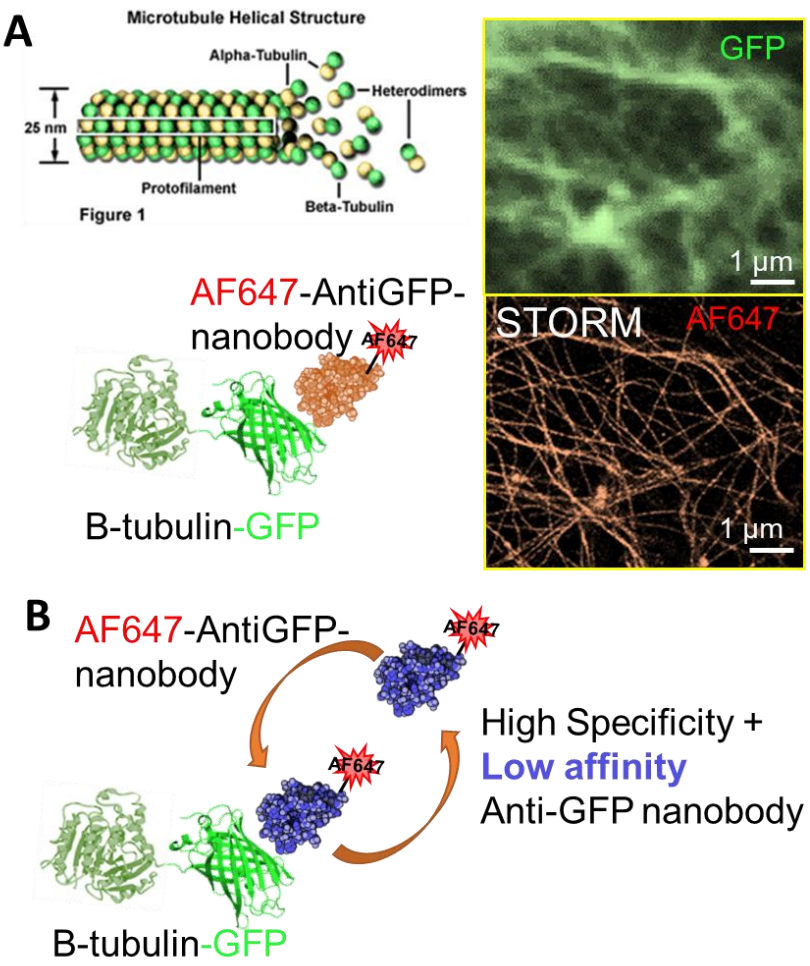

Figure 6.7 | Principle of "Scarless PAINT"

(A) Representative strategy for imaging microtubules via GFP-tagging on B-tubulin and secondary anti-GFP-AF647 labeling. GFP image and example STORM reconstruction using labeled AF647 anti-GFP nanobodies. (B) principle of Scarless PAINT, and representative model system, utilizing high specificity and low-affinity reagents to dynamically observe transient binding.

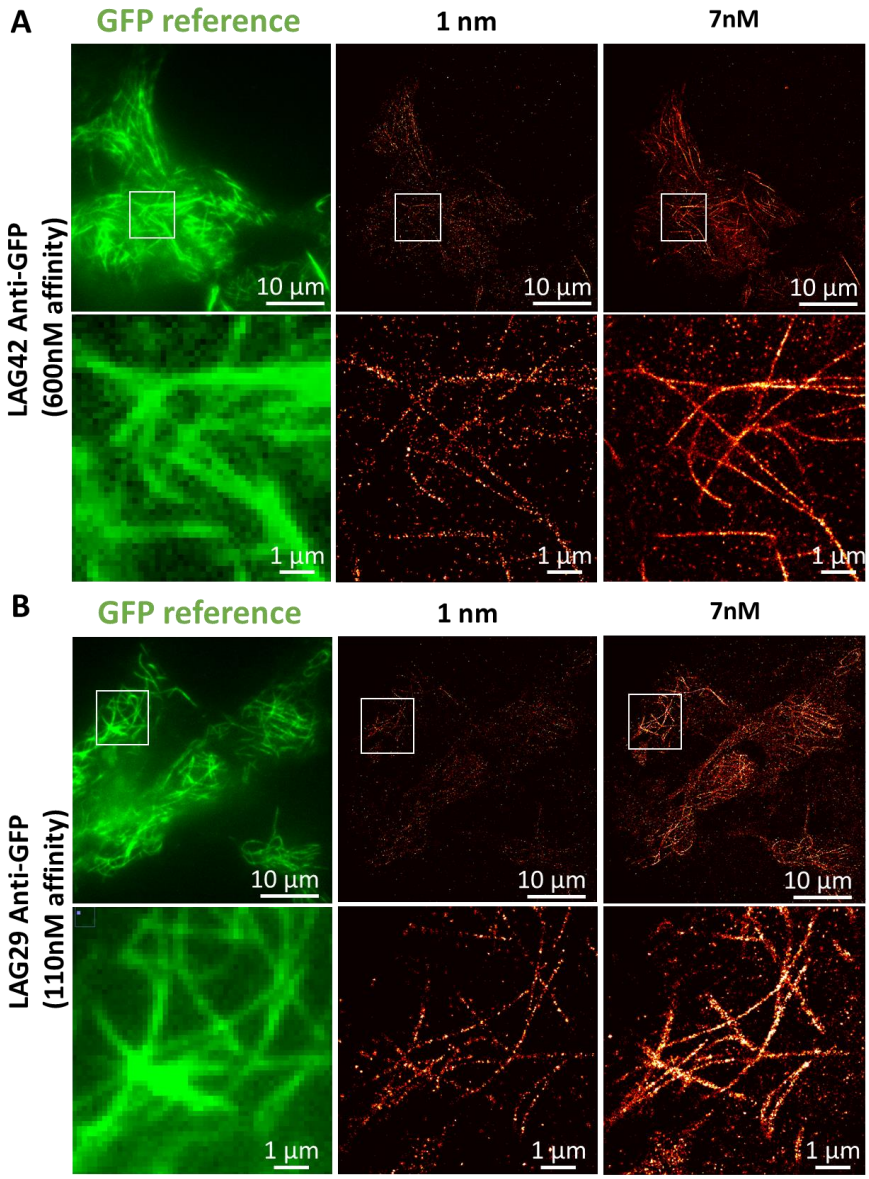

Figure 6.8 | Proof of principle Scarless PAINT

(A) GFP reference and 2 different concentrations of LAG42-AF647 anti-GFP nanobody PAINT (600 nM affinity), with matching magnified views. PAINT images acquired in 1% 0.5% BSA in PBS(-) solution for 10,000 frames at 100 ms exposures. (B) (A) GFP reference and 2 different concentrations of LAG42-AF647 anti-GFP nanobody PAINT (110 nM affinity), with matching magnified views. PAINT images acquired in 1% 0.5% BSA in PBS(-) solution for 10,000 frames at 100 ms exposures. Scale bars are 10 µm for the full FOVs and 1 µm for magnified FOVs.

Appendix A: Supplementary Figures

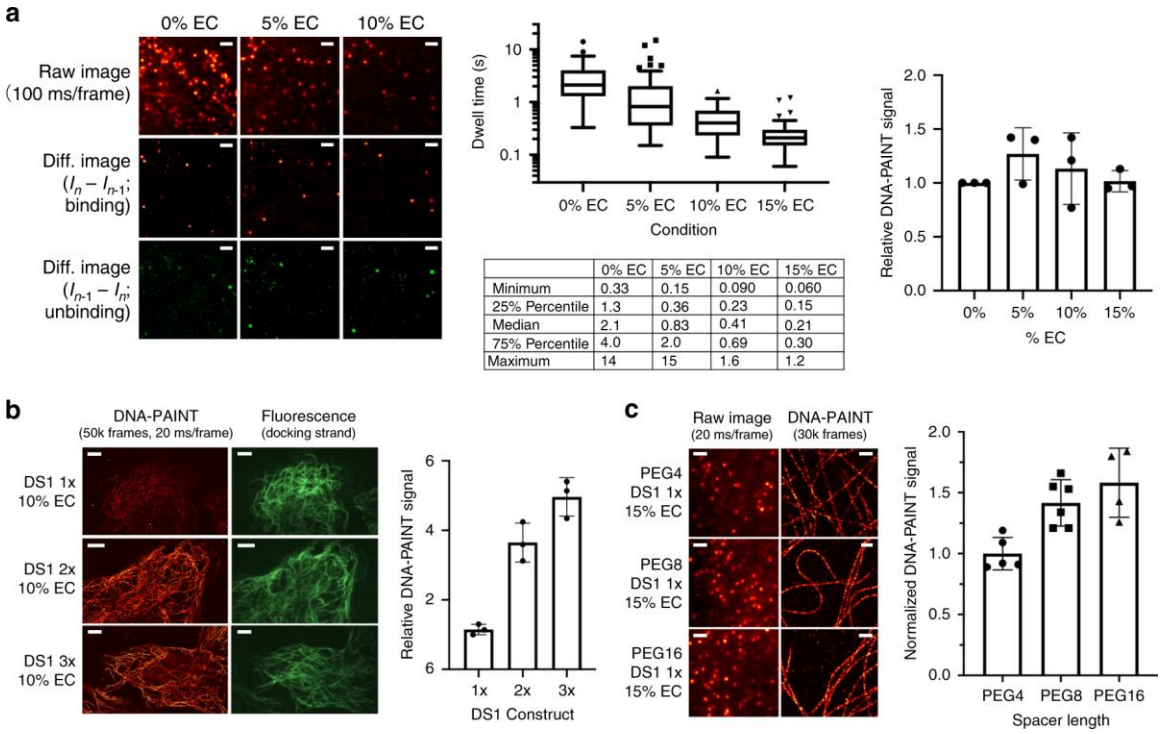

	0% EC	5% EC	10% EC	15% EC
Minimum	0.33	0.15	0.090	0.060
25% Percentile	1.3	0.36	0.23	0.15
Median	2.1	0.83	0.41	0.21
75% Percentile	4.0	2.0	0.69	0.30
Maximum	14	15	1.6	1.2

Figure A 2.1 | Accelerating DNA-PAINT with E, R, and S.

(A) EC accelerates DS-IS unbinding. First panel, single-molecule images of the same sample region at different EC concentrations (top) and the corresponding difference images for binding (the current frame minus the preceding frame; middle) and the reverse (unbinding; bottom). Middle panel shows dwell time (τon; plot at the top and key statistics at the bottom) at different EC%. Right panel shows the sorted number of localizations normalized to that at 0% EC. Images were acquired on U2OS cells labeled for microtubules using 0.25 nM IS1-CF660R at a low power density (~100 W cm−2) to minimize photobleaching. Three regions from two independent samples were analyzed at each EC concentration. (B) Sequence repeats speed up DS-IS hybridization. Left, exemplary images of microtubules in U2OS cells using DS1 with 1x (top), 2x (middle), and 3x (bottom) repeats, showing reconstructed DNA-PAINT images (left column) and epi-fluorescence images of Cy3-DS1 (right column). Right, DNA-PAINT signal normalized to the corresponding DS signal, at 1.1 ± 0.1, 3.7 ± 0.6, and 5.0 ± 0.6 (mean ± SD) for DS1 1x, 2x, and 3x, respectively. DNA-PAINT images were acquired in ~17 min (50,000 frames at 20 ms per frame) using 0.2 nM IS1-CF660R and 10% EC. Results from three experiments were analyzed. (C) Spacer between DS and antibody improves IS-DS binding. Left panel, example single-molecule images (left) and reconstructed DNA-PAINT images (right) of microtubules in U2OS cells using DS1-antibody conjugates with a PEG4 (top), a PEG8 (middle), or a PEG16 (bottom) spacer. Images were acquired in 10 min (30,000 frames at 20 ms per frame) using 2 nM IS1-CF660R and 15% EC. Right panel, total DNA-PAINT signals normalized to that using DS1-PEG4-antibody, showing 1.0 ± 0.1, 1.4 ± 0.2, and 1.6 ± 0.3 (mean ± SD) for PEG4, PEG8, and PEG16, respectively. Four to six regions of interest from two independent experiments were sampled for each spacer length. All error bars are SD. Scale bars are 2 μm in (a), 5 μm in (b), 2 μm in (c, left panel, left column), and 500 nm in (c, left panel, right column).

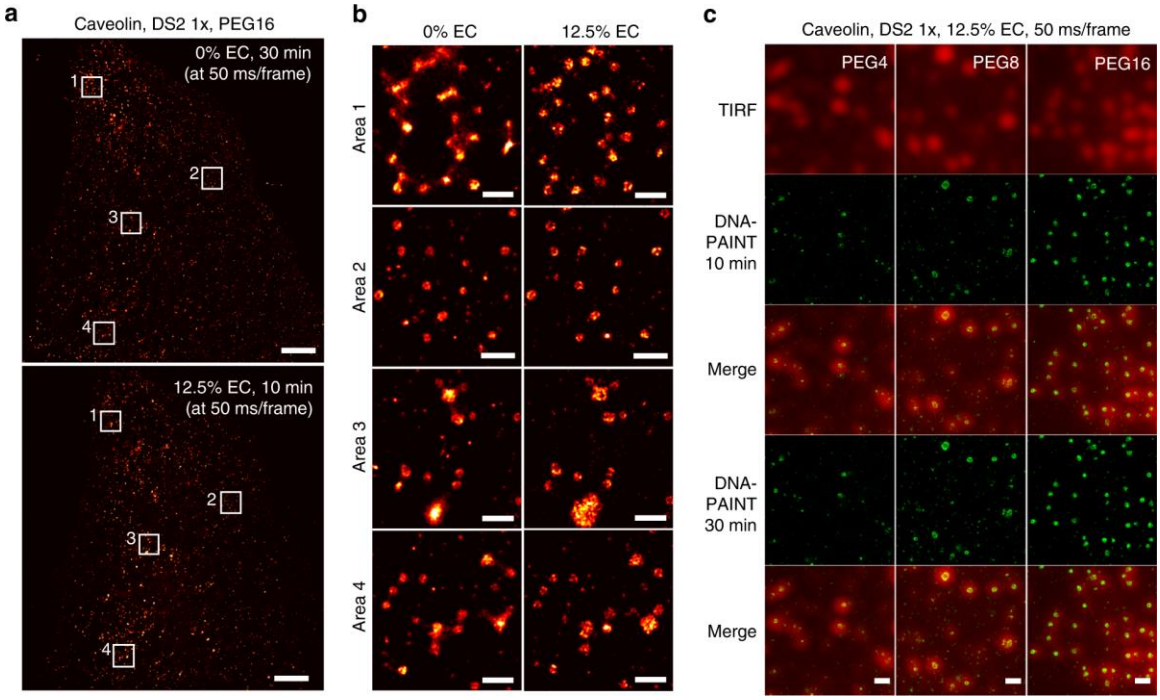

Figure A 2.2 | ERS improves DNA-PAINT image quality

a Reconstructed DNA-PAINT images of caveolae in U2OS cells in the absence (top, 30 min total acquisition time) or presence (bottom, 10 min total acquisition time) of 12.5% EC using the DS2-1x-PEG16 and the IS2 pair. The comparison was repeated four times in two independent experiments. b Zoom-in views of the boxed areas as shown in (a), representing the periphery (areas 1 and 4) and the center (areas 2 and 3) of the FOV, with results in the absence of EC shown on the left and those at 12.5% EC on the right. The center areas (2 and 3) features stronger laser intensities and therefore faster photobleaching of IS2-CF660R, which helps to improve the localization kinetics (specifically the apparent 'off' rate) and image quality. Similar results were obtained from four FOVs in two independent experiments. c Comparing reconstructed DNA-PAINT images of caveolae in U2OS cells using DS2-1x (paired with IS2-CF660R) with a PEG4 (left), PEG8 (middle), and PEG16 (right) linker. Rows 2 and 3 comprise reconstructed images using DNA-PAINT data acquired in the first 10 min (12,000 frames at 50 ms per frame), and rows 4 and 5 comprise images using data acquired in 30 min (36,000 frames at 50 ms per frame). All imaging was performed using 2 nM IS2 in buffer C supplemented with 12.5% EC. Similar results were observed from four FOVs in two independent experiments. Scale bars: 5 μm (a) and 500 nm (b and c).

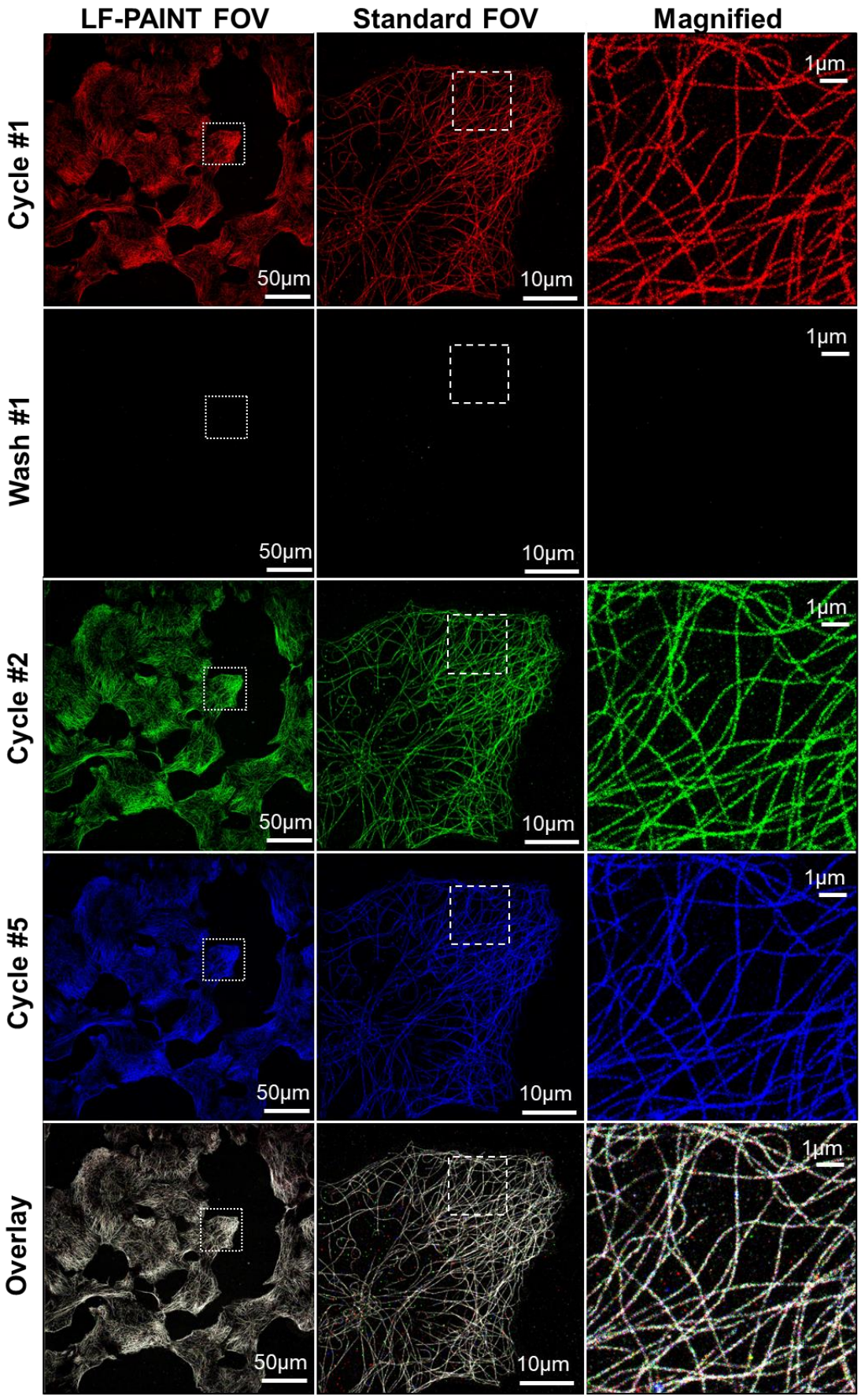
LF-PAINT FOV
Standard FOV
Magnified
Cycle #1
Wash #1
Cycle #2
Cycle #5
Overlay
50μm
10μm
1μm

Figure A 2.3 | Reproducible fluidic exchange via LF-PAINT.
Demonstration of repeated rounds of imaging and washing with representative image quality of Cos7 cell microtubules via LF-PAINT. Representative views from 1st, 2nd, and 5th cycles with intermediate 15 % EC (2 minute) washes shown in red, green, and blue, respectively. Overlay of the three indicated cycle colors shows high similarity converging onto white microtubules. Full LF-PAINT FOVs (left column) with matching views of a single cell within a smaller, more standard FOV of 50 µm (middle column). Final magnified views highlight microtubule quality (bottom row). Scale bars are 50 µm (top row), 10 µm (middle row) and 1 µm (right column).

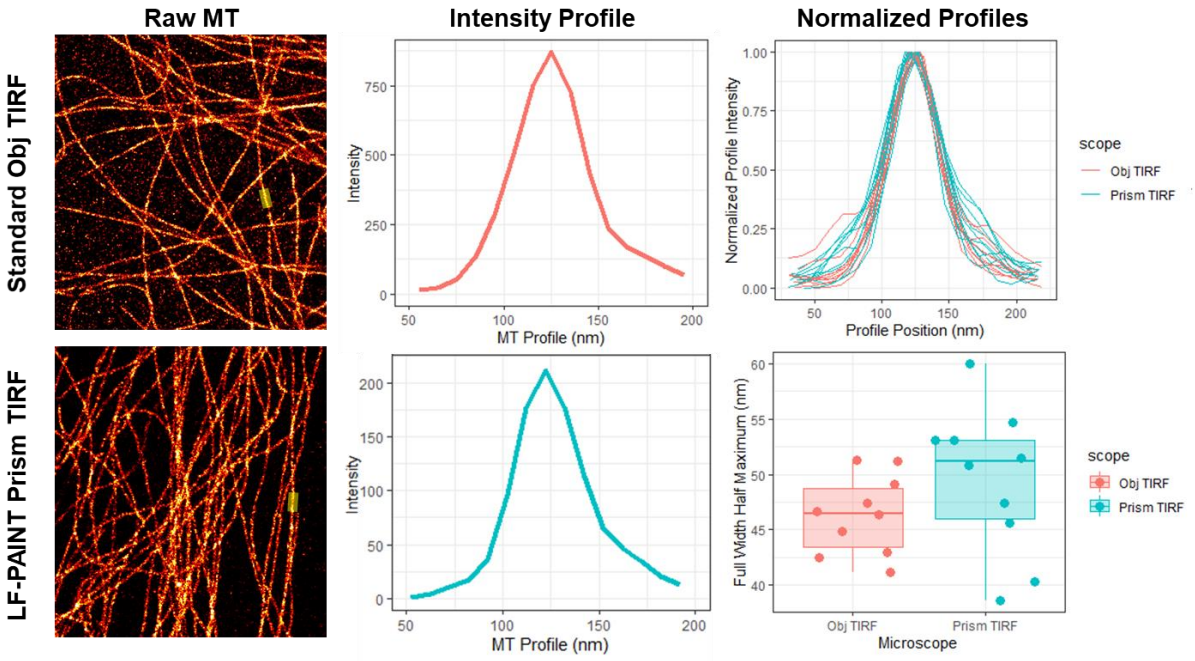

Figure A 2.4 | Resolution comparison between standard objective-type and LF-PAINT prism-type TIRF setups

Representative reconstructed images of microtubules from both microscopes (left column). Average intensity profile from 10 line-profiles of randomly selected microtubules from both microscopes (middle column). Normalized intensity for all 10 select line profiles from both microscopes and calculated Full-Width Half-Maximum (FWHM) resolution from both microscopes (right column). Both images were acquired with 30,000 frames at 30 ms exposure using 1 nM IS1-ATTO643 and 12.5 % EC.

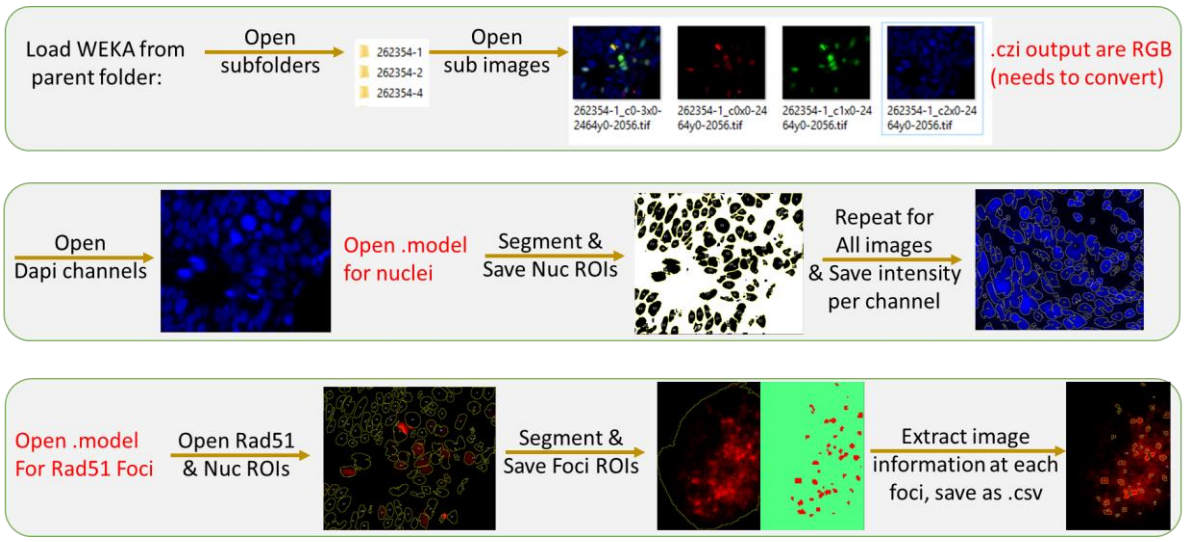

Figure A 3.1 | Workflow for automated DNA-Damage response utilizing two example classification models.

Proof of concept overview of both nuclear boundary identification and Rad51 foci analysis (using Dapi and immunolabeled Rad51 Af647 IF co-registered images). 1) First RGB images are split into corresponding channels, converting from commercial .czi files. Classification model for Dapi boundaries is loaded and iteratively applied to all images from multiple patients to save unique nuclear positions into a .roi file. After loading Rad51 foci .model file, all patient images are again re-opened, with Rad51 foci classification being identified per pre-determined nuclei .roi. Foci .roi list used to extract image attributes per classified foci per nuclei. All downstream data is saved as .csv files for downstream R analysis.

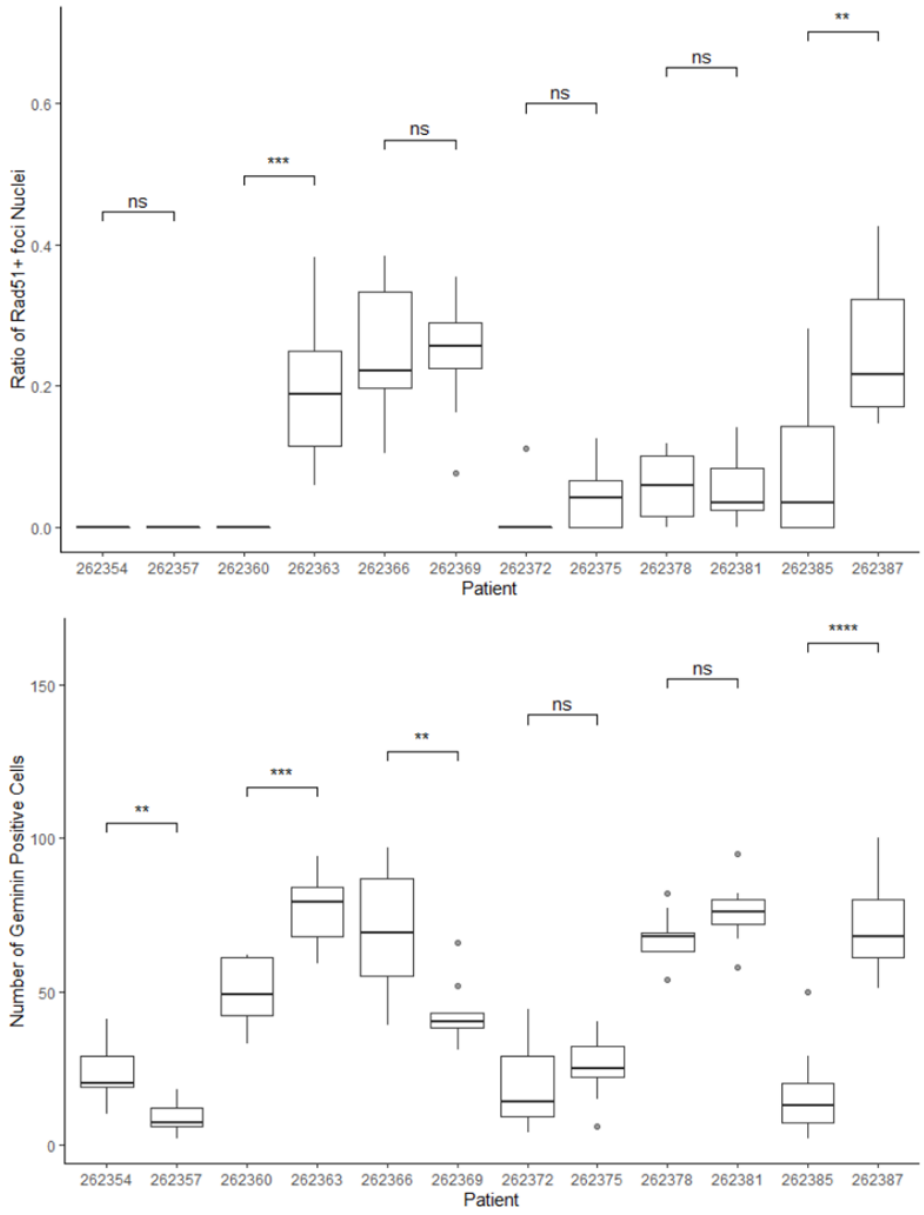

Figure A 3.2 | Statistical significance of Rad51+ foci & geminin treatments
Proof of concept prognostic changes within PDAC patients before or on PARPi treatment. Each patient sample (x axis) paired showing relative changes to both Rad51+ nuclei ratios (top plot).

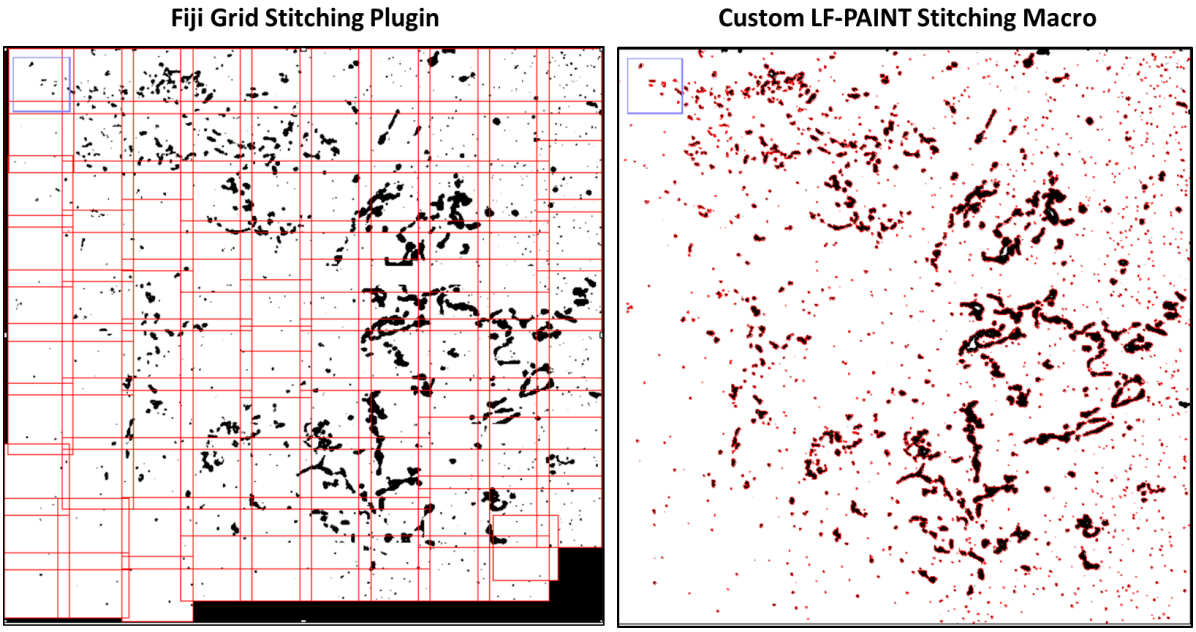

Figure A 3.3 | Comparison of Grid Stitching from WEKA ML outputs for LF-PAINT ROIs

Example 80 um x 80 um ROI from an LF-PAINT image with machine learning output from Mitochondria by alternative stitching strategies. Using assigned overlap spacing default Grid Stitching plugin shows high errors in regions with low abundance of mitochondria. Conversely, custom LF-PAINT macro recombines at original positions with overlaps removed.

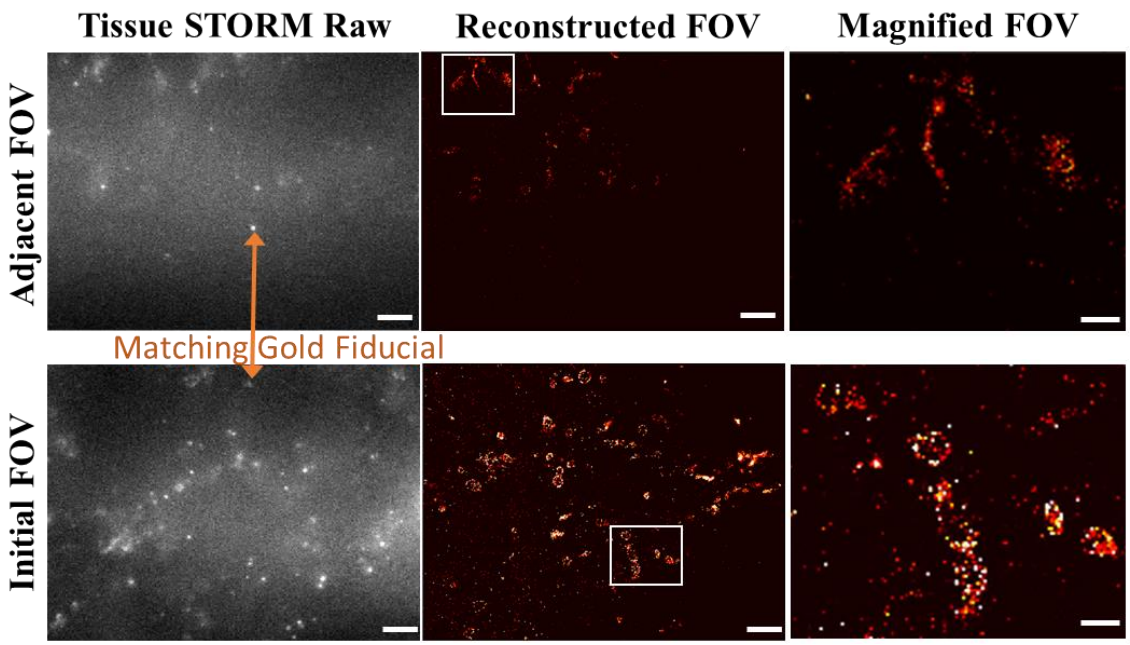

Figure A 4.1 | Photobleaching prevents Tissue-STORM larger FOV stitching (A) Raw images from tissue STORM of Tom20-AF647 from an initial FOV and adjacent FOV secondarily acquired with matching gold fiducial in orange. (B) Reconstructed images show clear mitochondria from initial FOV versus mostly photobleached and poorly visible mitochondria from Adjacent FOV. (C) Magnified regions showing clear individual mitochondria versus adjacent FOV with only poorly reconstructed mitochondria present farthest from the initial FOV. Tissue STORM images in were acquired for 50,000 frames at 20 ms exposure under strict TIR using traditional objective-type microscope. Scale bars in (A) are 5 µm, (B) are 5 µm, and (C) are 1 µm for top and bottom respectively.

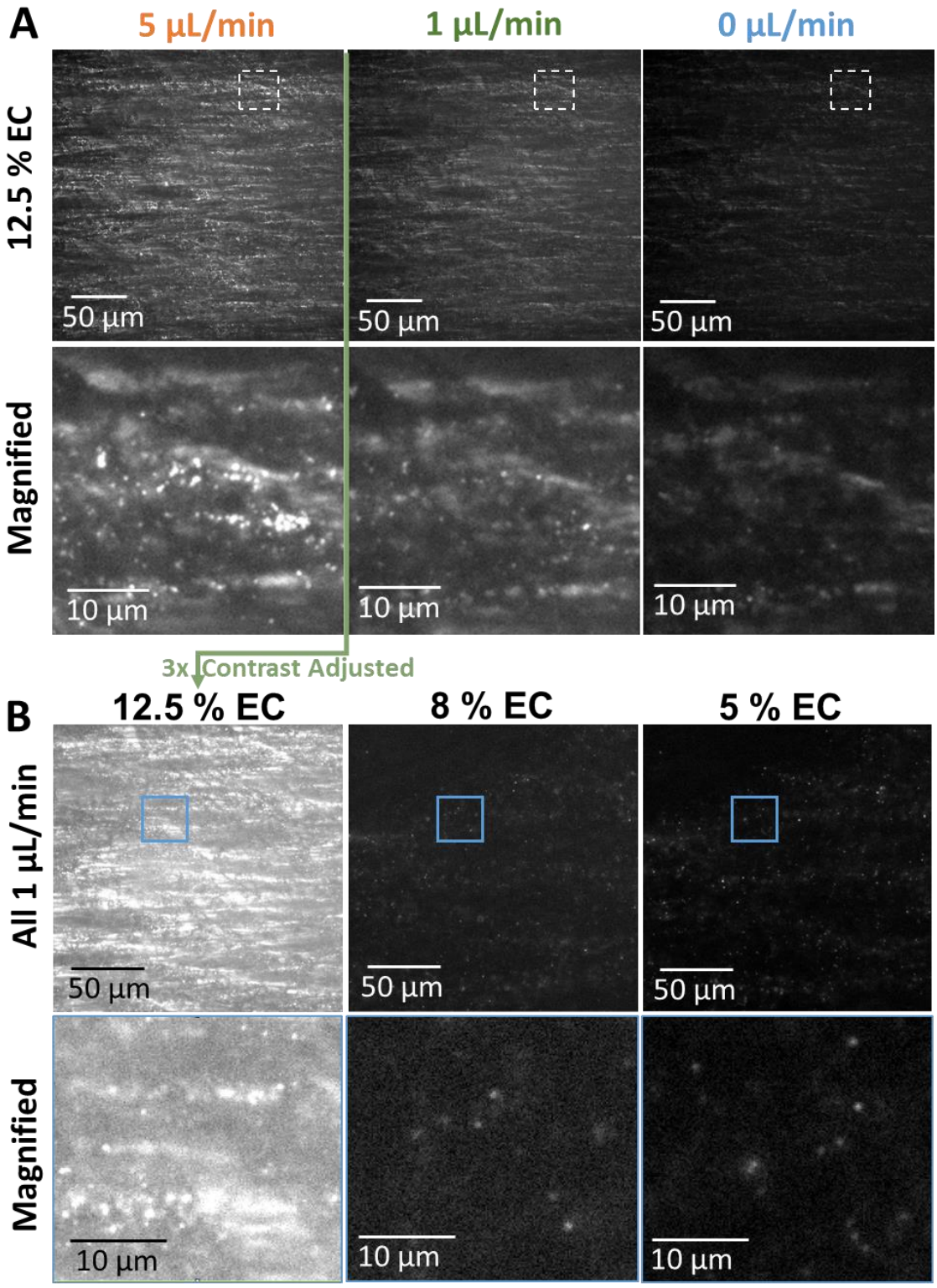
A
5 µL/min
1 µL/min
0 µL/min
12.5 % EC
Magnified
50 µm
10 µm
3x Contrast Adjusted
B
12.5 % EC
8 % EC
5 % EC
All 1 µL/min
Magnified

Figure A 4.2 | imaging buffer optimization for tissue via LF-PAINT
Representative raw frames of tissue DNA-PAINT on our LF-PAINT setup under varying EC concentration and “Flow-Assisted DNA-PAINT” flow rates. (A) Attempt at using 12.5% EC (optimal for cell-LF-PAINT imaging) results in substantial diffusive background, exacerbated under increased flow rate during imaging. Magnified views show DNA-PAINT localizations, however high diffusive background lowers image quality. (B) Matching FOV images under 1 µL / min flow while varying EC concentrations (12.5 %, 8 %, & 5 %EC). Magnified views show a dramatic lowering of background at reduced EC, while DNA-PAINT localizations are more easily resolved. All frames within (A) or (B) are shown at the same relative intensity range, with the 12.5 % EC and 1 µL / min condition being 3x contrast-adjusted between (A) and (B). Raw frames shown were all acquired using 500 pM IS2-ATTO643 and a 60 ms exposure. Scale bars in (A, B) are 50 µm (top row) and 10 µm (bottom row).

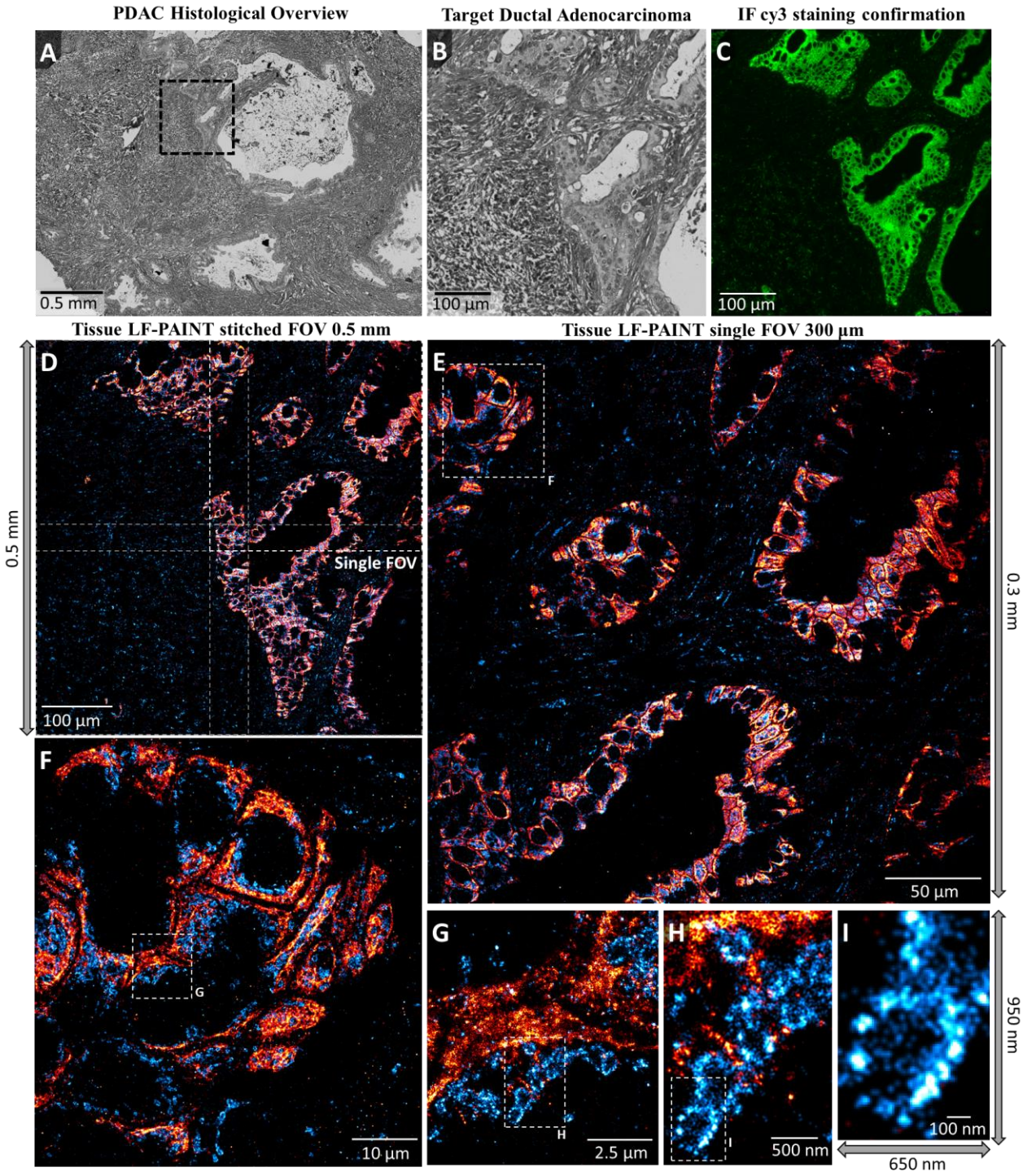
PDAC Histological Overview
Target Ductal Adenocarcinoma
IF cy3 staining confirmation
A
B
C
0.5 mm
100 µm
100 µm
Tissue LF-PAINT stitched FOV 0.5 mm
Tissue LF-PAINT single FOV 300 µm
D
E
F
Single FOV
0.5 mm
0.3 mm
100 µm
50 µm
F
G
10 µm
G
H
I
2.5 µm
500 nm
100 nm
950 nm
650 nm

Figure A 4.3 | Serial Magnification from additional FOV of multiplexed tissue LF-PAINT from clinical FFPE pancreatic cancer sample

Additional FOV of tissue DNA-PAINT from pancreatic cancer. (A) Histological overview of moderately differentiated PDAC within desmoplastic stroma acquired at 20x magnification. (B) Targeted Ductal Adenocarcinoma for imaging with LF-PAINT. (C) Immunofluorescent confirmation of Cy3 signal from secondary antibodies with DNA-PAINT oligomers showing strong pan-cytokeratin staining along the tumor and diffuse mitochondrial labeling within the tumor and adjacent stroma. (D) Stitched tissue DNA-PAINT image of entire 0.5 µm wide ductal adenocarcinoma with both prognostic Pan-cytokeratin in red and mitochondrial Tomm20 in blue. (E) Single tissue LF-PAINT image using “Flow-Assisted DNA-PAINT”. (F-I) Select serially magnified regions from (E) highlighting the increasingly fine features seen across different length scales. The entire tissue DNA-PAINT 2-target image (D-I) was acquired in 4 hours total (30,000 frames at 60 ms exposure for each target) using “Flow-Assisted DNA-PAINT” at 1 µL / min flow and 500 pM IS1-ATTO643 and 7 % EC, and 500 pM IS2-ATTO643 and 7 % EC for pan-cytokeratin and Tom20 respectively. Scale bars are 500 µm in (A), 100 uµ in (B-D), 50 µm in (E), 10 µm in (F), 2.5 µm in (G), 500 nm in (H), and 50 nm in (I).

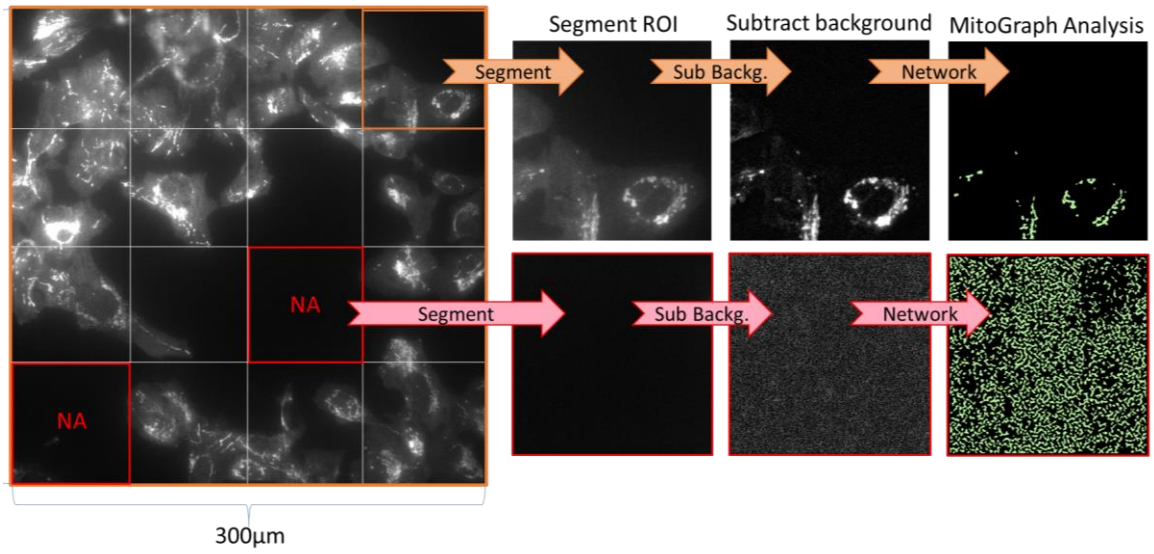

Figure A 5.1 | Automated mitochondrial network analysis using Fiji Macro and Mitograph

Representative IF FOV of U2OS cells with Tom20 labeled via AF647. Auto-scaling grid overlay subdivides each sub-ROI (example in orange), performs rolling pixel background subtraction via adjustable radius, and then performs downstream MitoGraph segmentation [119]. Notably, regions without cells (red boxes) are removed from analysis, as otherwise MitoGraph would auto-scale and determine mitochondria from camera noise.

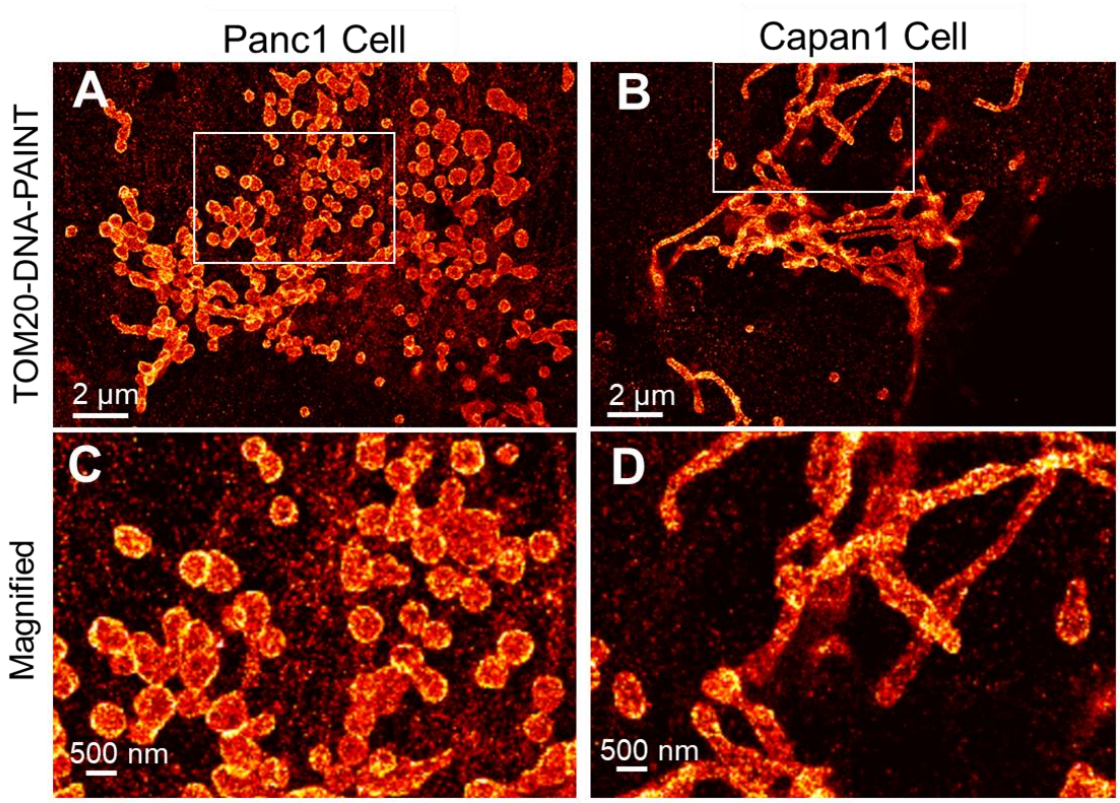

Figure A 5.2 | Mitochondrial connectivity tied to PDAC aggressiveness
(A) DNA-PAINT of Tom20 from aggressive/invasive primary tumor cell line Panc1. (B) DNA-PAINT of Tom20 from slower growing Capan1 PDAC cell line. (C & D) magnifications of Panc1 and Capan1 mitochondria respectively with clear abnormalities in connectivity. DNA PAINT images were acquired for 30,000 frames at 30 ms exposure using 1 nm IS2-ATTO643 and 12.5 % EC. Scale bar for (A&B) is 2 µm and (C&D) is 500 nm.

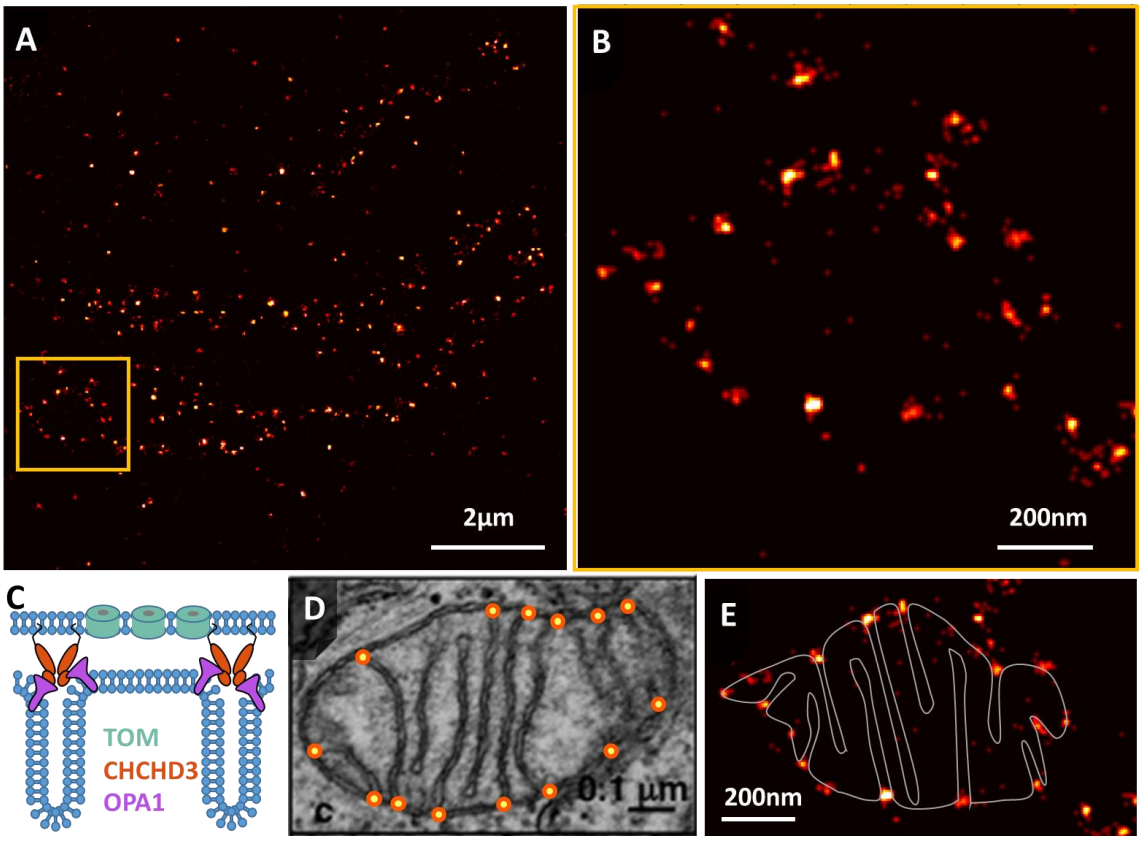

Figure A 5.3 | CHCHD3 DNA-PAINT may infer cristae structure and function
(A) Representative DNA-PAINT image of CHCHD3 in U2OS cells. (B) Magnified region from (A) showing apparent circular punctate border along mitochondria. (C) Schematic of reported CHCHD3 function to anchor cristae to the outer membrane. (D) Representative EM of mitochondria with punctate overlay at cristae/OMM junctions. (E) Manually annotated cristae drawn onto the punctate structure from (B) indicating potential cristae junction complexes visualized by DNA-PAINT. DNA PAINT images were acquired for 30,000 frames at 30 ms exposure using 1 nm IS2-CF660R at 12.5 % EC. Scale bar for (A) is 2 µm, (B) is 200 nm, (D) is 100 nm and (E) is 200 nm. (D) modified from [121].

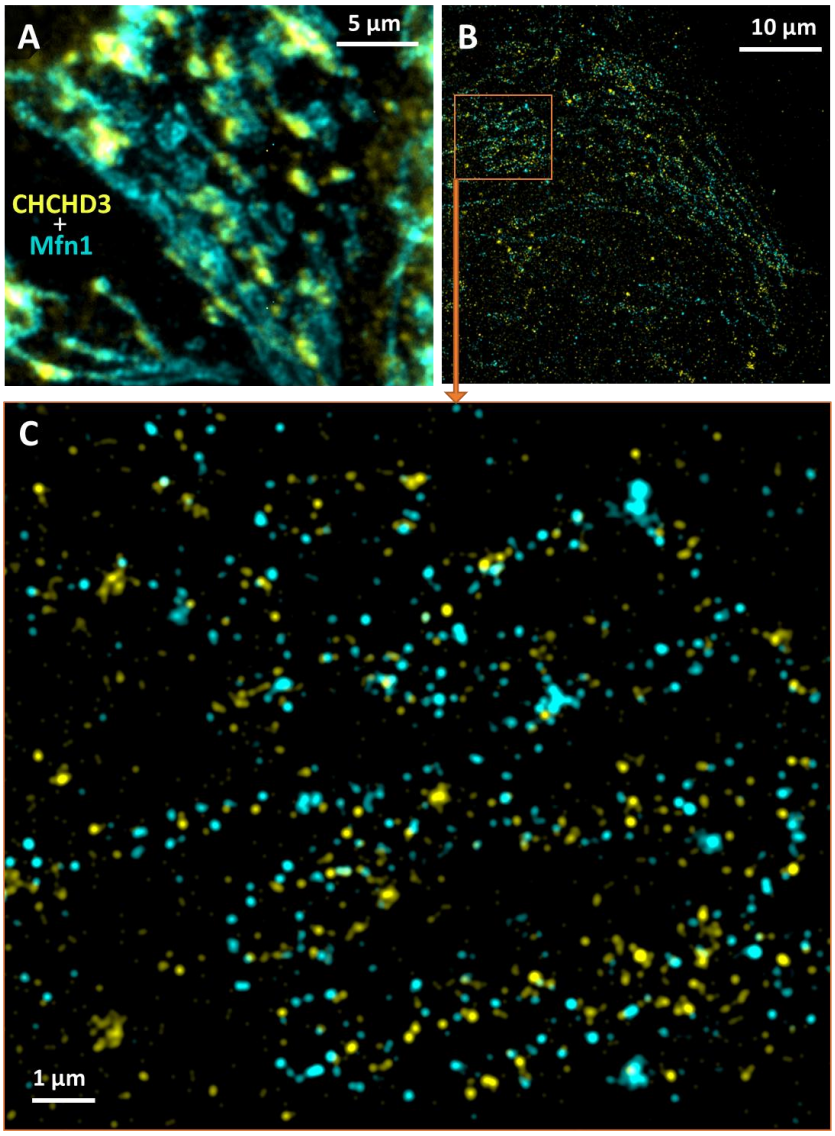

Figure A 5.4 | Relationship between CHCHD3 and Mfn1 in mitochondria
(A) Representative IF of U2OS cells dual-labeled with Mfn1 (AF488 in cyan) and CHCHD3 (AF647 in yellow). (B) Exchange paint of Mfn1 (anti-mouse DS1) and CHCHD3 (anti-rabbit DS2) from U2OS cells. (C) Magnified region from (B) with punctate clusters of both markers along mitochondria. DNA PAINT images were acquired for 30,000 frames at 30 ms exposure using 1 nm IS1-CF660R and 1 nm IS2-CF660R at 12.5 % EC. Scale bar for (A) is 5 µm, (B) is 10 µm and (C) 1 µm.

References

1. Surveilance, E., and End Results program. *Cancer Stat Facts: Pancreatic Cancer*. 2018 April 23rd 2018]; Available from: https://seer.cancer.gov/statfacts/html/pancreas.html.
2. Liberti, M.V. and J.W. Locasale, *The Warburg Effect: How Does it Benefit Cancer Cells?* Trends in biochemical sciences, 2016. **41**(3): p. 211-218.
3. Hanahan, D. and R.A. Weinberg, *Hallmarks of cancer: the next generation.* Cell, 2011. **144**(5): p. 646-74.
4. Jacquemin, V., et al., *Dynamic Cancer Cell Heterogeneity: Diagnostic and Therapeutic Implications.* Cancers (Basel), 2022. **14**(2).
5. Volonte, D., et al., *Caveolin-1 promotes the tumor suppressor properties of oncogene-induced cellular senescence.* J Biol Chem, 2018. **293**(5): p. 1794-1809.
6. Marusyk, A., M. Janiszewska, and K. Polyak, *Intratumor Heterogeneity: The Rosetta Stone of Therapy Resistance.* Cancer Cell, 2020. **37**(4): p. 471-484.
7. Cowell, C.F., et al., *Progression from ductal carcinoma in situ to invasive breast cancer: revisited.* Mol Oncol, 2013. **7**(5): p. 859-69.
8. Ramakrishna, G., et al., *From Cirrhosis to Hepatocellular Carcinoma: New Molecular Insights on Inflammation and Cellular Senescence.* Liver Cancer, 2013. **2**(3-4): p. 367-383.
9. Distler, M., et al., *Precursor Lesions for Sporadic Pancreatic Cancer: PanIN, IPMN, and MCN.* BioMed Research International, 2014. **2014**: p. 11.
10. Loud, J.T. and J. Murphy, *Cancer Screening and Early Detection in the 21(st) Century.* Seminars in oncology nursing, 2017. **33**(2): p. 121-128.
11. Donahue, T.R. and D.W. Dawson, *Leveraging mechanisms governing pancreatic tumorigenesis to reduce pancreatic cancer mortality.* Trends in endocrinology and metabolism: TEM, 2016. **27**(11): p. 770-781.
12. Iacobuzio-Donahue, C.A., *Genetic evolution of pancreatic cancer: lessons learnt from the pancreatic cancer genome sequencing project.* Gut, 2012. **61**(7): p. 1085-1094.
13. Ying, H., et al., *Oncogenic Kras Maintains Pancreatic Tumors through Regulation of Anabolic Glucose Metabolism.* Cell, 2012. **149**(3): p. 656-670.
14. Donahue, T.R. and D.W. Dawson, *Leveraging Mechanisms Governing Pancreatic Tumorigenesis To Reduce Pancreatic Cancer Mortality.* Trends Endocrinol Metab, 2016. **27**(11): p. 770-781.
15. Yu, M., et al., *Mitochondrial fusion exploits a therapeutic vulnerability of pancreatic cancer.* JCI Insight, 2019. **5**(16).
16. Yu, M., et al., *Mitochondrial Fusion Suppresses Pancreatic Cancer Growth via Reduced Oxidative Metabolism.* bioRxiv, 2018.
17. Yuen, A. and B. Díaz, *The impact of hypoxia in pancreatic cancer invasion and metastasis.* Hypoxia (Auckland, N.Z.), 2014. **2**: p. 91-106.
18. Fuhrmann, D.C. and B. Brüne, *Mitochondrial composition and function under the control of hypoxia.* Redox Biol, 2017. **12**: p. 208-215.
19. Lin, J.R., M. Fallahi-Sichani, and P.K. Sorger, *Highly multiplexed imaging of single cells using a high-throughput cyclic immunofluorescence method.* Nat Commun, 2015. **6**: p. 8390.

20. Eng, J., et al., *Cyclic Multiplexed-Immunofluorescence (cmIF), a Highly Multiplexed Method for Single-Cell Analysis.* Methods Mol Biol, 2020. **2055**: p. 521-562.
21. Van der Maaten, L. and G. Hinton, *Visualizing data using t-SNE.* Journal of machine learning research, 2008. **9**(11).
22. Allam, M., S. Cai, and A.F. Coskun, *Multiplex bioimaging of single-cell spatial profiles for precision cancer diagnostics and therapeutics.* NPJ Precis Oncol, 2020. **4**: p. 11.
23. Betzig, E., et al., *Imaging intracellular fluorescent proteins at nanometer resolution.* Science, 2006. **313**(5793): p. 1642-5.
24. Hess, S.T., T.P. Girirajan, and M.D. Mason, *Ultra-high resolution imaging by fluorescence photoactivation localization microscopy.* Biophys J, 2006. **91**(11): p. 4258-72.
25. Rust, M.J., M. Bates, and X. Zhuang, *Sub-diffraction-limit imaging by stochastic optical reconstruction microscopy (STORM).* Nat Methods, 2006. **3**(10): p. 793-5.
26. Gray, N., *Knowing the limit.* Nature Cell Biology, 2009. **11**(1): p. S8-S8.
27. Thompson, R.E., D.R. Larson, and W.W. Webb, *Precise Nanometer Localization Analysis for Individual Fluorescent Probes.* Biophysical Journal, 2002. **82**(5): p. 2775-2783.
28. van de Linde, S., et al., *The effect of photoswitching kinetics and labeling densities on super-resolution fluorescence imaging.* J Biotechnol, 2010. **149**(4): p. 260-6.
29. Li, L., et al., *Divide and conquer: real-time maximum likelihood fitting of multiple emitters for super-resolution localization microscopy.* Opt Express, 2019. **27**(15): p. 21029-21049.
30. Huang, B., et al., *Whole-cell 3D STORM reveals interactions between cellular structures with nanometer-scale resolution.* Nat Methods, 2008. **5**(12): p. 1047-52.
31. Ovesný, M., et al., *ThunderSTORM: a comprehensive ImageJ plug-in for PALM and STORM data analysis and super-resolution imaging.* Bioinformatics (Oxford, England), 2014. **30**(16): p. 2389-2390.
32. Pavani, S.R., et al., *Three-dimensional, single-molecule fluorescence imaging beyond the diffraction limit by using a double-helix point spread function.* Proc Natl Acad Sci U S A, 2009. **106**(9): p. 2995-9.
33. Pereira, C.F., et al., *HIV taken by STORM: Super-resolution fluorescence microscopy of a viral infection.* Virology Journal, 2012. **9**(1): p. 84.
34. Salvador-Gallego, R., et al., *Bax assembly into rings and arcs in apoptotic mitochondria is linked to membrane pores.* Embo j, 2016. **35**(4): p. 389-401.
35. Nan, X., et al., *Single-molecule superresolution imaging allows quantitative analysis of RAF multimer formation and signaling.* Proceedings of the National Academy of Sciences of the United States of America, 2013. **110**(46): p. 18519-18524.
36. Lee, Y., et al., *High-throughput, single-particle tracking reveals nested membrane domains that dictate KRasG12D diffusion and trafficking.* eLife, 2019. **8**: p. e46393.
37. Creech, M.K., et al., *Superresolution Imaging of Clinical Formalin Fixed Paraffin Embedded Breast Cancer with Single Molecule Localization Microscopy.* Sci Rep, 2017. **7**: p. 40766.
38. Xu, J., et al., *Super-resolution imaging reveals the evolution of higher-order chromatin folding in early carcinogenesis.* Nat Commun, 2020. **11**(1): p. 1899.

39. Schnitzbauer, J., et al., *Super-resolution microscopy with DNA-PAINT.* Nat Protoc, 2017. **12**(6): p. 1198-1228.
40. Sharonov, A. and R.M. Hochstrasser, *Wide-field subdiffraction imaging by accumulated binding of diffusing probes.* Proc Natl Acad Sci U S A, 2006. **103**(50): p. 18911-6.
41. Dempsey, G.T., et al., *Evaluation of fluorophores for optimal performance in localization-based super-resolution imaging.* Nat Methods, 2011. **8**(12): p. 1027-36.
42. Agasti, S.S., et al., *DNA-barcoded labeling probes for highly multiplexed Exchange-PAINT imaging.* Chem Sci, 2017. **8**(4): p. 3080-3091.
43. Nickerson, A., et al., *Photoactivated Localization Microscopy with Bimolecular Fluorescence Complementation (BiFC-PALM).* J Vis Exp, 2015(106): p. e53154.
44. Ester, M., et al. *A density-based algorithm for discovering clusters in large spatial databases with noise*. in *kdd*. 1996.
45. Willems, J. and H.D. MacGillavry, *A coordinate-based co-localization index to quantify and visualize spatial associations in single-molecule localization microscopy.* Scientific Reports, 2022. **12**(1): p. 4676.
46. Levet, F., et al., *A tessellation-based colocalization analysis approach for single-molecule localization microscopy.* Nature Communications, 2019. **10**(1): p. 2379.
47. Szymborska, A., et al., *Nuclear Pore Scaffold Structure Analyzed by Super-Resolution Microscopy and Particle Averaging.* Science, 2013. **341**(6146): p. 655-658.
48. Markus Mund, A.T., Yu-Le Wu, Felix Frey, Johanna L. Mehl, Marko Kaksonen, Ori Avinoam, Ulrich S. Schwarz, Jonas Ries, *Superresolution microscopy reveals partial preassembly and subsequent bending of the clathrin coat during endocytosis.* 2021.
49. Arganda-Carreras, I., et al., *Trainable Weka Segmentation: a machine learning tool for microscopy pixel classification.* Bioinformatics, 2017. **33**(15): p. 2424-2426.
50. Civitci, F., et al., *Fast and multiplexed superresolution imaging with DNA-PAINT-ERS.* Nat Commun, 2020. **11**(1): p. 4339.
51. Jungmann, R., et al., *Multiplexed 3D cellular super-resolution imaging with DNA-PAINT and Exchange-PAINT.* Nature methods, 2014. **11**(3): p. 313-318.
52. Stehr, F., et al., *Flat-top TIRF illumination boosts DNA-PAINT imaging and quantification.* Nature communications, 2019. **10**(1): p. 1-8.
53. Auer, A., et al., *Fast, background-free DNA-PAINT imaging using FRET-based probes.* Nano letters, 2017. **17**(10): p. 6428-6434.
54. Lee, J., et al., *Accelerated super-resolution imaging with FRET-PAINT.* Molecular brain, 2017. **10**(1): p. 1-9.
55. Lee, J., S. Park, and S. Hohng, *Accelerated fret-paint microscopy.* Molecular brain, 2018. **11**(1): p. 1-7.
56. Schueder, F., et al., *An order of magnitude faster DNA-PAINT imaging by optimized sequence design and buffer conditions.* Nat Methods, 2019. **16**(11): p. 1101-1104.
57. Menyhárt, O. and B. Győrffy, *Multi-omics approaches in cancer research with applications in tumor subtyping, prognosis, and diagnosis.* Comput Struct Biotechnol J, 2021. **19**: p. 949-960.
58. Hein, B., K.I. Willig, and S.W. Hell, *Stimulated emission depletion (STED) nanoscopy of a fluorescent protein-labeled organelle inside a living cell.* Proc Natl Acad Sci U S A, 2008. **105**(38): p. 14271-6.

59. Tröger, J., et al., *Comparison of Multiscale Imaging Methods for Brain Research.* Cells, 2020. **9**(6).
60. Zhao, Z., et al., *High-power homogeneous illumination for super-resolution localization microscopy with large field-of-view.* Opt Express, 2017. **25**(12): p. 13382-13395.
61. Mau, A., et al., *Fast widefield scan provides tunable and uniform illumination optimizing super-resolution microscopy on large fields.* Nat Commun, 2021. **12**(1): p. 3077.
62. Archetti, A., et al., *Waveguide-PAINT offers an open platform for large field-of-view super-resolution imaging.* Nat Commun, 2019. **10**(1): p. 1267.
63. Werbin, J.L., et al., *Multiplexed Exchange-PAINT imaging reveals ligand-dependent EGFR and Met interactions in the plasma membrane.* Sci Rep, 2017. **7**(1): p. 12150.
64. Fehmi Civitci, J.S., Ting Zheng, Kai Tao, Matthew Rames, Xiaolin Nan, *Sample preparation and imaging procedures for fast and multiplexed superresolution microscopy with DNA-PAINT-ERS.* Protocol Exchange, 2020.
65. Edelstein, A.D., et al., *Advanced methods of microscope control using μManager software.* J Biol Methods, 2014. **1**(2).
66. Matthiesen, S.H. and C.M. Hansen, *Fast and non-toxic in situ hybridization without blocking of repetitive sequences.* PloS one, 2012. **7**(7): p. e40675.
67. Prigodich, A.E., et al., *Tailoring DNA structure to increase target hybridization kinetics on surfaces.* Journal of the American Chemical Society, 2010. **132**(31): p. 10638-10641.
68. Bates, M., et al., *Multicolor super-resolution imaging with photo-switchable fluorescent probes.* Science, 2007. **317**(5845): p. 1749-1753.
69. Marsh, M. and H. McMahon, *The structural era of endocytosis.* Science, 1999. **285**(5425): p. 215-220.
70. Grove, J., et al., *Flat clathrin lattices: stable features of the plasma membrane.* Molecular biology of the cell, 2014. **25**(22): p. 3581-3594.
71. Jungmann, R., et al., *Quantitative super-resolution imaging with qPAINT.* Nature methods, 2016. **13**(5): p. 439-442.
72. Zhang, M., et al., *Rational design of true monomeric and bright photoactivatable fluorescent proteins.* Nat Methods, 2012. **9**(7): p. 727-9.
73. Strauss, S. and R. Jungmann, *Up to 100-fold speed-up and multiplexing in optimized DNA-PAINT.* Nat Methods, 2020. **17**(8): p. 789-791.
74. Axelrod, D., *Cell-substrate contacts illuminated by total internal reflection fluorescence.* J Cell Biol, 1981. **89**(1): p. 141-5.
75. *Silicone Immersion Objectives Boost 3D Live-Cell Imaging*, in *BioPhotonics*. Olympus: https://www.photonics.com/Articles/Silicone_Immersion_Objectives_Boost_3D_Live-Cell/a62855.
76. Squires, T.M. and S.R. Quake, *Microfluidics: Fluid physics at the nanoliter scale.* Reviews of Modern Physics, 2005. **77**(3): p. 977-1026.
77. Hirst, W.G., et al., *In Vitro Reconstitution and Imaging of Microtubule Dynamics by Fluorescence and Label-free Microscopy.* STAR Protoc, 2020. **1**(3): p. 100177.
78. Huang, F., et al., *Ultra-High Resolution 3D Imaging of Whole Cells.* Cell, 2016. **166**(4): p. 1028-1040.
79. Almada, P., et al., *Automating multimodal microscopy with NanoJ-Fluidics.* Nat Commun, 2019. **10**(1): p. 1223.

80. Klevanski, M., et al., *Automated highly multiplexed super-resolution imaging of protein nano-architecture in cells and tissues.* Nat Commun, 2020. **11**(1): p. 1552.
81. Oleksiievets, N., et al., *Fluorescence lifetime DNA-PAINT for multiplexed super-resolution imaging of cells.* Commun Biol, 2022. **5**(1): p. 38.
82. Yin, L., et al., *A review of the application of machine learning in molecular imaging.* Annals of translational medicine, 2021. **9**(9): p. 825-825.
83. Ouyang, W., et al., *Deep learning massively accelerates super-resolution localization microscopy.* Nature Biotechnology, 2018. **36**(5): p. 460-468.
84. Hosoya, N. and K. Miyagawa, *Targeting DNA damage response in cancer therapy.* Cancer science, 2014. **105**(4): p. 370-388.
85. Chi, J., et al., *The role of PARP inhibitors in BRCA mutated pancreatic cancer.* Therapeutic advances in gastroenterology, 2021. **14**: p. 17562848211014818-17562848211014818.
86. Cruz, C., et al., *RAD51 foci as a functional biomarker of homologous recombination repair and PARP inhibitor resistance in germline BRCA-mutated breast cancer.* Annals of oncology : official journal of the European Society for Medical Oncology, 2018. **29**(5): p. 1203-1210.
87. Eliceiri, K.W., et al., *Biological imaging software tools.* Nat Methods, 2012. **9**(7): p. 697-710.
88. Lin, J.-R., et al., *Highly multiplexed immunofluorescence imaging of human tissues and tumors using t-CyCIF and conventional optical microscopes.* eLife, 2018. **7**: p. e31657.
89. Nan, X., et al., *Ras-GTP dimers activate the Mitogen-Activated Protein Kinase (MAPK) pathway.* Proc Natl Acad Sci U S A, 2015. **112**(26): p. 7996-8001.
90. Anderson, R.G. and K. Jacobson, *A role for lipid shells in targeting proteins to caveolae, rafts, and other lipid domains.* Science, 2002. **296**(5574): p. 1821-5.
91. Basu Roy, U.K., et al., *Caveolin-1 is a novel regulator of K-RAS-dependent migration in colon carcinogenesis.* Int J Cancer, 2013. **133**(1): p. 43-57.
92. Smith, C.S., et al., *Fast, single-molecule localization that achieves theoretically minimum uncertainty.* Nat Methods, 2010. **7**(5): p. 373-5.
93. Przybylski, A., et al., *Gpufit: An open-source toolkit for GPU-accelerated curve fitting.* Sci Rep, 2017. **7**(1): p. 15722.
94. Li, Y., et al., *Real-time 3D single-molecule localization using experimental point spread functions.* Nat Methods, 2018. **15**(5): p. 367-369.
95. Graham, L. and J.M. Orenstein, *Processing tissue and cells for transmission electron microscopy in diagnostic pathology and research.* Nature Protocols, 2007. **2**(10): p. 2439-2450.
96. Collins, H.E., et al., *Mitochondrial Morphology and Mitophagy in Heart Diseases: Qualitative and Quantitative Analyses Using Transmission Electron Microscopy.* Frontiers in Aging, 2021. **2**.
97. Adhikari, P., et al., *Studying nanoscale structural alterations in cancer cells to evaluate ovarian cancer drug treatment, using transmission electron microscopy imaging.* Physical biology, 2020. **17**(3): p. 036005-036005.
98. Karreman, M.A., et al., *Correlating intravital multi-photon microscopy to 3D electron microscopy of invading tumor cells using anatomical reference points.* PLoS One, 2014. **9**(12): p. e114448.
99. Fortunato, F., et al., *Retrospective electron microscopy: Preservation of fine structure by freezing and aldehyde fixation.* Molecular & cellular oncology, 2016. **3**(6): p. e1251382-e1251382.

100. Jones, J.C.R., *Pre- and Post-embedding Immunogold Labeling of Tissue Sections.* Methods in molecular biology (Clifton, N.J.), 2016. **1474**: p. 291-307.
101. Yang, G., et al., *Probing Electrolyte Solvents at Solid/Liquid Interface Using Gap-Mode Surface-Enhanced Raman Spectroscopy.* Journal of The Electrochemical Society, 2019. **166**(2): p. A178-A187.
102. Prieto, J., et al., *Early ERK1/2 activation promotes DRP1-dependent mitochondrial fission necessary for cell reprogramming.* Nature Communications, 2016. **7**(1): p. 11124.
103. Wellen, K.E. and C.B. Thompson, *Cellular metabolic stress: Considering how cells respond to nutrient excess.* Molecular cell, 2010. **40**(2): p. 323-332.
104. Fuhrmann, D.C. and B. Brüne, *Mitochondrial composition and function under the control of hypoxia.* Redox Biology, 2017. **12**: p. 208-215.
105. Fogg, V.C., N.J. Lanning, and J.P. MacKeigan, *Mitochondria in cancer: at the crossroads of life and death.* Chinese Journal of Cancer, 2011. **30**(8): p. 526-539.
106. Simula, L., F. Nazio, and S. Campello, *The mitochondrial dynamics in cancer and immune-surveillance.* Seminars in Cancer Biology, 2017. **47**: p. 29-42.
107. Yuen, A. and B. Díaz, *The impact of hypoxia in pancreatic cancer invasion and metastasis.* Hypoxia, 2014. **2**: p. 91-106.
108. Feig, C., et al., *The Pancreas Cancer Microenvironment.* Clinical Cancer Research, 2012. **18**(16): p. 4266.
109. Erkan, M., et al., *Cancer-Stellate Cell Interactions Perpetuate the Hypoxia-Fibrosis Cycle in Pancreatic Ductal Adenocarcinoma.* Neoplasia, 2009. **11**(5): p. 497-508.
110. Taylor, E., et al., *Impact of tissue transport on PET hypoxia quantification in pancreatic tumours.* EJNMMI Research, 2017. **7**: p. 101.
111. Jayashankar, V. and S.M. Rafelski, *Integrating mitochondrial organization and dynamics with cellular architecture.* Current Opinion in Cell Biology, 2014. **26**: p. 34-40.
112. Kashatus, J.A., et al., *Erk2 phosphorylation of Drp1 promotes mitochondrial fission and MAPK-driven tumor growth.* Molecular cell, 2015. **57**(3): p. 537-551.
113. Prieto, J., et al., *Early ERK1/2 activation promotes DRP1-dependent mitochondrial fission necessary for cell reprogramming.* Nature Communications, 2016. **7**: p. 11124.
114. de Matos, L.L., et al., *Immunohistochemistry as an Important Tool in Biomarkers Detection and Clinical Practice.* Biomarker Insights, 2010. **5**: p. 9-20.
115. Rossignol, R., et al., *Energy Substrate Modulates Mitochondrial Structure and Oxidative Capacity in Cancer Cells.* Cancer Research, 2004. **64**(3): p. 985.
116. Hackenbrock, C.R., *ULTRASTRUCTURAL BASES FOR METABOLICALLY LINKED MECHANICAL ACTIVITY IN MITOCHONDRIA : I. Reversible Ultrastructural Changes with Change in Metabolic Steady State in Isolated Liver Mitochondria.* The Journal of Cell Biology, 1966. **30**(2): p. 269-297.
117. Paez Segala, M.G., et al., *Fixation-resistant photoactivatable fluorescent proteins for correlative light and electron microscopy.* Nature methods, 2015. **12**(3): p. 215-218.
118. Creech, M.K., et al., *Superresolution Imaging of Clinical Formalin Fixed Paraffin Embedded Breast Cancer with Single Molecule Localization Microscopy.* Scientific Reports, 2017. **7**: p. 40766.
119. Harwig, M.C., et al., *Methods for imaging mammalian mitochondrial morphology: A prospective on MitoGraph.* Anal Biochem, 2018. **552**: p. 81-99.
120. Suszynski, T.M., et al., *Metabolic profile of pancreatic acinar and islet tissue in culture.* Transplant Proc, 2014. **46**(6): p. 1960-2.

121. Darshi, M., et al., *ChChd3, an inner mitochondrial membrane protein, is essential for maintaining crista integrity and mitochondrial function.* J Biol Chem, 2011. **286**(4): p. 2918-32.
122. Ji, W.-k., et al., *Actin filaments target the oligomeric maturation of the dynamin GTPase Drp1 to mitochondrial fission sites.* eLife, 2015. **4**: p. e11553.
123. Kalia, R., et al., *Structural basis of mitochondrial receptor binding and constriction by DRP1.* Nature, 2018. **558**(7710): p. 401-405.
124. Nickerson, A., et al., *Photoactivated Localization Microscopy with Bimolecular Fluorescence Complementation (BiFC-PALM) for Nanoscale Imaging of Protein-Protein Interactions in Cells.* PLoS ONE, 2014. **9**(6): p. e100589.
125. Carmona-Carmona, C.A., et al., *Divergent Roles of Mitochondria Dynamics in Pancreatic Ductal Adenocarcinoma.* Cancers (Basel), 2022. **14**(9).
126. Shtengel, G., et al., *Interferometric fluorescent super-resolution microscopy resolves 3D cellular ultrastructure.* Proceedings of the National Academy of Sciences of the United States of America, 2009. **106**(9): p. 3125-3130.
127. Rothberg, K.G., et al., *Caveolin, a protein component of caveolae membrane coats.* Cell, 1992. **68**(4): p. 673-82.
128. Mazloom-Farsibaf, H., et al., *Comparing lifeact and phalloidin for super-resolution imaging of actin in fixed cells.* PLoS One, 2021. **16**(1): p. e0246138.
129. Pleiner, T., M. Bates, and D. Görlich, *A toolbox of anti-mouse and anti-rabbit IgG secondary nanobodies.* The Journal of cell biology, 2018. **217**(3): p. 1143-1154.
130. Eklund, A.S., et al., *Peptide-PAINT Super-Resolution Imaging Using Transient Coiled Coil Interactions.* Nano letters, 2020. **20**(9): p. 6732-6737.
131. Kozma, E. and P. Kele, *Fluorogenic probes for super-resolution microscopy.* Org Biomol Chem, 2019. **17**(2): p. 215-233.